

**Modeling the effect of a heterogeneous ecosystem  
on atmospheric energy transport**

Zur Erlangung des akademischen Grades einer  
DOKTORIN DER NATURWISSENSCHAFTEN (Dr. rer. nat.)

von der KIT-Fakultät für

Bauingenieur-, Geo- und Umweltwissenschaften des

Karlsruher Instituts für Technologie (KIT)

genehmigte

DISSERTATION

von

M.Sc. Luise Wanner

geb. in Stuttgart

Tag der mündlichen Prüfung:

04.03.2024

Referent: Matthias Mauder

Korreferent: Ankur Desai

Korreferent: Jan Cermak

Karlsruhe (2024)



# ABSTRACT

Measurements of atmospheric energy fluxes are highly relevant to a wide range of scientific applications, such as the investigation of climate change related feedback processes between ecosystems and the atmosphere and the validation of land surface models deployed in numerical weather prediction and climate models. However, research on the systematic non-closure of the surface energy balance has revealed that the widely used eddy covariance method underestimates atmospheric energy fluxes. The energy transport by so called secondary circulations was identified as one major contributor to this underestimation, especially in heterogeneous ecosystems. By definition, it cannot be captured by eddy covariance measurements and expensive and labor-intensive measurements would be required to quantify it.

The main objective of this work was therefore to investigate the influence of heterogeneous ecosystems on the energy transport by secondary circulations and develop a model that predicts it as a function of all relevant environmental factors, including the ecosystem heterogeneity. The model should be suitable for correcting the atmospheric energy fluxes measured at eddy covariance stations without the need for additional expensive measurements.

Since idealized large-eddy simulations are often used to systematically investigate atmospheric transport processes but were found to underestimate dispersive heat fluxes, which represent the energy transport by secondary circulations, a study was carried out to examine the effect of different lower boundary conditions on those dispersive heat fluxes. Using a set of idealized large-eddy simulations featuring heterogeneous surface temperatures, a previously existing model of the entire surface energy imbalance, including not only dispersive heat fluxes but also energy storage changes, was further developed to consider the effect of surface heterogeneity. It confirmed that the magnitude of the surface energy imbalance scales with thermal surface heterogeneity and depends on the shape of secondary circulations.

Finally, a comprehensive set of idealized large-eddy simulations was combined with a machine learning approach to develop a model of dispersive heat fluxes. Based on the learnings from the previous model, special care was taken to facilitate the applicability to field measurements, for example by using a spectral approach for determining the heterogeneity length scale. This approach can be applied to unstructured heterogeneity which is found in most landscapes. The model was further tested on realistic large-eddy simulations and field measurements from the CHEESEHEAD19 campaign. Despite some room for improvement, the comparison showed good agreements with the realistic large-eddy simulations and field measurements. It was furthermore shown that this model can be applied to field

measurements without any additional instrumentation, which even facilitates a retrospective application to long-term eddy covariance measurements.

# ZUSAMMENFASSUNG

Messungen der atmosphärischen Energieflüsse sind für ein breites Spektrum wissenschaftlicher Anwendungen von großer Bedeutung, wie beispielsweise für die Untersuchung von Rückkopplungsprozessen zwischen Ökosystemen und der Atmosphäre im Zusammenhang mit dem Klimawandel und für die Validierung von Landoberflächenmodellen, die in numerischen Wettervorhersage- und Klimamodellen eingesetzt werden. Die Erforschung der systematischen Lücke in der Energiebilanz der Erdoberfläche hat jedoch gezeigt, dass die weit verbreitete Eddy-Kovarianz-Methode die atmosphärischen Energieflüsse unterschätzt. Der Energietransport durch so genannte Sekundärzirkulationen wurde als einer der Hauptgründe für diese Unterschätzung identifiziert, insbesondere über heterogenen Ökosystemen. Er kann durch Eddy-Kovarianz-Messungen definitionsgemäß nicht erfasst werden. Teure und arbeitsintensive Messungen wären erforderlich, um ihn zu quantifizieren.

Das Hauptziel dieser Arbeit war es daher, den Einfluss heterogener Ökosysteme auf den Energietransport durch Sekundärzirkulationen zu untersuchen und ein Modell zu entwickeln, das diesen in Abhängigkeit von allen relevanten Umweltfaktoren, einschließlich der Ökosystemheterogenität, vorhersagt. Das Modell sollte dazu geeignet sein, die an Eddy-Kovarianz-Stationen gemessenen atmosphärischen Energieflüsse ohne zusätzliche teure Messungen zu korrigieren.

Idealisierte Large-Eddy-Simulationen werden häufig zur systematischen Untersuchung atmosphärischer Transportprozesse verwendet, unterschätzen jedoch die dispersiven Wärmeflüsse, die den Energietransport durch Sekundärzirkulationen repräsentieren. Deshalb wurde eine Studie durchgeführt, um die Auswirkungen verschiedener Randbedingungen auf die dispersiven Wärmeflüsse zu untersuchen. Mithilfe idealisierter Large-Eddy-Simulationen mit heterogenen Oberflächentemperaturen wurde anschließend ein bereits bestehendes Modell des gesamten Ungleichgewichts in der Energiebilanz weiterentwickelt, sodass der Effekt der Oberflächenheterogenität auch berücksichtigt wird. Zu diesem Ungleichgewicht tragen nicht nur die dispersiven Wärmeströme, sondern auch Energiespeicheränderungen bei. Diese Studie bestätigte, dass das Ausmaß des Ungleichgewichts in der Energiebilanz mit der thermischen Oberflächenheterogenität skaliert und von der Form der Sekundärzirkulationen abhängt.

Schließlich wurde ein Satz umfassender idealisierter Large-Eddy-Simulationen mit einem Machine Learning Ansatz kombiniert, um ein Modell der dispersiven Flüsse zu entwickeln. Auf Basis der Erkenntnisse aus dem vorangegangenen Modell wurde hierbei besonders darauf geachtet, die Anwendbarkeit auf Feldmessungen zu erleichtern, indem beispielsweise ein spektraler Ansatz zur Bestimmung der Heterogenitätsskalen verwendet wurde. Dieser kann auch bei unstrukturierter Heterogenität, die in den meisten Landschaften vorherrscht, angewendet werden. Das Modell wurde außerdem an realistischen Large-

Eddy-Simulationen und Feldmessungen aus der CHEESEHEAD19-Kampagne getestet. Trotz einiger Verbesserungsmöglichkeiten zeigte der Vergleich gute Übereinstimmungen mit den realistischen Large-Eddy-Simulationen und Feldmessungen. Darüber hinaus wurde gezeigt, dass das Modell ohne zusätzliche Instrumentierung auf Feldmessungen angewendet werden kann, was sogar eine rückwirkende Anwendung auf lange Eddy-Kovarianz-Messreihen ermöglicht.

# LIST OF MANUSCRIPTS

This is a cumulative thesis based on two articles that are published in peer reviewed journals and one submitted manuscript that is currently under review. The following manuscripts are included in this thesis:

**Wanner L**, De Roo F, Sühling M, Mauder M (2022): How Does the Choice of the Lower Boundary Conditions in LES Affect the Development of Dispersive Fluxes Near the Surface?, *Boundary-Layer Meteorol*, doi: 10.1007/s10546-021-00649-7

**Wanner L**, Calaf M, Mauder M (2022): Incorporating the effect of heterogeneous surface heating into a semi-empirical model of the surface energy balance closure, *PLoS ONE*, 17(6):e0268097, doi: 10.1371/journal.pone.0268097

**Wanner L**, Jung M, Paleri S, Butterworth B, Desai A, Sühling M, Mauder M (2023): Towards Energy-Balance Closure with a Model of Dispersive Heat Fluxes, *PREPRINT (Version 1)* available at Research Square, doi: 10.21203/rs.3.rs-3449667/v1

Other related manuscripts that I have contributed to during my doctoral research are

Mauder M, Eggert M, Gutsmuths C, Oertel S, Wilhelm P, Voelksch I, **Wanner L**, Tambke J, Bogoev I (2020): Comparison of turbulence measurements by a CSAT3B sonic anemometer and a high-resolution bistatic Doppler lidar. *Atmos Meas Tech*, 13, 969–983, doi: 10.5194/amt-13-969-2020

Butterworth B, Desai A, Townsend P, Petty G, ... **Wanner L**, et al. (2021): Connecting Land-Atmosphere Interactions to Surface Heterogeneity in CHEESEHEAD19. *Bull Amer Meteor Soc*:1–71. doi: 10.1175/BAMS-D-19-0346.1

Metzger S, Durden D, Paleri S, Sühling M, Butterworth B, Florian C, Mauder M, Plummer D, **Wanner L**, Xu K, Desai A (2021): Novel approach to observing system simulation experiments improves information gain of surface-atmosphere field measurements, *Atmos Meas Tech*, 14, 6929–6954, doi: 10.5194/amt-14-6929-2021

Mauder M, Ibrom A, **Wanner L**, De Roo F, Brugger P, Kiese R, Pilegaard K (2021): Options to correct local turbulent flux measurements for large-scale fluxes using a LES-based approach, *Atmos Meas Tech*, doi: 10.5194/amt-14-7835-2021

Desai A, Paleri S, Mineau J, Kadum H, **Wanner L**, Mauder M, Butterworth B, Durden D, Metzger S (2022): Scaling Land-Atmosphere Interactions: Special or Fundamental? *JGR Biogeosciences* 127:10. doi: 10.1029/2022JG007097

Paleri S, **Wanner L**, Sühling M, Desai A, Mauder M (2023) Coupled large eddy simulations of land surface heterogeneity effects and diurnal evolution of late summer and early autumn atmospheric boundary layers during the CHEESEHEAD19 field campaign. *EGUsphere* [preprint], doi: 10.5194/egusphere-2023-1721

Butterworth B, Desai A, Durden D, Kadum H, LaLuzerne D, Mauder M, Metzger S, Paleri S, **Wanner L** (2023) Resolving Atmospheric Flow in Complex Environments: Recent

Experiments in Terrain and Forest Canopies. *Frontiers in Earth Science*, section Atmospheric Science (in review)

Paleri S, **Wanner L**, Sühring M, Desai A, Mauder M, Metzger S (2023) Impact of Surface Heterogeneity Induced Secondary Circulations on the Atmospheric Boundary Layer. *Boundary-Layer Meteorology* (in review).

Huq S, De Roo F, Sühring M, **Wanner L**, Beyrich F, Mauder M (2023) High-resolution ensemble LES energy balance closure study of the LITFASS campaign. *Meteorologische Zeitschrift* (submitted)

Smidt J, **Wanner L**, Ibrom A, Schmid HP, Mauder M (2023) Effects of Heating and Filter Configurations on High Frequency Attenuation in Eddy Covariance Measurements with the LI-7200 Infrared Gas Analyser. *Agricultural and Forest Meteorology* (submitted)

# CONTENT

1	Introduction .....	1
1.1	The relevance of flux measurements in the atmospheric boundary layer.....	1
1.2	The surface energy balance closure problem.....	3
1.2.1	Net radiation .....	5
1.2.2	Atmospheric heat fluxes .....	5
1.2.3	Ground heat flux and storage change .....	7
1.2.4	Above-ground storage change .....	7
1.3	Atmospheric boundary layer processes .....	8
1.3.1	Secondary circulations.....	9
1.3.2	Advection by the mean flow and dispersive fluxes .....	10
1.3.3	Options to quantify dispersive fluxes .....	11
1.4	Ecosystem-scale surface heterogeneity .....	13
1.4.1	Surface characteristics causing thermal surface heterogeneity.....	13
1.4.2	Scales and spatial distribution of thermal surface heterogeneity.....	14
1.4.3	The thermal heterogeneity parameter .....	16
1.5	Objective.....	16
2	Methods.....	17
2.1	Idealized large-eddy simulation studies.....	17
2.1.1	Investigation of the effect of lower boundary conditions on the development of dispersive fluxes in large-eddy simulations.....	18
2.1.2	Incorporation of the effect of thermal surface heterogeneity in a model of the surface energy imbalance.....	20
2.1.3	Development of a model of dispersive heat fluxes.....	22
2.2	Evaluation of the model of dispersive heat fluxes for CHEESEHEAD19 .....	24
2.2.1	The CHEESEHEAD19 project.....	24
2.2.2	Application of the model to CHEESEHEAD19 large-eddy simulations.....	26
2.2.3	Application of the model to CHEESEHEAD19 field measurements.....	27
3	Results & Discussion .....	29
3.1	The choice of lower boundary conditions and its effect on dispersive fluxes .....	29
3.2	The surface energy imbalance model considering thermal surface heterogeneity.....	31
3.3	Development of a model of dispersive heat fluxes.....	34
3.3.1	Performance.....	34
3.3.2	Application .....	39
4	Conclusion.....	41
5	Outlook.....	43

References.....	44
Appendices.....	55
A Individual contributions to the joint publications .....	57
B How does the choice of the lower boundary conditions in LES affect the development of dispersive fluxes near the surface? .....	61
C Incorporating the effect of heterogeneous surface heating into a semi-empirical model of the surface energy balance closure.....	91
D Towards energy-balance closure with a model of dispersive heat fluxes .....	115
Acknowledgements.....	171

# 1 INTRODUCTION

This Chapter provides an overview of the research results from the literature on which this work is based. First, the importance of fully capturing the energy transport by atmospheric processes (Chapter 1.1), which are the subject of this research, is addressed. Then, the energy balance closure problem and its contribution to the realization that conventional measurement methods cannot fully capture the atmospheric energy transport is introduced (Chapter 1.2). Subsequently, the role of mesoscale atmospheric processes in the underestimation of atmospheric energy transport by conventional measurements (Chapter 1.3) and how they are linked to thermal surface heterogeneity (Chapter 1.4) is discussed. The objective of this work is presented in Chapter 1.5.

## 1.1 The relevance of flux measurements in the atmospheric boundary layer

Climate change is not only manifested by an increase in the mean global temperature but also a wide range of other changes that strongly influence life on earth, like major shifts in the spatial and temporal distribution of precipitation (Seneviratne et al. 2021). These are associated with increased occurrence and intensity of extreme events such as heavy rainfall (Du et al. 2019; Roxy et al. 2017; Seneviratne and Hauser 2020; Volosciuk et al. 2016; Zeder and Fischer 2020), storms (Balaguru et al. 2018; Bhatia et al. 2018; Kossin et al. 2020), heat waves (Ceccherini et al. 2017; Lhotka et al. 2018; Molina et al. 2020; Vincent et al. 2018; Winter et al. 2017), and drought spells (Bloomfield et al. 2019; Condon et al. 2020; Lorenzo-Lacruz et al. 2017; Williams et al. 2015). The consequences of climate change are, for example, reduced crop yields (Brás et al. 2021; Hochman et al. 2017; Kim et al. 2019; Lesk et al. 2016), more severe wildfires (Abatzoglou and Williams 2016; Nolan et al. 2020; Turco et al. 2019), and flooding of inhabited areas (Cho et al. 2016; Hettiarachchi et al. 2018; Rosenzweig et al. 2018), often with serious consequences for residents.

Vegetated ecosystems, especially forests, contribute greatly to carbon sequestration and thus their protection and management has great potential to mitigate or delay climate change (Ciais et al. 2019; Friedlingstein et al. 2020; Nabuurs et al. 2017; Nabuurs et al. 2022; Sarmiento et al. 2010). However, as ecosystems and the atmosphere interact with each other, climate change can trigger feedback processes that further amplify climate change (Jia et al. 2022). For example wildfires, droughts, and insect infestations, which occur more frequently and more intensively due to climate change, can severely damage forests, turning them from carbon dioxide (CO<sub>2</sub>) sinks to sources of CO<sub>2</sub> and thereby further amplifying climate change (Allen et al. 2010; Aragão et al. 2018; Berg et al. 2006;

Breshears et al. 2005; Kurz et al. 2008). It is therefore necessary to investigate under which circumstances ecosystems can continue to sequester carbon and which adaptation measures can be implemented to improve the resilience and carbon sequestration under current and further changing conditions (Barber et al. 2014; Bernacchi et al. 2005; Bernacchi et al. 2006; Ceschia et al. 2010; Ekholm 2020; Graham et al. 2016; Hurteau et al. 2019; Krofcheck et al. 2019; Lipsett-Moore et al. 2018; Nabuurs et al. 2017; O'Dell et al. 2020). The link between ecosystems and the atmosphere is the atmospheric boundary layer (ABL). Lee (2018) describes it as the interface between the Earth's surface and the free atmosphere. The movement of air masses within the ABL facilitates the exchange of energy, greenhouse gases, as well as particulate matter and pollen between the Earth's surface and the atmosphere. The quantification of these atmospheric fluxes of energy and matter therefore forms an important basis for many research and application fields, including climate impact research (Baldocchi 2020).

Atmospheric heat flux measurements are used to parametrize and validate land-surface models used in climate and numerical weather prediction models, as well as in high-resolution numerical models (Bonan et al. 2012; Cuxart et al. 2015; Gehrke et al. 2020; Jaeger et al. 2009; Kracher et al. 2009; Li et al. 2021; Pleim and Xiu 1995; Sridhar et al. 2002; Wang et al. 2007; Williams et al. 2009). The land surface models specify the partitioning of energy available at the Earth's surface as a function of the land surface, and thus have a large influence on the energy and water cycles in those models (Li et al. 2021).

As already indicated, a reliable climate prognosis is the basis for initiating appropriate long-term adaptation measures as early as possible. Weather forecasting is becoming increasingly important to take timely measures to protect the population from the consequences of extreme events (Majumdar et al. 2021), but at the same time also more difficult (Sheshadri et al. 2021). Continuous improvement of weather and climate models to produce robust climate and weather predictions is therefore essential.

Baldocchi (2020) gives a comprehensive overview of the use of carbon flux measurements to investigate ecosystem responses to climate change: Long-term measurements enable the study of ecosystem responses to changing climatic conditions, such as higher temperatures (Keenan et al. 2014) and changing precipitation patterns (Stocker et al. 2018). They can also capture discrete extreme events such as insect infestations (Clark et al. 2012), growing season frost events (Gu et al. 2008), windthrow (Barr et al. 2012; Knohl et al. 2002), heat waves and droughts (Ciais et al. 2005; Cremonese et al. 2017; Fu et al. 2020; Qu et al. 2016; Reichstein et al. 2007; Schwalm et al. 2012; van Gorsel et al. 2016; Wolf et al. 2016), as well as wildfires (Berlinger et al. 2007), which are expected to increase both in frequency and in severity under climate change (Seneviratne et al. 2021).

These research fields, and many more, require a reliable data basis in order to deliver robust results. For instance, if the validation of land surface models is based on inaccurate data, this will compromise the model results, adding uncertainty and errors to weather and

climate predictions. It is therefore important to fully understand the processes that contribute to the transport of energy and matter in the ABL and measure all contributions to atmospheric fluxes.

## 1.2 The surface energy balance closure problem

The earth receives energy from the sun as shortwave radiation, and the Earth's surface is the layer where most of this radiation is reflected or absorbed, transformed to other forms of energy and passed on to the atmosphere or the ground. The surface energy balance (SEB) is typically measured at ground-based stations where a variety of instruments quantifying all components of the SEB are deployed at towers that are 2-50 m tall, depending on the vegetation height.

Figure 1 shows a schematic illustration of the individual components of the SEB. If the surface was an infinitely thin layer, the components of the SEB would be net radiation ( $R_{net}$ ), atmospheric heat fluxes ( $H$  and  $\lambda E$ ), and soil heat flux ( $G$ ), as shown in Fig. 1a. However, due to vegetation cover, it is often not possible to define an infinitely thin surface layer, which is why a surface volume is considered, instead (Oke 1987). Additionally, most SEB components cannot be measured directly at the surface. Therefore, a variety of storage changes ( $\Delta S$ ) contribute to the SEB as shown in Fig. 1b. The individual components of the SEB and their measurement are considered in more detail in Chapters 1.2.1 to 1.2.4.

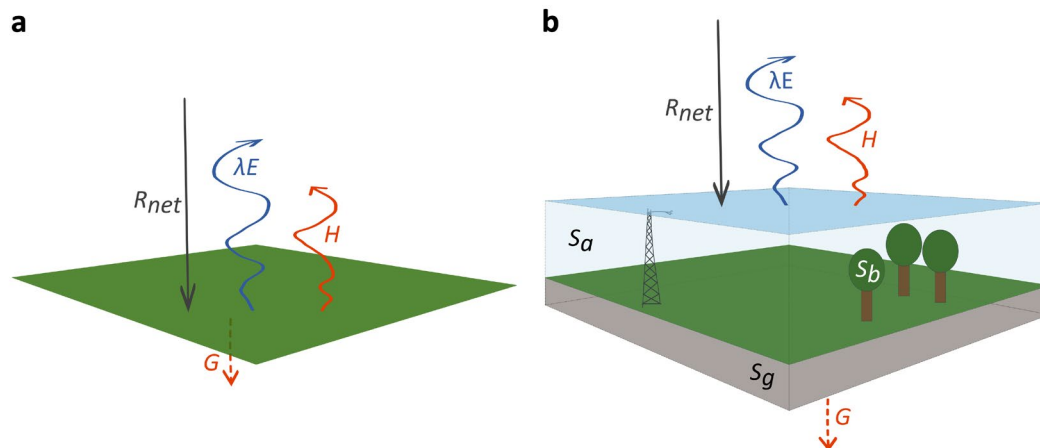


**Figure 1** Schematic illustration of the major contributions to the surface energy balance under daytime conditions when considering (a) an infinitely thin surface layer or (b) a surface volume. Since the sensible and latent atmospheric heat fluxes ( $H$ ,  $\lambda E$ ) and the ground heat flux ( $G$ ) are not measured directly at the surface, a surface volume is typically considered. Inside this volume, energy is stored in the air ( $S_a$ ), the biomass ( $S_b$ ), and the ground ( $S_g$ ).

The surface energy balance (SEB) is a widely used indicator to determine whether all energy transport towards and away from the Earth's surface has been fully captured in field measurements (e.g. Mauder et al. 2007c; Mauder et al. 2021; Mauder and Foken 2006; Oncley et al. 2007; Xu et al. 2020). In the field of boundary layer meteorology, the net radiation is typically defined to be positive during the day, which means that incoming

radiation is positive and outgoing radiation is negative. All other components are typically defined to be positive when they are directed away from the surface and negative when they are directed towards the surface (Foken 2017).

Due to energy conservation the energy leaving the surface must be equal to the energy reaching the surface. The SEB can therefore be described as

$$R_{net} = H + \lambda E + G + \Delta S. \quad (1)$$

Typically, however, the SEB measured at stationary towers all over the world is not closed, but the outgoing energy is substantially smaller than the incoming energy, resulting in an imbalance (*Imb*) of 10–30% in the SEB (Baldocchi et al. 2001; Hendricks-Franssen et al. 2010; Mauder et al. 2020; Soltani et al. 2018; Stoy et al. 2013; Wilson et al. 2002), often referred to as SEB gap, which is why Eq. 1 needs to be rewritten as

$$R_{net} = H + \lambda E + G + \Delta S + Imb. \quad (2)$$

The non-closure of the SEB indicates that a part of the energy is missed by the measurements, but as described in Chapter 1.1, many research fields rely on the accurate determination of all contributions to the SEB, especially those of the atmospheric heat fluxes. In the past decades, the measurement of all contributions has therefore been carefully revised in a multitude of studies to identify and eliminate the reasons for the SEB gap (Foken 2008; Mauder et al. 2020). After the improvement of instruments and data post-processing, it was found that instrument and set-up errors in measurements of different components of the SEB were not systematically contributing to the SEB gap across different sites (Foken 2008; Frank et al. 2013; Goulden et al. 1996; Kochendorfer et al. 2012; Kohsiek et al. 2007; Laubach et al. 1994; Liebethal et al. 2005; Mauder 2013; Mauder et al. 2020; Nakai and Shimoyama 2012). Specific challenges with quantifying each SEB component are further discussed in Chapters 1.2.1 to 1.2.4.

Despite careful measurement of all components and the application of required corrections, the SEB is still not closed (Mauder et al. 2020). A comprehensive experiment to close the SEB gap was the Energy Balance EXperiment (EBEX-2000), during which a lot of small terms that are often neglected (e.g., biomass heat storage and energy consumption by photosynthesis) were measured, but a SEB gap of roughly 10% remained (Oncley et al. 2007). One important reason for this is that parts of the atmospheric transport simply cannot be captured by single-tower flux measurements. To understand why this is the case, it is important to understand how fluxes are calculated with the eddy covariance method (Chapter 1.2.2), which atmospheric processes contribute to the transport of energy (Chapter 1.3), and how the latter are connected to thermal surface heterogeneity (Chapter 1.4).

### 1.2.1 Net radiation

The net radiation is defined as the difference between incoming and outgoing short- and longwave radiation:

$$R_{net} = R_{sw,in} + R_{lw,in} - R_{sw,out} - R_{lw,out}. \quad (3)$$

It can be measured by simply deploying paired up- and downward facing pyranometers and pyrgeometers, measuring short- and long-wave radiation, respectively. Nowadays, very accurate radiometers are available that provide a high data quality when they are cleaned regularly (Mauder et al. 2020). However, it is important that the instrument is aligned horizontally, otherwise large measurement errors can result, especially when the solar altitude is low. Since the radiation measurements are only representative of a relatively small area surrounding the instrument, it is furthermore crucial to ensure that the surface below the radiometer is representative of the much larger area covered by the atmospheric heat flux measurements which are introduced in Chapter 1.2.2 (Foken 2008; Göckede et al. 2008; Mauder et al. 2020; Schmid 1997). However, the scale mismatch between measurements of different SEB components was found to cause a random error which does not systematically contribute to the SEB gap (Richardson et al. 2012).

### 1.2.2 Atmospheric heat fluxes

Under daytime conditions, the energy surplus from the radiation balance causes the surface and the air layer above the surface to heat up strongly. Thus, the saturation deficit of the air increases, causing stronger evapotranspiration, if water is available at the surface. These effects lead to the formation of a strong vertical temperature and humidity gradient in the atmosphere near the surface. Atmospheric processes, mainly turbulence, mix the warm, moist air upward into the atmospheric boundary layer, creating sensible and latent heat fluxes, which transport much of the excess energy away from the surface (Foken 2017).

The turbulent atmospheric heat fluxes are typically measured using the eddy covariance (EC) method. It is currently the only method for measuring atmospheric heat fluxes at the ecosystem scale and also has the advantage of not disturbing the studied ecosystem itself (Baldochi 2003; Baldochi 2014; Foken et al. 2012; Foken 2017; Mauder et al. 2007b). The EC method measures vertical wind speed  $w$  and the concentration of a scalar (typically temperature  $T$  for sensible heat flux, absolute humidity  $a$  for latent heat flux) at a very high frequency of 10–20 Hz.

The resulting time series can be split into a mean  $\bar{s}$  over a defined period and the fluctuation around the mean by applying Reynolds' decomposition, which gives

$$s = \bar{s} + s', \quad (4)$$

where  $s$  represents  $w$  or another scalar. The overbar denotes temporal averaging over the chosen averaging period, which is typically 30 minutes (Mauder et al. 2020; Rebmann et

al. 2012), and the prime indicates the fluctuation around the mean. The fluctuations of  $w$  and another scalar  $s$  can be used to calculate the temporal covariance, following

$$\overline{w's'} = \frac{1}{nt} \sum_t (w_t - \bar{w})(s_t - \bar{s}). \quad (5)$$

The subscript  $t$  represents each measurement time step within the averaging period. Finally, the sensible and latent heat fluxes  $H$  and  $\lambda E$  can be calculated by converting  $\overline{w'T'}$  and  $\overline{w'q'}$  from kinematic units to energetic units, respectively. The partitioning between  $H$  and  $\lambda E$  is defined as the Bowen ratio  $\beta$ :

$$\beta = \frac{H}{\lambda E}. \quad (6)$$

The measurement height typically varies from 2 m to 50 m above the ground, depending on the vegetation type. To avoid the measurements being affected by individual elements, they should ideally be carried out at a height of at least two times the canopy height to avoid measurements being affected by the roughness layer (Foken 2017; Munger et al. 2012), which is a sublayer of the ABL where individual roughness elements affect the air flow (Oke 1987).

The EC method tends to underestimate atmospheric fluxes for several reasons related to the measurement and data processing methods. Instrument and set-up limitations can act as low-pass filters on the measurements (Haslwanter et al. 2009; Ibrom et al. 2007; Moore 1986). Due to the spatial separation between the wind speed and scalar sensors, sensor pathlengths and reaction times of the instruments, flux contributions by small eddies are missed. This problem has been known for a while and has been accounted for by improvement of instruments and the application of flux corrections in the data processing (Horst et al. 2015; Kaimal and Finnigan 1994; Mauder and Foken 2006; Moore 1986; Schotanus et al. 1983; Webb et al. 1980; Wilczak et al. 2001).

Today,  $w$  is typically measured with sonic anemometers because they can measure at a sufficient rate of 20 Hz and have been found to be very precise (Mauder and Zeeman 2018). However, possible errors in the vertical wind measurement with sonic anemometers can lead to the underestimation of  $H$  and  $\lambda E$  of up to 3–5 % (Frank et al. 2013; Horst et al. 2015; Kochendorfer et al. 2012; Mauder et al. 2020). If closed-path gas analyzers are used to measure the absolute humidity, tube attenuation can further increase low-pass filtering (Haslwanter et al. 2009). The low-pass filtering effects on the measurements can be corrected in the postprocessing (Fratini et al. 2012; Ibrom et al. 2007).

Several methods to correct for these issues in the data processing have been developed and are included in EC processing software (e.g., LI-COR Biosciences 2021; Mauder and Foken 2011). Small discrepancies were found between different correction methods and processing software but they cannot explain the SEB gap (Fratini and Mauder 2014; Mauder et al. 2006; Mauder et al. 2007c).

The averaging period defined to calculate the fluxes following Eq. 4–5 acts as a high-pass filter (Mauder et al. 2020). Because only the fluctuation is considered in the resulting fluxes, the energy transport by larger eddies that contribute to fluctuations of low frequencies is ignored, which needs to be corrected for (Foken et al. 2012; Mauder et al. 2020; Metzger and Holmes 2007; Segal and Arritt 1992). The wavelet (Terradellas et al. 2001) and ogive (Desjardins et al. 1989) methods are tools to determine relevant scales at which eddies contribute to the transport of energy.

It was suggested to increase the averaging period up to multiple days (Finnigan et al. 2003). However, it was shown that this increased the measured fluxes in only some cases (Cava et al. 2008; Charuchittipan et al. 2014; Foken et al. 2006; Mauder and Foken 2006; Oliphant et al. 2004). One explanation why the SEB closure is not always improved with increasing averaging times may be that part of the energy is transported by a certain type of mesoscale eddies that are not carried past EC stations, even with longer averaging periods, which is discussed in further detail in Chapter 1.3.1. Besides not always improving SEB closure, concerns were raised that extending the averaging period could create additional problems, such as violating the stationarity assumption underlying the EC method (Barr et al. 2006; Mauder et al. 2020; Mauder and Foken 2006). Regarding the limited success and possible complications, the extension of the averaging interval should be viewed critically.

### **1.2.3 Ground heat flux and storage change**

The heating of the surface also causes a temperature gradient in the soil, which is balanced by the conductive transport of heat in the soil. This soil heat flux can be determined by heat flux plates in the soil (Liebethal et al. 2005; Mauder et al. 2020). Ground heat flux measurements are limited to an even smaller area than radiation measurements and soil properties are highly variable. It is therefore recommended to perform heat flux measurements in multiple locations, whereas it is important to choose locations that are representative of the flux footprint (Mauder et al. 2020).

A portion of the ground heat flux heats the soil between the surface and the ground heat flux plate and is ignored in the measured ground heat flux. The resulting heat storage change in the ground  $\Delta S_g$  can be measured by soil temperature and moisture profiles with a high vertical resolution. It depends on the thickness of the soil layer above the soil heat flux plates and the soil properties (Liebethal et al. 2005).

### **1.2.4 Above-ground storage change**

As mentioned in Chapter 1.2.2, atmospheric heat fluxes are not measured directly at the surface. A portion of the atmospheric heat fluxes heats the air layer and biomass below the EC measurement and is therefore not included in the measured atmospheric heat fluxes. The above-ground storage change is therefore composed as follows:

$$\Delta S = \Delta S_a + \Delta S_b + \Delta S_m, \quad (7)$$

where  $\Delta S_a$  is the change in energy stored in the air, in the form of both sensible and latent heat,  $\Delta S_b$  is the heat storage change in the biomass, and  $\Delta S_m$  are minor metabolic storage terms. The contribution of storage changes to the SEB can be considerable when 30- or 60-minute intervals are chosen as averaging period (Haverd et al. 2007; Lindroth et al. 2010; Meyers and Hollinger 2004).

The change in  $S_a$  can be captured by measuring the vertical temperature and humidity profiles below the EC instruments (Haverd et al. 2007; Leuning et al. 2012, 2012; Lindroth et al. 2010, 2010; Moderow et al. 2009, 2009; Xu et al. 2019). The magnitude of the change in  $S_a$  depends on the volume of the heated air, and thus the measurement height. At low measurement heights it is very small and can probably be neglected, but at typical measurement heights above forests (30–50 m) it must be considered (Lindroth et al. 2010). In the Integrated Carbon Observation System (ICOS) network, measurements of air storage change are mandatory (Heiskanen et al. 2022), but also other sites have been equipped with the necessary instruments.

The change in  $S_b$  can be calculated from temperature measurements in tree trunks. Since the temperature variability within the biomass is very high, a large number of temperature sensors is needed (Lindroth et al. 2010). This may explain why  $S_b$  is often measured during individual measurement campaigns but is typically not included in long-term measurements. Studies have shown that the change in  $S_b$  is of the same magnitude (Lindroth et al. 2010) or even twice as high (Haverd et al. 2007) as the change in  $S_a$ . The magnitude of the change in  $S_b$  seems to depend on the biomass density (dos Santos Michiles and Gielow 2008; Haverd et al. 2007; Lindroth et al. 2010; McCaughey and Saxton 1988; Meesters and Vugts 1996; Moore and Fisch 1986).

In addition to  $S_a$  and  $S_b$ , there are minor metabolic storage terms like the energy uptake through photosynthesis (Blanken et al. 1997; Meyers and Hollinger 2004; Oncley et al. 2007; Schmid et al. 2000). The contribution to the SEB is on the order of 1-2% of  $R_{net}$ .

Much of the energy stored by the ground, air, and biomass during the day is released again at night to compensate for negative  $R_{net}$  (Oke 1987). Thus, under constant weather conditions with steady daily mean temperature over several days, the positive storage change during the day and the negative storage change at night balance each other out (Mauder et al. 2020). The storage changes can therefore often be neglected if daily values are considered instead of diurnal variations.

### 1.3 Atmospheric boundary layer processes

The ABL is the lower part of the troposphere and the region where the exchange of energy and matter, such as CO<sub>2</sub> and other greenhouse gases, between the atmosphere and the

Earth's surface takes place. The atmospheric boundary layer is characterized by turbulent flow. It is confined at the bottom by the Earth's surface and at the top by a temperature inversion that largely suppresses the exchange between the ABL and the layer above. The height of the boundary layer is highly variable and can range from a few meters under stable conditions to a few kilometers under unstable conditions where the inversion is lifted by strong convection (Foken 2017; Lee 2018).

### **1.3.1 Secondary circulations**

It was assumed for some time that most of the energy transport in the atmospheric boundary layer occurs through small-scale turbulence that can be captured by EC measurements with typical averaging periods of 30 minutes. However, because of the SEB gap, there has been increased investigation of the possible contribution of larger scale eddies that are inherently not considered in single-tower EC measurements, especially if they are not propagating with the wind (Bernhofer 1992; Etling and Brown 1993; Foken 2008; Segal and Arritt 1992). These mesoscale eddies are also referred to as secondary circulations (SCs) (Foken 2008). As mentioned earlier, some studies found that extending the averaging period to a few hours or even a full day partially reduced the SEB gap, which supports the assumption of energy being transported by such mesoscale eddies.

Using lidar measurements (Eder et al. 2015) and large-eddy simulations (De Roo and Mauder 2018; Inagaki et al. 2006; Kanda et al. 2004; Patton et al. 2016; Steinfeld et al. 2007), it was shown that SCs can in fact form in the atmospheric boundary layer under unstable stratification, spanning the entire boundary layer vertically and reaching a horizontal extent of up to 2–3 times the boundary layer height (Paleri et al. 2022a; Stull 1988). Two different types of SCs can be distinguished:

In idealized large-eddy simulations (LESs, see Chapter 1.3.3), it has been shown that SCs can spontaneously occur over homogeneous surfaces (Kanda et al. 2004). In this case, they are called turbulent organized structures (TOSs). They form at random positions and migrate over the surface with time. However, since the surface temperature is influenced by the overlying air layer, TOSs produce a spatially heterogeneous distribution of surface temperature, which can lead to a reinforcement of the TOSs.

Over heterogeneous surfaces, secondary circulations occur due to thermal differences at the surfaces. Over the warmer patches, the air heats up stronger than over the cooler patches. The resulting pressure difference is balanced by the movement of air masses and so called thermally induced mesoscale circulations (TMCs) develop (Inagaki et al. 2006; Letzel and Raasch 2003) as shown in Fig. 2. The temperature amplitude and heterogeneity scale influences the strength of the TMCs (Inagaki et al. 2006; Letzel and Raasch 2003; Sühling et al. 2018; Zhou et al. 2019). Unlike TOSs, TMCs cannot change their position over time because they are bound to surfaces of different temperature (Bou-Zeid et al. 2020; Etling and Brown 1993; Kenny et al. 2017).

Under strongly convective conditions, when the horizontal wind speed is low, SCs form cellular structures, and with increasing horizontal wind speed, they become more elongated as they get carried away with the wind and form roll vortices (Deardorff 1972; Khanna and Brasseur 1998; Schmidt and Schumann 1989). Under neutral to stable conditions with high geostrophic wind speeds, the horizontal mixing is therefore enhanced and the influence of TOSs and TMCs on the SEB gap is smaller than under free convective conditions (Katul 2019; Schalkwijk et al. 2016). However, no clear stability threshold for the shift between cell and roll regimes was found. Instead, under moderately unstable conditions, transitional structures occur (Park and Baik 2014; Salesky et al. 2017).

The occurrence of TOSs and TMCs may explain the improved SEB closure in some studies but not in others (see Chapter 1.2.2). As TOSs slowly move past the EC station, their contribution to the energy transport can be captured when long averaging periods are used. However, since TMCs are bound to the underlying surface, they do not move past the EC station, which is why their contribution to the SEB cannot be captured (Etling and Brown 1993; Segal and Arritt 1992). The surroundings of the stations where the SEB could be closed may have been more homogeneous, so that the SCs were predominantly TOSs.

In studies with spatial EC measurements and LESs it was shown that SCs transport a considerable amount of energy. In general, the vertical energy transport by SCs increases with height and reaches its maximum in the center of the boundary layer (Paleri et al. 2023b; Steinfeld et al. 2007). In a multitude of studies, it was found that the magnitude of the energy transport by secondary circulations is related to the friction velocity  $u_*$  and atmospheric stability (Barr et al. 2006, Hendricks-Franssen et al. 2010, Stoy et al. 2006, Stoy et al. 2013, Wilson et al. 2002, Schalkwijk et al. 2016), and the surface heterogeneity (Foken et al. 2010, Mauder et al. 2007a, Morrison et al. 2021, Panin et al. 1998, Panin and Bernhofer 2008).

### **1.3.2 Advection by the mean flow and dispersive fluxes**

Depending on the size of the study domain, SCs contribute to either advection by the mean flow or dispersive fluxes. In Fig. 2, two different observation areas are shown. In case A, a small volume surrounding an EC station is considered. In case B, a horizontal plane extending over several kilometers is considered. In case A, SCs contribute to vertical advection, which is the transport through the upper boundary of the volume by the mean wind, and horizontal advection, which is the transport through the walls of the volume by the mean wind (Foken 2017). The horizontal advection is a combination of the transport by the horizontal background wind and the horizontal transport by SCs. It thus includes the energy transported by the background wind, e.g., heat or moisture carried into the volume from a neighboring warmer or moister surface (Oke 1987). In this case, it is therefore more difficult to determine the energy transport by SCs alone.

However, in case B, the atmospheric transport by SCs can be described as the dispersive flux. Similar to the turbulent flux being calculated as the temporal covariance at one point (Eq. 5), the dispersive flux can be calculated as a spatial covariance of the Reynolds averaged vertical wind speed  $w$  and scalar of interest  $s$  (Raupach and Shaw 1982; Wilson and Shaw 1977) following

$$\langle \bar{w}^* \bar{s}^* \rangle = \frac{1}{n_x \times n_y} \sum_x \sum_y (\overline{w_{x,y}} - \langle \bar{w} \rangle) (\overline{s_{x,y}} - \langle \bar{s} \rangle). \quad (8)$$

The angled brackets denote spatial averaging over the chosen area in the  $x$ - and  $y$ -direction, and the star superscript denotes the spatial fluctuation around the spatial mean.  $n_x$  and  $n_y$  are the number of observations in  $x$ - and  $y$ -directions, respectively. It is also possible to calculate dispersive fluxes from a one-dimensional transect instead of a plane, i.e.,  $n_y=1$ , which is often done in aircraft-based measurements (Metzger et al. 2012; Paleri et al. 2022b). If the extent of the area or transect covers multiple complete secondary circulations, the dispersive fluxes calculated from measurements distributed over this plane represent nearly the entire energy transport by secondary circulations.

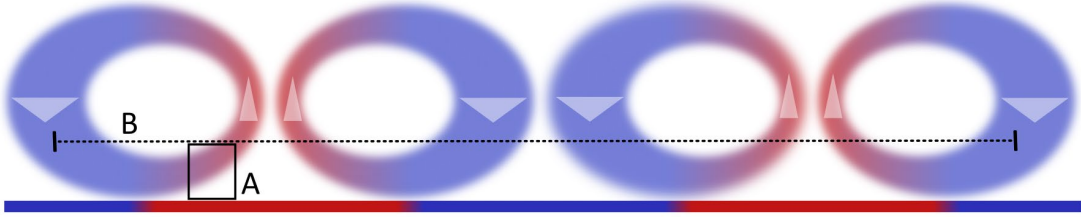


**Figure 2** Vertical cross section through thermal surface heterogeneity induced secondary circulations and spatial representativeness of different measurement domains with regard to heat transport by secondary circulations. Red colors indicate high surface/air temperatures and blue colors indicate low surface/air temperatures. The arrows show the rotation direction of the secondary circulations. Case A represents a small control volume where secondary circulations contribute to horizontal and vertical advection through the boundaries of the box. Case B represents a large horizontal plane that spans multiple secondary circulations where the secondary circulations contribute to the dispersive flux.

### 1.3.3 Options to quantify dispersive fluxes

As mentioned in Chapter 1.2, the SEB remains unclosed even after numerous measures to improve the measurements and post processing were deployed (Mauder et al. 2020). As discussed in Chapters 1.2.2 and 1.3.1, one major reason for this is the underestimation of atmospheric heat fluxes due to the formation of SCs in the ABL whose contribution to the energy transport cannot, by definition, be captured by the EC method. The energy transport by TOSs and TMCs therefore must be quantified in addition to conventional EC measurements.

It is possible to capture the energy transport by SCs by deploying spatial EC measurements such as aircraft measurements (Foken et al. 2010; Mahrt 1998; Mauder et al. 2007b; Metzger et al. 2012; Metzger et al. 2021; Paleri et al. 2022b) or multi-tower setups (Butterworth et al. in review; Engelmann and Bernhofer 2016; Feigenwinter et al. 2008; Mahrt 1998;

Mauder et al. 2008; Mauder et al. 2010; Morrison et al. 2022; Oncley et al. 2007; Steinfeld et al. 2007), and calculating the dispersive flux following Eq. 8. Analogous to calculating dispersive fluxes from spatially distributed measurements, the energy transport by SCs can be determined in LESs. This has been done, e.g., by Kanda et al. (2004), Inagaki et al. (2006), Steinfeld et al. (2007), and Margairaz et al. (2020a).

We can therefore consider the total atmospheric heat fluxes to be a combination of heat fluxes generated by small-scale turbulence and captured by single-tower EC measurements ( $H_{turb}$ ,  $\lambda E_{turb}$ ), and the heat fluxes generated by SCs, i.e., the dispersive heat flux ( $H_{disp}$ ,  $\lambda E_{disp}$ ):

$$H = H_{turb} + H_{disp}, \quad (9)$$

and

$$\lambda E = \lambda E_{turb} + \lambda E_{disp}. \quad (10)$$

In LESs, atmospheric heat fluxes are not affected by sensor errors and uncertainties in the field conditions (Inagaki et al. 2006: 188; Metzger and Holmes 2007). However, former LES studies were not able to investigate the SEB gap near the surface due to the coarse vertical grid resolution of 20–25 m (Huang et al. 2008; Kanda et al. 2004). A LES with a finer grid resolution still seemed to underestimate the dispersive heat fluxes compared to SEB gaps in field measurements, especially near the bottom of the domain (Steinfeld et al. 2007). One reason might be the still rather low model resolution of 10 m that does not allow to properly resolve secondary circulations near the surface. A possible solution for this problem is to further decrease the grid spacing. However, the vertical grid spacing is limited by the roughness length, as the Monin-Obukhov similarity theory used at the lower boundary is not applicable within the roughness sublayer (Basu and Lacser 2017). With very high resolutions, canopies with high roughness length therefore have to be explicitly resolved in a plant canopy model (PCM) in the LES. Another reason might be the use of prescribed surface fluxes, which inhibits the reinforcement of TOSs and TMCs described in Chapter 1.3.1. It is possible, that the use of a land surface model (LSM) or a PCM may therefore lead to stronger secondary circulations.

Spatial EC approaches are very costly and partly also labor intensive and realistic LESs are computationally expensive. Therefore, these methods cannot be used on a long-term basis at every EC station to quantify the energy transport by SCs. However, they can be applied to perform systematic experiments that can be used to improve the understanding of ABL processes with regard to surface heterogeneity (Beyrich et al. 2006; Butterworth et al. 2021; Morrison et al. 2021) and develop a model that predicts the energy transport by SCs based on parameters that can be measured more easily in situ or obtained from other sources. The resulting model could then be used to correct the atmospheric heat fluxes (Eder et al. 2014; Mauder et al. 2021).

Such models have already been developed by, for instance, Huang et al. (2008) and De Roo et al. (2018) and applied to field measurements (Eder et al. 2014; Mauder et al. 2021). However, they do not directly predict the energy transport by SCs, but the combination of storage changes (see Chapter 1.2.4) and dispersive fluxes, i.e., energy transported by SCs. Both models consider the atmospheric stability and the measurement height, that were found to be major drivers for the magnitude of the SEB gap. However, they were developed using idealized LESs with homogeneous surfaces, which is why they do not consider the transport by TMCs caused by thermal surface heterogeneity.

Because the imbalance model by De Roo et al. (2018) forms the basis of one of the models developed in this work (Chapter 2.1.2), it is shortly introduced here:

Previous studies found the magnitude of the SEB gap to be correlated to friction velocity  $u_*$  (Barr et al. 2006; Hendricks-Franssen et al. 2010; Schalkwijk et al. 2016; Stoy et al. 2013; Wilson et al. 2002), atmospheric stability (Barr et al. 2006; Hendricks-Franssen et al. 2010; Huang et al. 2008; Schalkwijk et al. 2016; Stoy et al. 2006; Stoy et al. 2013), and the measurement height  $z$  (Huang et al. 2008; Kanda et al. 2004). Following the Buckingham Pi theory (Stull 1988), the variables known to affect the magnitude of the SEB gap were grouped into dimensionless groups, so called Pi groups, which are the measurement height normalized with the boundary layer height  $z/z_i$  and the atmospheric stability parameter  $u_*/w_*$ .

The friction velocity  $u_*$  can be calculated as

$$u_* = \langle (\overline{u'w'^2} + \overline{v'w'^2})^{1/4} \rangle, \quad (11)$$

where  $u$  and  $v$  are the horizontal wind speed components in  $x$ - and  $y$ -direction, the Deardorff velocity  $w_*$  can be calculated as

$$w_* = \langle \left( \frac{g}{\theta} z_i \overline{w'\theta'} \right)^{1/3} \rangle, \quad (12)$$

where  $g$  is the gravitational acceleration ( $9.81 \text{ m s}^{-2}$ ), and  $z_i$  is the height of the ABL.

Finally, two scaling functions were fitted to describe the magnitude of the imbalance ratio  $I$  based on  $z/z_i$  and  $u_*/w_*$ :

$$I \left( \frac{u_*}{w_*}, \frac{z}{z_i} \right) = F_1 \left( \frac{u_*}{w_*} \right) F_2 \left( \frac{z}{z_i} \right). \quad (13)$$

## 1.4 Ecosystem-scale surface heterogeneity

### 1.4.1 Surface characteristics causing thermal surface heterogeneity

Most surfaces on Earth are heterogeneous on the ecosystem scale, i.e., on the scale of 100 m to a few kilometers. Even some landscapes that appear homogeneous at first glance, in fact, feature heterogeneities of different surface properties. The 2019 Idealized Planar-Array experiment for Quantifying Spatial heterogeneity (IPAQS) (Morrison et al. 2021) was carried

out in a flat area with very low and uniform surface roughness in a dry-lake-bed desert south-west of Salt Lake City (Utah). Nevertheless, large spatial variability in surface temperature was observed due to the heterogeneous coverage of the soil by salt crusts that alter the albedo (Morrison et al. 2021).

The albedo describes the share of incoming solar radiation that is reflected at a surface and thus influences how much energy is available to heat the surface and the overlying air. It varies strongly between different surface types, with very high albedos found in fresh snow and very low albedos found in dark, wet soils and coniferous forests. The albedo of a surface can vary on different temporal scales: the albedo of water depends on the solar altitude and therefore varies over the course of a day, the albedo of snow decreases as the snow cover ages and becomes dirty, and the albedo of deciduous trees varies seasonally (Oke 1987).

However, there are more surface characteristics that influence the surface temperature: The orientation of a sloped surface determines the radiation density of the incoming solar radiation. This also influences the available energy at the surface and resulting heating. The magnitude of surface heating caused by a certain amount of available energy further depends on the heat capacity of the material and the material's ability to transport heat, since these parameters determine the volume over which the supplied energy is distributed (Oke 1987).

Another parameter that has a strong influence on the surface temperature is the water availability at the surface. Not only does it affect the heat capacity and conductivity of the soil but it also enables the vaporization of water. During vaporization, the water absorbs energy which is then transported away from the surface through the latent heat flux. The surface is thus not heated as much as a similar but dry surface (Oke 1987).

In field measurements, however, it is very difficult to consider the effect of thermal surface heterogeneity in isolation, as the parameters determining the surface temperature do not change independently, but in combination with other properties of different surface types, which can affect ABL processes in different ways (Panin et al. 1998). For example, vegetation types differ in roughness, which can affect atmospheric transport processes (Panin et al. 1998; Panin and Bernhofer 2008), large differences in vegetation height can cause forest edge effects (Kanani-Sühring and Raasch 2015, 2017; Kenny et al. 2017), and in landscapes with pronounced topography, dynamic effects strongly influence the wind in addition to thermodynamic effects caused by the thermal surface heterogeneity (Oke 1987).

#### **1.4.2 Scales and spatial distribution of thermal surface heterogeneity**

As mentioned in Chapter 1.3.1, thermal surface heterogeneity can cause the development of TMCs and thereby influences the mechanisms of energy transport in the ABL. By comparing SEB gaps observed at different EC sites and deploying spatial EC measurements, it was found that not only the flux footprint but the entire landscape surrounding an EC station

had to be considered, as TMCs are caused by thermal surface heterogeneity of larger scales (Foken et al. 2010; Mauder et al. 2007a; Panin and Bernhofer 2008; Xu et al. 2017).

Zhou et al. (2019) found that the magnitude of the SEB gap increased with increasing heterogeneity length scale until the heterogeneity length scale was on the order of the boundary layer height. With larger heterogeneity scales, the SEB gap was found to decrease again. This supports the findings from field measurements and indicates that thermal surface heterogeneities with spatial scales on the order of the boundary layer height cause the strongest TMCs, thereby decreasing the share of atmospheric energy transported by single-tower EC measurements.

Bou-Zeid et al. (2020) further discussed different classes of surface heterogeneity and their influence on the ABL: Semi-infinite interfaces are regions where two very large patches such as ocean and land meet and contribute to macroscale heterogeneity. Since they exhibit much larger scales than the height of the ABL, they behave largely like homogeneous surfaces with respect to TMCs, except for the boundary regions where temperature differences can cause large circulations, such as the land-sea breeze (Bou-Zeid et al. 2020; van Heerwaarden et al. 2014). Statistically homogeneous patches of land are surfaces that are patchy on a smaller scale (micro – meso) and appear homogeneous at regional scales (Brutsaert 1998). If the patches are very small (microscale), the heterogeneity affects only a few meters near the surface and above, the ABL processes are similar to those over homogeneous surfaces (Bou-Zeid et al. 2004; Mahrt 2000). However, if the patches are on the order of a few hundred meters to kilometers (mesoscale), they can cause TMCs (Inagaki et al. 2006; Kang and Lenschow 2014; Patton et al. 2005; Sühring and Raasch 2013; van Heerwaarden et al. 2014). Large, isolated patches differ from their surroundings and contribute to heterogeneity on the mesoscale. They can also cause TMCs (Eder et al. 2015; Omidvar et al. 2020). Finally, unstructured heterogeneity is a mix of the previously described heterogeneity classes.

Especially in landscapes with unstructured heterogeneity, which is the most common heterogeneity class (Bou-Zeid et al. 2020), it is difficult to determine the heterogeneity length scale, as each patch has a different size and shape. One option to determine the heterogeneity length scale is the approach presented by Panin and Bernhofer (2008): By applying a Fourier transform to transect measurements of the scalar of interest across the landscape, spatial spectra are calculated. The location of the maximum of the spectrum represents the predominant length scale that contributes most to the variability of the scalar. Panin and Bernhofer (2008) used this method to calculate the length scale of roughness length heterogeneity, but it can be applied similarly to thermal surface heterogeneity (Wanner et al. (2023) in Appendix D).

### 1.4.3 The thermal heterogeneity parameter

Based on a set of idealized LESs with thermally heterogeneous surfaces featuring varying patch sizes, Margairaz et al. (2020b) developed a nondimensional thermal heterogeneity parameter. It depends on both the heterogeneity length scale ( $L_h$ , in this case the patch size) and the amplitude of surface temperatures  $\Delta T_s$ , normalized with the temporally and spatially averaged surface temperature  $\langle \bar{T} \rangle$ . It also takes the characteristic length scale of the SCs into account, that are influenced by buoyancy and wind speed which determine the shape of the SCs (Chapter 1.3.1). The thermal heterogeneity parameter is defined as

$$\mathcal{H} = \frac{g L_h \Delta T}{\langle U_g \rangle^2 \langle \bar{T}_s \rangle}, \quad (14)$$

with  $U_g$  being the geostrophic wind speed and

$$\Delta \bar{T} = \langle |\bar{T}_s - \langle \bar{T}_s \rangle| \rangle. \quad (15)$$

## 1.5 Objective

The main objective of this work is to develop a model of the energy transport by secondary circulations (TOSs and TMCs) using a semi-empirical approach. This model is supposed to be applicable to any EC station without many additional measurements to correct the atmospheric heat fluxes.

To achieve this goal, the following intermediate objectives were defined:

- (1) Investigate which conditions lead to the most realistic energy transport by secondary circulations in LESs.
- (2) Further develop the imbalance model of De Roo et al. (2018) to include the effect of thermal surface heterogeneity.
- (3) Develop a comprehensive and universally applicable model for the transport of sensible and latent heat by secondary circulations.
- (4) Test the new model and demonstrate how it can be applied to correct EC field measurements.

## 2 METHODS

To achieve the objectives defined in Chapter 1.5, different methods were combined. To systematically develop the models of the surface energy imbalance and dispersive fluxes, idealized LESs were applied (Chapter 2.1). To test the resulting model of energy transport by SCs, realistic LESs and EC field measurements were used. The realistic simulations and field measurements were generated within the NSF/DFG-funded Chequamegon Heterogeneous Ecosystem Energy-balance Study Enabled by a High-density Extensive Array of Detectors project (CHEESEHEAD19, Butterworth et al. 2021) which is introduced in Chapter 2.2.1. The field measurements were furthermore complemented by additional datasets generated from satellite imagery and reanalysis data presented in Chapter 2.2.3. This Chapter provides an overview of the used methods. Further details can be found in the respective publications in the Appendices B-D.

### 2.1 Idealized large-eddy simulation studies

This work is mainly built upon idealized LESs. Similar to direct numerical simulations (DNSs), LESs are based on the Navier Stokes equations which describe the laminar and turbulent motion of viscous fluids (Fröhlich 2006). In DNSs, however, the grid spacing must be sufficiently small to resolve even the smallest eddies explicitly, which is why such a simulation of the entire ABL would not be feasible (Foken 2017). In LESs, larger grid spacings can be applied, since only the larger eddies have to be explicitly resolved, while the smaller ones are parameterized with a sub-grid scale model (Foken 2017; Fröhlich 2006). Since approximated Navier Stokes equations are solved for each individual time step, spatial structures are resolved much better in LESs than in so-called RANS (Reynolds-averaged Navier Stokes). The latter only solve simplified stationary, i.e., Reynolds-averaged, Navier Stokes equations (Fröhlich 2006). Thus, LESs provide a compromise between spatial and temporal resolution and computation time and are widely used in the field of micrometeorology to simulate the ABL (Foken 2017; Fröhlich 2006).

LESs offer several advantages over field measurements that are relevant to addressing the objectives. The most important advantage is that it is possible to control a wide range of factors, such as atmospheric conditions, surface characteristics and boundary conditions, and that the boundary conditions are known (Inagaki et al. 2006; Sühling et al. 2018). This enables the targeted variation of a single parameter while all other parameters remain unchanged, which is an important prerequisite for studying the influence of a single parameter on atmospheric processes. Additionally, by using cyclic horizontal boundary conditions, it is possible to investigate a quasi-infinite area without any possible influences by neighboring surfaces with different characteristics.

Furthermore, advanced LES codes generally enable high spatial and temporal resolution through massive parallelization on a suitable high-performance computing infrastructure. All atmospheric information is available in each grid point at each time step (Schalkwijk et al. 2016). Such a spatial coverage would not be possible in field measurements. Additionally, the virtual measurements in LESs are not affected by possible measurement errors and gaps in the data (Inagaki et al. 2006; Schalkwijk et al. 2016; Sühling et al. 2018).

Three studies using different sets of idealized LESs were carried out. First, the effect of lower boundary conditions on the development of dispersive fluxes in LESs was investigated (Chapter 2.1.1). Second, an existing model of the surface energy imbalance over homogeneous surfaces was developed further to consider the effect of thermal surface heterogeneity (Chapter 2.1.2). Finally, a model of dispersive heat fluxes, representing the energy transport by TOSs and TMCs, was developed, including the effect on the transport of water vapor (Chapter 2.1.3).

### **2.1.1 Investigation of the effect of lower boundary conditions on the development of dispersive fluxes in large-eddy simulations**

This Chapter is a summary of the methods used to compare the effect of different lower boundary conditions on dispersive fluxes in LESs. A more detailed description of both, the LES setup and the data processing procedure, can be found in Wanner et al. (2022a) in Appendix B.

#### **Set-up of the large-eddy simulations**

In this study, PALM v6 was used, which is a parallelized LES model based on the non-hydrostatic Boussinesq approximation to the incompressible Navier Stokes equations (Maronga et al. 2020). A highly idealized set-up was employed, that comprised homogeneous surfaces and cyclic horizontal boundary conditions. To increase the resolution near the surface, a vertically nested child domain with a small grid spacing was deployed in the lowest 240 m of the domain, using the vertical two-way coupled grid nesting technique by Hellsten et al. (2021) that was already implemented in PALM.

Two different vegetation types were used to compare prescribed surface fluxes (PSF) with a LSM (Gehrke et al. 2020) or a combination of the LSM and a PCM (Maronga et al. 2015) provided in PALM. For the comparison with the LSM only, a short grassland was chosen as vegetation type, and for the comparison with LSM+PCM, a forest was used, which was explicitly resolved by the PCM, as shown in Fig. 3. Since the LSM calculates the surface fluxes based on  $R_{net}$ , a radiation model needed to be deployed. The built-in clear sky radiation model was used, but a constant solar zenith angle was applied for improved comparability with the PSF simulations, and to systematically change  $R_{net}$ .

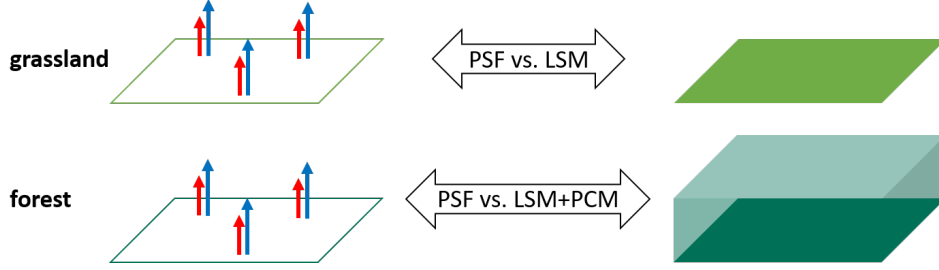


**Figure 3** Schematic illustration of the lower boundary conditions that are compared for the two investigated vegetation types. The red and blue arrows represent the sensible and latent surface heat fluxes in the simulations with prescribed surface fluxes (PSF). The colored area represents the land surface model (LSM), and the box represents the resolved canopy in the simulations with plant canopy model (PCM) (from Wanner et al. (2022a)).

The varying  $R_{net}$  was combined with different geostrophic wind speeds ( $U_g$ ) to generate a range of atmospheric stability regimes: free convective ( $R_{net} = 450 \text{ W m}^{-2}$ ,  $U_g = 0 \text{ m s}^{-1}$ ), strongly unstable ( $R_{net} = 350 \text{ W m}^{-2}$ ,  $U_g = 2 \text{ m s}^{-1}$ ), and moderately unstable conditions ( $R_{net} = 250 \text{ W m}^{-2}$ ,  $U_g = 5 \text{ m s}^{-1}$ ).

In the LSM+PCM simulations, the vegetation was explicitly resolved by PALM’s PCM that adds a momentum sink, interacts with radiation, and calculates the volume of heat and water vapor released by the canopy (Krč et al. 2021; Maronga et al. 2015). However, the PCM is not coupled with the LSM and assumes no limitation to transpiration due to the water availability in the soil. A horizontally uniform leaf area density profile following (Patton et al. 2016) was used to inform the PCM.

The PSF simulations were set up with temporally and spatially constant prescribed surface fluxes based on the temporally and spatially averaged fluxes resulting from different  $R_{net}$  in the LSM and LSM+PCM simulations. Furthermore, the roughness lengths were set to match the vegetation types used in the LSM and LSM+PCM simulations. However, the roughness length for the forest simulations had to be decreased to 0.25 m due to the low grid resolution.

### Data processing

To investigate how comparable the PSF and LSM(+PCM) simulations are, 30-minute surface fluxes of sensible and latent heat and horizontally averaged vertical profiles of horizontal wind speed, the vertical component of the wind speed, and potential temperature were compared. The surface was defined to be located at the canopy top in all simulations, i.e., at the lower boundary of the domain in the PSF and LSM simulations, and at 20 m above the lower boundary in the LSM+PCM simulations.

The dispersive heat fluxes were calculated following Eq. 8. For better comparability among different atmospheric conditions, the dispersive flux contributions were scaled with the surface fluxes. For the PSF and LSM simulations, the surface fluxes are directly provided in the LES output. However, for the simulations with the PCM, the surface flux was

calculated as the sum of the resolved heat fluxes, calculated following Eq. 5, and sub-grid-scale contributions 20 m above the lower boundary.

Furthermore, flux-variance similarity functions were investigated to explain the differences in dispersive heat fluxes over the forest. Following Panofsky et al. (1977), the similarity function for the wind component in  $x$ -direction ( $\Phi_u$ ) was calculated as

$$\frac{\langle u'u' \rangle}{u_*} = \Phi_u \left( \frac{z_b}{L} \right), \quad (16)$$

where  $u$  is the wind component in  $x$ -direction,  $u_*$  is the friction velocity (Eq. 11),  $z_b$  is the height above the lower boundary, and  $L$  is the Obukhov length. The flux-variance similarity functions for the vertical wind component ( $\Phi_w$ ) and the potential temperature ( $\Phi_\theta$ ) were calculated by replacing  $u$  with the vertical wind speed  $w$  and the potential temperature  $\theta$ , respectively, and  $u_*$  with the temperature scale  $T_*$ .

### 2.1.2 Incorporation of the effect of thermal surface heterogeneity in a model of the surface energy imbalance

This Chapter summarizes the methods used to further develop the surface energy imbalance model by De Roo et al. (2018) by including the thermal heterogeneity parameter introduced by Margairaz et al. (2020b) to account for the effect of thermal surface heterogeneity on the surface energy imbalance. A more detailed description of both, the LES setup and the data processing procedure, can be found in Wanner et al. (2022b) in Appendix C.

#### The large-eddy simulation dataset

For this study, a LES dataset originally developed by Margairaz et al. (2020a), who employed a pseudo-spectral LES approach (Albertson and Parlange 1999; Bou-Zeid et al. 2005; Calaf et al. 2011; Margairaz et al. 2018; Moeng 1984), was used.

The dataset consists of 32 simulations in total, with different combinations of surface temperature distribution and geostrophic wind speed. In all simulations, an idealized dry ABL was simulated over a flat surface with homogeneous roughness with a domain size of  $(l_x, l_y, l_z) = (2\pi, 2\pi, 2)$  km and a grid-spacing of  $(\Delta x, \Delta y, \Delta z) = (24.5, 24.5, 7.8)$  m. The atmospheric conditions were forced by geostrophic wind speed, varying between  $1 \text{ m s}^{-1}$  and  $15 \text{ m s}^{-1}$  at the top, and a fixed surface temperature at the bottom of the domain. In one set of simulations, the surface temperature was homogeneous (HM). In the other three simulation sets (HT200, HT400, HT800), spatially heterogeneous surface temperatures with patch sizes of 200 m, 400 m, and 800 m were prescribed as shown in Fig. 4. The surface temperature  $T_s$  was always 295 K on average, with a standard deviation of  $\pm 5$  K in the simulations with heterogeneous  $T_s$ . The initial air temperature was 290 K, i.e., 5 K lower than  $T_s$ , causing the development of a convective ABL. The analysis is based on data collected for 30 minutes after a spin-up time of 4 hours.

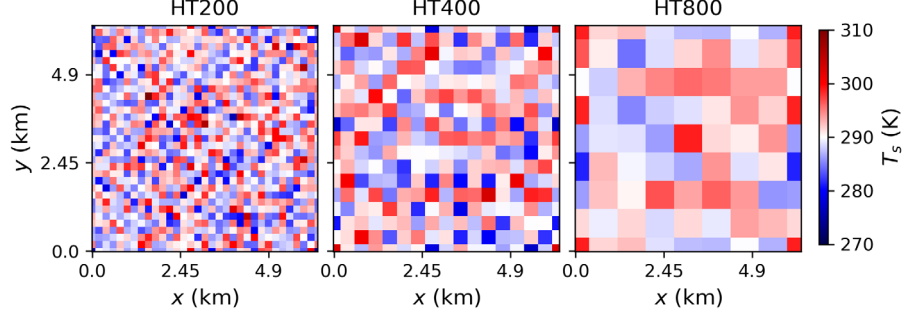


**Figure 4** Temperature distribution at the surface for the three sets of simulations with heterogeneous surfaces. The patch sizes from left to right are 200 m, 400 m, and 800 m (from Wanner et al. (2022b)).

### Model development

The Buckingham Pi theory was followed to further develop the model of De Roo et al. (2018). According to Stull (1988), it follows four steps, which are (1) select variables that are relevant to the problem, (2) organize the selected variables into dimensionless groups, (3) perform an experiment to determine the values of those dimensionless groups, and (4) describe the relationship by fitting an empirical curve to the data.

The dimensionless groups used by De Roo et al. (2018) are  $u_*/w_*$ , a measure of atmospheric stability, and  $z/z_i$ , which accounts for the influence of the measurement height. To include the effect of thermal surface heterogeneity, a third dimensionless variable group, the thermal heterogeneity parameter  $\mathcal{H}$  introduced by Margairaz et al. (2020b), was added. This resulted in a set of three scaling functions to model the imbalance ratio  $I$ :

$$I\left(\frac{u_*}{w_*}, \frac{z}{z_i}, \mathcal{H}\right) = F_1\left(\frac{u_*}{w_*}\right) F_2\left(\frac{z}{z_i}\right) F_3(\mathcal{H}). \quad (17)$$

The first dimensionless variable group  $u_*/w_*$  was calculated following Eq. 11–12. The ABL height  $z_i$  was determined as the height at which the total sensible heat flux becomes zero before reaching the capping inversion. The second dimensionless variable group  $z/z_i$  is the measurement height normalized with the height of the ABL.

The third dimensionless variable group is the thermal heterogeneity parameter  $\mathcal{H}$  defined by Margairaz et al. (2020b) and was calculated following Eq. 14–15. As heterogeneity length scale  $\overline{L}_h$ , the patch sizes (i.e., 0 m, 200 m, 400 m, 800 m) were used.

Because only 30-minute averages were available, the spatially averaged turbulent heat flux  $H$ , i.e., the flux contribution that would be captured by typical single-tower EC measurements, was calculated as

$$H = \langle \overline{w\theta} - \overline{w}\overline{\theta} + \overline{H_{sgs}} \rangle, \quad (18)$$

where temporal averaging over 30 minutes is indicated by the overbar and spatial averaging is indicated by the angled brackets. The surface heat flux  $H_s$  was extracted from the heat flux  $H$  at the lowest grid point. For each level, the imbalance ratio  $I$  was then calculated as

$$I(z) = \frac{H_s - H(z)}{H_s}, \quad (19)$$

where  $z$  is the height above the surface.

Following De Roo et al. (2018),  $F_1$  was assumed to be an exponential function of the form  $F_1 = a \exp(b u_* / w_*) + c$  and  $F_2$  was assumed to be a linear function of the form  $F_2 = i z / z_i + j$ , with  $a$ ,  $b$ ,  $c$ ,  $d$ , and  $e$  being fitting constants.

First, a set of reference models consisting of only  $F_1$  and  $F_2$  like the model by De Roo et al. (2018) (Eq. 13) was developed:  $F_1$  was fitted to  $I(0.04 z_i)$  separately for each set of simulations (HM, HT200, HT400, and HT800). The height of  $0.04 z_i$  was chosen following De Roo et al. (2018) to represent the conditions within the surface layer where EC measurements are typically performed. Second, one joint  $F_2$  was fitted to  $I/F_1$  for all simulation sets, where  $F_{1,HM}$ ,  $F_{1,HT200}$ ,  $F_{1,HT400}$ , or  $F_{1,HT800}$  were used as  $F_1$ , respectively.

To include  $F_3$  accounting for the effect of thermal surface heterogeneity in the model, the first scaling function for the homogeneous cases, i.e.,  $F_{1,HM}$  was used for all simulation sets. To describe the remaining variability due to thermal surface heterogeneity,  $F_3$  was fit to  $I(0.04 z_i) / F_{1,HM}$ . Based on the investigation of the relationship between  $I(0.04 z_i) / F_{1,HM}$  and  $\mathcal{H}$ ,  $F_3$  was assumed to be a linear function of the form  $F_3 = m \mathcal{H} + n$  with  $m$  and  $n$  as fitting constants. After determining  $F_3$  by fitting it to  $I(0.04 z_i) / F_{1,HM}$ ,  $F_2$  was determined by fitting it to  $I / F_{1,HM} / F_3$ .

### 2.1.3 Development of a model of dispersive heat fluxes

This Chapter is a summary of the methods used to develop a dispersive heat flux model. More information on both the LESs and the data processing can be found in Wanner et al. (2023) in Appendix D. The methods used to apply the model are described in Chapters 2.2.2 and 2.2.3.

#### Setup of the large-eddy simulations

PALM v6 (Maronga et al. 2020) was used for this study. Generally, the setup was based on the simulations by Margairaz et al. (2020a), which were used to include the effect of thermal surface heterogeneity in the model of the surface energy imbalance (Wanner et al. 2022b) and the same domain size, grid-spacing, and patch sizes were used (Chapter 2.1.2). However, it was not possible to prescribe temporally constant and spatially heterogeneous surface temperatures ( $T_s$ ) in PALM. The simulations were therefore initiated with a spatially homogeneous surface temperature of 285 K, and spatially heterogeneous surface fluxes of sensible and latent heat ( $H_s$ ,  $\lambda E_s$ ) were directly prescribed rather than caused by differences in  $T_s$ .

Since both sensible and latent heat fluxes are simulated, the Bowen ratio was varied (0.1–1.3) in addition to different geostrophic wind speeds ( $0.5\text{--}9 \text{ m s}^{-1}$ ) and patch sizes (homogeneous, 200–800 m). Furthermore, simulations were performed with different standard deviations of the surface fluxes ( $H_s$ :  $52\text{--}70 \text{ W m}^{-2}$ ,  $\lambda E_s$ :  $64\text{--}86 \text{ W m}^{-2}$ ) and different sums of  $H_s$  and  $\lambda E_s$  ( $189\text{--}741 \text{ W m}^{-2}$ ). A total of 148 simulations were performed with different

combinations of surface heterogeneity, surface fluxes, and moderately to strongly convective atmospheric conditions.

In all simulations, the same initial vertical profiles of potential temperature and mixing ratio were used, following De Roo et al. (2018). Data was collected for a 30-minute averaging period after 4 hours of spin-up time.

### Model development

The data set generated in the 148 simulations is very complex due to variation in numerous parameters, making it difficult to identify relationships with individual groups of variables and fit appropriate scaling functions. In addition, the surface temperature evolves as a function of atmospheric fluxes. As a result, the surface temperature is not truly homogeneous even in simulations with spatially homogeneous surface fluxes (Fig. 11 in Wanner et al. (2023), Appendix D) and the heterogeneous surface fluxes do not yield surface temperatures quite as systematic as in the previous idealized LESs. This complicates the definition of a reference group, as used in Wanner et al. (2022b) to fit  $F_{1,HM}$  (Chapter 2.1.2). To address this complexity, a machine learning approach was used to develop the model. The training data was collected from the LESs:

The dispersive fluxes at each height  $z$  were calculated following

$$H_d(z) = \langle \bar{w}^* \bar{\theta}^* \rangle(z) c_p \rho \quad (20)$$

and

$$\lambda E_d(z) = \langle \bar{w}^* \bar{q}^* \rangle(z) \lambda_v \rho, \quad (21)$$

where the spatial covariances  $\langle \bar{w}^* \bar{\theta}^* \rangle$  and  $\langle \bar{w}^* \bar{q}^* \rangle$  were calculated following Eq. 8,  $c_p$  is the heat capacity of air,  $\rho$  is the air density, and  $\lambda_v$  is the latent heat of vaporization.

The same dimensionless variable groups as in Wanner et al. (2022b) were used as predictors, but supplemented with vertical gradients of potential temperature  $\theta$  and mixing ratio  $q$  to account for the different magnitude in gradients to be balanced by the transport by SCs.

Again,  $u_*/w_*$  was calculated following Eq. 11–12 for one grid level near the surface and  $z$  was normalized with the ABL height  $z_i$ , defined as the height where  $\langle \overline{w'\theta'} \rangle$  becomes negative for the first time from the surface. The thermal heterogeneity parameter  $\mathcal{H}$  was calculated following Eq. 14–15. Instead of simply using the patch sizes, the heterogeneity length scale  $\bar{L}_h$  was calculated following the spectral approach by Panin and Bernhofer (2008) (Chapter 1.4.2), and  $\Delta\bar{T}$  was calculated as the standard deviation of  $\bar{T}_s$ . All predictor variables were temporally averaged over 30 minutes and spatially averaged over the entire horizontal extent of the domain.

The vertical gradients of  $\theta$  and  $q$  were calculated between the surface values and the center of the ABL following

$$\langle \Delta \bar{s} \rangle = \langle \bar{s} \rangle(0 \text{ m}) - \langle \bar{s} \rangle(0.5 z_i), \quad (22)$$

where  $s$  represents  $\theta$  and  $q$ , respectively.

A random forest machine-learning model (Breiman 2001) was used to predict  $H_d$  and  $\lambda E_d$  from all 148 simulations and at different heights within the surface layer. Two separate models were trained for  $H_d$  and  $\lambda E_d$ , with  $\langle \Delta \bar{\theta} \rangle$  as a fourth predictor variable for  $H_d$  and  $\langle \Delta \bar{q} \rangle$  as a fourth predictor variable for  $\lambda E_d$ .

The resulting models were evaluated with a leave-one-simulation-out-cross-validation where  $H_d$  and  $\lambda E_d$  were predicted for each simulation with the model trained with the data from all other simulations but not the respective simulation itself. Because the result of the random forest algorithm slightly varies due to the randomly chosen samples, this was repeated 100 times. Furthermore, so-called SHAP (Shapley Additive explanation) values (Lundberg et al. 2020; Lundberg and Lee 2017), which estimate the contribution of each predictor variable to the variation of the predictions, were calculated as a metric of the importance of each predictor variable.

## 2.2 Evaluation of the model of dispersive heat fluxes for CHEESEHEAD19

This Chapter is a summary of the methods used to apply the dispersive heat flux model, hereafter referred to as DHFM, to CHEESEHEAD19 LESs and field measurements. First, the CHEESEHEAD19 project (Butterworth et al. 2021) is introduced (Chapter 2.2.1). Second, the application of the DHFM to LESs is described, where the focus lies on the direct comparison of dispersive heat fluxes predicted by the DHFM and the dispersive heat fluxes produced by the LESs (Chapter 2.2.2). Finally, the model is applied to CHEESEHEAD19 field measurements to investigate, how well it is suited as a correction method to close the SEB gap in conventional EC measurements (Chapter 2.2.3).

### 2.2.1 The CHEESEHEAD19 project

The CHEESEHEAD19 (Chequamegon Heterogeneous Ecosystem Energy-balance Study Enabled by a High-density Extensive Array of Detectors) campaign was carried out in northern Wisconsin from June to October in 2019 on a  $10 \times 10 \text{ km}^2$  area centered around the 400 m tall AmeriFlux tower US-PFa (45.9459, -90.2723, Desai et al. (2022)). As shown in Fig. 5, the area is covered by deciduous and coniferous forests, swamplands, and water bodies. Numerous collaborators contributed a large variety of ground based and airborne measurements, including flux measurements at EC towers and with aircraft, profile measurements of different variables using radiosondes and lidars, airborne surface temperature measurements, and phenological observations. Some measurements were performed over the entire duration of the campaign, while others were executed additionally during three

intensive observation periods (IOPs). Butterworth et al. (2021) provide a detailed description of the campaign.

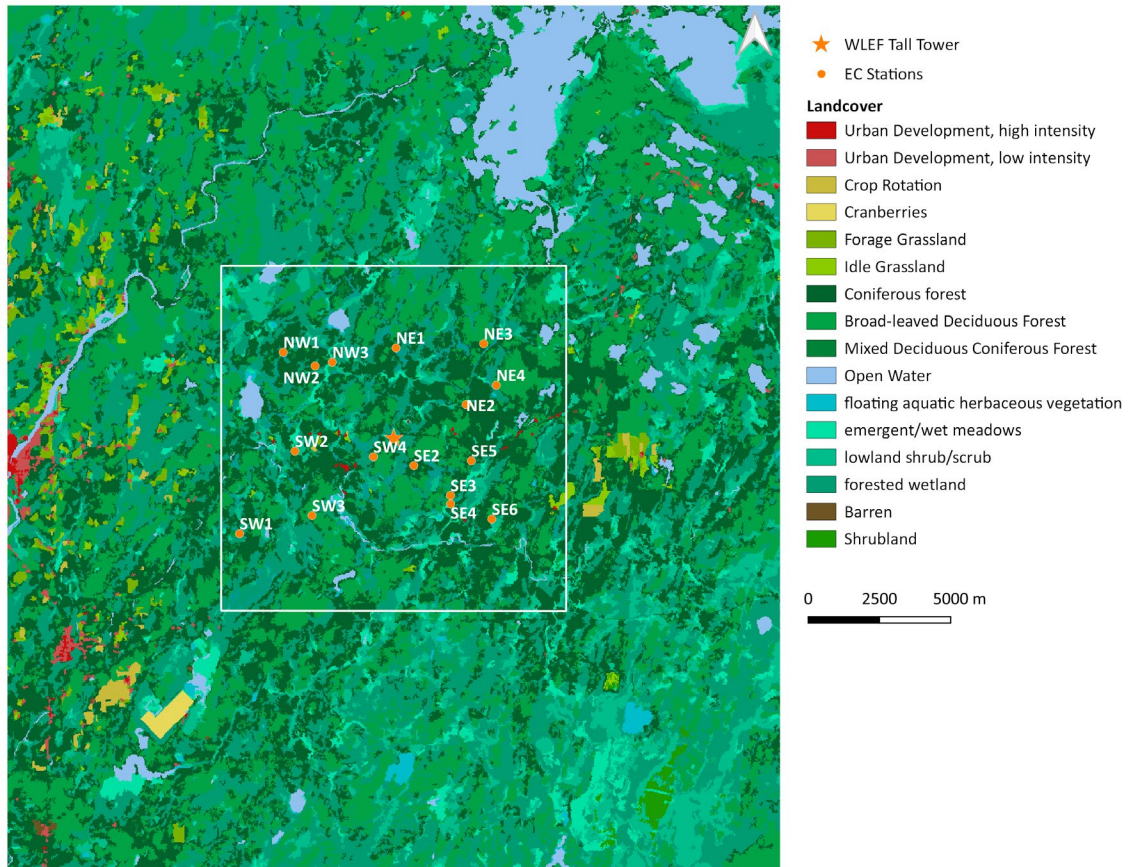


**Figure 5** Land cover map featuring EC tower locations and LES domain extents. The map shows landcover types extracted from the WISCLAND 2.0 dataset (Wisconsin Department of Natural Resources 2016). The orange points show the locations of the 16 EC field stations used to test the dispersive heat flux model. The extent of the map corresponds to the C1 domain in the CHEESEHEAD19 LESs and the white square shows the border of the C2 domain. The domains are centered around the WLEF Tall Tower (US-PFa, 45.9459, -90.2723) depicted by the star (from Wanner et al. (2023)).

### The CHEESEHEAD19 large-eddy simulations

A variety of observations gathered during the CHEESEHEAD19 campaign was used to inform realistic LESs of several days during two of the intensive observation periods (IOPs). To test the DHFM, the simulations of two days during the August IOP (Aug 22–23 2019) were used, which consist of eight ensemble simulations. The simulations were carried out with PALM v6 and consist of a parent domain with two 3D child domains that were recursively nested within each other to provide a high spatial resolution at the location of the CHEESEHEAD19 area. The areas covered by the child1 (C1, medium spatial resolution) and child2 (C2, high spatial resolution) domains are shown in Fig. 5. Lateral and top boundary conditions were informed by the National Centers for Environmental Prediction (NCEP) High Resolution Rapid Refresh data assimilation product (Blaylock et al. 2017; Horel and Blaylock 2017). At the lower boundary, a LSM and a PCM were used,

which were informed by the WISCHLAND 2.0 dataset (Wisconsin Department of Natural Resources 2016) and a variety of observations from the CHEESEHEAD19 campaign.

### The CHEESEHEAD19 EC measurements

Throughout the entire duration of the campaign, a tower network comprising 17 EC towers was operated by the National Science Foundation Lower Atmosphere Observing Facility’s Integrated Surface Flux System. The resulting dataset was used to test the DHFM. One station was discarded from the analysis due to its location at a steep lake shore, since topography effects are not considered in the DHFM. The locations of the remaining 16 EC stations are shown in Fig. 5. The EC stations are placed above different vegetation types, that are pine forest (NW1, NE1, NE2, SE6), aspen forest (NW2, SW1, SW2, SE3, SE5), maple forest (NE4), hardwood forest (NE3, SW3, SW4, SE2), and tussock (NW3, SE4). The measurement heights were adapted to the vegetation heights, and thus were only 3 m above the ground at the tussock sites and varied between 12 m and 32 m at the forested sites (Table 2 in Wanner et al. (2023), Appendix D).

$H_t$  and  $\lambda E_t$  were calculated from detrended 20 Hz measurements of vertical wind speed, dry air temperature, and water vapor concentration. A double rotation coordinate rotation was applied to the wind measurements, a correction for the effect of water vapor on the sonic speed was applied to extract the dry air temperature from sonic temperature measurements, and density effects were corrected.

### 2.2.2 Application of the model to CHEESEHEAD19 large-eddy simulations

To model the dispersive fluxes in the CHEESEHEAD19 LESs with the DHFM, all predictor variables had to be computed from the LES output. For each 30-minute interval,  $u_*/w_*$  was calculated directly above the surface following Eq. 11–12 and then horizontally averaged. The surface is defined to be located at the lower boundary of the domain in all non-forested locations, and at the canopy height  $z_c$  in all forested locations, where the canopy was explicitly resolved by the PCM.

Again,  $z_i$  was defined as the height where  $\langle w'\theta' \rangle$  becomes negative for the first time from the surface. Different height levels up to 60 m above  $\langle z_c \rangle$  (22.08 m) were considered, but only if  $z/\langle z_i \rangle \leq 0.1$ , because the DHFM can only be applied within the surface layer. The domain-averaged displacement height introduced by the canopy was estimated to be 15.46 m and was considered in the calculation of  $z/\langle z_i \rangle$ .

To calculate  $\mathcal{H}$  following Eq. 14–15,  $\bar{T}_s$  was extracted from the LES surface temperature in all non-forested locations and from the air temperature at  $z_c$  in all forested locations. To calculate  $\Delta\bar{T}$ ,  $\langle \bar{T}_s \rangle$ , and  $\bar{L}_h$ , the extent of the C2 domain was used.  $\Delta\bar{T}$  was calculated as the standard deviation of  $\bar{T}_s$ , and the spectral approach by Panin and Bernhofer (2008) was used to determine  $\bar{L}_h$ .  $\langle \bar{U}_g \rangle$  was extracted from the horizontal wind speed at  $1.1 \langle z_i \rangle$ .

The gradients of  $\langle \bar{\theta} \rangle$  and  $\langle q \rangle$  were calculated following Eq. 22 with values extracted from the C1 domain at the second grid layer and  $0.5 \langle z_i \rangle$ .

To exclude 30-minute intervals with stable or neutral atmospheric conditions, the sensible surface heat flux was extracted. Again, the surface flux provided by the LESs was used in the non-forested locations. In the forested locations, the surface heat flux was calculated as

$$H_s = \left( \langle \bar{w}\bar{\theta} - \bar{w}\bar{\theta} \rangle(z_c) + \langle \bar{w}^* \bar{\theta}^* \rangle(z_c) \right) c_p \rho(z_c) + \overline{H_{sgs}}(z_c). \quad (23)$$

All 30-minute intervals with  $\langle H_s \rangle < 10 \text{ W m}^{-2}$  were discarded.

The DHFM was set up by training the random forest algorithm with the data extracted from the 148 idealized LESs (Chapter 2.1.3) and applied to all remaining 30-minute intervals to predict the sensible and latent dispersive heat fluxes ( $H_{d,mod}$  and  $\lambda E_{d,mod}$ ). For the results presented in Chapter, the fit and application of the DHFM was repeated 100 times and the predictions of all 100 cycles were averaged, whereas the results in Wanner et al. (2023) were so far based on only one random fit of the DHFM. To evaluate how well the DHFM predicts the dispersive heat fluxes,  $H_{d,mod}$  and  $\lambda E_{d,mod}$  were compared to the dispersive heat fluxes produced by the LESs ( $H_{d,LES}$  and  $\lambda E_{d,LES}$ ) which were calculated following Eq. 8 and Eq. 20–21.

### 2.2.3 Application of the model to CHEESEHEAD19 field measurements

The model was applied as a SEB correction method to the flux measurement dataset from the 16 CHEESEHEAD19 EC stations. Therefore, only 30-minute intervals during which all available SEB measurements were running could be considered. These are measurements of net radiation ( $R_{net}$ ), sensible and latent turbulent heat fluxes ( $H_t$  and  $\lambda E_t$ ), latent and sensible heat storage changes in the air ( $H_{\Delta St}$  and  $\lambda E_{\Delta St}$ ), and ground heat flux ( $G$ ). Only 30-minute intervals with  $R_{net} \geq 0 \text{ W m}^{-2}$  and  $H_t \geq 10 \text{ W m}^{-2}$  were used for this analysis, since the DHFM was only developed for unstable conditions. Furthermore, 30-minute intervals with  $(H_t + \lambda E_t) > 1.5 R_{net}$  or  $(H_t + \lambda E_t + H_{\Delta St} + \lambda E_{\Delta St}) < 0.5 R_{net}$  were discarded, because the first case is very unrealistic and in the second case, the SEB gap would be larger than the measured fluxes and storage terms, resulting in a very high uncertainty. Since the DHFM uses spatially averaged predictor variables, it is not possible to gather the necessary information at typical EC stations. While a lot of additional measurements were performed during the CHEESEHEAD19 campaign that could at least partially provide the predictor variables, this is not the case at typical EC stations, either. To test the model under realistic conditions, no additional CHEESEHEAD19 data was used.

Instead, the atmospheric variables were extracted from ERA5 reanalysis data (Hersbach et al. 2023a, 2023b). Variables provided at pressure levels were extracted by deriving the height of each pressure level with the barometric formula and then linearly interpolating to the desired height.  $U_g$  is the horizontal wind speed at  $1.1 z_i$ , and  $\theta$  and  $q$  were derived from

the output at  $0.5 z_i$ . The single level output directly provided  $z_i$  and  $u_*$  and the 2 m values of  $\theta$ ,  $q$ , and  $w_*$  were also derived from the single level output.

The surface variables were extracted from land surface temperature fusion maps provided by Desai et al. (2021). These surface temperature maps have a spatial resolution of 50 m and a temporal resolution of 1 hour and were developed by combining observations from different satellites. For each EC station, a  $10 \times 10 \text{ km}^2$  area centered around the station was used to calculate  $\Delta \overline{T_s}$ ,  $\langle \overline{T_s} \rangle$ , and  $\overline{L_h}$ .

All predictor variables were then fed into the DHFM to predict the sensible and latent dispersive heat fluxes ( $H_{d,mod}$  and  $\lambda E_{d,mod}$ ). This step was repeated 100 times and the predictions of all cycles were averaged. The sum of  $H_t$ ,  $\lambda E_t$ ,  $H_{\Delta St}$ ,  $\lambda E_{\Delta St}$ ,  $H_{d,mod}$ , and  $\lambda E_{d,mod}$  was then compared to the total available energy ( $R_{net} - G$ ) to investigate if the SEB could be closed.

## 3 RESULTS & DISCUSSION

In this Chapter, the main findings from the three studies contributing to this work are presented and discussed. First, the influence of lower boundary conditions on the magnitude of dispersive fluxes is investigated (Chapter 3.1), and second, the further developed model of the surface energy imbalance with respect to thermal surface heterogeneity is presented (Chapter 3.2). Finally, the MDHF is introduced and applied to realistic LESs and field measurements, where the focus lies not only on evaluating the performance itself, but also on its applicability as a correction method for EC field measurements (Chapter 3.3).

### 3.1 The choice of lower boundary conditions and its effect on dispersive fluxes

This Chapter summarizes the main findings from the study on the effect of different lower boundary conditions on dispersive fluxes. More details can be found in Wanner et al. (2022a) in Appendix B.

To investigate whether surface conditions allowing for feedbacks between the surface and the atmosphere cause stronger dispersive fluxes in LESs, idealized simulations were carried out with traditionally used PSF and with a LSM and PCM over two different vegetation types. For a grassland, simulations with PSF were compared to simulations with a LSM, and for a forest, simulations with PSF were compared to a combination of a LSM and a PCM.

A comparison of horizontal cross-sections of 30-minute averaged vertical wind speed  $w$  between forest simulations with PSF and LSM+PCM as lower boundary conditions shows that cellular and striped patterns near the canopy top are more pronounced in the LSM+PCM simulations across all atmospheric stabilities (see Fig. 3–5 in Wanner et al. (2022a) in Appendix B). This implies that secondary circulations reach closer to the canopy top when the LSM and PCM are used. With larger distance to the canopy top, a difference can still be observed, but is less pronounced.

To investigate the effect of PSF and LSM(+PCM) on the dispersive fluxes, the differences between total dispersive fluxes  $F_d = H_d + \lambda E_d$  are shown for each height  $z$  up to 100 m above the canopy in Fig 6. Positive values indicate that  $F_d$  observed in the LSM(+PCM) simulations is larger than  $F_d$  in the PSF simulations. In the grassland simulations (light green),  $F_{d,LSM}$  is always smaller than  $F_{d,PSF}$  and the difference increases linearly with height and also with instability.

The behavior of  $F_d$  in the forest simulations (dark green) is more complex.  $F_{d,PSF}$  approaches zero near the canopy top, while  $F_{d,LSM+PCM}$  does not decrease so strongly near the surface and instead reaches values of  $1.14 \pm 0.09\%$  under moderately unstable

conditions (MU),  $2.76 \pm 0.21\%$  under strongly unstable conditions (SU), and  $5.78 \pm 0.45\%$  under free convective conditions (FC). Therefore,  $F_{d,LSM+PCM}$  is larger than  $F_{d,PSF}$  near the canopy top and the difference increases with instability. However, further up in the ABL, no uniform behavior of  $F_d$  can be observed across the different atmospheric conditions. About 20 m above the canopy top,  $F_{d,LSM+PCM}$  is smaller than  $F_{d,PSF}$  under MU conditions, but similar to  $F_{d,PSF}$  under SU and FC conditions. Even further up, at about 80 m above the canopy top,  $F_{d,LSM+PCM}$  is similar to  $F_{d,PSF}$  under MU conditions, larger than  $F_{d,PSF}$  under SU conditions, and smaller than  $F_{d,PSF}$  under FC conditions. Generally, the differences are smaller under MU and SU conditions compared to the differences under FC conditions.

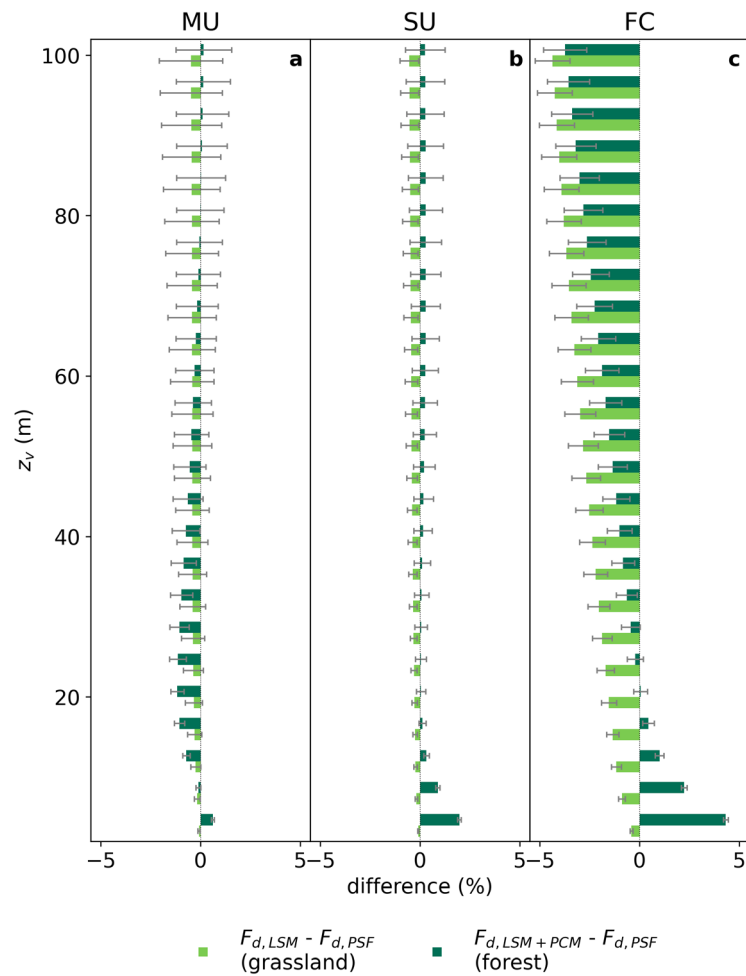


**Figure 6** Profiles of differences between 30-min averaged dispersive fluxes in LSM(+PCM) simulations and respective PSF simulations for moderately unstable (MU), strongly unstable (SU), and free convective (FC) atmospheric stabilities. The  $y$ -axis shows the height above the vegetation top  $z_v$ . Modified after Wanner et al. (2022a).

The investigation of vertical profiles of the flux variance similarity functions  $\Phi_u$  and  $\Phi_w$  helps to explain this behavior. Similar to the magnitude of dispersive fluxes,  $\Phi_u$  and  $\Phi_w$  depend on the atmospheric stability and for all stabilities, they are larger in the LSM+PCM simulations compared to the PSF simulations near the canopy top.

The reason is that  $\Phi_u$  and  $\Phi_w$  are forced to zero at the lower boundary of the domain, which represents the canopy top in the PSF simulations. In the LSM+PCM simulations the canopy is resolved, the canopy top is lifted up from the lower domain boundary, and  $\Phi_u$  and  $\Phi_w$  are not forced to zero at the canopy top, resulting in larger dispersive fluxes.

At about 20 m above the canopy top,  $\Phi_u$  and  $\Phi_w$  from the PSF simulations become larger than  $\Phi_u$  and  $\Phi_w$  from the LSM+PCM simulation, explaining why  $F_{d,PSF}$  becomes larger than  $F_{d,LSM+PCM}$  with increasing height.  $\Phi_u$  features a bulbous shape with a maximum at 20 m while  $\Phi_w$  increases with altitude, which implies that secondary circulations develop, contributing to larger variance in the vertical wind far away from the canopy top and to larger variance in the horizontal wind near the canopy top. All described features of  $\Phi_u$  and  $\Phi_w$  are strongly pronounced in the simulations with FC conditions, but very weak in the simulations with SU or MU conditions.

The hypothesis that the LSM alone may increase the magnitude of dispersive fluxes by allowing for feedback between the surface and the atmosphere could not be verified. In fact, the resulting dispersive fluxes in the LSM simulations are smaller than in the PSF simulations. The use of the LSM in combination with the PCM allows for larger dispersive fluxes directly above the canopy, but further up, it depends on the atmospheric stability and height above the canopy determine whether the use of LSM+PCM yield larger dispersive fluxes or not.

### 3.2 The surface energy imbalance model considering thermal surface heterogeneity

This Chapter presents and discusses the final surface energy imbalance model including thermal surface heterogeneity. More information, also on the reference models, which are not shown here, can be found in Wanner et al. (2022b) in Appendix C.

The fits of the scaling functions contributing to the final imbalance model are shown in Fig. 7. Figure 7a shows the relationship between the imbalance  $I$  and  $u_*/w_*$ . The black curve shows  $F_{1,HM}$  fitted to the set of simulations with homogeneous surface temperature, which is

$$F_{1,HM} = 0.133 \exp\left(-15.3 \frac{u_*}{w_*}\right) + 0.056. \quad (24)$$

The red curves show the fits to each set with heterogeneous  $T_s$ , which deviate stronger from  $F_{1,HM}$  with increasing heterogeneity length scales. This variability is captured by the additional scaling function  $F_3$  which is shown in Fig. 7b. Two linear relationships were defined to describe the relationship between  $I(0.04 z_i)/F_{1,HM}$  and  $\mathcal{H}$ . For strongly unstable cases with  $u_*/w_* < 0.1$ , the resulting scaling function is

$$F_{3,c} = 0.018 \mathcal{H} + 0.973 \quad (25)$$

and for moderately unstable cases with  $u_*/w_* > 0.14$  it is

$$F_{3,r} = 0.016 \mathcal{H} + 1.07. \quad (26)$$

Analyzing horizontal cross sections of the 30-minute averaged vertical wind speed (Fig. 5 in Wanner et al. (2022b) in Appendix C) revealed that these groups correspond to the formation of cellular structures in simulations with  $U_g = 1 \text{ m s}^{-1}$  and a strongly unstable ABL and roll-like structures in simulations with  $U_g \geq 3 \text{ m s}^{-1}$  and a moderately unstable ABL. Because no clear cellular or roll-like shapes could be identified in the vertical wind speed in simulations with  $U_g = 2 \text{ m s}^{-1}$ , those simulations were discarded from the analysis.

As shown in Fig. 7c, the vertical profiles of  $I$  collapse into nearly one line for  $z/z_i < 0.07$  after normalizing  $I$  with  $F_{1,HM}$  and  $F_{3,c}$  or  $F_{3,r}$ , respectively. The relationship between  $I/F_{1,HM}/F_3$  can be described by

$$F_2 = 20.2 \frac{z}{z_i} + 0.153. \quad (27)$$

Comparing the vertical profiles of  $I/F_{1,HM}/F_3$  to profiles of  $I$  normalized with  $F_{1,HM}$ ,  $F_{1,HT200}$ ,  $F_{1,HT400}$ , or  $F_{1,HT800}$  respectively (see Fig. 2 in Wanner et al. (2022b) in Appendix C), shows that  $F_{3,c}$  and  $F_{3,r}$  capture the variability in  $I$  introduced by the thermal surface heterogeneity very well, since all profiles collapse equally into one line.

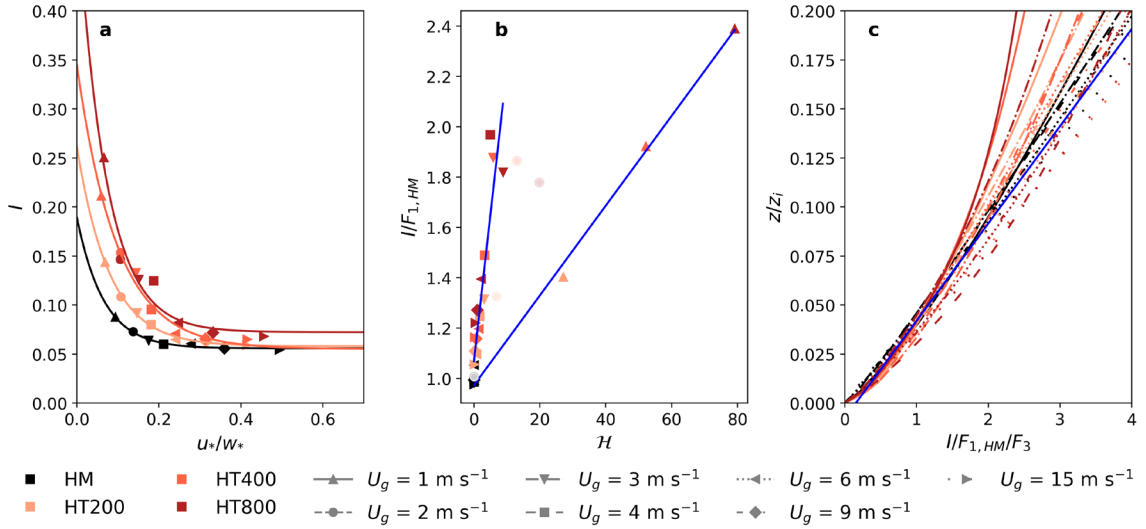


**Figure 7** Representation of the three scaling functions that form the surface energy imbalance model. Panel a shows the imbalance ratio  $I$  at  $0.04 z/z_i$  as a function of the stability parameter  $u_*/w_*$ . The four simulation sets of different surface heterogeneity are represented by different colors. The atmospheric stability is steered by changes in  $U_g$ , shown by different marker shapes. For each simulation set, a separate fit of the scaling function  $F_1$  was performed, represented by the curves. Only the fit for the homogeneous simulations ( $F_{1,HM}$ , Eq. 24) shown by the black curve is used in the model. Panel b shows  $I$  at  $0.04 z/z_i$  normalized with  $F_{1,HM}$  against the heterogeneity parameter  $\mathcal{H}$ . The data is separated into two groups: (1) simulations with  $U_g = 1 \text{ m s}^{-1}$  that show cellular shaped secondary circulations, and (2) simulations with  $U_g \geq 3 \text{ m s}^{-1}$  that show roll-shaped secondary circulations. Simulations with  $U_g = 2 \text{ m s}^{-1}$  are discarded because they show no clearly cellular nor

roll-shaped structures. The two blue lines show the fits of the third scaling functions to the two groups ( $F_{3,c}$  and  $F_{3,r}$ , Eq. 25–26). Panel c shows the vertical profiles of  $I$  normalized with  $F_{1,HM}$  and the respective scaling functions  $F_{3,c}$  or  $F_{3,r}$ . The blue line shows the fitted scaling function  $F_2$  (Eq. 27). Modified after Wanner et al. (2022b).

The model can be applied to correct EC measurements following

$$I = \frac{F_{1,HM} \left( \frac{u_*}{w_*} \right) F_2 \left( \frac{z}{z_i} \right) F_3(\mathcal{H})}{1 - F_{1,HM} \left( \frac{u_*}{w_*} \right) F_2 \left( \frac{z}{z_i} \right) F_3(\mathcal{H})} H_t, \quad (28)$$

where  $F_3$  is  $F_{3,c}$  or  $F_{3,r}$ , depending on  $u_*/w_*$ , and  $H_t$  is the sensible turbulent heat flux captured by the EC measurement.

There are a few limitations to the application of the model with regard to the atmospheric and surface conditions under which it can be applied, which are discussed in detail in Wanner et al. (2022b) in Appendix C. Furthermore, three fundamental weaknesses of the model were identified: the lack of a model of the imbalance in the latent heat flux, the transferability of the patch-size based heterogeneity length scale to environmental conditions, and the fact that the entire imbalance is modelled instead of the energy transport by secondary circulations.

To close the SEB gap by correcting EC measurements, both the sensible and the latent heat flux must be corrected. The model can be applied to the latent heat flux as well, assuming that the Bowen ratio of the surface energy imbalance, including  $H_{disp}$ ,  $\lambda E_{disp}$ ,  $\Delta S_a$ , and  $\Delta S_b$ , equals the Bowen ratio of the measured fluxes  $H_{turb}$  and  $\lambda E_{turb}$ . Adapting  $H_{turb}$  and  $\lambda E_{turb}$  to close the SEB gap while preserving the Bowen ratio has been suggested before (Twine et al. 2000), and spatial EC measurements confirm that the Bowen ratio is similar in small and mesoscale flux contributions (Eder et al. 2014; Mauder et al. 2007b). However, for single-tower measurements, this assumption can only hold if the measured small-scale turbulent flux is representative of the surrounding area over which the SCs develop.

As mentioned in Chapter 1.4.2, most landscapes feature what Bou-Zeid et al. (2020) classify as unstructured heterogeneity, where the individual patches differ greatly in size and shape. It is therefore not possible to specify the heterogeneity length scale by a simple patch size. Spectral approaches, like the one by Panin and Bernhofer (2008) can be used to determine a characteristic heterogeneity length scale. However, this does not represent the patch size which was used as heterogeneity length scale in the model development. If a spectral approach was applied to the surface temperature distributions in the LESs, the resulting heterogeneity length scales would be larger than the sizes of the individual patches because multiple warm or cool patches are often clustered, forming larger warm and cool areas, as shown in Fig. 4.

Finally, modeling the entire surface energy imbalance can serve to close the SEB gap, but does not provide any information on how the SEB gap is composed, i.e., how much storage changes and the energy transport by SCs contribute to it. Depending on the intended use,

however, this distinction can be important. To accomplish the main goal of this work, which is investigating how heterogeneous ecosystems affect atmospheric transport processes, it is necessary to investigate dispersive heat fluxes separately. To determine the fluxes between an ecosystem and the atmosphere, only the dispersive heat fluxes should be added to the turbulent fluxes measured by the EC station. In contrast, if the flux measurements are used to validate surface fluxes provided by land surface models, it would be reasonable to additionally include the storage changes. However, as mentioned in Chapter 1.2.4, storage changes can be measured at single-tower stations which is a more direct way of determining their contribution, and if only the daily SEB is of interest, it may even be possible to neglect them. These considerations support the direct modeling of energy transport by SCs as dispersive fluxes.

### 3.3 Development of a model of dispersive heat fluxes

To directly predict the energy transport by TOSs and TMCs, the DHFM was developed, which is presented in this Chapter. During the development of the DHFM, special attention was paid to overcome the weaknesses identified in the previously developed surface energy imbalance model by predicting the sensible and latent dispersive heat fluxes separately and using the spectral approach by Panin and Bernhofer (2008), which can also be applied to real landscapes, to determine the predominant heterogeneity length scale and calculate  $\mathcal{H}$ . First, the performance of the DHFM is evaluated (Chapter 3.3.1). Second, an option to apply the DHFM to EC stations without using any additional in-situ measurements is presented and discussed (Chapter 3.3.2), since one of the requirements for the model of dispersive heat fluxes was that it can be used to correct atmospheric heat fluxes without much additional measurement effort at existing EC stations (Chapter 1.5). More details can be found in Wanner et al. (2023) in Appendix D.

#### 3.3.1 Performance

To evaluate the performance of the DHFM, a cross validation was performed. Figure 8a shows that for the sensible dispersive heat fluxes, the prediction agrees very well with the values directly calculated from the LESs. The agreement is not as satisfactory for the latent dispersive heat flux. The comparison between predicted and LES values shown in Fig. 8b exhibits a larger scatter, which results in a substantially lower  $R^2$  of 0.75. This indicates that another predictor variable may be needed to explain the remaining variance. One factor that was not considered in this study but could have a strong effect on the energy transported by SCs, especially in the form of latent heat, is the entrainment of air at the upper boundary of the ABL which can affect the vertical profiles of  $\theta$  and  $q$ , especially in the upper half of the ABL (Gao et al. 2017; Huang et al. 2008; Mauder et al. 2020).

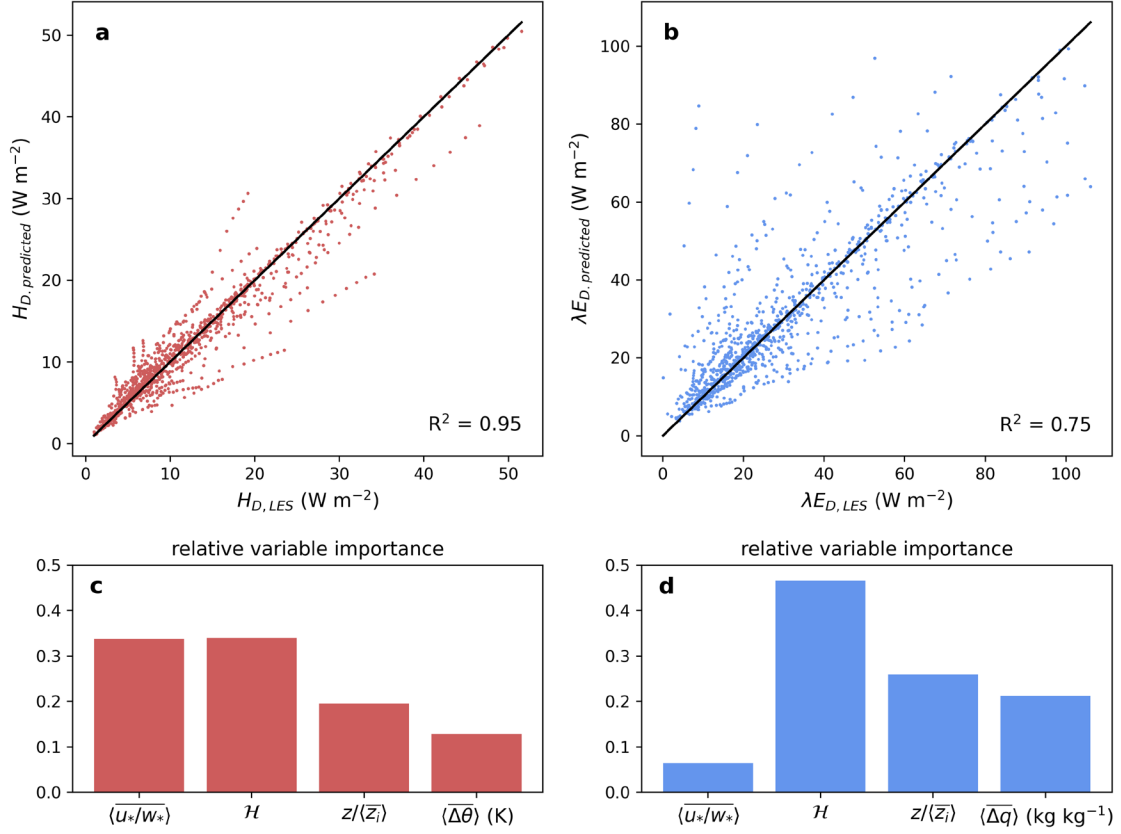


**Figure 8** Performance of the dispersive heat flux model based on the cross-validation. Panels a-b show comparisons of modeled dispersive heat fluxes ( $y$ -axis) against true dispersive heat fluxes calculated directly from the LES output ( $x$ -axis) for (a) sensible and (b) latent dispersive heat fluxes. Panels c-d show the relative importance of predicting variables in the models of (c) sensible and (d) latent dispersive heat flux. Modified after Wanner et al. (2023).

In Fig. 8c–d, the relative contributions of the predictor variables to explaining the variance in the dispersive fluxes are shown. In both cases,  $\mathcal{H}$  has a large share and the normalized measurement height and corresponding vertical gradients have about half as large a share. It is striking that the atmospheric stability explains a lot of the variance in the sensible dispersive heat flux, but only very little of the variance in the latent dispersive heat flux. One possible explanation is that the atmospheric stability is strongly related to the vertical gradient of  $\theta$ . A stronger gradient in  $\theta$  leads to more strongly convective conditions, under which more pronounced SCs develop, which transport warm air from the surface to the upper ABL and cold air from the upper ABL to the surface. Therefore,  $\langle \overline{u_*}/w_* \rangle$  alone can explain much of the variance in  $H_{disp}$ . However, the vertical gradient of  $q$  is not necessarily related to atmospheric stability. Under strongly convective conditions,  $\langle \overline{\Delta q} \rangle$  may be very small, in which case strong SCs would develop, but not contribute much to the transport of latent heat. This explains why  $\langle \overline{\Delta q} \rangle$  is more important than  $\langle \overline{u_*}/w_* \rangle$  for predicting  $\lambda E_{disp}$ . The DHFM was applied to the CHEESEHEAD19 LESs to directly compare the predicted dispersive heat fluxes ( $F_{d,mod}$ ) to the ones calculated from the LES output ( $F_{d,LES}$ ) as shown in Fig. 9. The DHFM clearly overestimates  $H_{disp}$  by 17.3% and also slightly overestimates

$\lambda E_{disp}$  by 4.9%, resulting in an 8.5% overestimation of the total dispersive heat flux. One possible explanation for the overestimation is that a LSM and a PCM were deployed in the realistic CHEESEHEAD19 LESs, whereas PSF were used in the idealized LESs on which the DHFM is based. The dispersive fluxes were compared for heights of 10–60m above the canopy top, at which the use of the LSM and PCM resulted in smaller dispersive heat fluxes than were observed in simulations with PSF (Fig. 6) (Wanner et al. 2022a).

The stronger overestimation of  $H_{disp}$  results in a larger Bowen ratio in  $F_{d,mod}$  compared to  $F_{d,LES}$  as shown in Table 1. However, it must be noted that in the idealized LESs used to develop the DHFM, the Bowen ratio of dispersive fluxes almost equals the Bowen ratio of turbulent fluxes (see Table 3 in Wanner et al. (2023) in Appendix D), similar to observations in the field (Eder et al. 2014; Mauder et al. 2007b). In contrast, in the CHEESE-HEAD19 LESs, the Bowen ratio of dispersive fluxes is much lower than the Bowen ratio of the turbulent fluxes (see Table 4 in Wanner et al. (2023) in Appendix D). Nevertheless, the DHFM partially captured the different flux partitioning in the dispersive fluxes.

**Table 1** Bowen ratios ( $\beta$ ) show the different partitioning into sensible and latent heat in the domain-averaged surface fluxes ( $\langle F_s \rangle$ ), turbulent fluxes ( $\langle F_t \rangle$ ), and true ( $F_{d,LES}$ ) dispersive heat fluxes directly calculated from the LES output, as well as modelled ( $F_{d,mod}$ ) dispersive heat fluxes.

	$\langle F_s \rangle$	$\langle F_t \rangle$	$F_{d,LES}$	$F_{d,mod}$
$\beta$	0.669±0.129	0.647±0.115	0.461±0.176	0.519±0.208

The difference in Bowen ratios of turbulent and dispersive heat fluxes in the CHEESE-HEAD19 LESs may again be related to the effect of entrainment on the vertical profiles of  $\theta$  and  $q$  (Gao et al. 2017; Huang et al. 2008; Mauder et al. 2020), affecting the partitioning of energy transport by SCs that span the entire ABL vertically, but not so much the energy transport by small-scale turbulence near the surface. Furthermore, the use of LSM and PCM could play a role. A closer look at Fig. 8 in Wanner et al. (2022a) in Appendix B reveals that the sensible and latent dispersive heat fluxes react differently to PSF and LSM(+PCM) as lower boundary condition. At 40m above the grass surface, the sensible dispersive heat fluxes in the LSM simulations are slightly larger than in the PSF simulations, whereas the latent dispersive heat fluxes are considerably smaller in the LSM simulations than in the PSF simulations. The resulting Bowen ratio is larger in the LSM simulations, compared to the PSF simulations. Above the forest, the behavior is not so uniform.

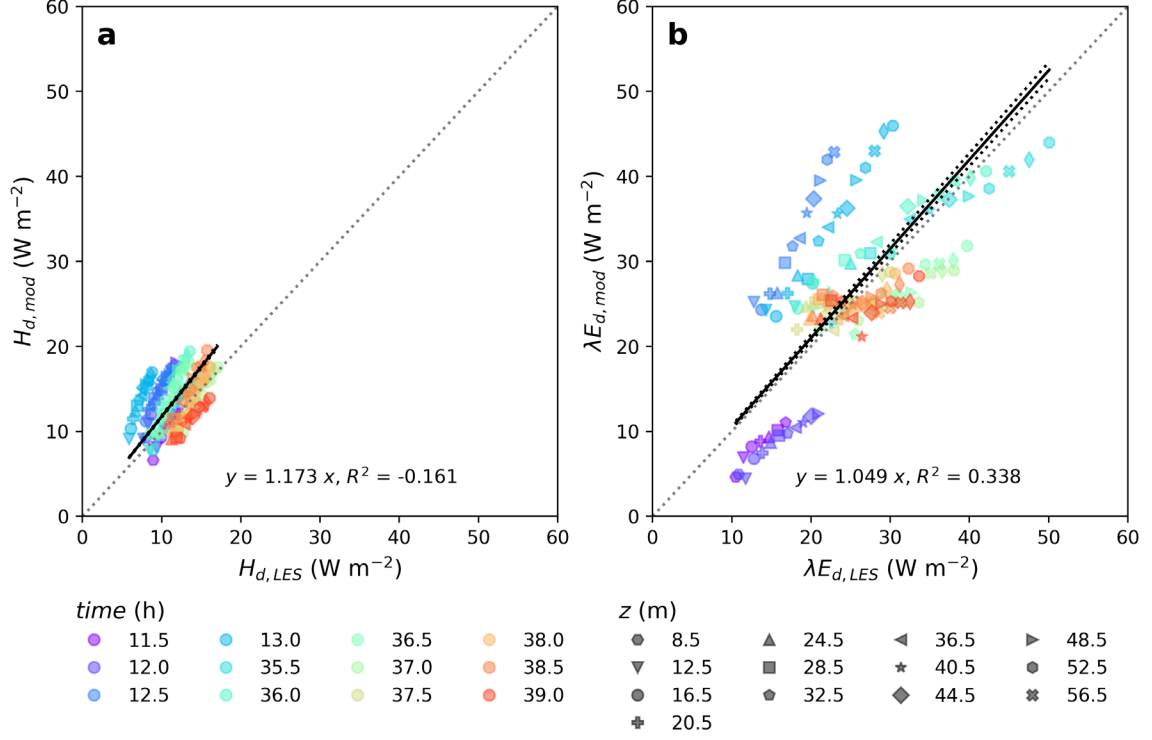


**Figure 9** Comparison of modeled (a) sensible and (b) latent dispersive heat fluxes with the sensible and latent dispersive heat fluxes calculated as spatial covariances from the output of the more realistic CHEESE-HEAD19 LESs. The black lines show an orthogonal distance regression (ODR) forced through the origin, with the solid line representing the ODR with the mean values of the 100 predictions, and the dotted lines representing the standard deviation of ODRs with each of the 100 predictions. The  $y$ -values of the markers show the dispersive fluxes averaged over the 100 predictions. The colors represent 30-minute observation periods used for this analysis and the symbols represent the height above the displacement height. Modified after Wanner et al. (2023).

Finally, the DHFM was applied to CHEESEHEAD19 field measurements to show if the correction of atmospheric heat fluxes by adding the modeled dispersive heat fluxes to the turbulent heat fluxes measured at the EC stations improves the SEB closure. It could be only applied to a very limited number of observations because many predictor variables collected to apply the DHFM to the field measurements lay outside the range of predictor variables used to train the model. While  $\langle \overline{u_* / w_*} \rangle$ ,  $\mathcal{H}$  and  $\langle \overline{\Delta q} \rangle$  were covered quite well, there were large deficits in  $z / \langle \overline{z_i} \rangle$  and  $\langle \overline{\Delta \theta} \rangle$ . Due to the rather coarse grid resolution of the idealized LESs used to train the DHFM, measurement heights near the surface could not be considered. The range of measurement heights to which the DHFM can be applied could therefore be increased by generating a training data set with a high resolution LES. However, this would be very computationally expensive. The insufficient coverage of  $\langle \overline{\Delta \theta} \rangle$  seems to be partially caused by an overestimation of  $\langle \overline{\Delta \theta} \rangle$  from the ERA5 reanalysis data (Fig. 10 in Wanner et al. (2023), Appendix D). It may still be beneficial to expand the training data set to include larger values in  $\langle \overline{\Delta \theta} \rangle$ ,  $\langle \overline{\Delta q} \rangle$ , and  $\langle \overline{u_* / w_*} \rangle$ , as further discussed in Wanner et al. (2023) in Appendix D.

For all remaining observations, Fig. 10 shows the distribution of the available energy ( $R_{net} - G$ ) between the measured heat fluxes ( $H_t, \lambda E_t$ ), heat storage changes in the air ( $H_{\Delta St}, \lambda E_{\Delta St}$ ) and modeled dispersive heat fluxes ( $H_{d,mod}, \lambda E_{d,mod}$ ). The measured heat fluxes account for about 75% on average, resulting in an SEB gap of about 25%. Including the storage changes in air only slightly reduces the SEB gap to about 22.8% on average, and adding the modelled dispersive fluxes reduces the SEB gap to 15.7% on average.

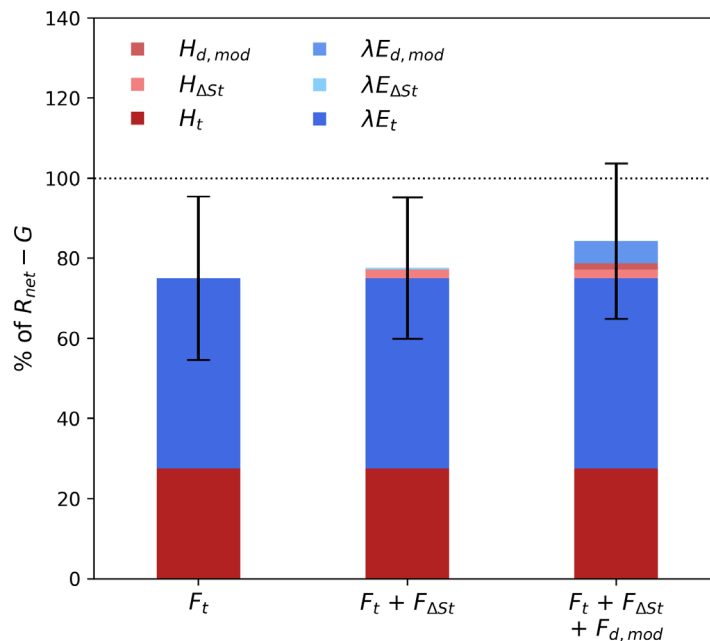


**Figure 10** Share of turbulent heat fluxes ( $H_t, \lambda E_t$ ), energy storage change in air ( $H_{\Delta St}, \lambda E_{\Delta St}$ ), and modeled dispersive heat fluxes ( $H_{d,mod}, \lambda E_{d,mod}$ ) of the total available energy ( $R_{net} - G$ ). The error bars represent the standard deviation of the sums shown in each bar (from Wanner et al. (2023)).

The remaining SEB gap is still very large. However, several contributions to the SEB are still neglected, which are estimated to account for about 13% of the available energy: The storage change in the biomass was not measured at all stations throughout the campaign, which is why it is not included in the analysis. However, at the end of the campaign, biomass heat storage change was measured at a few stations and was found to account for 6.5% of ( $R_{net} - G$ ). Furthermore, CSAT3AW sonic anemometers were deployed during the CHEESEHEAD19 campaign, which can cause an underestimation of the measured turbulent fluxes by up to 5% (Horst et al. 2015). Finally, energy consumption by photosynthesis may account for 1–2% of the available energy (Blanken et al. 1997; Meyers and Hollinger 2004; Oncley et al. 2007; Schmid et al. 2000).

After taking these factors into account, the remaining SEB gap would be reduced to around 3% of the available energy. The remaining SEB gap could be caused by an underestimation of the dispersive fluxes by the DHFM. On the one hand, the dispersive fluxes may be underestimated in the idealized LESs used to develop the DHFM due to the rather coarse spatial resolution, and on the other hand, weak topography in the field could slightly amplify the dispersive fluxes, which is not considered in the DHFM.

### 3.3.2 Application

The DHFM consists of a training data set based on the output of all 148 LESs (see Chapter 2.1.3) and a python script to apply the model. It is applied by fitting the models of  $H_{disp}$  and  $\lambda E_{disp}$  to the training data set and then applying them to the predictor variables collected for 30-minute intervals to predict  $H_{disp}$  and  $\lambda E_{disp}$ . The python script to apply the model and the training data set will be published as an electronic supplement to Wanner et al. (2023).

The DHFM predicts the absolute dispersive heat fluxes in contrast to former SEB correction models, which predict the surface energy imbalance by scaling the measured turbulent and sensible latent heat fluxes (De Roo et al. 2018; Huang et al. 2008; Wanner et al. 2022b). However, the fluxes measured at an EC station represent a rather small footprint area, whereas a much larger area influences the energy transport by secondary circulations (Mauder et al. 2007a; Panin and Bernhofer 2008). The measured fluxes may vary strongly between different locations within the source area of the dispersive fluxes, especially in heterogeneous ecosystems. It is therefore not possible to determine the dispersive heat flux as a factor of the turbulent heat flux measured at any location within the source area.

This further implies that other local measurements at EC stations are not well suited to predict dispersive fluxes, but spatially averaged values representing the surrounding landscape should be used. Therefore, ERA5 reanalysis data, representing an area of roughly  $28 \times 28 \text{ km}^2$ , was used to collect the atmospheric variables contributing to the predictor variables, and land surface temperature fusion maps of  $10 \times 10 \text{ km}^2$  around each CHEESEHEAD19 EC station, derived from satellite observations, were used to collect the surface variables.

To estimate how well these two data sets are suited to provide the predicting variables for the DHFM, the predicting variables were compared against the ones determined in the CHEESEHEAD19 LESs (see Fig. 10 in Wanner et al. (2023) in Appendix D), which, in turn, was shown to agree well with field observations (Paleri et al. 2023a). On average, the agreement in  $\mathcal{H}$  and  $\langle \bar{z}_l \rangle$  is quite good. However, less variance in  $\langle \bar{z}_l \rangle$  is captured by ERA5. Furthermore,  $\langle \overline{u_* / w_*} \rangle$  is considerably lower in ERA5 and  $\langle \overline{\Delta q} \rangle$  and  $\langle \overline{\Delta \theta} \rangle$  are considerably larger.

This comparison was limited to one location and only a few hours and therefore does not allow any conclusions to be drawn about the general suitability of ERA5. However, it suggests that there is still room for improvement in the use of ERA5 to determine the predictor variables for the DHFM, and reasons for the discrepancies are discussed in Wanner et al. (2023) in Appendix D.

Apart from that, the use of ERA5 reanalysis data and satellite-based surface temperature maps offers the great advantage that no additional instrumentation is needed at the EC stations to apply the DHFM. The necessary satellite observations of the surface temperature

and ERA5 reanalysis data can be obtained at most locations around the world and even for the past. This approach can therefore be used to correct atmospheric flux measurements consistently in already existing long time series.

## 4 CONCLUSION

In this work, a variety of methods was combined with numerous different datasets to further advance the understanding of the influence of heterogeneous ecosystems on the atmospheric transport of energy. The first objective was to investigate whether lower boundary conditions that allow feedbacks between the surface and the atmosphere cause larger dispersive fluxes in LESs. An idealized study was set up, to compare the dispersive fluxes developing with typically used PSF to dispersive fluxes developing when a LSM or PCM is deployed (Wanner et al. 2022a). However, the use of the LSM led to smaller dispersive fluxes. The use of the PCM resulted in larger dispersive fluxes directly above the canopy top, but yielded contrasting results under different atmospheric conditions with greater distance to the canopy top.

The second objective was to further develop the surface energy imbalance model provided by De Roo et al. (2018). This was done by including the thermal heterogeneity parameter developed by Margairaz et al. (2020b), to account for the effect of thermal surface heterogeneity in heterogeneous ecosystems on the energy transport by secondary circulations, and thereby the surface energy imbalance (Wanner et al. 2022b). This study confirmed that the magnitude surface energy imbalance is related to the thermal surface heterogeneity, which is caused likely by the strengthening of secondary circulations due to thermal surface heterogeneity. It was shown that the relation between surface energy imbalance and thermal surface heterogeneity also depend on the type of secondary circulations, which can be either roll-like or cellular.

Finally, the last two objectives were realized by creating a comprehensive set of LESs based on the findings from the previous surface energy imbalance model and covering a variety of atmospheric and surface conditions to develop a model of dispersive heat fluxes (Wanner et al. 2023). A different method was chosen to determine the surface heterogeneity length scale used to calculate the thermal heterogeneity parameter, which is transferable to field conditions. Furthermore, a machine learning algorithm was used to capture the complexity introduced by the many factors affecting the magnitude of the energy transport by secondary circulations. The resulting model directly predicts dispersive heat fluxes and was tested on realistic LESs and field measurements from the CHEESEHEAD19 campaign. Despite some areas for improvement, such as the insufficient coverage of atmospheric and surface conditions encountered in field conditions, the model provides promising results. The predicted dispersive heat fluxes agree considerably well with the dispersive heat fluxes in the realistic LESs and contribute to almost entirely closing the surface energy balance gap in field measurements, when other missing terms are estimated and included.

It was furthermore shown that the model of dispersive heat fluxes can be applied to correct atmospheric heat flux measurements without deploying any additional instrumentation by

deriving the needed values for the predictor variables from ERA5 reanalysis data and satellite observations of the surface temperature. This not only facilitates the modeling of dispersive heat fluxes at almost any location in the world, but also the retrospective application of the model to consistently correct long-term measurements at EC stations, for instance for all historical FLUXNET data.

## 5 OUTLOOK

The prediction of latent dispersive heat fluxes in the DHFM may be further improved by including the effect of entrainment. Additionally, the training data set should be extended to allow for the model to be applied to a wider range of atmospheric conditions and lower measurement heights. Since no additional measurements are required, the DHFM could be tested at a larger number of EC stations in different regions and over different ecosystems. This work focused on the atmospheric sensible and latent heat fluxes, but as mentioned in the introduction, the quantification of fluxes of CO<sub>2</sub> and other greenhouse gases are just as important. It would therefore be interesting, to further apply the methods used in this work to investigate the effect of SCs on the transport of CO<sub>2</sub> and other greenhouse gases. The DHFM could be further extended facilitate the correction of atmospheric trace gas fluxes, as well.

## REFERENCES

- Abatzoglou JT, Williams AP (2016) Impact of anthropogenic climate change on wildfire across western US forests. *Proc Natl Acad Sci U S A* 113:11770–11775. <https://doi.org/10.1073/pnas.1607171113>
- Albertson JD, Parlange MB (1999) Surface length scales and shear stress: Implications for land-atmosphere interaction over complex terrain. *Water Resour. Res.* 35:2121–2132. <https://doi.org/10.1029/1999WR900094>
- Allen CD, Macalady AK, Chenchouni H, Bachelet D, McDowell N, Vennetier M, Kitzberger T, Rigling A, Breshears DD, Hogg EH, Gonzalez P, Fensham R, Zhang Z, Castro J, Demidova N, Lim J-H, Allard G, Running SW, Semerci A, Cobb N (2010) A global overview of drought and heat-induced tree mortality reveals emerging climate change risks for forests. *Forest Ecology and Management* 259:660–684. <https://doi.org/10.1016/j.foreco.2009.09.001>
- Aragão LEOC, Anderson LO, Fonseca MG, Rosan TM, Vedovato LB, Wagner FH, Silva CVJ, Silva Junior CHL, Arai E, Aguiar AP, Barlow J, Berenguer E, Deeter MN, Domingues LG, Gatti L, Gloor M, Malhi Y, Marengo JA, Miller JB, Phillips OL, Saatchi S (2018) 21st Century drought-related fires counteract the decline of Amazon deforestation carbon emissions. *Nat Commun* 9:536. <https://doi.org/10.1038/s41467-017-02771-y>
- Balaguru K, Foltz GR, Leung LR (2018) Increasing Magnitude of Hurricane Rapid Intensification in the Central and Eastern Tropical Atlantic. *Geophys. Res. Lett.* 45:4238–4247. <https://doi.org/10.1029/2018GL077597>
- Baldocchi D (2014) Measuring fluxes of trace gases and energy between ecosystems and the atmosphere - the state and future of the eddy covariance method. *Global Change Biol* 20:3600–3609. <https://doi.org/10.1111/gcb.12649>
- Baldocchi D, Falge E, Gu L, Olson R, Hollinger D, Running S, Anthoni P, Bernhofer C, Davis K, Evans R, Fuentes J, Goldstein A, Katul G, Law B, Lee X, Malhi Y, Meyers T, Munger W, Oechel W, Paw KT, Pilegaard K, Schmid HP, Valentini R, Verma S, Vesala T, Wilson K, Wofsy S (2001) FLUXNET: A New Tool to Study the Temporal and Spatial Variability of Ecosystem-Scale Carbon Dioxide, Water Vapor, and Energy Flux Densities. *Bull. Amer. Meteor. Soc.* 82(11):2415–2434. [https://doi.org/10.1175/1520-0477\(2001\)082<2415:FANTTS>2.3.CO;2](https://doi.org/10.1175/1520-0477(2001)082<2415:FANTTS>2.3.CO;2)
- Baldocchi DD (2003) Assessing the eddy covariance technique for evaluating carbon dioxide exchange rates of ecosystems: past, present and future. *Global Change Biol* 9:479–492. <https://doi.org/10.1046/j.1365-2486.2003.00629.x>
- Baldocchi DD (2020) How eddy covariance flux measurements have contributed to our understanding of Global Change Biology. *Global Change Biol* 26:242–260. <https://doi.org/10.1111/gcb.14807>
- Barber CP, Cochrane MA, Souza CM, Laurance WF (2014) Roads, deforestation, and the mitigating effect of protected areas in the Amazon. *Biological Conservation* 177:203–209. <https://doi.org/10.1016/j.biocon.2014.07.004>
- Barr AG, Morgenstern K, Black TA, McCaughey JH, Nesic Z (2006) Surface energy balance closure by the eddy-covariance method above three boreal forest stands and implications for the measurement of the CO<sub>2</sub> flux. *Agricultural and Forest Meteorology* 140:322–337. <https://doi.org/10.1016/j.agrformet.2006.08.007>
- Barr JG, Engel V, Smith TJ, Fuentes JD (2012) Hurricane disturbance and recovery of energy balance, CO<sub>2</sub> fluxes and canopy structure in a mangrove forest of the Florida Everglades. *Agricultural and Forest Meteorology* 153:54–66. <https://doi.org/10.1016/j.agrformet.2011.07.022>
- Basu S, Lacser A (2017) A Cautionary Note on the Use of Monin–Obukhov Similarity Theory in Very High-Resolution Large-Eddy Simulations. *Boundary-Layer Meteorol* 163(2):351–355. <https://doi.org/10.1007/s10546-016-0225-y>
- Berg EE, David Henry J, Fastie CL, Volder AD de, Matsuoka SM (2006) Spruce beetle outbreaks on the Kenai Peninsula, Alaska, and Kluane National Park and Reserve, Yukon Territory: Relationship to summer temperatures and regional differences in disturbance regimes. *Forest Ecology and Management* 227:219–232. <https://doi.org/10.1016/j.foreco.2006.02.038>
- Beringer J, Hutley LB, Tapper NJ, Cernusak LA (2007) Savanna fires and their impact on net ecosystem productivity in North Australia. *Global Change Biol* 13:990–1004. <https://doi.org/10.1111/j.1365-2486.2007.01334.x>
- Bernacchi CJ, Hollinger SE, Meyers T (2005) The conversion of the corn/soybean ecosystem to no-till agriculture may result in a carbon sink. *Global Change Biol* 0:051013014052001-??? <https://doi.org/10.1111/j.1365-2486.2005.01050.x>
- Bernacchi CJ, Hollinger SE, Meyers TP (2006) The conversion of the corn/soybean ecosystem to no-till agriculture may result in a carbon sink. *Global Change Biol* 12:1585–1586. <https://doi.org/10.1111/j.1365-2486.2006.01195.x>
- Bernhofer C (1992) Applying a simple three-dimensional eddy correlation system for latent and sensible heat flux to contrasting forest canopies. *Theor Appl Climatol* 46:163–172. <https://doi.org/10.1007/BF00866096>
- Beyrich F, Bruin HAR de, Etling D, Foken T (2006) Preface: The LITFASS-2003 experiment. *Boundary-Layer Meteorol* 121:1–4. <https://doi.org/10.1007/s10546-006-9082-4>
- Bhatia K, Vecchi G, Murakami H, Underwood S, Kossin J (2018) Projected Response of Tropical Cyclone Intensity and Intensification in a Global Climate Model. *J. Climate* 31:8281–8303. <https://doi.org/10.1175/JCLI-D-17-0898.1>
- Blanken PD, Black TA, Yang PC, Neumann HH, Nesic Z, Staebler R, Hartog G den, Novak MD, Lee X (1997) Energy balance and canopy conductance of a boreal aspen forest: Partitioning overstory and understory components. *J. Geophys. Res. Atmos.* 102:28915–28927. <https://doi.org/10.1029/97JD00193>
- Blaylock BK, Horel JD, Liston ST (2017) Cloud archiving and data mining of High-Resolution Rapid Refresh forecast model output. *Computers & Geosciences* 109:43–50. <https://doi.org/10.1016/j.cageo.2017.08.005>
- Bloomfield JP, Marchant BP, McKenzie AA (2019) Changes in groundwater drought associated with anthropogenic warming. *Hydrol. Earth Syst. Sci.* 23:1393–1408. <https://doi.org/10.5194/hess-23-1393-2019>

- Bonan GB, Oleson KW, Fisher RA, Lasslop G, Reichstein M (2012) Reconciling leaf physiological traits and canopy flux data: Use of the TRY and FLUXNET databases in the Community Land Model version 4. *JGR Biogeosciences* 117:n/a-n/a. <https://doi.org/10.1029/2011JG001913>
- Bou-Zeid E, Meneveau C, Parlange M (2005) A scale-dependent Lagrangian dynamic model for large eddy simulation of complex turbulent flows. *J. Fluid Mech.* 17(2):25105. <https://doi.org/10.1063/1.1839152>
- Bou-Zeid E, Anderson W, Katul GG, Mahrt L (2020) The Persistent Challenge of Surface Heterogeneity in Boundary-Layer Meteorology: A Review. *Boundary-Layer Meteorol* 177(2-3):227–245. <https://doi.org/10.1007/s10546-020-00551-8>
- Bou-Zeid E, Meneveau C, Parlange MB (2004) Large-eddy simulation of neutral atmospheric boundary layer flow over heterogeneous surfaces: Blending height and effective surface roughness. *Water Resour. Res.* 40. <https://doi.org/10.1029/2003WR002475>
- Brás TA, Seixas J, Carvalhais N, Jägermeyr J (2021) Severity of drought and heatwave crop losses tripled over the last five decades in Europe. *Environ. Res. Lett.* 16:65012. <https://doi.org/10.1088/1748-9326/abf004>
- Breiman L (2001) Random Forests. *Machine Learning* 45:5–32. <https://doi.org/10.1023/A:1010933404324>
- Breshears DD, Cobb NS, Rich PM, Price KP, Allen CD, Balice RG, Romme WH, Kastens JH, Floyd ML, Belnap J, Anderson JJ, Myers OB, Meyer CW (2005) Regional vegetation die-off in response to global-change-type drought. *Proc Natl Acad Sci U S A* 102:15144–15148. <https://doi.org/10.1073/pnas.0505734102>
- Brutsaert W (1998) Land-surface water vapor and sensible heat flux: Spatial variability, homogeneity, and measurement scales. *Water Resour. Res.* 34:2433–2442. <https://doi.org/10.1029/98WR01340>
- Butterworth BJ, Desai AR, Durden D, Kadum H, LaLuzerne D, Mauder M, Metzger S, Paleri S, Wanner L (in review) Characterizing Energy Balance Closure over a Heterogeneous Ecosystem Using Multi-Tower Eddy Covariance. Submitted to *Frontiers in Earth Science*, section Atmospheric Science
- Butterworth BJ, Desai AR, Metzger S, Townsend PA, Schwartz MD, Petty GW, Mauder M, Vogelmann H, Andresen CG, Augustine TJ, Bertram TH, Brown WO, Buban M, Clearly P, Durden DJ, Florian CR, Iglinski TJ, Kruger EL, Lantz K, Lee TR, Meyers TP, Mineau JK, Olson ER, Oncley SP, Paleri S, Pertzborn RA, Pettersen C, Plummer DM, Riihimaki L, Guzman ER, Sedlar J, Smith EN, Speidel J, Stoy PC, Sührling M, Thom JE, Turner DD, Vermeuel MP, Wagner TJ, Wang Z, Wanner L, White LD, Wilczak JM, Wright DB, Zheng T (2021) Connecting Land-Atmosphere Interactions to Surface Heterogeneity in CHEESEHEAD19. *Bull. Amer. Meteor. Soc.* 102(2):E421-E445. <https://doi.org/10.1175/BAMS-D-19-0346.1>
- Calaf M, Meneveau C, Parlange M (2011) Large Eddy Simulation study of a fully developed thermal wind-turbine array boundary layer. In: Kuerten H, Geurts B, Armenio V, Fröhlich J (eds) *Direct and Large-Eddy Simulation VIII*, vol 15. Springer Netherlands, Dordrecht, pp 239–244
- Cava D, Contini D, Donato A, Martano P (2008) Analysis of short-term closure of the surface energy balance above short vegetation. *Agricultural and Forest Meteorology* 148:82–93. <https://doi.org/10.1016/j.agrformet.2007.09.003>
- Ceccherini G, Russo S, Amezttoy I, Marchese AF, Carmona-Moreno C (2017) Heat waves in Africa 1981–2015, observations and reanalysis. *Nat. Hazards Earth Syst. Sci.* 17:115–125. <https://doi.org/10.5194/nhess-17-115-2017>
- Ceschia E, Béziat P, Dejoux JF, Aubinet M, Bernhofer C, Bodson B, Buchmann N, Carrara A, Cellier P, Di Tommasi P, Elbers JA, Eugster W, Grünwald T, Jacobs C, Jans W, Jones M, Kutsch W, Lanigan G, Magliulo E, Marloie O, Moors EJ, Moureaux C, Olioso A, Osborne B, Sanz MJ, Saunders M, Smith P, Soegaard H, Wattenbach M (2010) Management effects on net ecosystem carbon and GHG budgets at European crop sites. *Agriculture, Ecosystems & Environment* 139:363–383. <https://doi.org/10.1016/j.agee.2010.09.020>
- Charuchittipan D, Babel W, Mauder M, Leps J-P, Foken T (2014) Extension of the Averaging Time in Eddy-Covariance Measurements and Its Effect on the Energy Balance Closure. *Boundary-Layer Meteorol* 152(3):303–327. <https://doi.org/10.1007/s10546-014-9922-6>
- Cho C, Li R, Wang S-Y, Yoon J-H, Gillies RR (2016) Anthropogenic footprint of climate change in the June 2013 northern India flood. *Clim Dyn* 46:797–805. <https://doi.org/10.1007/s00382-015-2613-2>
- Ciais P, Reichstein M, Viovy N, Granier A, Ogee J, Allard V, Aubinet M, Buchmann N, Bernhofer C, Carrara A, Chevallier F, Noblet N de, Friend AD, Friedlingstein P, Grünwald T, Heinesch B, Keronen P, Knohl A, Krinner G, Loustau D, Manca G, Matteucci G, Miglietta F, Ourcival JM, Papale P, Papale D, Pilegaard K, Rambal S, Seufert G, Soussana JF, Sanz MJ, Schulze ED, Vesala T, Valentini R (2005) Europe-wide reduction in primary productivity caused by the heat and drought in 2003. *Nature* 437:529–533. <https://doi.org/10.1038/nature03972>
- Ciais P, Tan J, Wang X, Roedenbeck C, Chevallier F, Piao S-L, Moriarty R, Broquet G, Le Quéré C, Canadell JG, Peng S, Poulter B, Liu Z, Tans P (2019) Five decades of northern land carbon uptake revealed by the interhemispheric CO<sub>2</sub> gradient. *Nature* 568:221–225. <https://doi.org/10.1038/s41586-019-1078-6>
- Clark KL, Skowronski N, Gallagher M, Renninger H, Schäfer K (2012) Effects of invasive insects and fire on forest energy exchange and evapotranspiration in the New Jersey pinelands. *Agricultural and Forest Meteorology* 166-167:50–61. <https://doi.org/10.1016/j.agrformet.2012.07.007>
- Condon LE, Atchley AL, Maxwell RM (2020) Evapotranspiration depletes groundwater under warming over the contiguous United States. *Nat Commun* 11:873. <https://doi.org/10.1038/s41467-020-14688-0>
- Cremonese E, Filippa G, Galvagno M, Siniscalco C, Oddi L, Di Morra Cella U, Migliavacca M (2017) Heat wave hinders green wave: The impact of climate extreme on the phenology of a mountain grassland. *Agricultural and Forest Meteorology* 247:320–330. <https://doi.org/10.1016/j.agrformet.2017.08.016>

- Cuxart J, Conangla L, Jiménez MA (2015) Evaluation of the surface energy budget equation with experimental data and the ECMWF model in the Ebro Valley. *J. Geophys. Res. Atmos.* 120(3):1008–1022. <https://doi.org/10.1002/2014JD022296>
- De Roo F, Mauder M (2018) The influence of idealized surface heterogeneity on virtual turbulent flux measurements. *Atmos. Chem. Phys.* 18(7):5059–5074. <https://doi.org/10.5194/acp-18-5059-2018>
- De Roo F, Zhang S, Huq S, Mauder M (2018) A semi-empirical model of the energy balance closure in the surface layer. *PLoS ONE* 13(12):e0209022. <https://doi.org/10.1371/journal.pone.0209022>
- Deardorff JW (1972) Numerical Investigation of Neutral and Unstable Planetary Boundary Layers. *J. Atmos. Sci.* 29:91–115. [https://doi.org/10.1175/1520-0469\(1972\)029<0091:NIONAU>2.0.CO;2](https://doi.org/10.1175/1520-0469(1972)029<0091:NIONAU>2.0.CO;2)
- Desai AR, Khan AM, Zheng T, Paleri S, Butterworth B, Lee TR, Fisher JB, Hulley G, Kleynhans T, Gerace A, Townsend PA, Stoy P, Metzger S (2021) Multi-Sensor Approach for High Space and Time Resolution Land Surface Temperature. *Earth and Space Science* 8. <https://doi.org/10.1029/2021EA001842>
- Desai AR, Murphy BA, Wiesner S, Thom J, Butterworth BJ, Koupaei-Abyazani N, Muttaqin A, Paleri S, Talib A, Turner J, Mineau J, Merrelli A, Stoy P, Davis K (2022) Drivers of Decadal Carbon Fluxes Across Temperate Ecosystems. *JGR Biogeosciences* 127:e2022JG007014. <https://doi.org/10.1029/2022JG007014>
- Desjardins RL, Macpherson JJ, Schuepp PH, Karanja F (1989) An evaluation of aircraft flux measurements of CO<sub>2</sub>, water vapor and sensible heat. *Boundary-Layer Meteorol* 47:55–69. <https://doi.org/10.1007/BF00122322>
- dos Santos Michiles AA, Gielow R (2008) Above-ground thermal energy storage rates, trunk heat fluxes and surface energy balance in a central Amazonian rainforest. *Agricultural and Forest Meteorology* 148:917–930. <https://doi.org/10.1016/j.agrformet.2008.01.001>
- Du H, Alexander LV, Donat MG, Lippmann T, Srivastava A, Salinger J, Kruger A, Choi G, He HS, Fujibe F, Rusticucci M, Nandintsetseg B, Manzanar R, Rehman S, Abbas F, Zhai P, Yabi I, Stambaugh MC, Wang S, Batbold A, Oliveira PT de, Adrees M, Hou W, Zong S, Santos e Silva CM, Lucio PS, Wu Z (2019) Precipitation From Persistent Extremes is Increasing in Most Regions and Globally. *Geophys. Res. Lett.* 46:6041–6049. <https://doi.org/10.1029/2019GL081898>
- Eder F, De Roo F, Kohnert K, Desjardins RL, Schmid HP, Mauder M (2014) Evaluation of Two Energy Balance Closure Parametrizations. *Boundary-Layer Meteorol* 151(2):195–219. <https://doi.org/10.1007/s10546-013-9904-0>
- Eder F, De Roo F, Rotenberg E, Yakir D, Schmid HP, Mauder M (2015) Secondary circulations at a solitary forest surrounded by semi-arid shrubland and their impact on eddy-covariance measurements. *Agricultural and Forest Meteorology* 211–212:115–127. <https://doi.org/10.1016/j.agrformet.2015.06.001>
- Ekholm T (2020) Optimal forest rotation under carbon pricing and forest damage risk. *Forest Policy and Economics* 115:102131. <https://doi.org/10.1016/j.forpol.2020.102131>
- Engelmann C, Bernhofer C (2016) Exploring Eddy-Covariance Measurements Using a Spatial Approach: The Eddy Matrix. *Boundary-Layer Meteorol* 161:1–17. <https://doi.org/10.1007/s10546-016-0161-x>
- Etling D, Brown RA (1993) Roll vortices in the planetary boundary layer: A review. *Boundary-Layer Meteorol* 65:215–248. <https://doi.org/10.1007/BF00705527>
- Feigenwinter C, Bernhofer C, Eichelmann U, Heinesch B, Hertel M, Janous D, Kolle O, Lagergren F, Lindroth A, Minerbi S, Moderow U, Mölder M, Montagnani L, Queck R, Rebmann C, Vestin P, Yernaux M, Zeri M, Ziegler W, Aubinet M (2008) Comparison of horizontal and vertical advective CO<sub>2</sub> fluxes at three forest sites. *Agricultural and Forest Meteorology* 148:12–24. <https://doi.org/10.1016/j.agrformet.2007.08.013>
- Finnigan JJ, Clement R, Malhi Y, Leuning R, Cleugh HA (2003) A Re-Evaluation of Long-Term Flux Measurement Techniques Part I: Averaging and Coordinate Rotation. *Boundary-Layer Meteorol* 107(1):1–48. <https://doi.org/10.1023/A:1021554900225>
- Foken T, Wimmer F, Mauder M, Thomas C, Liebethal C (2006) Some aspects of the energy balance closure problem. *Atmos. Chem. Phys.* 6(12):4395–4402. <https://doi.org/10.5194/acp-6-4395-2006>
- Foken T (2008) The Energy Balance Closure Problem: An Overview. *Ecological Applications* 18(6):1351–1367. <https://doi.org/10.1890/06-0922.1>
- Foken T (2017) *Micrometeorology*. Springer Berlin Heidelberg, Berlin, Heidelberg
- Foken T, Mauder M, Liebethal C, Wimmer F, Beyrich F, Leps J-P, Raasch S, DeBruin HAR, Meijninger WML, Bange J (2010) Energy balance closure for the LITFASS-2003 experiment. *Theor Appl Climatol* 101(1-2):149–160. <https://doi.org/10.1007/s00704-009-0216-8>
- Foken T, Aubinet M, Leuning R (2012) The Eddy Covariance Method. In: Aubinet M, Vesala T, Papale D (eds) *Eddy covariance: A practical guide to measurement and data analysis*. Springer, Dordrecht, Heidelberg, London, New York, pp 1–19
- Frank JM, Massman WJ, Ewers BE (2013) Underestimates of sensible heat flux due to vertical velocity measurement errors in non-orthogonal sonic anemometers. *Agricultural and Forest Meteorology* 171–172:72–81. <https://doi.org/10.1016/j.agrformet.2012.11.005>
- Fratini G, Ibrom A, Arriga N, Burba G, Papale D (2012) Relative humidity effects on water vapour fluxes measured with closed-path eddy-covariance systems with short sampling lines. *Agricultural and Forest Meteorology* 165:53–63. <https://doi.org/10.1016/j.agrformet.2012.05.018>
- Fratini G, Mauder M (2014) Towards a consistent eddy-covariance processing: an intercomparison of EddyPro and TK3. *Atmos. Meas. Tech.* 7:2273–2281. <https://doi.org/10.5194/amt-7-2273-2014>
- Friedlingstein P, O'Sullivan M, Jones MW, Andrew RM, Hauck J, Olsen A, Peters GP, Peters W, Pongratz J, Sitch S, Le Quéré C, Canadell JG, Ciais P, Jackson RB, Alin S, Aragão LEOC, Arneeth A, Arora V, Bates NR, Becker M,

- Benoit-Cattin A, Bittig HC, Bopp L, Bultan S, Chandra N, Chevallier F, Chini LP, Evans W, Florentie L, Forster PM, Gasser T, Gehlen M, Gilfillan D, Gkritzalis T, Gregor L, Gruber N, Harris I, Hartung K, Haverd V, Houghton RA, Ilyina T, Jain AK, Joetzjer E, Kadono K, Kato E, Kitidis V, Korsbakken JI, Landschützer P, Lefèvre N, Lenton A, Lienert S, Liu Z, Lombardozi D, Marland G, Metzl N, Munro DR, Nabel JEMS, Nakaoka S-I, Niwa Y, O'Brien K, Ono T, Palmer PI, Pierrot D, Poulter B, Resplandy L, Robertson E, Rödenbeck C, Schwinger J, Séférian R, Skjelvan I, Smith AJP, Sutton AJ, Tanhua T, Tans PP, Tian H, Tilbrook B, van der Werf G, Vuichard N, Walker AP, Wanninkhof R, Watson AJ, Willis D, Wiltshire AJ, Yuan W, Yue X, Zaehle S (2020) Global Carbon Budget 2020. *Earth Syst. Sci. Data* 12:3269–3340. <https://doi.org/10.5194/essd-12-3269-2020>
- Fröhlich J (2006) *Large Eddy Simulation turbulenter Strömungen*, 1st edn. Teubner, s.l.
- Fu Z, Ciais P, Bastos A, Stoy PC, Yang H, Green JK, Wang B, Yu K, Huang Y, Knohl A, Šigut L, Gharun M, Cuntz M, Arriga N, Roland M, Peichl M, Migliavacca M, Cremonese E, Varlagin A, Brümmer C, La Gourlez de Motte L, Fares S, Buchmann N, El-Madany TS, Pitacco A, Vendrame N, Li Z, Vincke C, Magliulo E, Koebisch F (2020) Sensitivity of gross primary productivity to climatic drivers during the summer drought of 2018 in Europe. *Philos Trans R Soc Lond B Biol Sci* 375:20190747. <https://doi.org/10.1098/rstb.2019.0747>
- Gao Z, Liu H, Katul GG, Foken T (2017) Non-closure of the surface energy balance explained by phase difference between vertical velocity and scalars of large atmospheric eddies. *Environ. Res. Lett.* 12(3):34025. <https://doi.org/10.1088/1748-9326/aa625b>
- Gehrke KF, Sühling M, Maronga B (2020) Modeling of land-surface interactions in the PALM model system 6.0: Land surface model description, first evaluation, and sensitivity to model parameters. *Geosci Model Dev Discuss* [preprint]. <https://doi.org/10.5194/gmd-2020-197>
- Göckede M, Foken T, Aubinet M, Aurela M, Banza J, Bernhofer C, Bonnefond JM, Brunet Y, Carrara A, Clement R, Dellwik E, Elbers J, Eugster W, Fuhrer J, Granier A, Grünwald T, Heinesch B, Janssens IA, Knohl A, Koeble R, Laurila T, Longdoz B, Manca G, Marek M, Markkanen T, Mateus J, Matteucci G, Mauder M, Migliavacca M, Minerbi S, Moncrieff J, Montagnani L, Moors E, Ourcival J-M, Papale D, Pereira J, Pilegaard K, Pita G, Rambal S, Rebmann C, Rodrigues A, Rotenberg E, Sanz MJ, Sedlak P, Seufert G, Siebicke L, Soussana JF, Valentini R, Vesala T, Verbeeck H, Yakir D (2008) Quality control of CarboEurope flux data – Part 1: Coupling footprint analyses with flux data quality assessment to evaluate sites in forest ecosystems. *Biogeosciences* 5:433–450. <https://doi.org/10.5194/bg-5-433-2008>
- Goulden ML, Munger JW, Fan S-M, Daube BC, Wofsy SC (1996) Measurements of carbon sequestration by long-term eddy covariance: methods and a critical evaluation of accuracy. *Global Change Biol* 2(3):169–182. <https://doi.org/10.1111/j.1365-2486.1996.tb00070.x>
- Graham SL, Kochendorfer J, McMillan AM, Duncan MJ, Srinivasan MS, Hertzog G (2016) Effects of agricultural management on measurements, prediction, and partitioning of evapotranspiration in irrigated grasslands. *Agricultural Water Management* 177:340–347. <https://doi.org/10.1016/j.agwat.2016.08.015>
- Gu L, Hanson PJ, Post WM, Kaiser DP, Yang B, Nemani R, Pallardy SG, Meyers T (2008) The 2007 Eastern US Spring Freeze: Increased Cold Damage in a Warming World? *BioScience* 58:253–262. <https://doi.org/10.1641/B580311>
- Haslwanter A, Hammerle A, Wohlfahrt G (2009) Open- vs. closed-path eddy covariance measurements of the net ecosystem carbon dioxide and water vapour exchange: a long-term perspective. *Agricultural and Forest Meteorology* 149:291–302. <https://doi.org/10.1016/j.agrformet.2008.08.011>
- Haverd V, Cuntz M, Leuning R, Keith H (2007) Air and biomass heat storage fluxes in a forest canopy: Calculation within a soil vegetation atmosphere transfer model. *Agricultural and Forest Meteorology* 147:125–139. <https://doi.org/10.1016/j.agrformet.2007.07.006>
- Heiskanen J, Brümmer C, Buchmann N, Calfapietra C, Chen H, Gielen B, Gkritzalis T, Hammer S, Hartman S, Herbst M, Janssens IA, Jordan A, Juurola E, Karstens U, Kasurinen V, Kruijt B, Lankreijer H, Levin I, Linderson M-L, Loustau D, Merbold L, Myhre CL, Papale D, Pavelka M, Pilegaard K, Ramonet M, Rebmann C, Rinne J, Rivier L, Saltikoff E, Sanders R, Steinbacher M, Steinhoff T, Watson A, Vermeulen AT, Vesala T, Vítková G, Kutsch W (2022) The Integrated Carbon Observation System in Europe. *Bull. Amer. Meteor. Soc.* 103:E855–E872. <https://doi.org/10.1175/BAMS-D-19-0364.1>
- Hellsten A, Ketelsen K, Sühling M, Auvinen M, Maronga B, Knigge C, Barmpas F, Tsegas G, Moussiopoulos N, Raasch S (2021) A nested multi-scale system implemented in the large-eddy simulation model PALM model system 6.0. *Geosci. Model Dev.* 14:3185–3214. <https://doi.org/10.5194/gmd-14-3185-2021>
- Hendricks-Franssen HJ, Stöckli R, Lehner I, Rotenberg E, Seneviratne SI (2010) Energy balance closure of eddy-covariance data: A multisite analysis for European FLUXNET stations. *Agricultural and Forest Meteorology* 150(12):1553–1567. <https://doi.org/10.1016/j.agrformet.2010.08.005>
- Hersbach H, Bell B, Berrisford P, Biavati G, Horányi A, Muñoz Sabater J, Nicolas J, Peubey C, Radu R, Rozum I, Schepers D, Simmons A, Soci C, Dee D, Thépaut J-N (2023a) ERA5 hourly data on pressure levels from 1940 to present. Copernicus Climate Change Service (C3S) Climate Data Store (CDS). <https://doi.org/10.24381/cds.adbb2d47>. Accessed 13 July 2023
- Hersbach H, Bell B, Berrisford P, Biavati G, Horányi A, Muñoz Sabater J, Nicolas J, Peubey C, Radu R, Rozum I, Schepers D, Simmons A, Soci C, Dee D, Thépaut J-N (2023b) ERA5 hourly data on single levels from 1940 to present. Copernicus Climate Change Service (C3S) Climate Data Store (CDS). <https://doi.org/10.24381/cds.adbb2d47>. Accessed 14 July 2023

- Hettiarachchi S, Wasko C, Sharma A (2018) Increase in flood risk resulting from climate change in a developed urban watershed – the role of storm temporal patterns. *Hydrol. Earth Syst. Sci.* 22:2041–2056. <https://doi.org/10.5194/hess-22-2041-2018>
- Hochman Z, Gobbett DL, Horan H (2017) Climate trends account for stalled wheat yields in Australia since 1990. *Global Change Biol* 23:2071–2081. <https://doi.org/10.1111/gcb.13604>
- Horst TW, Semmer SR, Maclean G (2015) Correction of a Non-orthogonal, Three-Component Sonic Anemometer for Flow Distortion by Transducer Shadowing. *Boundary-Layer Meteorol* 155:371–395. <https://doi.org/10.1007/s10546-015-0010-3>
- Huang J, Lee X, Patton EG (2008) A Modelling Study of Flux Imbalance and the Influence of Entrainment in the Convective Boundary Layer. *Boundary-Layer Meteorol* 127(2):273–292. <https://doi.org/10.1007/s10546-007-9254-x>
- Hurteau MD, North MP, Koch GW, Hungate BA (2019) Opinion: Managing for disturbance stabilizes forest carbon. *Proc Natl Acad Sci U S A* 116:10193–10195. <https://doi.org/10.1073/pnas.1905146116>
- Ibrom A, Dellwik E, Flyvbjerg H, Jensen NO, Pilegaard K (2007) Strong low-pass filtering effects on water vapour flux measurements with closed-path eddy correlation systems. *Agricultural and Forest Meteorology* 147:140–156. <https://doi.org/10.1016/j.agrformet.2007.07.007>
- Inagaki A, Letzel MO, Raasch S, Kanda M (2006) Impact of Surface Heterogeneity on Energy Imbalance: A Study Using LES. *JMSJ* 84(1):187–198. <https://doi.org/10.2151/jmsj.84.187>
- Jaeger EB, Stöckli R, Seneviratne SI (2009) Analysis of planetary boundary layer fluxes and land-atmosphere coupling in the regional climate model CLM. *J. Geophys. Res. Atmos.* 114. <https://doi.org/10.1029/2008JD011658>
- Jia G, Shevliakova E, Artaxo P, Noblet-Ducoudré N de, Houghton R, House J, Kitajima K, Lennard C, Popp A, Sirin A, Sukumar R, Vercho L (2022) Land–climate interactions. In: IPCC (ed) *Climate Change and Land: an IPCC special report on climate change, desertification, land degradation, sustainable land management, food security, and greenhouse gas fluxes in terrestrial ecosystems* [P.R. Shukla, J. Skea, E. Calvo Buendia, V. Masson-Delmotte, H.-O. Pörtner, D.C. Roberts, P. Zhai, R. Slade, S. Connors, R. van Diemen, M. Ferrat, E. Haughey, S. Luz, S. Neogi, M. Pathak, J. Petzold, J. Portugal, Pereira, P. Vyas, E. Huntley, K. Kissick, M. Belkacemi, J. Malley, (eds)]. Cambridge University Press, pp 131–248
- Kaimal JC, Finnigan JJ (1994) *Atmospheric Boundary Layer Flows*. Oxford University Press
- Kanani-Sühring F, Raasch S (2015) Spatial Variability of Scalar Concentrations and Fluxes Downstream of a Clearing-to-Forest Transition: A Large-Eddy Simulation Study. *Boundary-Layer Meteorol* 155(1):1–27. <https://doi.org/10.1007/s10546-014-9986-3>
- Kanani-Sühring F, Raasch S (2017) Enhanced Scalar Concentrations and Fluxes in the Lee of Forest Patches: A Large-Eddy Simulation Study. *Boundary-Layer Meteorol* 164(1):1–17. <https://doi.org/10.1007/s10546-017-0239-0>
- Kanda M, Inagaki A, Letzel MO, Raasch S, Watanabe T (2004) LES Study of the Energy Imbalance Problem with Eddy Covariance Fluxes. *Boundary-Layer Meteorol* 110(3):381–404. <https://doi.org/10.1023/B:BOUN.0000007225.45548.7a>
- Kang S-L, Lenschow DH (2014) Temporal Evolution of Low-Level Winds Induced by Two-dimensional Mesoscale Surface Heat-Flux Heterogeneity. *Boundary-Layer Meteorol* 151:501–529. <https://doi.org/10.1007/s10546-014-9912-8>
- Katul GG (2019) The anatomy of large-scale motion in atmospheric boundary layers. *J. Fluid Mech.* 858:1–4. <https://doi.org/10.1017/jfm.2018.731>
- Keenan TF, Gray J, Friedl MA, Toomey M, Bohrer G, Hollinger DY, Munger JW, O’Keefe J, Schmid HP, Wing IS, Yang B, Richardson AD (2014) Net carbon uptake has increased through warming-induced changes in temperate forest phenology. *Nature Clim Change* 4:598–604. <https://doi.org/10.1038/nclimate2253>
- Kenny WT, Bohrer G, Morin TH, Vogel CS, Matheny AM, Desai AR (2017) A Numerical Case Study of the Implications of Secondary Circulations to the Interpretation of Eddy-Covariance Measurements Over Small Lakes. *Boundary-Layer Meteorol* 165(2):311–332. <https://doi.org/10.1007/s10546-017-0268-8>
- Khanna S, Brasseur JG (1998) Three-Dimensional Buoyancy- and Shear-Induced Local Structure of the Atmospheric Boundary Layer. *J. Atmos. Sci.* 55:710–743. [https://doi.org/10.1175/1520-0469\(1998\)055<0710:TDBASI>2.0.CO;2](https://doi.org/10.1175/1520-0469(1998)055<0710:TDBASI>2.0.CO;2)
- Kim W, Iizumi T, Nishimori M (2019) Global Patterns of Crop Production Losses Associated with Droughts from 1983 to 2009. *J. Appl. Meteor. Climatol.* 58:1233–1244. <https://doi.org/10.1175/JAMC-D-18-0174.1>
- Knohl A, Kolle O, Minayeva TY, Milyukova IM, Vygodskaya NN, Foken T, Schulze E-D (2002) Carbon dioxide exchange of a Russian boreal forest after disturbance by wind throw. *Global Change Biol* 8:231–246. <https://doi.org/10.1046/j.1365-2486.2002.00475.x>
- Kochendorfer J, Meyers TP, Frank J, Massman WJ, Heuer MW (2012) How Well Can We Measure the Vertical Wind Speed? Implications for Fluxes of Energy and Mass. *Boundary-Layer Meteorol* 145(2):383–398. <https://doi.org/10.1007/s10546-012-9738-1>
- Kohsiek W, Liebenthal C, Foken T, Vogt R, Oncley SP, Bernhofer C, Debruin HAR (2007) The Energy Balance Experiment EBEX-2000. Part III: Behaviour and quality of the radiation measurements. *Boundary-Layer Meteorol* 123(1):55–75. <https://doi.org/10.1007/s10546-006-9135-8>
- Kossin JP, Knapp KR, Olander TL, Velden CS (2020) Global increase in major tropical cyclone exceedance probability over the past four decades. *Proc Natl Acad Sci U S A* 117:11975–11980. <https://doi.org/10.1073/pnas.1920849117>
- Kracher D, Mengelkamp H-T, Foken T (2009) The residual of the energy balance closure and its influence on the results of three SVAT models. *metz* 18:647–661. <https://doi.org/10.1127/0941-2948/2009/0412>

- Krč P, Resler J, Sührling M, Schubert S, Salim MH, Fuka V (2021) Radiative Transfer Model 3.0 integrated into the PALM model system 6.0. *Geosci. Model Dev.* 14:3095–3120. <https://doi.org/10.5194/gmd-14-3095-2021>
- Krofcheck DJ, Remy CC, Keyser AR, Hurteau MD (2019) Optimizing Forest Management Stabilizes Carbon Under Projected Climate and Wildfires. *JGR Biogeosciences* 124:3075–3087. <https://doi.org/10.1029/2019JG005206>
- Kurz WA, Dymond CC, Stinson G, Rampley GJ, Neilson ET, Carroll AL, Ebata T, Safranyik L (2008) Mountain pine beetle and forest carbon feedback to climate change. *Nature* 452:987–990. <https://doi.org/10.1038/nature06777>
- Laubach J, Raschendorfer M, Kreilein H, Gravenhorst G (1994) Determination of heat and water vapour fluxes above a spruce forest by eddy correlation. *Agricultural and Forest Meteorology* 71(3-4):373–401. [https://doi.org/10.1016/0168-1923\(94\)90021-3](https://doi.org/10.1016/0168-1923(94)90021-3)
- Lee X (2018) *Fundamentals of Boundary-Layer Meteorology*. Springer International Publishing, Cham
- Lesk C, Rowhani P, Ramankutty N (2016) Influence of extreme weather disasters on global crop production. *Nature* 529:84–87. <https://doi.org/10.1038/nature16467>
- Letzel MO, Raasch S (2003) Large Eddy Simulation of Thermally Induced Oscillations in the Convective Boundary Layer. *J. Atmos. Sci.* 60(18):2328–2341. [https://doi.org/10.1175/1520-0469\(2003\)060<2328:LESOTI>2.0.CO;2](https://doi.org/10.1175/1520-0469(2003)060<2328:LESOTI>2.0.CO;2)
- Leuning R, van Gorsel E, Massman WJ, Isaac PR (2012) Reflections on the surface energy imbalance problem. *Agricultural and Forest Meteorology* 156:65–74. <https://doi.org/10.1016/j.agrformet.2011.12.002>
- Lhotka O, Kyselý J, Farda A (2018) Climate change scenarios of heat waves in Central Europe and their uncertainties. *Theor Appl Climatol* 131:1043–1054. <https://doi.org/10.1007/s00704-016-2031-3>
- Li J, Miao C, Wei W, Zhang G, Hua L, Chen Y, Wang X (2021) Evaluation of CMIP6 Global Climate Models for Simulating Land Surface Energy and Water Fluxes During 1979–2014. *J. Adv. Model. Earth Syst.* 13. <https://doi.org/10.1029/2021MS002515>
- LI-COR Biosciences (2021) Eddy Covariance Processing Software (Version 7.0.8) [Software]. [www.licor.com/EddyPro](http://www.licor.com/EddyPro)
- Liebenthal C, Huwe B, Foken T (2005) Sensitivity analysis for two ground heat flux calculation approaches. *Agricultural and Forest Meteorology* 132(3-4):253–262. <https://doi.org/10.1016/j.agrformet.2005.08.001>
- Lindroth A, Mölder M, Lagergren F (2010) Heat storage in forest biomass improves energy balance closure. *Biogeosciences* 7(1):301–313. <https://doi.org/10.5194/bg-7-301-2010>
- Lipsett-Moore GJ, Wolff NH, Game ET (2018) Emissions mitigation opportunities for savanna countries from early dry season fire management. *Nat Commun* 9:2247. <https://doi.org/10.1038/s41467-018-04687-7>
- Lorenzo-Lacruz J, Garcia C, Morán-Tejeda E (2017) Groundwater level responses to precipitation variability in Mediterranean insular aquifers. *Journal of Hydrology* 552:516–531. <https://doi.org/10.1016/j.jhydrol.2017.07.011>
- Lundberg SM, Erion G, Chen H, DeGrave A, Prutkin JM, Nair B, Katz R, Himmelfarb J, Bansal N, Lee S-I (2020) From Local Explanations to Global Understanding with Explainable AI for Trees. *Nat Mach Intell* 2:56–67. <https://doi.org/10.1038/s42256-019-0138-9>
- Mahrt L (1998) Flux Sampling Errors for Aircraft and Towers. *J. Atmos. Oceanic Technol.* 15(2):416–429. [https://doi.org/10.1175/1520-0426\(1998\)015<0416:FSEFAA>2.0.CO;2](https://doi.org/10.1175/1520-0426(1998)015<0416:FSEFAA>2.0.CO;2)
- Mahrt L (2000) Surface Heterogeneity and Vertical Structure of the Boundary Layer. *Boundary-Layer Meteorol* 96(1-2):33–62. <https://doi.org/10.1023/A:1002482332477>
- Majumdar SJ, Sun J, Golding B, Joe P, Dudhia J, Caumont O, Chandra Gouda K, Steinle P, Vincendon B, Wang J, Yussouf N (2021) Multiscale Forecasting of High-Impact Weather: Current Status and Future Challenges. *Bull. Amer. Meteor. Soc.* 102:E635–E659. <https://doi.org/10.1175/BAMS-D-20-0111.1>
- Margairaz F, Giometto MG, Parlange MB, Calaf M (2018) Comparison of dealiasing schemes in large-eddy simulation of neutrally stratified atmospheric flows. *Geosci. Model Dev.* 11:4069–4084. <https://doi.org/10.5194/gmd-11-4069-2018>
- Margairaz F, Pardyjak ER, Calaf M (2020a) Surface Thermal Heterogeneities and the Atmospheric Boundary Layer: The Relevance of Dispersive Fluxes. *Boundary-Layer Meteorol* 175:369–395. <https://doi.org/10.1007/s10546-020-00509-w>
- Margairaz F, Pardyjak ER, Calaf M (2020b) Surface Thermal Heterogeneities and the Atmospheric Boundary Layer: The Thermal Heterogeneity Parameter. *Boundary-Layer Meteorol* 177:49–68. <https://doi.org/10.1007/s10546-020-00544-7>
- Maronga B, Gryschka M, Heinze R, Hoffmann F, Kanani-Sührling F, Keck M, Ketelsen K, Letzel MO, Sührling M, Raasch S (2015) The Parallelized Large-Eddy Simulation Model (PALM) version 4.0 for atmospheric and oceanic flows: model formulation, recent developments, and future perspectives. *Geosci. Model Dev.* 8(8):2515–2551. <https://doi.org/10.5194/gmd-8-2515-2015>
- Maronga B, Banzhaf S, Burmeister C, Esch T, Forkel R, Fröhlich D, Fuka V, Gehrke KF, Geletič J, Giersch S, Gronemeier T, Groß G, Heldens W, Hellsten A, Hoffmann F, Inagaki A, Kadasch E, Kanani-Sührling F, Ketelsen K, Khan BA, Knigge C, Knoop H, Krč P, Kurppa M, Maamari H, Matzarakis A, Mauder M, Pallasch M, Pavlik D, Pfafferott J, Resler J, Rissmann S, Russo E, Salim M, Schrempf M, Schwenkel J, Seckmeyer G, Schubert S, Sührling M, Tils R von, Vollmer L, Ward S, Witha B, Wurps H, Zeidler J, Raasch S (2020) Overview of the PALM model system 6.0. *Geosci. Model Dev.* 13(3):1335–1372. <https://doi.org/10.5194/gmd-13-1335-2020>
- Mauder M, Foken T (2006) Impact of post-field data processing on eddy covariance flux estimates and energy balance closure. *metz* 15(6):597–609. <https://doi.org/10.1127/0941-2948/2006/0167>
- Mauder M, Foken T (2011) *Documentation and Instruction Manual of the Eddy-Covariance Software Package TK3*

- Mauder M, Jegede OO, Okogbue EC, Wimmer F, Foken T (2007a) Surface energy balance measurements at a tropical site in West Africa during the transition from dry to wet season. *Theor Appl Climatol* 89(3-4):171–183. <https://doi.org/10.1007/s00704-006-0252-6>
- Mauder M, Desjardins RL, Pattey E, Gao Z, van Haarlem R (2008) Measurement of the Sensible Eddy Heat Flux Based on Spatial Averaging of Continuous Ground-Based Observations. *Boundary-Layer Meteorol* 128(1):151–172. <https://doi.org/10.1007/s10546-008-9279-9>
- Mauder M (2013) A Comment on “How Well Can We Measure the Vertical Wind Speed? Implications for Fluxes of Energy and Mass” by Kochendorfer et al. *Boundary-Layer Meteorol* 147(2):329–335. <https://doi.org/10.1007/s10546-012-9794-6>
- Mauder M, Zeeman MJ (2018) Field intercomparison of prevailing sonic anemometers. *Atmos. Meas. Tech.* 11:249–263. <https://doi.org/10.5194/amt-11-249-2018>
- Mauder M, Liebenthal C, Göckede M, Leps J-P, Beyrich F, Foken T (2006) Processing and quality control of flux data during LITFASS-2003. *Boundary-Layer Meteorol* 121(1):67–88. <https://doi.org/10.1007/s10546-006-9094-0>
- Mauder M, Desjardins RL, MacPherson I (2007b) Scale analysis of airborne flux measurements over heterogeneous terrain in a boreal ecosystem. *J. Geophys. Res. Atmos.* 112(D13):n/a-n/a. <https://doi.org/10.1029/2006JD008133>
- Mauder M, Oncley SP, Vogt R, Weidinger T, Ribeiro L, Bernhofer C, Foken T, Kohsiek W, Bruin HAR de, Liu H (2007c) The energy balance experiment EBEX-2000. Part II: Intercomparison of eddy-covariance sensors and post-field data processing methods. *Boundary-Layer Meteorol* 123:29–54. <https://doi.org/10.1007/s10546-006-9139-4>
- Mauder M, Desjardins RL, Pattey E, Worth D (2010) An Attempt to Close the Daytime Surface Energy Balance Using Spatially-Averaged Flux Measurements. *Boundary-Layer Meteorol* 136(2):175–191. <https://doi.org/10.1007/s10546-010-9497-9>
- Mauder M, Foken T, Cuxart J (2020) Surface-Energy-Balance Closure over Land: A Review. *Boundary-Layer Meteorol* 9(8):3587. <https://doi.org/10.1007/s10546-020-00529-6>
- Mauder M, Ibrom A, Wanner L, De Roo F, Brügger P, Kiese R, Pilegaard K (2021) Options to correct local turbulent flux measurements for large-scale fluxes using an approach based on large-eddy simulation. *Atmos. Meas. Tech.* 14:7835–7850. <https://doi.org/10.5194/amt-14-7835-2021>
- McCaughey JH, Saxton WL (1988) Energy balance storage terms in a mixed forest. *Agricultural and Forest Meteorology* 44:1–18. [https://doi.org/10.1016/0168-1923\(88\)90029-9](https://doi.org/10.1016/0168-1923(88)90029-9)
- Meesters A, Vugts HF (1996) Calculation of heat storage in stems. *Agricultural and Forest Meteorology* 78:181–202. [https://doi.org/10.1016/0168-1923\(95\)02251-1](https://doi.org/10.1016/0168-1923(95)02251-1)
- Metzger M, Holmes H (2007) Time Scales in the Unstable Atmospheric Surface Layer. *Boundary-Layer Meteorol* 126:29–50. <https://doi.org/10.1007/s10546-007-9219-0>
- Metzger S, Junkermann W, Mauder M, Beyrich F, Butterbach-Bahl K, Schmid HP, Foken T (2012) Eddy-covariance flux measurements with a weight-shift microlight aircraft. *Atmos. Meas. Tech.* 5:1699–1717. <https://doi.org/10.5194/amt-5-1699-2012>
- Metzger S, Durden D, Paleri S, Sühling M, Butterworth BJ, Florian C, Mauder M, Plummer DM, Wanner L, Xu K, Desai AR (2021) Novel approach to observing system simulation experiments improves information gain of surface-atmosphere field measurements. *Atmos. Meas. Tech.* 14:6929–6954. <https://doi.org/10.5194/amt-14-6929-2021>
- Meyers TP, Hollinger SE (2004) An assessment of storage terms in the surface energy balance of maize and soybean. *Agricultural and Forest Meteorology* 125:105–115. <https://doi.org/10.1016/j.agrformet.2004.03.001>
- Moderow U, Aubinet M, Feigenwinter C, Kolle O, Lindroth A, Mölder M, Montagnani L, Rebmann C, Bernhofer C (2009) Available energy and energy balance closure at four coniferous forest sites across Europe. *Theor Appl Climatol* 98:397–412. <https://doi.org/10.1007/s00704-009-0175-0>
- Moeng C-H (1984) A Large-Eddy-Simulation Model for the Study of Planetary Boundary-Layer Turbulence. *J. Atmos. Sci.* 41:2052–2062. [https://doi.org/10.1175/1520-0469\(1984\)041<2052:ALESMF>2.0.CO;2](https://doi.org/10.1175/1520-0469(1984)041<2052:ALESMF>2.0.CO;2)
- Molina MO, Sánchez E, Gutiérrez C (2020) Future heat waves over the Mediterranean from an Euro-CORDEX regional climate model ensemble. *Sci Rep* 10:8801. <https://doi.org/10.1038/s41598-020-65663-0>
- Moore CJ (1986) Frequency response corrections for eddy correlation systems. *Boundary-Layer Meteorol* 37:17–35. <https://doi.org/10.1007/BF00122754>
- Moore CJ, Fisch G (1986) Estimating heat storage in Amazonian tropical forest. *Agricultural and Forest Meteorology* 38:147–168. [https://doi.org/10.1016/0168-1923\(86\)90055-9](https://doi.org/10.1016/0168-1923(86)90055-9)
- Morrison T, Calaf M, Higgins CW, Drake SA, Perelet A, Pardyjak E (2021) The Impact of Surface Temperature Heterogeneity on Near-Surface Heat Transport. *Boundary-Layer Meteorol* 180:247–272. <https://doi.org/10.1007/s10546-021-00624-2>
- Morrison T, Pardyjak ER, Mauder M, Calaf M (2022) The Heat-Flux Imbalance: The Role of Advection and Dispersive Fluxes on Heat Transport Over Thermally Heterogeneous Terrain. *Boundary-Layer Meteorol* 183:227–247. <https://doi.org/10.1007/s10546-021-00687-1>
- Munger JW, Loeschner HW, Luo H (2012) Measurement, Tower, and Site Design Considerations. In: Aubinet M, Vesala T, Papale D (eds) *Eddy covariance: A practical guide to measurement and data analysis*. Springer, Dordrecht, Heidelberg, London, New York, pp 21–58
- Nabuurs G-J, Delacote P, Ellison D, Hanewinkel M, Hetemäki L, Lindner M (2017) By 2050 the Mitigation Effects of EU Forests Could Nearly Double through Climate Smart Forestry. *Forests* 8:484. <https://doi.org/10.3390/f8120484>
- Nabuurs G-J, Mrabet R, Abu Hatab A, Bustamante M, Clark H, Havlik P, House J, Mbow C, Ninan KN, Popp A, Roe S, Sohngen B, Towprayoon S (2022) Agriculture, Forestry and Other Land Uses (AFOLU). In: IPCC (ed) *Climate*

- Change 2022: Mitigation of Climate Change [P.R. Shukla, J. Skea, R. Slade, A. Al Khourdajie, R. van Diemen, D. McCollum, M. Pathak, S. Some, P. Vyas, R. Fradera, M. Belkacemi, A. Hasija, G. Lisboa, S. Luz, J. Malley, (eds.)]. Cambridge University Press, Cambridge, UK and New York, NY, USA, pp 747–860
- Nakai T, Shimoyama K (2012) Ultrasonic anemometer angle of attack errors under turbulent conditions. *Agricultural and Forest Meteorology* 162-163:14–26. <https://doi.org/10.1016/j.agrformet.2012.04.004>
- Nolan RH, Boer MM, Collins L, Resco de Dios V, Clarke H, Jenkins M, Kenny B, Bradstock RA (2020) Causes and consequences of eastern Australia's 2019-20 season of mega-fires. *Global Change Biol* 26:1039–1041. <https://doi.org/10.1111/gcb.14987>
- O'Dell D, Eash NS, Hicks BB, Oetting JN, Sauer TJ, Lambert DM, Thierfelder C, Muoni T, Logan J, Zahn JA, Goddard JJ (2020) Conservation agriculture as a climate change mitigation strategy in Zimbabwe. *International Journal of Agricultural Sustainability* 18:250–265. <https://doi.org/10.1080/14735903.2020.1750254>
- Oke TR (1987) *Boundary layer climates*. 2nd ed. Methuen (reprinted by Routledge), London
- Oliphant AJ, Grimmond C, Zutter HN, Schmid HP, Su H-B, Scott SL, Offerle B, Randolph JC, Ehman J (2004) Heat storage and energy balance fluxes for a temperate deciduous forest. *Agricultural and Forest Meteorology* 126:185–201. <https://doi.org/10.1016/j.agrformet.2004.07.003>
- Omidvar H, Bou-Zeid E, Li Q, Mellado J-P, Klein P (2020) Plume or bubble? Mixed-convection flow regimes and city-scale circulations. *J. Fluid Mech.* 897. <https://doi.org/10.1017/jfm.2020.360>
- Onclay SP, Foken T, Vogt R, Kohsiek W, Debruin HAR, Bernhofer C, Christen A, van Gorsel E, Grantz D, Feigenwinter C, Lehner I, Liebethal C, Liu H, Mauder M, Pitacco A, Ribeiro L, Weidinger T (2007) The Energy Balance Experiment EBEX-2000. Part I: overview and energy balance. *Boundary-Layer Meteorol* 123(1):1–28. <https://doi.org/10.1007/s10546-007-9161-1>
- Paleri S, Butterworth B, Desai AR (2022a) Here, There and Everywhere: Spatial Patterns and Scales. In: Hiscox AL (ed) *Conceptual boundary layer meteorology: The air near here*. Academic Press, Cambridge, MA USA
- Paleri S, Desai AR, Metzger S, Durden D, Butterworth BJ, Mauder M, Kohnert K, Serafimovich A (2022b) Space-Scale Resolved Surface Fluxes Across a Heterogeneous, Mid-Latitude Forested Landscape. *J. Geophys. Res. Atmos.* 127. <https://doi.org/10.1029/2022JD037138>
- Paleri S, Wanner L, Sührling M, Desai A, Mauder M (2023a) Coupled large eddy simulations of land surface heterogeneity effects and diurnal evolution of late summer and early autumn atmospheric boundary layers during the CHEESE-HEAD19 field campaign. *EGUsphere* [preprint]. <https://doi.org/10.5194/egusphere-2023-1721>
- Paleri S, Wanner L, Sührling M, Desai AR, Mauder M, Metzger S (2023b) Impact of Surface Heterogeneity Induced Secondary Circulations on the Atmospheric Boundary Layer. Submitted to *Boundary-Layer Meteorology* (in review)
- Paleri S, Wanner L, Sührling M, Desai A, Mauder M (2023c) PALM Model System v 6.0 input and configuration files for coupled large eddy simulations of land surface heterogeneity effects and diurnal evolution of late summer and early autumn atmospheric boundary layers during the CHEESEHEAD19 field campaign. <https://doi.org/10.5281/zenodo.8179065>
- Panin GN, Bernhofer C (2008) Parametrization of turbulent fluxes over inhomogeneous landscapes. *Izv. Atmos. Ocean. Phys.* 44(6):701–716. <https://doi.org/10.1134/S0001433808060030>
- Panin GN, Tetzlaff G, Raabe A (1998) Inhomogeneity of the Land Surface and Problems in the Parameterization of Surface Fluxes in Natural Conditions. *Theor Appl Climatol* 60(1-4):163–178. <https://doi.org/10.1007/s007040050041>
- Panofsky HA, Tennekes H, Lenschow DH, Wyngaard JC (1977) The characteristics of turbulent velocity components in the surface layer under convective conditions. *Boundary-Layer Meteorol* 11(3):355–361. <https://doi.org/10.1007/BF02186086>
- Park S-B, Baik J-J (2014) Large-Eddy Simulations of Convective Boundary Layers over Flat and Urbanlike Surfaces. *J. Atmos. Sci.* 71:1880–1892. <https://doi.org/10.1175/JAS-D-13-0191.1>
- Patton EG, Sullivan PP, Moeng C-H (2005) The Influence of Idealized Heterogeneity on Wet and Dry Planetary Boundary Layers Coupled to the Land Surface. *J. Atmos. Sci.* 62(7):2078–2097. <https://doi.org/10.1175/JAS3465.1>
- Patton EG, Sullivan PP, Shaw RH, Finnigan JJ, Weil JC (2016) Atmospheric Stability Influences on Coupled Boundary Layer and Canopy Turbulence. *J. Atmos. Sci.* 73(4):1621–1647. <https://doi.org/10.1175/JAS-D-15-0068.1>
- Pleim JE, Xiu A (1995) Development and Testing of a Surface Flux and Planetary Boundary Layer Model for Application in Mesoscale Models. *J. Appl. Meteor.* 34:16–32. <https://doi.org/10.1175/1520-0450-34.1.16>
- Qu L, Chen J, Dong G, Jiang S, Li L, Guo J, Shao C (2016) Heat waves reduce ecosystem carbon sink strength in a Eurasian meadow steppe. *Environ Res* 144:39–48. <https://doi.org/10.1016/j.envres.2015.09.004>
- Raupach MR, Shaw RH (1982) Averaging procedures for flow within vegetation canopies. *Boundary-Layer Meteorol* 22:79–90. <https://doi.org/10.1007/BF00128057>
- Rebmann C, Kolle O, Heinesch B, Queck R, Ibrom A, Aubinet M (2012) Data Acquisition and Flux Calculations. In: Aubinet M, Vesala T, Papale D (eds) *Eddy covariance: A practical guide to measurement and data analysis*. Springer, Dordrecht, Heidelberg, London, New York, pp 59–83
- Reichstein M, Ciais P, Papale D, Valentini R, Running S, Viovy N, Cramer W, Granier A, Ogée J, Allard V, Aubinet M, Bernhofer C, Buchmann N, Carrara A, Grünwald T, Heimann M, Heinesch B, Knohl A, Kutsch W, Loustau D, Manca G, Matteucci G, Miglietta F, Ourcival JM, Pilegaard K, Pumpanen J, Rambal S, Schaphoff S, Seufert G, Soussana J-F, Sanz M-J, Vesala T, Zhao M (2007) Reduction of ecosystem productivity and respiration during the European summer 2003 climate anomaly: a joint flux tower, remote sensing and modelling analysis. *Global Change Biol* 13:634–651. <https://doi.org/10.1111/j.1365-2486.2006.01224.x>

- Richardson AD, Aubinet M, Barr AG (2012) Uncertainty quantification. In: Aubinet M, Vesala T, Papale D (eds) *Eddy covariance: A practical guide to measurement and data analysis*. Springer, Dordrecht, Heidelberg, London, New York, pp 173–210
- Rosenzweig BR, McPhillips L, Chang H, Cheng C, Welty C, Matsler M, Iwaniec D, Davidson CI (2018) Pluvial flood risk and opportunities for resilience. *WIREs Water* 5. <https://doi.org/10.1002/wat2.1302>
- Roxy MK, Ghosh S, Pathak A, Athulya R, Mujumdar M, Murtugudde R, Terray P, Rajeevan M (2017) A threefold rise in widespread extreme rain events over central India. *Nat Commun* 8:708. <https://doi.org/10.1038/s41467-017-00744-9>
- Salesky ST, Chamecki M, Bou-Zeid E (2017) On the Nature of the Transition Between Roll and Cellular Organization in the Convective Boundary Layer. *Boundary-Layer Meteorol* 163(1):41–68. <https://doi.org/10.1007/s10546-016-0220-3>
- Sarmiento JL, Gloor M, Gruber N, Beaulieu C, Jacobson AR, Mikaloff Fletcher SE, Pacala S, Rodgers K (2010) Trends and regional distributions of land and ocean carbon sinks. *Biogeosciences* 7:2351–2367. <https://doi.org/10.5194/bg-7-2351-2010>
- Schalkwijk J, Jonker HJJ, Siebesma AP (2016) An Investigation of the Eddy-Covariance Flux Imbalance in a Year-Long Large-Eddy Simulation of the Weather at Cabauw. *Boundary-Layer Meteorol* 160(1):17–39. <https://doi.org/10.1007/s10546-016-0138-9>
- Schmid HP (1997) Experimental design for flux measurements: matching scales of observations and fluxes. *Agricultural and Forest Meteorology* 87:179–200. [https://doi.org/10.1016/S0168-1923\(97\)00011-7](https://doi.org/10.1016/S0168-1923(97)00011-7)
- Schmid HP, Grimmond CSB, Cropley F, Offerle B, Su HB (2000) Measurements of CO<sub>2</sub> and energy fluxes over a mixed hardwood forest in the mid-western United States. *Agricultural and Forest Meteorology* 103:357–374. [https://doi.org/10.1016/S0168-1923\(00\)00140-4](https://doi.org/10.1016/S0168-1923(00)00140-4)
- Schmidt H, Schumann U (1989) Coherent structure of the convective boundary layer derived from large-eddy simulations. *J. Fluid Mech.* 200:511–562. <https://doi.org/10.1017/S0022112089000753>
- Schotanus P, Nieuwstadt F, Bruin H de (1983) Temperature measurement with a sonic anemometer and its application to heat and moisture fluxes. *Boundary-Layer Meteorol* 26:81–93. <https://doi.org/10.1007/BF00164332>
- Schwalm CR, Williams CA, Schaefer K, Baldocchi D, Black TA, Goldstein AH, Law BE, Oechel WC, Paw U KT, Scott RL (2012) Reduction in carbon uptake during turn of the century drought in western North America. *Nat Geosci* 5:551–556. <https://doi.org/10.1038/ngeo1529>
- Segal M, Arritt RW (1992) Nonclassical Mesoscale Circulations Caused by Surface Sensible Heat-Flux Gradients. *Bull. Amer. Meteor. Soc.* 73:1593–1604. [https://doi.org/10.1175/1520-0477\(1992\)073<1593:NMCCBS>2.0.CO;2](https://doi.org/10.1175/1520-0477(1992)073<1593:NMCCBS>2.0.CO;2)
- Seneviratne SI, Hauser M (2020) Regional Climate Sensitivity of Climate Extremes in CMIP6 Versus CMIP5 Multimodel Ensembles. *Earths Future* 8:e2019EF001474. <https://doi.org/10.1029/2019EF001474>
- Seneviratne SI, Zhang X, Adnan M, Badi W, Dereczynski C, Di Luca A, Ghosh S, Iskandar I, Kossin J, Lewis S, Otto F, Pinto I, Satoh M, Vicente-Serrano SM, Wehner M, Zhou B (2021) Weather and Climate Extreme Events in a Changing Climate. In: IPCC (ed) *Climate Change 2021: The Physical Science Basis* [Masson-Delmotte, V., P. Zhai, A. Pirani, S.L. Connors, C. Péan, S. Berger, N. Caud, Y. Chen, L. Goldfarb, M.I. Gomis, M. Huang, K. Leitzell, E. Lonnoy, J.B.R. Matthews, T.K. Maycock, T. Waterfield, O. Yelekçi, R. Yu, and B. Zhou (eds.)]. Cambridge University Press, Cambridge, UK and New York, NY, USA, pp 1513–1766
- Sheshadri A, Borrus M, Yoder M, Robinson T (2021) Midlatitude Error Growth in Atmospheric GCMs: The Role of Eddy Growth Rate. *Geophys. Res. Lett.* 48. <https://doi.org/10.1029/2021GL096126>
- Soltani M, Mauder M, Laux P, Kunstmann H (2018) Turbulent flux variability and energy balance closure in the TERENO prealpine observatory: a hydrometeorological data analysis. *Theor Appl Climatol* 133(3-4):937–956. <https://doi.org/10.1007/s00704-017-2235-1>
- Sridhar V, Elliott RL, Chen F, Brotzge JA (2002) Validation of the NOAA-OSU land surface model using surface flux measurements in Oklahoma. *J. Geophys. Res. Atmos.* 107. <https://doi.org/10.1029/2001JD001306>
- Steinfeld G, Letzel MO, Raasch S, Kanda M, Inagaki A (2007) Spatial representativeness of single tower measurements and the imbalance problem with eddy-covariance fluxes: results of a large-eddy simulation study. *Boundary-Layer Meteorol* 123(1):77–98. <https://doi.org/10.1007/s10546-006-9133-x>
- Stocker BD, Zscheischler J, Keenan TF, Prentice IC, Peñuelas J, Seneviratne SI (2018) Quantifying soil moisture impacts on light use efficiency across biomes. *New Phytol* 218:1430–1449. <https://doi.org/10.1111/nph.15123>
- Stoy PC, Katul GG, Siqueira MBS, Juang J-Y, Novick KA, McCarthy HR, Christopher Oishi A, Uebelherr JM, Kim H-S, Oren RA (2006) Separating the effects of climate and vegetation on evapotranspiration along a successional chronosequence in the southeastern US. *Global Change Biol* 12:2115–2135. <https://doi.org/10.1111/j.1365-2486.2006.01244.x>
- Stoy PC, Mauder M, Foken T, Marcolla B, Boegh E, Ibrom A, Arain MA, Arneth A, Aurela M, Bernhofer C, Cescatti A, Dellwik E, Duce P, Gianelle D, van Gorsel E, Kiely G, Knohl A, Margolis H, McCaughey H, Merbold L, Montagnani L, Papale D, Reichstein M, Saunders M, Serrano-Ortiz P, Sottocornola M, Spano D, Vaccari F, Varlagin A (2013) A data-driven analysis of energy balance closure across FLUXNET research sites: The role of landscape scale heterogeneity. *Agricultural and Forest Meteorology* 171-172:137–152. <https://doi.org/10.1016/j.agrformet.2012.11.004>
- Stull RB (1988) *An Introduction to Boundary Layer Meteorology*. Atmospheric Sciences Library, vol 13. Springer, Dordrecht

- Sühring M, Raasch S (2013) Heterogeneity-Induced Heat-Flux Patterns in the Convective Boundary Layer: Can they be Detected from Observations and is There a Blending Height?—A Large-Eddy Simulation Study for the LITFASS-2003 Experiment. *Boundary-Layer Meteorol* 148(2):309–331. <https://doi.org/10.1007/s10546-013-9822-1>
- Sühring M, Metzger S, Xu K, Durden D, Desai A (2018) Trade-Offs in Flux Disaggregation: A Large-Eddy Simulation Study. *Boundary-Layer Meteorol* 170(1):69–93. <https://doi.org/10.1007/s10546-018-0387-x>
- Terradellas E, Morales G, Cuxart J, Yagüe C (2001) Wavelet methods: application to the study of the stable atmospheric boundary layer under non-stationary conditions. *Dynamics of Atmospheres and Oceans* 34:225–244. [https://doi.org/10.1016/S0377-0265\(01\)00069-0](https://doi.org/10.1016/S0377-0265(01)00069-0)
- Turco M, Jerez S, Augusto S, Tarin-Carrasco P, Ratola N, Jiménez-Guerrero P, Trigo RM (2019) Climate drivers of the 2017 devastating fires in Portugal. *Sci Rep* 9:13886. <https://doi.org/10.1038/s41598-019-50281-2>
- Twine TE, Kustas WP, Norman JM, Cook DR, Houser PR, Meyers TP, Prueger JH, Starks PJ, Wesely ML (2000) Correcting eddy-covariance flux underestimates over a grassland. *Agricultural and Forest Meteorology* 103:279–300. [https://doi.org/10.1016/S0168-1923\(00\)00123-4](https://doi.org/10.1016/S0168-1923(00)00123-4)
- van Gorsel E, Wolf S, Cleverly J, Isaac P, Haverd V, Ewenz C, Arndt S, Beringer J, Resco de Dios V, Evans BJ, Griebel A, Hutley LB, Keenan T, Kljun N, Macfarlane C, Meyer WS, McHugh I, Pendall E, Prober SM, Silberstein R (2016) Carbon uptake and water use in woodlands and forests in southern Australia during an extreme heat wave event in the “Angry Summer” of 2012/2013. *Biogeosciences* 13:5947–5964. <https://doi.org/10.5194/bg-13-5947-2016>
- van Heerwaarden CC, Mellado JP, Lozar A de (2014) Scaling Laws for the Heterogeneously Heated Free Convective Boundary Layer. *J. Atmos. Sci.* 71:3975–4000. <https://doi.org/10.1175/JAS-D-13-0383.1>
- Vincent LA, Zhang X, Mekis É, Wan H, Bush EJ (2018) Changes in Canada's Climate: Trends in Indices Based on Daily Temperature and Precipitation Data. *Atmosphere-Ocean* 56:332–349. <https://doi.org/10.1080/07055900.2018.1514579>
- Volosciuk C, Maraun D, Semenov VA, Tilinina N, Gulev SK, Latif M (2016) Rising Mediterranean Sea Surface Temperatures Amplify Extreme Summer Precipitation in Central Europe. *Sci Rep* 6:32450. <https://doi.org/10.1038/srep32450>
- Wang YP, Baldocchi D, Leuning R, Falge E, Vesala T (2007) Estimating parameters in a land-surface model by applying nonlinear inversion to eddy covariance flux measurements from eight FLUXNET sites. *Global Change Biol* 13:652–670. <https://doi.org/10.1111/j.1365-2486.2006.01225.x>
- Wanner L, De Roo F, Sühring M, Mauder M (2022a) How Does the Choice of the Lower Boundary Conditions in Large-Eddy Simulations Affect the Development of Dispersive Fluxes Near the Surface? *Boundary-Layer Meteorol* 182:1–27. <https://doi.org/10.1007/s10546-021-00649-7>
- Wanner L, Calaf M, Mauder M (2022b) Incorporating the effect of heterogeneous surface heating into a semi-empirical model of the surface energy balance closure. *PLoS ONE* 17:e0268097. <https://doi.org/10.1371/journal.pone.0268097>
- Wanner L, Jung M, Paleri S, Butterworth B, Desai AR, Sühring M, Mauder M (2023) Towards Energy-Balance Closure with a Model of Dispersive Heat Fluxes. PREPRINT (Version 1) available at Research Square. <https://doi.org/10.21203/rs.3.rs-3449667/v1>
- Webb EK, Pearman GI, Leuning R (1980) Correction of flux measurements for density effects due to heat and water vapour transfer. *Q.J.R. Meteorol. Soc* 106:85–100. <https://doi.org/10.1002/qj.49710644707>
- Wilczak JM, Oncley SP, Stage SA (2001) Sonic Anemometer Tilt Correction Algorithms. *Boundary-Layer Meteorol* 99:127–150. <https://doi.org/10.1023/A:1018966204465>
- Williams M, Richardson AD, Reichstein M, Stoy PC, Peylin P, Verbeeck H, Carvalhais N, Jung M, Hollinger DY, Kattge J, Leuning R, Luo Y, Tomelleri E, Trudinger CM, Wang Y-P (2009) Improving land surface models with FLUXNET data. *Biogeosciences* 6:1341–1359. <https://doi.org/10.5194/bg-6-1341-2009>
- Williams AP, Seager R, Abatzoglou JT, Cook BI, Smerdon JE, Cook ER (2015) Contribution of anthropogenic warming to California drought during 2012–2014. *Geophys. Res. Lett.* 42:6819–6828. <https://doi.org/10.1002/2015GL064924>
- Wilson K, Goldstein A, Falge E, Aubinet M, Baldocchi D, Berbigier P, Bernhofer C, Ceulemans R, Dolman H, Field C, Grelle A, Ibrom A, Law B, Kowalski A, Meyers T, Moncrieff J, Monson R, Oechel W, Tenhunen J, Valentini R, Verma S (2002) Energy balance closure at FLUXNET sites. *Agricultural and Forest Meteorology* 113(1-4):223–243. [https://doi.org/10.1016/S0168-1923\(02\)00109-0](https://doi.org/10.1016/S0168-1923(02)00109-0)
- Wilson NR, Shaw RH (1977) A Higher Order Closure Model for Canopy Flow. *J. Appl. Meteor.* 16:1197–1205. [https://doi.org/10.1175/1520-0450\(1977\)016<1197:AHOCMF>2.0.CO;2](https://doi.org/10.1175/1520-0450(1977)016<1197:AHOCMF>2.0.CO;2)
- Winter HC, Brown SJ, Tawn JA (2017) Characterising the changing behaviour of heatwaves with climate change. *climatesystem:dzw006*. <https://doi.org/10.1093/climsys/dzw006>
- Wisconsin Department of Natural Resources (2016) Land Cover Data Wiscland 2.0. <https://dnr.wisconsin.gov/maps/WISCLAND>
- Wolf S, Keenan TF, Fisher JB, Baldocchi DD, Desai AR, Richardson AD, Scott RL, Law BE, Litvak ME, Brunsell NA, Peters W, van der Laan-Luijckx IT (2016) Warm spring reduced carbon cycle impact of the 2012 US summer drought. *Proc Natl Acad Sci U S A* 113:5880–5885. <https://doi.org/10.1073/pnas.1519620113>
- Xu F, Wang W, Wang J, Xu Z, Qi Y, Wu Y (2017) Area-averaged evapotranspiration over a heterogeneous land surface: aggregation of multi-point EC flux measurements with a high-resolution land-cover map and footprint analysis. *Hydrol. Earth Syst. Sci.* 21:4037–4051. <https://doi.org/10.5194/hess-21-4037-2017>

- Xu K, Pingingtha-Durden N, Luo H, Durden D, Sturtevant C, Desai AR, Florian C, Metzger S (2019) The eddy-covariance storage term in air: Consistent community resources improve flux measurement reliability. *Agricultural and Forest Meteorology* 279:107734. <https://doi.org/10.1016/j.agrformet.2019.107734>
- Xu K, Sühling M, Metzger S, Durden D, Desai AR (2020) Can Data Mining Help Eddy Covariance See the Landscape? A Large-Eddy Simulation Study. *Boundary-Layer Meteorol* 176(1):85–103. <https://doi.org/10.1007/s10546-020-00513-0>
- Zeder J, Fischer EM (2020) Observed extreme precipitation trends and scaling in Central Europe. *Weather and Climate Extremes* 29:100266. <https://doi.org/10.1016/j.wace.2020.100266>
- Zhou Y, Li D, Li X (2019) The Effects of Surface Heterogeneity Scale on the Flux Imbalance under Free Convection. *J. Geophys. Res. Atmos.* <https://doi.org/10.1029/2018JD029550>

### **Recognition of used data-sets and code**

The PALM model system is freely available from <https://palm.muk.uni-hannover.de> and is distributed under the GNU General Public License v3 (<https://www.gnu.org/licenses/gpl-3.0.html>). The idealized large-eddy simulation data-set by Calaf et al. (2022) is available at <https://zenodo.org/records/6342278>. The model configurations and inputs of for the CHEESEHEAD19 LESs are available at <https://doi.org/10.5281/zenodo.8179066> (Paleri et al. 2023c). The CHEESEHEAD19 observations are archived at the NCAR EOL repository at [www.eol.ucar.edu/field\\_projects/cheesehead](http://www.eol.ucar.edu/field_projects/cheesehead). More information on the CHEESEHEAD19 project is available on the CHEESEHEAD19 website at [www.cheesehead19.org](http://www.cheesehead19.org). The WISCLAND 2.0 data-set is available via the DNR GIS Open Data Portal at <https://data-wi-dnr.opendata.arcgis.com/documents/wi-dnr::wiscland-2/about>. The HRRR data (Blaylock et al. 2017) is available at [https://home.chpc.utah.edu/~u0553130/Brian\\_Blaylock/](https://home.chpc.utah.edu/~u0553130/Brian_Blaylock/). Hersbach et al. (2023a, 2023b) was downloaded from the Copernicus Climate Change Service (C3S) (2023). The results contain modified Copernicus Climate Change Service information 2023. Neither the European Commission nor ECMWF is responsible for any use that may be made of the Copernicus information or data it contains.

# APPENDICES



# **A Individual contributions to the joint publications**

This is a cumulative thesis based on three scientific publications in which other people were involved. This Chapter therefore presents my own contributions and those of the co-authors to the work presented in each publication.

## **Appendix B**

Wanner L, De Roo F, Sührling M, Mauder M (2022a): How Does the Choice of the Lower Boundary Conditions in LES Affect the Development of Dispersive Fluxes Near the Surface?, *Boundary-Layer Meteorol*, doi: 10.1007/s10546-021-00649-7

Matthias Mauder and I developed the idea for this paper together. I decided which vegetation types and surface conditions to compare. The choice of atmospheric conditions was largely based on previous simulations by Frederik De Roo. I performed the LES runs with support from Matthias Sührling and Frederik De Roo Sührling. I conducted the data analysis, where Matthias Mauder suggested to further investigate the cause for the different behavior of dispersive fluxes by analyzing the variance similarity functions. I was further responsible for the visualization of results, and wrote most of the manuscript, where Matthias Sührling has contributed the description of PALM. Frederik De Roo, Matthias Sührling, and Matthias Mauder helped to improve the manuscript during an internal review process.

## **Appendix C**

Wanner L, Calaf M, Mauder M (2022b): Incorporating the effect of heterogeneous surface heating into a semi-empirical model of the surface energy balance closure, *PLoS ONE*, 17(6):e0268097, doi: 10.1371/journal.pone.0268097

Matthias Mauder and I developed the idea for this paper with the aim to further develop the SEB imbalance model by De Roo et al. (2018) to account for thermal surface heterogeneity by including the thermal heterogeneity parameter introduced by Margairaz et al. (2020b). We therefore decided to ask Marc Calaf for a collaboration. Since the set of idealized LES used to develop the thermal heterogeneity parameter seemed to be ideally suited for our purpose, Marc Calaf provided the LES output for this study. After consultation with Matthias Mauder, I developed a strategy to derive and systematically test a new set of scaling functions, to model the energy imbalance. I was responsible for the processing of LES output, model development, and visualization of results. I also wrote the manuscript, with contributions by Marc Calaf to the sections on the LES set up and the thermal heterogeneity

parameter. Matthias Mauder and Marc Calaf helped to improve the manuscript during an internal review process.

## Appendix D

Wanner L, Jung M, Paleri S, Butterworth B, Desai A, Sühling M, Mauder M (2023): Towards Energy-Balance Closure with a Model of Dispersive Heat Fluxes, PREPRINT (Version 1) available at Research Square, doi: 10.21203/rs.3.rs-3449667/v1

I developed the idea to further improve the model of SEB imbalance by directly modeling sensible and latent dispersive heat fluxes and including the vertical gradients of potential temperature and mixing ratio. Furthermore, I decided to directly model dispersive heat fluxes instead of the SEB imbalance, as I was interested in the magnitude of energy transport by secondary circulations, but not the contribution of storage change to the SEB imbalance. I therefore developed a concept to recreate the scenarios used in the idealized heterogeneity LES to develop the SEB imbalance model in PALM, which allows for the simulation of latent heat flux, and to expand the set by including various combinations of sensible and latent surface heat fluxes.

The increased complexity of the dataset made it impossible to identify relationships between individual variables and the resulting dispersive fluxes, and to fit scaling functions to develop a model. Matthias Mauder therefore suggested to follow a machine learning approach and to bring in Martin Jung's expertise. Martin Jung suggested to use a Random Forest algorithm and to expand the dataset for improved coverage of different cases. Matthias and I then decided to include more simulations with different surface temperature amplitudes and lower total surface fluxes. I processed the LES output and used a python script to run the Random Forest algorithm provided by Martin Jung to develop the model. I then decided to test the model by directly comparing the modelled dispersive heat fluxes to the dispersive heat fluxes in the more realistic CHEESEHEAD19 LES, and by applying it as a correction method to the CHEESEHEAD19 field measurements.

The CHEESEHEAD19 LES was mainly set up and performed by Sreenath Paleri and me. We wrote a proposal to perform the computationally expensive simulations on the Cheyenne super computer. Sreenath Paleri developed the atmospheric forcing input, and I developed the surface input by compiling information from multiple datasets that were produced by various collaborators during the CHEESEHEAD19 campaign. Matthias Sühling, Ankur Desai, and Matthias Mauder were also involved in the planning and implementation of the LES.

The CHEESEHEAD19 campaign was carried out by a variety of collaborators, but Ankur Desai took the lead role in conceptualizing it, especially with respect to the EC

measurements. Brian Butterworth performed the EC processing and provided me with a 30-min flux dataset. I used this dataset, in combination with reanalysis data, to apply the model.

I was responsible for most of the data processing and analysis, as described above. I also visualized the results and wrote the manuscript. Martin Jung provided a short section on the Random Forest algorithm, Sreenath Paleri and Matthias Sühring contributed to the description of the CHEESEHEAD LES, and Brian Butterworth contributed a short section on the processing of CHEESEHEAD field measurements. All co-authors helped to improve the manuscript during an internal review process.



## **B How does the choice of the lower boundary conditions in LES affect the development of dispersive fluxes near the surface?**

Wanner L, De Roo F, Sühring M, Mauder M (2022): How Does the Choice of the Lower Boundary Conditions in LES Affect the Development of Dispersive Fluxes Near the Surface?, *Boundary-Layer Meteorol*, doi: 10.1007/s10546-021-00649-7





# How Does the Choice of the Lower Boundary Conditions in Large-Eddy Simulations Affect the Development of Dispersive Fluxes Near the Surface?

Luise Wanner<sup>1</sup> · Frederik De Roo<sup>2</sup> · Matthias Sühling<sup>3</sup> · Matthias Mauder<sup>1,4</sup>

Received: 18 December 2020 / Accepted: 29 June 2021 / Published online: 10 August 2021  
© The Author(s) 2021

## Abstract

Large-eddy simulations (LES) are an important tool for investigating the longstanding energy-balance-closure problem, as they provide continuous, spatially-distributed information about turbulent flow at a high temporal resolution. Former LES studies reproduced an energy-balance gap similar to the observations in the field typically amounting to 10–30% for heights on the order of 100 m in convective boundary layers even above homogeneous surfaces. The underestimation is caused by dispersive fluxes associated with large-scale turbulent organized structures that are not captured by single-tower measurements. However, the gap typically vanishes near the surface, i.e. at typical eddy-covariance measurement heights below 20 m, contrary to the findings from field measurements. In this study, we aim to find a LES set-up that can represent the correct magnitude of the energy-balance gap close to the surface. Therefore, we use a nested two-way coupled LES, with a fine grid that allows us to resolve fluxes and atmospheric structures at typical eddy-covariance measurement heights of 20 m. Under different stability regimes we compare three different options for lower boundary conditions featuring grassland and forest surfaces, i.e. (1) prescribed surface fluxes, (2) a land-surface model, and (3) a land-surface model in combination with a resolved canopy. We show that the use of prescribed surface fluxes and a land-surface model yields similar dispersive heat fluxes that are very small near the vegetation top for both grassland and forest surfaces. However, with the resolved forest canopy, dispersive heat fluxes are clearly larger, which we explain by a clear impact of the resolved canopy on the relationship between variance and flux–variance similarity functions.

**Keywords** Energy-balance closure · Land-surface model · Large-eddy simulation · Plant-canopy model · Prescribed surface fluxes

---

✉ Luise Wanner  
luise.wanner@kit.edu

Extended author information available on the last page of the article

## 1 Introduction

The eddy-covariance (EC) method is well established and used worldwide in various networks for long-term measurements of energy and gas fluxes between ecosystems and the atmosphere (e.g., Baldocchi et al. 2001; Novick et al. 2018). However, the EC method often systematically underestimates these fluxes, which leads to a gap in the energy balance of about 10 to 30% (Hendricks-Franssen et al. 2010; Stoy et al. 2013; Soltani et al. 2018). This phenomenon has been widely discussed in the literature in the last few decades, and some possible causes, such as instrument and set-up errors in EC measurements (Laubach et al. 1994; Goulden et al. 1996; Kochendorfer et al. 2012; Nakai and Shimoyama 2012; Frank et al. 2013; Mauder 2013), or measurement errors of other components of the energy balance, such as soil heat flux or net radiation (Liebethal et al. 2005; Kohsiek et al. 2007; Foken 2008), have already been excluded as a general problem across different sites (Foken 2008; Mauder et al. 2020).

An important reason for the underestimation of fluxes using single-tower measurements is the missed dispersive flux, i.e. the transport carried out by secondary circulations. These secondary circulations can be divided into two types, thermally-induced mesoscale circulations (TMC), which are generated by surface heterogeneity and are therefore spatially bound to the surface conditions (Foken 2008; Kenny et al. 2017; Bou-Zeid et al. 2020; Mauder et al. 2020), and slow-moving turbulent organized structures (TOS) that can develop even over homogeneous surfaces (Kanda et al. 2004; Inagaki et al. 2006). Both types of secondary circulations contribute to the vertical transport by a non-zero mean vertical velocity component, which cannot be captured by the EC method, since only the small-scale turbulent part of the flux (i.e. the temporal covariance-heat flux) is resolved. Field measurements have shown that secondary circulations reach well into the surface layer (Eder et al. 2015a) and contribute to the energy-balance gap (Eder et al. 2015b). In a large-eddy simulation (LES) study over a homogeneous forest where the canopy was explicitly resolved by the grid, Patton et al. (2016) showed that atmospheric structures that scale with the atmospheric boundary-layer height reach down to the canopy top and also occur in the understorey air space.

The use of long averaging intervals up to 24 h can reduce the energy-balance gap as they include the energy transport by TOS (Finnigan et al. 2003; Foken et al. 2006). With this approach, however, the temporal resolution is reduced. Thus, flux measurements on a half-hourly basis that are required for comparisons against numerical models are no longer available and diurnal variations are no longer detectable. Moreover, it is questionable whether stationarity can still be assumed, which is a prerequisite for applying Gaussian statistics, such as the calculation of a covariance (Mauder et al. 2006).

Biomass heat storage is another major contributor to the energy-balance gap, especially in high vegetation such as forests (Lindroth et al. 2010; Leuning et al. 2012; Swenson et al. 2019). In this study, however, we do not address this factor.

In recent years, various experimental designs have been developed to systematically investigate the energy-balance-closure (EBC) problem in field measurements (Oncley et al. 2007; Foken et al. 2010; Butterworth et al. 2021). This requires a large number of spatially-distributed EC measurements (Kanda et al. 2004; Xu et al. 2020), making the measurement campaigns accordingly complex and expensive.

Complementarily, LES are particularly well suited to investigating the influence of secondary circulations, as they provide continuous information with a high temporal and three-dimensional spatial resolution and can capture atmospheric motions on a wide

range of scales (Inagaki et al. 2006; Schalkwijk et al. 2016). Furthermore, LES provide a controlled environment in which the boundary conditions are known, as opposed to real-world conditions, and virtual measurements without instrument errors (Inagaki et al. 2006; Schalkwijk et al. 2016; Sühling et al. 2018).

In recent years, computational resources have increased significantly, enabling LES with high spatial resolution. This, in turn, facilitates the investigation of turbulence structures and flow components near the surface, including the canopy layer (e.g., Kanani-Sühling and Raasch 2017; Kröniger et al. 2018). It is particularly important to investigate the EBC problem near the surface since EC measurements are typically taken in the surface layer at a height of 2–40 m, depending on the vegetation height (Hendricks-Franssen et al. 2010; Butterworth et al. 2021).

Several studies have already investigated the EBC problem using LES. Kanda et al. (2004), Steinfeld et al. (2007), and Huang et al. (2008) analyzed the height dependency of the imbalance and found that virtual tower measurements at higher altitudes underestimated sensible heat fluxes even if the surface itself was homogeneous and no TMCs were generated by heterogeneous surface heating (Inagaki et al. 2006). However, using a rather large vertical grid spacing of 25 m (Kanda et al. 2004) and 20 m (Huang et al. 2008), it was found that the energy-balance gap vanished near the surface. Moreover, using simulations of similar grid resolution, Steinfeld et al. (2007) showed that the imbalance close to the ground reduced to less than 5%, which does not match field observations. Hence, they concluded that TOS could not explain the magnitude of the energy-balance gap. Zhou et al. (2019) examined the magnitude of the energy-balance gap in relation to landscape heterogeneity and found it to be largest for heterogeneities on the scale of the boundary-layer height. However, Inagaki et al. (2006) studied the influence of surface heterogeneity on the imbalance and found the imbalance above a homogeneous surface to be on the same order of magnitude as above a heterogeneous surface. This was also supported by Margairaz et al. (2020), who showed that persistent structures in half-hourly averaged vertical wind velocity were as pronounced above homogeneous surfaces as over heterogeneous surfaces.

We hypothesize that the common use of prescribed surface fluxes (PSF) is one important reason why former LES studies underestimate the energy balance. With prescribed fluxes, the surface–atmosphere exchange is decoupled from the atmosphere (i.e. the atmosphere responds to the surface) while the surface does not respond to the atmosphere. With this mutual feedback missing, possibly important aspects such as self-reinforcement or weakening of secondary circulations are not accounted for in the simulations.

In the present study, we aim to discover the reasons why LES studies have so far been unable to reproduce near-surface EBC gaps that were similar to observations and if different lower boundary conditions have an influence on dispersive heat fluxes.

In order to answer our research question, we set up two branches of numerical experiments, one for short grass and one for tall vegetation. We performed LES with varying surface-boundary conditions (as illustrated in Fig. 1) and evaluated the effect of the surface-boundary condition with regard to the energy-balance closure for varying atmospheric stability.

For the short-grass experiments, we set up LES with an interactive land-surface model (LSM, Gehrke et al. 2020) where the surface–atmosphere exchange concerning water and heat exchange is modelled explicitly, and compared these against simulations with prescribed surface fluxes where the surface does not interact with the atmosphere at all. Maronga et al. (2020) describe in detail how near-surface air temperature feeds into the LSM.

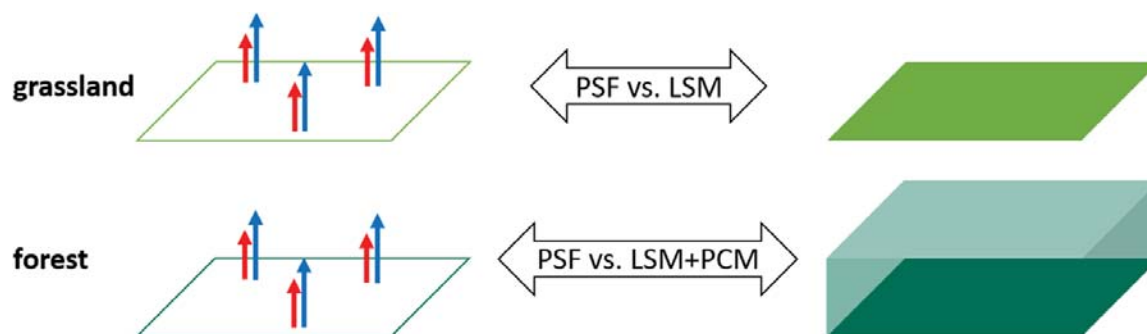


**Fig. 1** Schematic illustration of the lower boundary conditions that are compared for the two vegetation types investigated

For the tall-vegetation experiments, we set up simulations with an interactive LSM combined with a plant-canopy model (PCM) where trees are explicitly resolved by the numerical grid. Again, these were compared against simulations with prescribed surface fluxes with respect to the energy-balance closure. We aim to assess the importance of land-surface representation in LES for different kinds of land use.

Since we use an idealized, homogeneous set-up, we investigate the contribution of vertical transport by TOS only, hereafter referred to as the dispersive heat flux. We wish to test if the use of LSM and PCM lead to larger dispersive fluxes by adapting to changes in the atmosphere.

The next section describes our procedure divided into set-up of the different simulations (Sect. 2.1) and evaluation of the simulations, i.e. the calculation of the heat flows (Sect. 2.2). Section 3 presents the results, first considering the comparability of the respective PSF and LSM(+PCM) studies (Sect. 3.1), before we examine the formation of TOS at different lower boundary conditions (Sect. 3.2), the resulting dispersive fluxes (Sect. 3.3) and finally the influences of the LSM in different set-ups (Sect. 3.4). The results are then analyzed and discussed against the background of other findings from the field in Sect. 4 and our findings are summarized in Sect. 5.

## 2 Methods

In this study, we compared different lower boundary conditions using PALM v6 (Maronga et al. 2020). We used a highly idealized set-up with homogeneous surfaces and cyclic lateral boundary conditions, while the stability classes were similar to previous LES studies, such as Patton et al. (2016) and De Roo et al. (2018). To obtain a representative result, the simulations were carried out for various combinations of two different land-cover types, grassland (G) and forest (F), as well as for moderately unstable (MU), strongly unstable (SU), and free convective (FC) conditions. An overview of the combinations of lower boundary conditions and atmospheric stabilities is shown in Table 1.

### 2.1 Large-Eddy Simulation Set-up

We used the LES Model PALM, version 6, revision 4529 (Maronga et al. 2020), for the numerical simulations. PALM solves the non-hydrostatic incompressible Boussinesq equations. For the subgrid model, the kinetic energy scheme of Deardorff (1980) modified by

**Table 1** Overview of the individual simulations with different combinations of atmospheric stability, vegetation type, lower boundary condition and subgrid-scale model

Simulation number	Atmospheric stability	Vegetation type	Lower boundary condition
1	MU	Grassland	LSM
2	SU	Grassland	LSM
3	FC	Grassland	LSM
4	MU	Forest	LSM + PCM
5	SU	Forest	LSM + PCM
6	FC	Forest	LSM + PCM
7	MU	Grassland	PSF
8	SU	Grassland	PSF
9	FC	Grassland	PSF
10	MU	Forest	PSF
11	SU	Forest	PSF
12	FC	Forest	PSF

Moeng and Wyngaard (1988) and Saiki et al. (2000) was used. The advection terms were discretized using a fifth-order scheme (Wicker and Skamarock 2002), and a third-order Runge–Kutta scheme by Williamson (1980) was used for the time integration.

To achieve a high grid resolution near the surface, we employed the vertical grid nesting technique available with PALM (Hellsten et al. 2021) where a child domain with smaller grid spacing but the same horizontal extent is placed within the parent domain with larger grid spacing, while these two domains interact with each other. The horizontal domain measured  $7200 \times 7200 \text{ m}^2$ , with the parent domain reaching up to 2400 m and the child domain up to 240 m. In the coarse grid, the horizontal and vertical grid spacings were 30 m and 20 m, respectively, resulting in  $(x, y, z) = 240 \times 240 \times 120$  grid points, whereas, in the fine grid, the horizontal and vertical grid spacings were 6 m and 4 m, respectively, which yields  $(x, y, z) = 1200 \times 1200 \times 60$  grid points. The parent and child domains both reached down to the lower boundary of the domain and simulations in the both domains were run parallelly with two-way nesting. The timestep was set to a constant value of 0.5 s. Each simulation consisted of 2 h of model spin-up time followed by a 4-h period during which data were captured. The latitude was set to 46 degrees north.

The initialization of the atmospheric conditions follows De Roo et al. (2018). The initial horizontal velocity profile was vertically constant and homogeneous over the entire horizontal extent of the domain, with velocity in the  $x$ -direction and geostrophic wind speed varying among the simulations (see Table 2). The geostrophic velocity here featured a horizontal pressure gradient that is oriented in  $x$ -direction. Different geostrophic wind speeds are used for the three atmospheric stabilities as shown in Table 2.

The initial potential temperature at the surface was set to 295 K. Between 40 and 800 m, a vertical gradient of  $3 \times 10^{-3} \text{ K m}^{-1}$  was added and above, the gradient was  $8 \times 10^{-3} \text{ K m}^{-1}$ . The mixing ratio at the surface was set to  $8 \times 10^{-3} \text{ kg kg}^{-1}$ . Between 1000 and 1100 m, a vertical gradient of  $-1 \times 10^{-5} \text{ m}^{-1}$  was imposed, while below and above this area, no vertical gradient was applied. All profiles used for initialization (shown in Appendix, Fig. 11) were homogeneous over the entire horizontal extent of the domain. A stable inversion layer at the top of the domain ensured that the processes within the boundary layer were not affected by the vertical extent of the domain. The

**Table 2** Settings for different combinations of land-cover type and atmospheric stabilities in LSM (simulation numbers 1–3), LSM+PCM (simulation numbers 4–6) and PSF (simulation numbers 7–12) simulations. The roughness lengths for momentum ( $z_0$ ) and heat ( $z_{0h}$ ) are based on the vegetation types that are predefined in the PALM LSM (Gehrke et al. 2020), based on ECMWF-IFS classification

Simulation number	$U_g(\text{m s}^{-1})$	$z_0(\text{m})$	$z_{0h}(\text{m})$	$\cos(\text{zenith})$	$H_s(\text{W m}^{-2})$	$\lambda E_s(\text{W m}^{-2})$
1	5	0.3	$3\text{e}^{-4}$	0.46	–	–
2	2	0.3	$3\text{e}^{-4}$	0.62	–	–
3	0	0.3	$3\text{e}^{-4}$	0.76	–	–
4	5	0.25	0.25	0.42	–	–
5	2	0.25	0.25	0.54	–	–
6	0	0.25	0.25	0.65	–	–
7	5	0.3	$3\text{e}^{-4}$	–	21.96	172.57
8	2	0.3	$3\text{e}^{-4}$	–	42.24	225.09
9	0	0.3	$3\text{e}^{-4}$	–	54.55	282.61
10	5	0.25	0.25	–	38.64	237.59
11	2	0.25	0.25	–	84.31	302.62
12	0	0.25	0.25	–	123.99	372.65

horizontal extent of the domain was at least seven times the boundary-layer depth for all atmospheric conditions. Randomly distributed perturbations were imposed on the horizontal velocity fields at the beginning of each simulation to initiate turbulence.

At the lateral boundaries, cyclic conditions were applied. At the surface, we set an impermeable boundary with zero vertical velocity and imposed surface stress by applying Monin–Obukhov similarity theory (MOST) locally between the surface and the first vertical grid level. The resulting surface fluxes of horizontal momentum are then entered as lower boundary conditions via the subgrid-scale term. More precisely, surface horizontal momentum fluxes  $w'u'_i$  were computed from

$$\frac{\partial u}{\partial z} = \frac{\overline{w'u'_i}}{u_* \kappa z} \phi\left(\frac{z}{L}\right), \quad (1)$$

(Maronga et al. 2015), where  $\partial u/\partial z$  is the vertical gradient of horizontal wind speed between the first prognostic grid level and the surface;  $u_*$  is the friction velocity;  $\kappa = 0.4$  is the von Kármán constant, and  $\phi(z/L)$  is the similarity function for momentum in the formulation of Businger–Dyer (see e.g. Panofsky and Dutton (1984)), with  $L$  being the Obukhov length.

For the potential-temperature and mixing-ratio equations we also employed a flux-boundary condition at the surface, with fluxes either prescribed or computed by the land-surface model (Gehrke et al. 2020). For the boundary values of potential temperature and mixing ratio itself, we employed a zero-gradient Neumann boundary condition at the surface. This is to ensure that no flux contribution from the resolved-scale advection arises at the surface, leading to any double counting of the vertical transport.

At the domain top, we set zero-gradient Neumann conditions for the horizontal velocity components, reflecting the geostrophic wind in the upper part of the model domain. The vertical wind velocity at the domain top was set to zero to maintain continuity.

Zero-gradient Neumann conditions at the top boundary were also applied for potential temperature and mixing ratio. Moreover, as in De Roo et al. (2018), a vertical subsidence-velocity gradient of  $4 \times 10^{-5} \text{ m s}^{-1} \text{ m}^{-1}$  up to 800 m and  $2 \times 10^{-5} \text{ m s}^{-1} \text{ m}^{-1}$  between 800 and 1000 m was prescribed. By this, the boundary-layer depth during the analysis period was kept constant. At the surface, the subsidence velocity was zero.

In addition to varying geostrophic wind speeds, the three different atmospheric stabilities were defined by different prescribed surface fluxes, or incoming radiation where the LSM was used, as shown in Table 2. To ensure highest comparability between PSF and LSM(+PCM) simulations, the resulting surface-heat fluxes for each atmospheric stability and vegetation type combination have to be similar in PSF and LSM(+PCM) simulations, which is why we first ran the simulations with LSM(+PCM) as a boundary condition and then used the resulting surface-heat fluxes in the PSF simulations as described below.

### 2.1.1 Set-up of the Land-Surface Model Simulations

In the LSM simulations (simulation numbers 1–3) over grassland, the vegetation type (VT) short grass (VT=3) as specified in PALM (Gehrke et al. 2020; Maronga et al. 2020) was used. The VT parameter provides predefined values of various vegetation parameters (e.g., leaf-area density, heat-capacity, canopy-specific resistance, aerodynamic roughness length  $z_0$ , etc.) that determine the influence of vegetation on atmospheric processes that are shown in Table 2. For details of the default bulk parameters, we refer to Gehrke et al. (2020).

To ensure the highest comparability of simulations with the LSM to simulations with prescribed surface fluxes, a time-constant net radiation at the surface is necessary. Therefore, we used the PALM built-in clear-sky radiation model with a constant zenith angle and thus obtained a net radiation that remained almost constant over the 4 h of data acquisition. The zenith angles and resulting net radiation at the surface used for each stability and land-cover combination can be found in Table 2. The zenith angles were chosen to give different net radiation at the surface for each atmospheric condition. For net radiation, we used  $250 \text{ W m}^{-2}$  (MU),  $350 \text{ W m}^{-2}$  (SU), and  $450 \text{ W m}^{-2}$  (FC) following De Roo et al. (2018).

The LSM is coupled with a soil model for which we chose a medium-fine soil type (Gehrke et al. 2020). Since Liu and Shao (2013) have noted that a very thin top soil layer can lead to feedback effects as soil temperature and moisture can change due to short-term changes in the atmosphere directly above the soil, we have also adjusted the layer thickness in the soil model. The thickness of each soil layer, as well as initial soil temperature and moisture values, are shown in the Appendix, Table 6. The wilting point of the soil is defined at a soil moisture of  $0.133 \text{ m}^3 \text{ m}^{-3}$  (Gehrke et al. 2020) and the soil moisture in our simulations never fell below this value, therefore water availability for the plants was sufficient in all simulations.

### 2.1.2 Set-up of Land-Surface Model and Plant-Canopy Model Simulations

For the land-cover type forest, the land-surface model was additionally combined with PALM's embedded plant-canopy model (PCM) (Maronga et al. 2015) which explicitly considers the impact of grid-resolved vegetation on the momentum, potential temperature and heat equation (see simulations 4–6). The PCM was used with the horizontally homogeneous prescribed leaf-area density (*LAD*) profile shown in Fig. 2. The PCM follows Shaw and Schumann (1992) and Watanabe (2004), and adds a momentum sink. It was validated against wind-tunnel and lidar observations in Kanani et al. (2014). The PCM furthermore

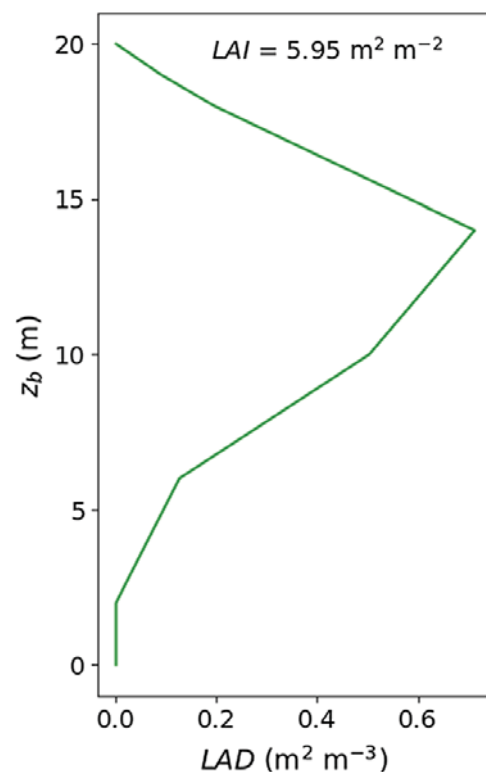
interacts with radiation (absorption, transmission, reflections) and provides volume sources of sensible and latent heat that enter the prognostic equations of potential temperature and mixing ratio, respectively (Krč et al. 2021). The PCM is currently not coupled with the LSM but assumes that water availability is always sufficient for transpiration. The shape of the  $LAD$  profile used in the fine grid (Fig. 2) is based on the plant-area density ( $PAD$ ) profile used in Patton et al. (2016) but has a higher leaf-area index ( $LAI$ ) of  $5.95 \text{ m}^2 \text{ m}^{-2}$ .

Below the canopy, at the bottom boundary, we also used the LSM that provides a small part of the sensible and latent heat fluxes based on the radiation that penetrates the resolved canopy. Here, we used the vegetation type deciduous broadleaf forest ( $VT=7$ ), the characteristic parameters of which are also shown in Table 2. However, the roughness length is determined by the vegetation resolved in the PCM.

### 2.1.3 Set-up of Prescribed Surface-Flux Simulations

To set up PSF simulations comparable to the LSM simulations (simulation numbers 7–9), the sensible and latent surface-heat fluxes ( $H_s$  and  $\lambda E_s$ ) resulting from the grassland LSM simulations were horizontally averaged over the entire domain and temporally averaged canopy top were averaged and used over the four hours of data acquisition and then used as prescribed surface fluxes in the PSF simulations. For PSF simulations comparable to LSM+PCM simulations (simulation numbers 10–12), the fluxes at the as prescribed surface-heat fluxes (see Eqs. 2, 3). The exact approach for calculating the surface fluxes is described in Sect. 2.2. The prescribed  $H_s$  and  $\lambda E_s$  in each PSF simulation are shown in Table 2. The roughness lengths  $z_0$  and  $z_{0h}$  were set according to the vegetation types used in the LSM(+PCM) simulations.

**Fig. 2**  $LAD$  profile of the resolved canopy that is used in the fine grid for LSM+PCM simulations;  $z_b$  denotes the height above the bottom of the domain



## 2.2 Data Processing

30-min surface fluxes were calculated for each simulation and profiles of horizontal wind speed in the  $x$ - and  $y$ -directions ( $u$ ,  $v$ ), the component of vertical wind ( $w$ ), and potential temperature ( $\theta$ ) were compared to estimate if the LSM(+PCM) simulations are comparable to the respective PSF simulations, respectively. In this study, “surface” always refers to the canopy top unless stated otherwise, which means that the surface is at  $z_b = 0$  in PSF and LSM simulations, and at  $z_b = 20$  m in LSM + PCM simulations, where  $z_b$  is the height above the bottom of the domain. Therefore, for the LSM + PCM simulations, the latent and sensible heat fluxes at  $z_b = 20$  m were used as surface fluxes.

The contributions of the 30-min individual flux components to the total energy fluxes originating from the vegetation surface  $H_s$  and  $\lambda E_s$  were calculated for all simulations. The surface-heat fluxes used in the PSF and LSM-only simulations were calculated directly by PALM as horizontal domain averages. For the simulations with PCM, we used the sum of the resolved heat fluxes, i.e. the temporal covariances  $\overline{w'\theta'}$  and  $\overline{w'q'}$ , and the SGS fluxes  $\overline{w'\theta'_{SGS}}$  and  $\overline{w'q'_{SGS}}$  provided by the SGS model at the canopy top, i.e. at  $z_b = 20$  m

$$H_{s,PCM} = \left( \left\langle \overline{w'_{20}\theta'_{20}} \right\rangle + \left\langle \overline{w'_{20}\theta'_{20}_{SGS}} \right\rangle \right) c_p \rho, \quad (2)$$

$$\lambda E_{s,PCM} = \left( \left\langle \overline{w'_{20}q'_{20}} \right\rangle + \left\langle \overline{w'_{20}q'_{20}_{SGS}} \right\rangle \right) \lambda. \quad (3)$$

The overbar denotes temporal averaging over 30 min at each grid point. Furthermore, the covariances were spatially averaged in the  $x$ - and  $y$ -directions which is denoted by the angled brackets. To convert the heat fluxes from kinematic units to dynamic units ( $\text{W m}^{-2}$ ), they were multiplied with the latent heat of vaporization of air ( $c_p$ ) and density ( $\rho$ ) and the latent heat of vaporization ( $\lambda$ ), respectively.

In the surface layer, the total heat flux, i.e. the heat flux originating from the surface, is divided into individual flux components

$$H_s + \lambda E_s = H_t + \lambda E_t + H_d + \lambda E_d + S, \quad (4)$$

where  $H_t$  and  $\lambda E_t$  are the temporal covariance-heat fluxes,  $H_d$  and  $\lambda E_d$  are the dispersive heat fluxes, and  $S$  is the energy stored in the underlying air mass.

We calculated  $H_t$ ,  $\lambda E_t$ ,  $H_d$ , and  $\lambda E_d$  for each vertical grid level.  $H_t$  and  $\lambda E_t$  were calculated similarly to the surface fluxes in the PCM simulations (see Eqs. 2, 3)

$$H_t = \left( \left\langle \overline{w'\theta'} \right\rangle + \left\langle \overline{w'\theta'_{SGS}} \right\rangle \right) c_p, \quad (5)$$

$$\lambda E_t = \left( \left\langle \overline{w'q'} \right\rangle + \left\langle \overline{w'q'_{SGS}} \right\rangle \right) \lambda. \quad (6)$$

The resolved 30-min temporal covariances  $\overline{w'\theta'}$  and  $\overline{w'q'}$  in Eqs. 2, 3 and 5, 6 were calculated from the temporal deviations from half-hourly averages of  $w$ ,  $\theta$ , and  $q$ , respectively:

$$\overline{w'\theta'_{x,y}} = \frac{1}{nt} \sum_0^{nt} (w_{t,x,y} - \overline{w_{x,y}})(\theta_{t,x,y} - \overline{\theta_{x,y}}), \quad (7)$$

where  $nt$  is the number of timesteps in each 30-min averaging interval. To calculate  $\overline{w'q'}$ ,  $\theta$  was replaced by  $q$  in Eq. 7. Those 30-min covariances were then spatially averaged over each  $x$ - and  $y$ -grid point with

$$\langle \overline{w'\theta'} \rangle = \frac{1}{nx \times ny} \sum_0^{nx} \sum_0^{ny} \overline{w'\theta'_{x,y}}, \quad (8)$$

where  $nx$  and  $ny$  are the number of grid points in  $x$  and  $y$  directions. Again,  $\theta$  was replaced by  $q$  to calculate  $\langle \overline{w'q'} \rangle$  in Eq. 8. Similarly, the SGS fluxes calculated by PALM were spatially averaged over the entire domain, which is denoted by the angular brackets.

The dispersive fluxes were calculated at each grid level from the spatial covariance, where the local deviations of 30-min averages of vertical wind velocity  $\bar{w}$ , potential temperature  $\bar{\theta}$ , and specific humidity  $\bar{q}$ , marked by the star, from the spatial average were considered

$$H_d = \langle \bar{w}^* \bar{\theta}^* \rangle c_p, \quad (9)$$

$$\lambda E_d = \langle \bar{w}^* \bar{q}^* \rangle \lambda, \quad (10)$$

with

$$\langle \bar{w}^* \bar{\theta}^* \rangle = \frac{1}{nx \times ny} \sum_0^x \sum_0^y (\bar{w}_{x,y} - \langle \bar{w} \rangle) (\bar{\theta}_{x,y} - \langle \bar{\theta} \rangle). \quad (11)$$

Again,  $\langle \bar{w}^* \bar{\theta}^* \rangle$  was calculated by replacing  $\theta$  by  $q$  in Eq. 11. The resulting surface-heat fluxes, temporal covariance-heat fluxes and dispersive heat fluxes were temporally averaged over 30 min and horizontally averaged over the entire domain. Those values were then averaged over the entire data-capture period, i.e. 4 h.

We investigated the dispersive heat fluxes ( $F_d$ ), as these are typically considered as the energy-balance residual (e.g., Steinfeld et al. 2007). Because the absolute surface-heat fluxes of the compared simulations differ slightly, and because some energy-balance terms like ground heat flux and energy stored within the canopy cannot be considered in the PSF simulations, the relative contributions of  $H_d$  and  $\lambda E_d$  to the total surface heat flux  $F_s = H_s + \lambda E_s$  at the canopy top were investigated. The resulting  $F_d$  values of the LSM(+PCM) and corresponding PSF simulations were then compared at each grid level up to 100 m above the vegetation top.

We also analyzed  $xy$  cross-sections of 30-min averaged surface temperature ( $\bar{\theta}_s$ ) and vertical wind velocity ( $\bar{w}$ ) at different heights above the surface to see if the differences in  $F_d$  are associated with the formation of mesoscale structures in the atmosphere and if these spatial structures are linked to surface properties. Furthermore, the Bowen ratio was evaluated to see whether the proportion of sensible and latent heat fluxes in the dispersive heat fluxes not captured by single-tower EC measurements in the field is the same as in the temporal covariance-heat fluxes.

### 3 Results

The focus in the data evaluation is on  $F_d$  resulting from different lower boundary conditions since the main objective is how different surface-flux boundary conditions affect the surface energy balance and the occurrence of dispersive fluxes. However, before we

analyze the impact of lower boundary conditions on  $F_d$ , we evaluate the comparability of the LSM(+PCM) simulations with the PSF simulations by comparing general boundary layer characteristics. Furthermore,  $xy$  cross-sections are presented to demonstrate that secondary circulations develop depending on the height and the lower boundary conditions.

### 3.1 Comparability of Simulations with Different Lower Boundary Conditions

In the simulations with prescribed surface-heat fluxes, the surface-heat fluxes are constant over the entire simulation period. To enhance comparability, the surface-heat fluxes in LSM(+PCM) simulations should also be fairly constant in time. We therefore used constant sun angles, which lead to an almost constant net radiation. Figure 3 shows that the surface-heat fluxes are quasi-steady-state in the LSM simulations over grassland. Only when additionally using the PCM over forest does the temporal covariance-heat fluxes at the vegetation top fluctuate slightly, being almost constant during the first 2.5 h of data assimilation and then decreasing slightly. Overall, the surface-heat fluxes of LSM(+PCM) simulations are constant within  $\pm 12.2\%$  and only deviate from the surface fluxes of the corresponding PSF simulations by 6.2% at maximum.

Figure 4 shows profiles of horizontally averaged turbulence kinetic energy ( $\langle TKE \rangle$ ),  $\langle \bar{\theta} \rangle$  and  $\langle \bar{q} \rangle$ . Here, the results of an LSM(+PCM) and the respective PSF simulation are compared in each sub-panel. The profiles of  $\langle TKE \rangle$ ,  $\langle \bar{\theta} \rangle$  and  $\langle \bar{q} \rangle$  are almost identical in the LSM(+PCM) and respective PSF simulations.

### 3.2 Development of Turbulent Organized Structures for Different Lower Boundary Conditions

Figures 5, 6 and 7 show  $xy$  cross-sections averaged over the fifth 30-min interval of the data assimilation period for the three different atmospheric stabilities over forest with PSF (a–c) and LSM+PCM (d–f) as lower boundary conditions for three different heights above the vegetation top denoted by  $z_v$ . Panels a, d in Figs. 5, 6 and 7 show the deviation from the spatially averaged temperature at the vegetation top  $\langle \bar{\theta}_s \rangle$ . In the MU case (Fig. 5), a striped pattern occurs at  $z_v = 0$  both with PSF (Fig. 5a) and with LSM+PCM (Fig. 5d), but it is much more pronounced with LSM+PCM, which is confirmed by the higher spatial standard deviation in Table 3. In the SU case (Fig. 6), cold and warm areas also appear in the surface temperature, but here, the stripes are more fractured. Again, the cold and

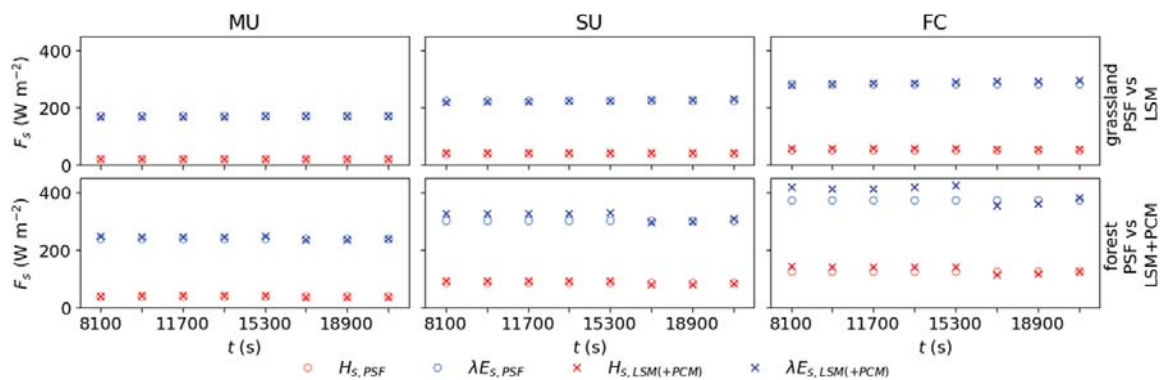


**Fig. 3** Time series of 30-min sensible (red) and latent (blue) surface-heat fluxes at the canopy top for LSM(+PCM) simulations (cross) and corresponding PSF simulations (dot)

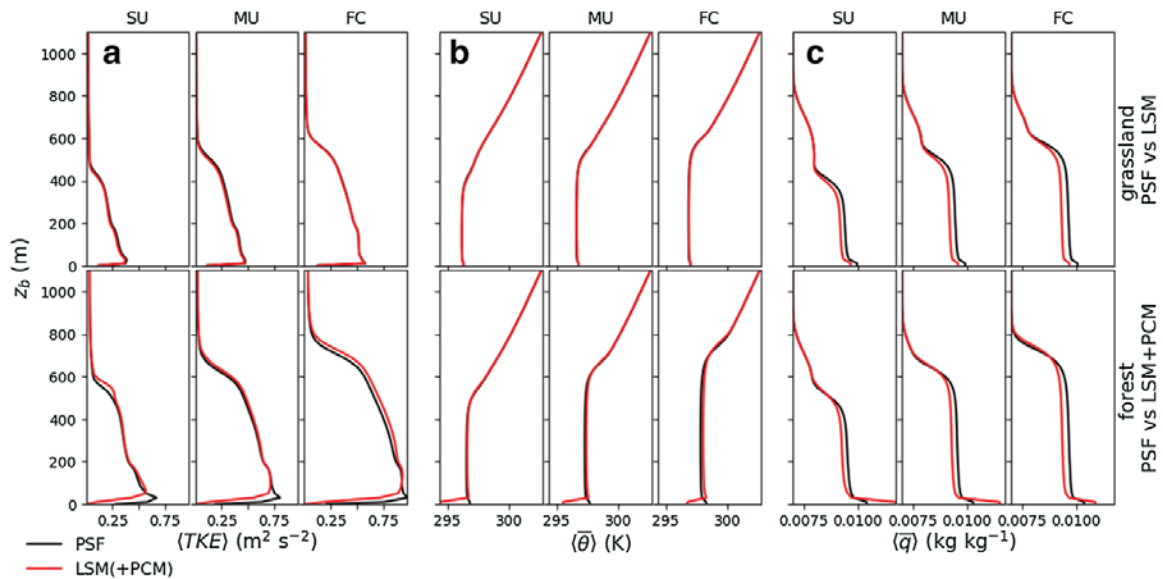


**Fig. 4** Profiles of horizontally-averaged TKE (**a**), potential temperature (**b**), and water mixing ratio (**c**) for all atmospheric stability and lower boundary condition combinations (see Table 1) temporally averaged over the entire data assimilation period. The results of the PSF simulations are displayed as a black line, while the results of the corresponding LSM(+PCM) simulations are displayed as red lines. Here, we show the output of the parent domain to cover a larger vertical extent

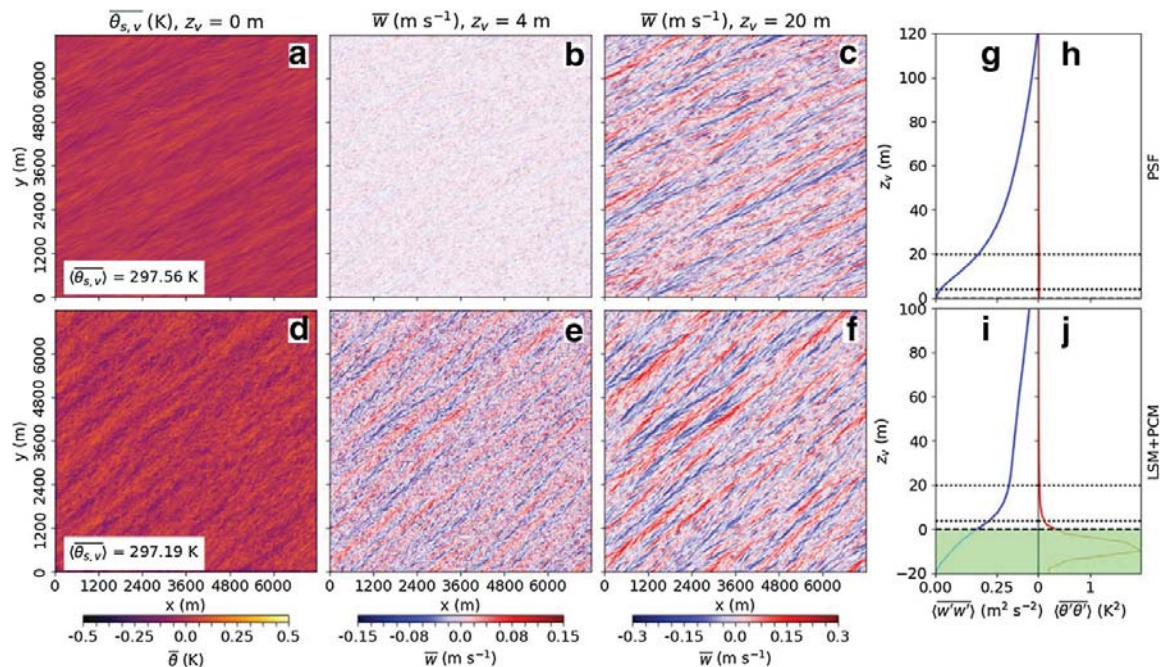


**Fig. 5**  $xy$  cross-sections and profiles for MU PSF and LSM+PCM simulations averaged over the fifth 30-min interval of data assimilation. Panels **a–f** show  $xy$  cross-sections of 30-min averaged potential temperature at the surface or at the canopy top, respectively, **a, d** and vertical wind velocity at 4 m **b, e**, and 20 m **c, f** above the canopy top over forest with PSF **a–c** and LSM+PCM **d–f** as lower boundary conditions. Panels **g–j** show 30-min and horizontally-averaged profiles of  $\overline{w'w'}$  (**g, i**) and  $\overline{\theta'\theta'}$  (**h, j**) over the lower boundary of the domain. The dashed line represents the canopy top ( $z_v = 0\text{m}$ ) and the dotted lines show the levels of the  $xy$  cross-sections of vertical wind at  $z_v = 4\text{m}$  and  $z_v = 20\text{m}$ . In panels **h** and **j**, the height of the resolved canopy in the LSM+PCM simulation is shown by the green area

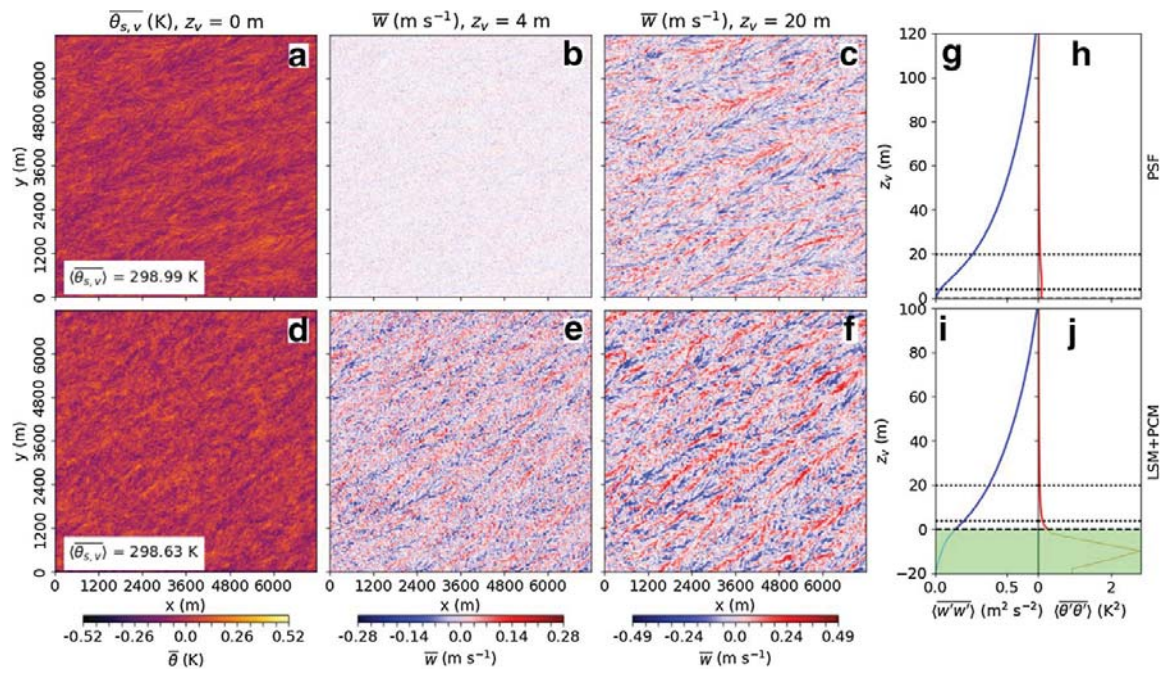


**Fig. 6**  $xy$  cross-sections and profiles for SU PSF and LSM+PCM simulations averaged over the fifth 30-min interval of data assimilation. For a detailed description of each panel see Fig. 5

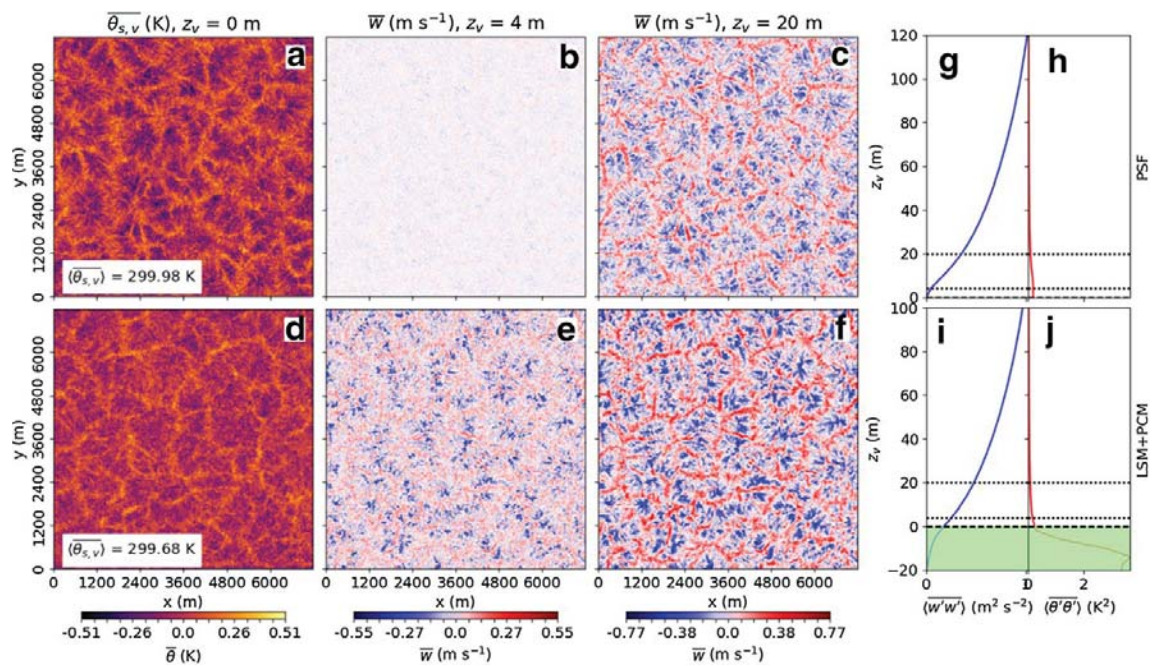


**Fig. 7**  $xy$  cross-sections and profiles for FC PSF and LSM+PCM simulations averaged over the fifth 30-min interval of data assimilation. For a detailed description of each panel see Fig. 5

warm patches are more pronounced with LSM+PCM. In the FC case (Fig. 7), the warm and cold areas appear in a cell-like structure and are, unlike in the first two cases, considerably more pronounced with PSF at the surface (Fig. 7a) than with LSM+PCM at  $z_v = 0$  (Fig. 7d). This is also reflected in the standard deviations of 0.119 K (PSF) and 0.096 K (LSM+PCM) shown in Table 3.

**Table 3** Standard deviations ( $\sigma_{xy}$ ) calculated in a spatial framework across  $xy$  cross-sections as the square root of the variances of 30-min averaged surface temperature  $\overline{\theta_s}$  and vertical wind speed  $\overline{w_s}$ , at 4 and 20 m above the surface in three different atmospheric stabilities (MU, SU, FC) over forest with two different lower boundary conditions (PSF, LSM+PCM)

	MU		SU		FC	
	F PSF	LSM+PCM	F PSF	LSM+PCM	F PSF	LSM+PCM
$\sigma_{xy}(\overline{\theta_s})$ (K)	0.032	0.062	0.064	0.073	0.119	0.096
$\sigma_{xy}(\overline{w_{4m}})$ (m s <sup>-1</sup> )	0.010	0.031	0.014	0.052	0.019	0.082
$\sigma_{xy}(\overline{w_{20m}})$ (m s <sup>-1</sup> )	0.053	0.057	0.077	0.098	0.132	0.169

The structures in the vertical velocity (Figs. 5, 6, 7b–c, e–f) under different atmospheric conditions match the patterns in the surface temperature, respectively. Under all atmospheric conditions, updrafts and downdrafts in the vertical wind at  $z_v = 4$  m are significantly weaker in PSF boundary conditions (Figs. 5, 6, 7b) than in LSM+PCM boundary conditions (Figs. 5, 6, 7e) which is also reflected in the spatial standard deviations shown in Table 3. With greater distance from the surface, the patterns are still less distinct in the PSF simulations (Figs. 5, 6, 7c), but the difference to the LSM+PCM simulations (Figs. 5, 6, 7f) is reduced as shown, for example, at 20 m above the surface.

Panels g–j of Fig. 5, 6 and 7 additionally display profiles of  $\overline{\langle w'w' \rangle}$  and  $\overline{\langle \theta'\theta' \rangle}$  for the same 30-min interval. The profiles show that  $\overline{\langle w'w' \rangle}$  at the vegetation top is under all atmospheric conditions significantly larger in the LSM+PCM simulations (Figs. 5, 6, 7g) than in the PSF simulations (Figs. 5, 6, 7i) due to the resolved vegetation. However, the difference between PSF and LSM+PCM simulations becomes smaller with increasing height.

Due to the resolved vegetation, small differences between PSF (Figs. 5, 6, 7h) and LSM+PCM (Figs. 5, 6, 7j) simulations also arise for  $\overline{\langle \theta'\theta' \rangle}$ , especially directly above the vegetation top. These differences are, however, pronounced to varying degrees under different atmospheric conditions. While in the MU case,  $\overline{\langle \theta'\theta' \rangle}$  is larger for LSM+PCM (Fig. 5h) than for PSF (Fig. 5j), the profiles look almost the same above the canopy top with both lower boundary conditions in the FC case (Fig. 7).

### 3.3 Dispersive Fluxes for Different Lower Boundary Conditions

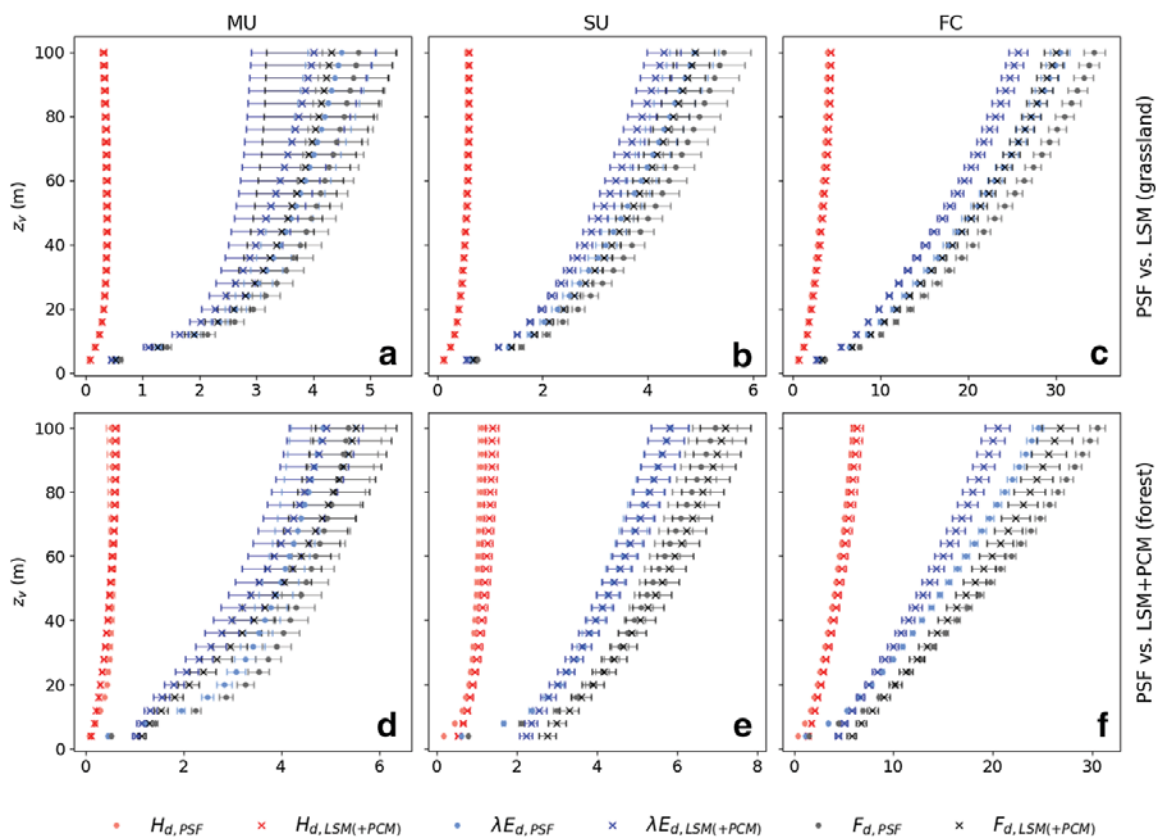
Table 4 shows that the Bowen ratios of temporal covariance ( $Bo_t$ ) and dispersive ( $Bo_d$ ) heat fluxes at 20 m above are almost equal and that they match the Bowen ratio of surface-heat fluxes ( $Bo_s$ ). It furthermore shows that  $Bo$  values for LSM(+PCM) and comparable PSF simulations agree quite well.

Figure 8 shows comparisons of latent and sensible, as well as total dispersive fluxes ( $F_d$ ) that are normalized with  $F_s$  between the simulations with land surface model ( $F_{d,LSM}$ ) (Fig. 8a–c) or land-surface and plant-canopy model ( $F_{d,LSM+PCM}$ ) (Fig. 8d–f) and the respective simulations with prescribed surface fluxes ( $F_{d,PSF}$ ) for each stability and VT combination.

For both VTs,  $F_d$  increases with atmospheric instability and with distance from the vegetation top. The Bowen ratios of  $F_d$  ( $Bo_d$ ) nearly equal the Bowen ratio of  $F_t$  ( $Bo_t$ ) in all simulations (see Table 4);  $F_d$  is dominated by  $\lambda E_d$  in all simulations (Fig. 8). In the

**Table 4** Bowen ratios of surface-heat fluxes ( $Bo_s$ ), as well as temporal covariance-heat fluxes ( $Bo_t$ ), and dispersive heat fluxes ( $Bo_d$ ) at 20 m above the vegetation top for all stability, vegetation type (VT) and lower boundary condition (LBC) combinations. The errors are calculated as the temporal standard deviation of the 8 30-min intervals during the data assimilation period

Stability	VT	LBC	Simulation number	$Bo_s$	$Bo$ (20 m)	$Bo_t$ (20 m)	$Bo_d$ (20 m)
MU	G	PSF	7	$0.13 \pm 0.00$	$0.12 \pm 0.0$	$0.12 \pm 0.00$	$0.11 \pm 0.00$
		LSM	1	$0.13 \pm 0.00$	$0.13 \pm 0.0$	$0.13 \pm 0.00$	$0.14 \pm 0.00$
	F	PSF	10	$0.16 \pm 0.00$	$0.16 \pm 0.0$	$0.16 \pm 0.00$	$0.15 \pm 0.00$
		LSM+PCM	4	$0.16 \pm 0.01$	$0.16 \pm 0.01$	$0.16 \pm 0.01$	$0.16 \pm 0.01$
SU	G	PSF	8	$0.19 \pm 0.00$	$0.18 \pm 0.0$	$0.18 \pm 0.00$	$0.17 \pm 0.00$
		LSM	2	$0.19 \pm 0.00$	$0.19 \pm 0.0$	$0.19 \pm 0.00$	$0.21 \pm 0.00$
	F	PSF	11	$0.28 \pm 0.00$	$0.27 \pm 0.0$	$0.27 \pm 0.00$	$0.26 \pm 0.00$
		LSM+PCM	5	$0.28 \pm 0.01$	$0.28 \pm 0.01$	$0.28 \pm 0.01$	$0.3 \pm 0.01$
FC	G	PSF	9	$0.19 \pm 0.00$	$0.18 \pm 0.0$	$0.19 \pm 0.00$	$0.17 \pm 0.00$
		LSM	3	$0.20 \pm 0.01$	$0.2 \pm 0.01$	$0.2 \pm 0.01$	$0.21 \pm 0.01$
	F	PSF	12	$0.33 \pm 0.00$	$0.32 \pm 0.0$	$0.32 \pm 0.00$	$0.3 \pm 0.00$
		LSM+PCM	6	$0.33 \pm 0.01$	$0.34 \pm 0.01$	$0.34 \pm 0.01$	$0.35 \pm 0.01$



**Fig. 8** Comparisons of dispersive fluxes for  $H_d$ ,  $\lambda E_d$  and the sum of both  $F_d$  resulting from different lower boundary conditions as a function of height above the vegetation top  $z_v$ . The dispersive fluxes are normalized by the total surface flux ( $F_s$ ) at the canopy top and averaged over the entire data assimilation period and the error bars show the standard deviation of the 30-min averages. Panels a–c show the comparison between LSM and PSF over grassland for different atmospheric stabilities. Panels d–f show comparisons for different atmospheric stabilities over forest between LSM+PCM and PSF. The total dispersive heat flux is displayed in black, and the shares of sensible and latent dispersive heat fluxes are displayed in red and blue, respectively

grassland case,  $F_{d,PSF}$  is slightly smaller than  $F_{d,LSM}$  under all atmospheric conditions as indicated by Fig. 8a, b.

Figure 8d–f show the comparison between  $F_{d,PSF}$  and  $F_{d,LSM+PCM}$  over forest and demonstrate that the dispersive fluxes above the resolved vegetation behave differently than with PSF. In contrast to  $F_{d,PSF}$ ,  $F_{d,LSM+PCM}$  does not approach zero close to the canopy top but remains significantly larger.  $F_{d,PSF}$  accounts for  $0.52 \pm 0.01\%$  ( $1.44 \pm 0.0 \text{ W m}^{-2}$ , MU case),  $0.79 \pm 0.02\%$  ( $3.05 \pm 0.0 \text{ W m}^{-2}$ , SU case), and  $1.46 \pm 0.01\%$  ( $7.27 \pm 0.0 \text{ W m}^{-2}$ , FC case) of  $F_{s,PSF}$  4 m above the canopy top, whereas  $F_{d,LSM+PCM}$  contributes  $1.14 \pm 0.09\%$  ( $3.23 \pm 0.01 \text{ W m}^{-2}$ , MU case),  $2.76 \pm 0.21\%$  ( $11.23 \pm 0.04 \text{ W m}^{-2}$ , SU case), and  $5.78 \pm 0.45\%$  ( $30.7 \pm 0.17 \text{ W m}^{-2}$ , FC case) to  $F_{s,LSM+PCM}$ , respectively. In the FC case, this leads to an absolute difference of  $23.42 \text{ W m}^{-2}$ , though it must also be noted here that  $F_d$  slightly differs between PSF and LSM + PCM simulations. Therefore  $F_{d,LSM+PCM}$  is significantly larger near the surface than  $F_{d,PSF}$  under all atmospheric conditions. However, with increasing distance from the surface,  $F_{d,LSM+PCM}$  behaves very differently under changing atmospheric conditions. While  $F_{d,LSM+PCM}$  under MU conditions is smaller than  $F_{d,PSF}$  already 8 m above the vegetation top, it is never smaller than  $F_{d,PSF}$  under SU conditions. Under FC conditions,  $F_{d,LSM+PCM}$  becomes smaller than  $F_{d,PSF}$  20 m above the vegetation top.

Figure 9 shows the differences between  $F_{d,PSF}$  and  $F_{d,LSM}$  or  $F_{d,LSM+PCM}$  in more detail. It demonstrates that the differences between  $F_{d,PSF}$  and  $F_{d,LSM}$  increase linearly with height over grassland under all atmospheric conditions. The differences between  $F_{d,PSF}$  and  $F_{d,LSM+PCM}$  over forest are not linear due to the different behaviour of  $F_{d,LSM+PCM}$ .

In the MU case, this leads to  $F_{d,LSM+PCM}$  being smaller than  $F_{d,PSF}$  already at 8 m above the canopy. However, since  $F_{d,LSM+PCM}$  increases more strongly again from about 20 m above the canopy,  $F_{d,LSM+PCM}$  and  $F_{d,PSF}$  are equal again, at about 80 m above the vegetation top (Fig. 9a). In the SU case, the difference between  $F_{d,LSM+PCM}$  and  $F_{d,PSF}$  initially becomes smaller with increasing height, but always remains slightly larger and the difference increases, again, from about 30 m above the surface as shown in Fig. 9b. In the FC case, the difference between  $F_{d,LSM+PCM}$  and  $F_{d,PSF}$  close to the vegetation top is largest (Fig. 9c) with  $4.32 \pm 0.47\%$  ( $23.43 \pm 0.17 \text{ W m}^{-2}$ ). Here, again,  $F_{d,LSM+PCM}$  approaches  $F_{d,PSF}$  with increasing height but here, it becomes smaller than  $F_{d,PSF}$  from 24 m above the canopy.

### 3.4 Comparison of Vegetation Types in Land-Surface Model and Plant-Canopy Model Simulations and Surface-Heat Fluxes from the Land-Surface Model in General

Table 5 shows the contributions of different water vapour sources to the latent surface-heat flux directly at the bottom of the domain ( $\lambda E_{s,b}$ ) where the LSM is embedded. In the grassland simulations, the entire  $\lambda E_{s,b}$  originates from the transpiration of plants ( $\lambda E_{s,veg}$ ). Here, no water evaporates directly from the soil ( $\lambda E_{s,soil}$ ) as the plant coverage is set to 100%.

For VT 7 (broadleaf forest) that is used for the LSM + PCM simulations, the share of  $\lambda E_{s,soil}$  in  $\lambda E_{s,b}$  amounts to less than 10%. Furthermore, the contributions from liquid water on plants ( $\lambda E_{s,liq}$ ) are negative here, which is defined as the condensation of water vapour. Overall,  $\lambda E_{s,b}$  in the simulations with PCM are very small compared to the total latent heat flux at the canopy top, meaning that the main portion of the latent heat flux originates from the crown space of the resolved plants.

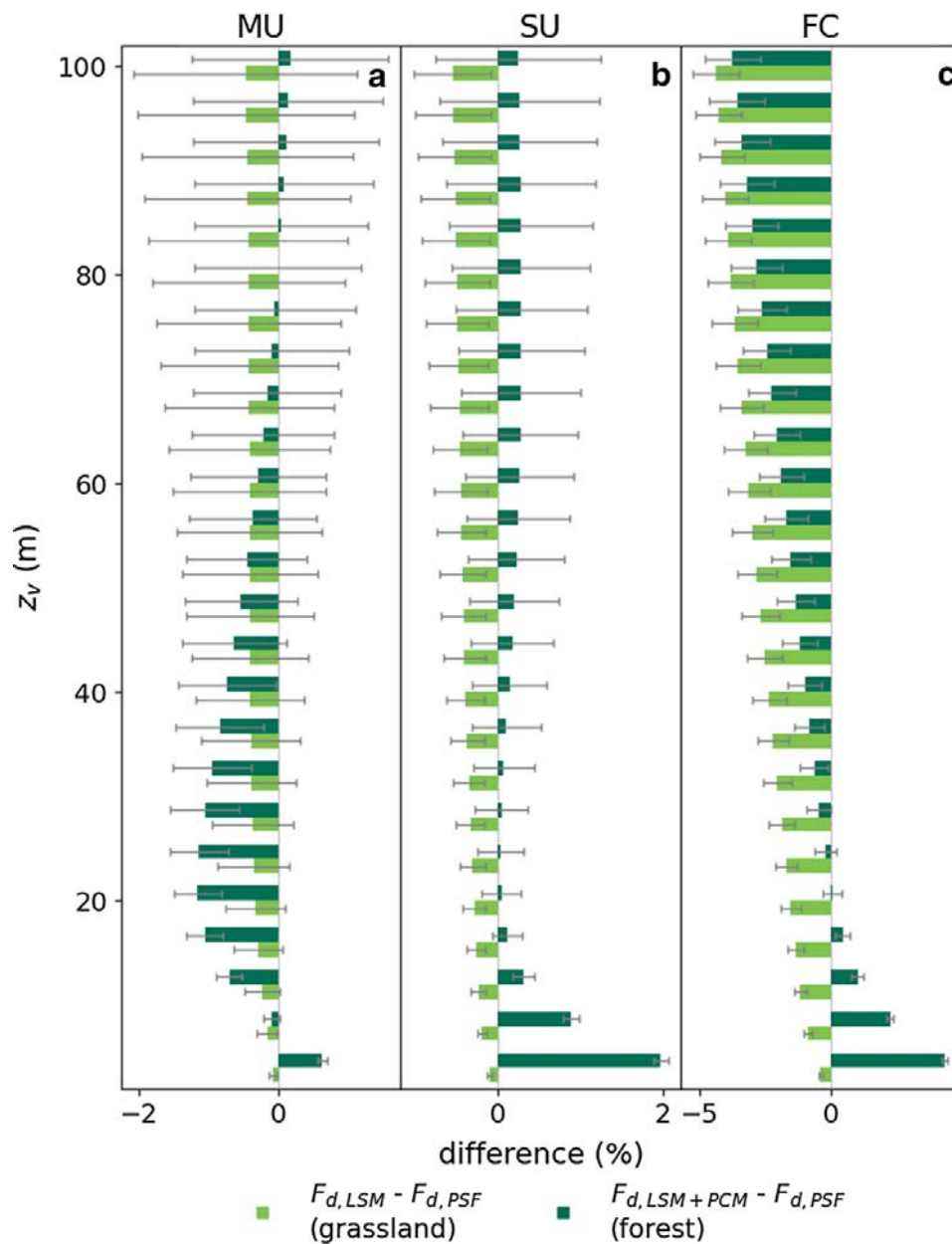


**Fig. 9** Profiles of differences between 30-min averaged dispersive fluxes in LSM(+PCM) simulations and respective PSF simulations for different atmospheric stabilities. The y-axis shows the height above the vegetation top  $z_v$ .

In comparison to  $\lambda E_{s,b}$  at the bottom of the domain shown in Table 5, the latent heat fluxes at the canopy top ( $\lambda E_{s,v}$ ) are significantly larger with  $243.13 \pm 4.46 \text{ W m}^{-2}$  (MU),  $318.50 \pm 12.81 \text{ W m}^{-2}$  (SU), and  $398.74 \pm 26.56 \text{ W m}^{-2}$  (FC). In the LSM+PCM simulations, the sensible surface-heat flux at the bottom of the domain ( $H_{s,b}$ ) shown in Table 5 are negative, indicating that the canopy heats up more than the shaded ground, causing warm air masses to sink towards the ground. At the canopy top, however, the sensible heat fluxes ( $H_{s,v}$ ) are similar to the prescribed sensible heat fluxes shown in Table 2 with  $39.63 \pm 1.89 \text{ W m}^{-2}$  (MU),  $88.20 \pm 5.39 \text{ W m}^{-2}$  (SU), and  $132.37 \pm 11.56 \text{ W m}^{-2}$  (FC).

**Table 5** Absolute sensible and latent surface-heat fluxes at the bottom of the domain ( $H_{s,b}$ ,  $\lambda E_{s,b}$ ) and contributions of evaporation or condensation of liquid water on plants ( $\lambda E_{s,liq}$ ), bare soil evaporation or precipitation ( $\lambda E_{s,soil}$ ), and transpiration of plants ( $\lambda E_{s,veg}$ ) to  $\lambda E_{s,b}$  for simulations with LSM as lower boundary condition (LBC)

Stability	VT	LBC	$H_{s,b}$ ( $\text{W m}^{-2}$ )	$\lambda E_{s,b}$ ( $\text{W m}^{-2}$ )	$\lambda E_{s,liq}$ (%)	$\lambda E_{s,soil}$ (%)	$\lambda E_{s,veg}$ (%)
MU	G	LSM	$22.80 \pm 0.06$	$172.12 \pm 1.36$	$0.00 \pm 0.00$	$0.00 \pm 0.00$	$100.00 \pm 0.79$
	F	LSM+PCM	$-9.99 \pm 0.62$	$3.82 \pm 0.49$	$-2.02 \pm 1.10$	$8.70 \pm 1.09$	$93.33 \pm 10.78$
SU	G	LSM	$43.75 \pm 0.33$	$225.47 \pm 3.21$	$0.00 \pm 0.00$	$0.00 \pm 0.00$	$100.00 \pm 1.42$
	F	LSM+PCM	$-10.94 \pm 0.45$	$4.84 \pm 0.91$	$-4.13 \pm 2.44$	$8.02 \pm 1.40$	$96.10 \pm 15.06$
FC	G	LSM	$58.51 \pm 0.70$	$288.53 \pm 4.57$	$0.00 \pm 0.00$	$0.00 \pm 0.00$	$100.00 \pm 1.58$
	F	LSM+PCM	$-14.79 \pm 2.28$	$6.74 \pm 1.34$	$-4.13 \pm 3.35$	$9.26 \pm 1.89$	$94.87 \pm 14.88$

## 4 Discussion

The investigation of  $F_d$  resulting from different lower boundary conditions showed that the differences between LSM and PSF close to the vegetation top are very small for simulations over grassland. The PSF lower boundary condition results in slightly larger  $F_d$  with increasing distance from the canopy top than when using the LSM.

The comparison between the LSM+PCM and the PSF over the forest shows varying results depending on which height is considered. Close to the surface, the LSM+PCM boundary condition yields significantly larger  $F_d$  values, and this difference increases with increasing instability. This agrees well with the developing TOS, i.e. roll-like structures in MU and SU cases, and cell-like structures in the FC case, being much more pronounced near the vegetation top in LSM+PCM simulations than in PSF and LSM-only simulations. This indicates that the magnitude of dispersive fluxes is correlated with the strength of TOS when averaged over 30 min.

One reason for the undeveloped structures close to the surface despite high heterogeneity in surface temperature in PSF simulations might be the fact that structures at the lowest grid levels are only partially resolved in LES and significant parts of the vertical transport are carried out by the SGS model (Bou-Zeid et al. 2005). When using the PCM, the canopy top is at the fifth grid level, so structures directly above the trees can be resolved well. Other studies also found that resolved canopies enhance the turbulence, e.g. by causing ejection sweep events (Finnigan et al. 2009), which explains why the dispersive fluxes behave so differently with the PCM than with PSF or the LSM only. However, in our study, resolved vegetation affects dispersive fluxes only directly above the vegetation top and no consistent positive effect on dispersive fluxes is observed as distance increases. Patton et al. (2016) observed that the structures form already within the trunk layer, vanish at the treetop, and are more pronounced again above the forest. We do not observe this effect in our simulations. Instead, the structures in our simulations become constantly more pronounced with increasing height. This discrepancy might be explained by the different canopy structure of Patton et al. (2016), where the crown layer has a lower plant area density.

To investigate how the height-dependent differences in dispersive heat fluxes over the forest in Fig. 9 can be explained and whether the different behaviour of the variance profiles in Figs. 5, 6 and 7, especially for  $w$ , provided an explanation, we investigated

flux–variance similarity functions for  $u$ ,  $w$ , and  $\theta$  variances. The similarity function for  $u$  ( $\phi_u$ ) was calculated based on Panofsky et al. (1977)

$$\frac{\langle \overline{u'u'} \rangle}{u_*} = \phi_u \left( \frac{z_b}{L} \right). \tag{12}$$

The variance similarity functions for  $w$  ( $\phi_w$ ) and  $\theta$  ( $\phi_\theta$ ) were calculated similarly by replacing  $\overline{u'u'}$  with  $\overline{w'w'}$  and  $\overline{\theta'\theta'}$ , respectively, and  $u_*$  with the temperature scale  $T_*$ . The differences in  $\phi_\theta$  between PSF and LSM+PCM simulations were very small and are hence not shown. However, we found significant differences between PSF and LSM+PCM simulations in the  $\phi_u$  and  $\phi_w$  profiles that are shown in Fig. 10. We furthermore compared the profiles obtained from the simulations to theoretical variance similarity functions based on (Foken et al. 2004) using

$$\frac{\langle \overline{u'u'} \rangle}{u_*} = c_1 \phi_u \left( \frac{z_b}{L} \right)^{c_2}, \tag{13}$$

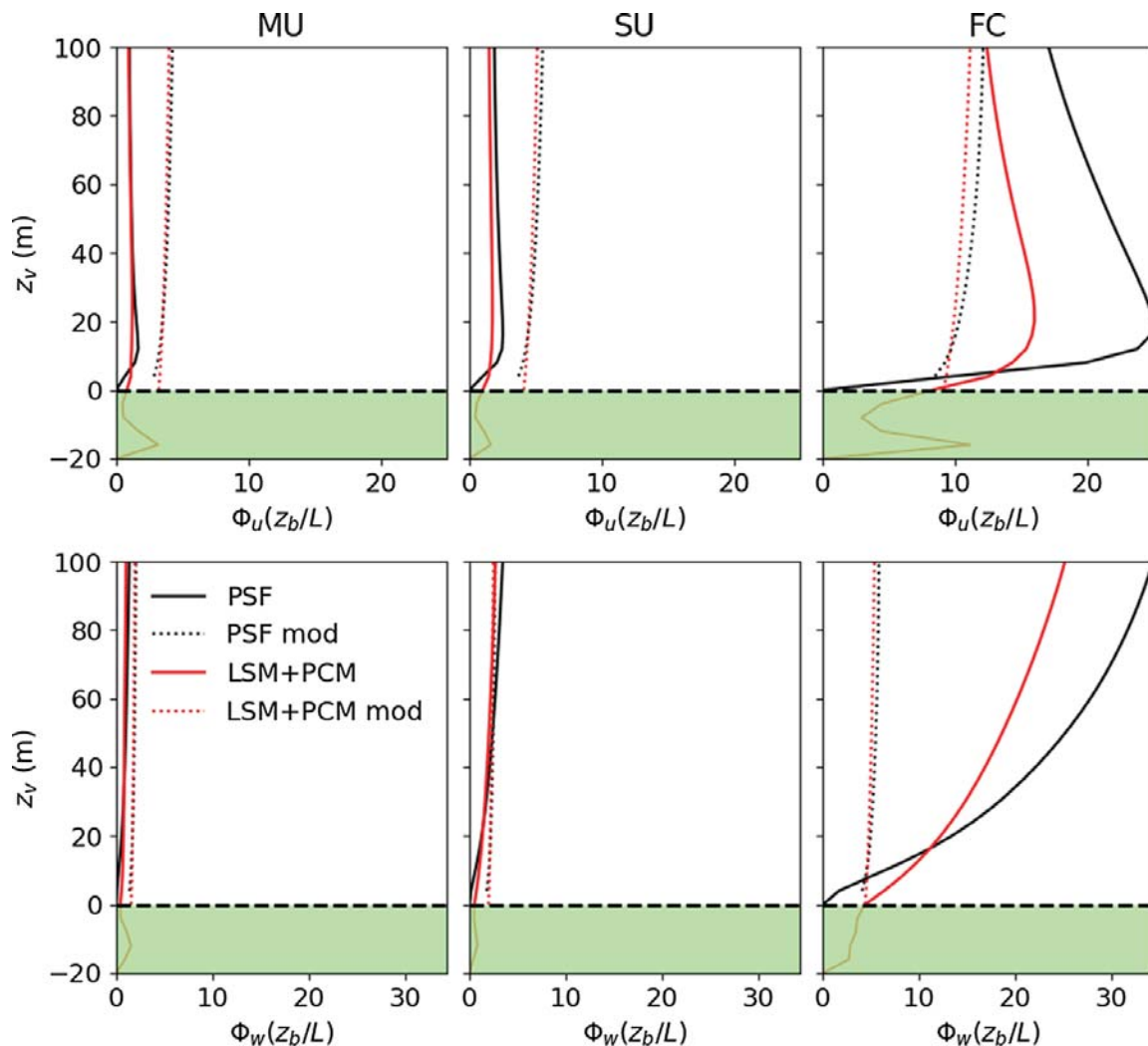


**Fig. 10** Profiles of flux–variance similarity functions for  $\overline{u'u'}$  ( $\phi_u$ , top) and  $\overline{w'w'}$  ( $\phi_w$ , bottom) for PSF simulations (black) and LSM+PCM simulations (red) over forest. The solid lines show the profiles of the flux–variance similarity functions obtained in the simulations and the dotted lines show theoretical flux–variance similarity functions as shown in Eqs. 13, 14

with

$$\begin{aligned} c_1 = 2.7, c_2 = 0 & \quad \text{if } 0 > z_b/L > -0.032 \\ c_1 = 4.15, c_2 = 1/8 & \quad \text{if } -0.032 > z_b/L \end{aligned}$$

and

$$\frac{\overline{w'w'}}{u_*} = c_1 \phi_w \left( \frac{z_b}{L} \right)^{c_2}, \quad (14)$$

with

$$\begin{aligned} c_1 = 1.3, c_2 = 0 & \quad \text{if } 0 > z_b/L > -0.032 \\ c_1 = 2.0, c_2 = 1/8 & \quad \text{if } -0.032 > z_b/L \end{aligned}$$

Figure 10 shows a clear dependence of the  $\phi_u$  and  $\phi_w$  profiles on stability, as does the proportion of dispersive heat fluxes in the total surface-heat fluxes in Fig. 8. For all atmospheric stabilities,  $\phi_u$  and  $\phi_w$  are larger in the LSM+PCM simulations than in the PSF simulations directly above the canopy top. This is because the profiles in the PSF simulations are forced to zero at the canopy top. Within the canopy,  $\phi_u$  and  $\phi_w$  are highly variable and depend on the vegetation and canopy structure at each site (Rannik et al. 2003) and we do not expect the model to provide realistic values in this range. However, a clear effect of the resolved vegetation is that  $\phi_u$  and  $\phi_w$  are not forced to zero at the vegetation top, which explains why the resulting dispersive heat fluxes near the canopy top are larger in the LSM+PCM simulations than in the PSF simulations (see Fig. 9). The fact that  $\phi_w$  becomes larger in the PSF simulations than in the PCM+LSM simulations from a height of about 20 m above the canopy top also explains the negative difference further away from the canopy top in Fig. 9. The bulbous shape of  $\phi_u$ , and  $\phi_w$  increasing with altitude suggest that secondary circulations are forming that provide greater variance in the vertical wind at higher altitudes and greater variance in the horizontal wind at lower altitudes. Both effects are very pronounced in the FC case, which causes the profiles derived from the simulations to deviate strongly from the profiles calculated using the theoretical functions, which only include the purely turbulent fluxes. This indicates more intensive secondary circulations for the FC case, which is why the dispersive heat fluxes are also larger here than for the less unstable cases.

Whether the use of PSF or LSM(+PCM) as lower boundary condition yields larger dispersive heat fluxes, depends on the land cover type, the measurement height and atmospheric stability. For more realistic simulations over heterogeneous surfaces of energy-balance closure field experiments, it should therefore be considered which type of vegetation is predominant. Moreover, the PCM can be used only for those areas where the vegetation is tall enough to be resolved by the grid. In most cases, depending on the grid spacing, only a forest can be resolved using the PCM and the grassland would be simulated by using the LSM or the PSF method. Assuming a typical EC set-up is roughly mounted 4 m above the canopy for grasslands and 12 m above the canopy for forests, the use of the LSM instead of PSF as the lower boundary condition for grasslands would decrease the contribution of  $F_d$  to  $F_s$  by only  $-0.08 \pm 0.06\%$  ( $-0.16 \pm 0.0 \text{ W m}^{-2}$ ) for the MU case,  $-0.09 \pm 0.03$  ( $-0.24 \pm 0.0 \text{ W m}^{-2}$ ) for the SU case, and  $-0.41 \pm 0.08\%$

( $-1.05 \pm 0.0 \text{ W m}^{-2}$ ) for the FC case. Over the forest, the use of LSM+PCM instead of PSF would decrease the dispersive heat fluxes by  $-0.71 \pm 0.19\%$  ( $-1.86 \pm 0.01 \text{ W m}^{-2}$ ) in the MU case, but increase them by  $0.32 \pm 0.14\%$  ( $1.89 \pm 0.04 \text{ W m}^{-2}$ ) and  $1.0 \pm 0.22\%$  ( $7.67 \pm 0.2 \text{ W m}^{-2}$ ) for SU and FC cases, respectively.

Additional factors should also be considered when choosing the lower boundary condition, such as the fact that the flow modification by forest edges cannot be represented by PSF or LSM. These effects are not investigated in this study, although they can have a strong influence on temporal covariance and dispersive heat fluxes (Kanani-Sühring and Raasch 2017; Kenny et al. 2017).

Furthermore, forests typically have a roughness length of  $> 1 \text{ m}$  (Foken 2017). However,  $z_0$  is limited to a quarter of the vertical grid spacing in PALM because MOST is not valid within the roughness sublayer (Basu and Lacser 2017). Therefore, forests cannot be represented correctly by the LSM with vertical grid spacings  $< 4 \text{ m}$ . To estimate the roughness length resulting from the resolved canopy in the LSM+PCM simulations over forest, we have performed an additional simulation with near neutral atmospheric stratification. We fitted

$$U(z_v) = \frac{u_*}{\kappa} \ln \left( \frac{z_v - d}{z_0} \right), \quad (15)$$

where  $\kappa$  is the von Kármán constant (0.4) and  $d$  is the zero-plane displacement to the horizontal wind profile and found  $z_0$  to be 2.2 m. Thus,  $z_0$  is almost a factor of 10 larger than in the PSF simulations and much closer to  $z_0$  determined from various field measurements over forests (Reithmaier et al. 2006).

Finally, when using the PCM, we found fluxes from the ground to be very small. Most of the incoming shortwave radiation is converted into longwave radiation and heat fluxes at the top of the tree canopy. Due to the shading by the trees, almost no energy reaches the ground where it is fed into the LSM and coupled soil model. This also means that the choice of vegetation type in LSM in combination with the PCM plays hardly any role.

As mentioned earlier, biomass heat storage was found to play a major role in energy-balance closure, especially in forests (Lindroth et al. 2010; Swenson et al. 2019). However, the simulations with PSF or LSM only do not provide information on biomass storage or processes within the canopy and in the understory air space. To answer our research question about the influence of lower boundary conditions on dispersive heat fluxes, we have therefore limited ourselves to the area above the vegetation surface, i.e. dispersive flux components relative to the total heat flux at the canopy top. Therefore, we cannot draw any conclusions on the influence of biomass heat storage.

## 5 Conclusion

To answer whether the choice of lower boundary conditions has an influence on the resulting dispersive heat fluxes in LES, we compared two different boundary conditions over grass and forest, respectively, using different atmospheric conditions. We found that especially the use of the PCM, i.e. resolving the vegetation in the model, indeed has a significant influence on the dispersive fluxes. The comparison between PSF and LSM for

grassland shows no significant differences near the vegetation top for all atmospheric conditions with respect to the proportion of dispersive heat fluxes to the total surface-heat flux. The use of LSM+PCM for forests causes significantly larger dispersive fluxes than PSF near the surface regardless of the stability regime. The more unstable the atmospheric conditions are, the greater this difference. At larger measurement heights, however, the effect is reversed depending on the atmospheric stability. We showed that resolving the vegetation in the PCM also has a clear impact on the relationship between variance and flux–variance similarity functions, which is related to the relative importance of dispersive heat fluxes. The use of the PCM is therefore recommended for low measurement heights within 20 m above the vegetation top, which is the case for many field measurement set-ups. Nevertheless, these simulated dispersive fluxes are much smaller than the EBC gap of real-world EC measurements. Despite this discrepancy, the PCM also has other advantages, for example, it allows for surface types with a high roughness, such as forests, to be correctly represented even at high grid resolutions on the order of metres. In the case of heterogeneous surfaces, resolved forest edges can also have an additional effect on dispersive fluxes which was, however, not investigated in this study, where only homogeneous conditions were analyzed.

## Appendix: Initialization Profiles

Figure 11 shows horizontally-averaged profiles for  $\theta$ ,  $q$ , and  $w$  that were used to initiate all simulations. Within the 2-h spin-up time, the boundary layer develops so that the profiles evolve into those shown in Fig. 4.

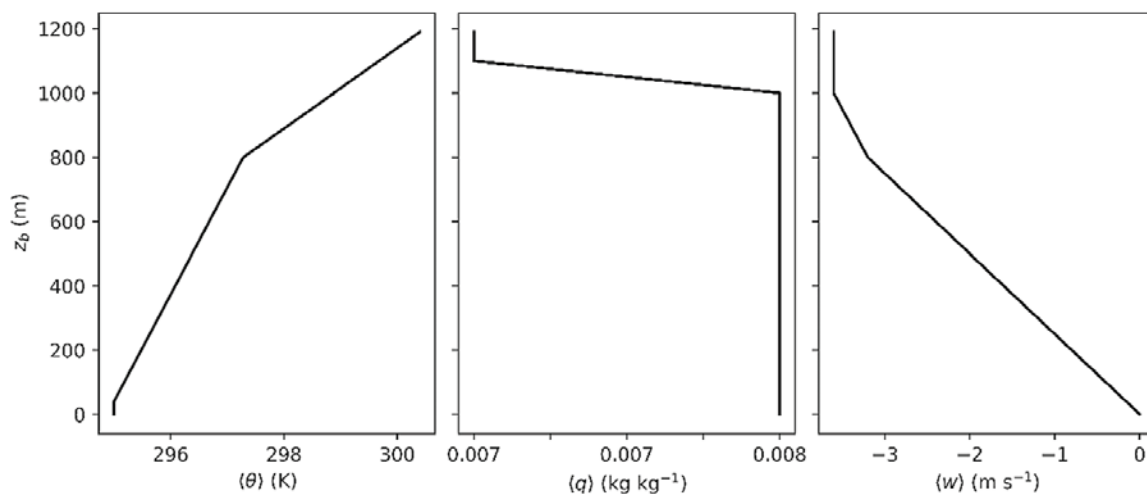


**Fig. 11** Initialization profiles of spatially-averaged  $\theta$ ,  $q$ , and  $w$  for all simulations

**Table 6** Initial soil model set-up for all simulations with LSM(+PCM) as lower boundary condition

Depth (m)	Soil temperature (K)	Soil moisture (m <sup>3</sup> m <sup>-3</sup> )
0–0.001	291.35	0.32
0.001–0.01	291.25	0.32
0.01–0.02	291.15	0.32
0.02–0.04	290.95	0.32
0.04–0.08	290.60	0.32
0.08–0.14	290.15	0.32
0.14–0.27	289.45	0.32
0.27–0.53	288.30	0.31
0.53–1.07	286.65	0.30
1.07–2.93	283.20	0.28

Table 6 shows the initial set-up of the soil model that is part of the LSM. The soil temperature and moisture were applied in each layer throughout the entire horizontal extent of the domain. This set-up was used in all simulations where LSM(+PCM) was employed as lower boundary condition.

**Acknowledgements** This project was financially supported by Deutsche Forschungsgemeinschaft (DFG) Award #406980118 and the MICMoR Research School of KIT.

**Funding** Open Access funding enabled and organized by Projekt DEAL.

**Open Access** This article is licensed under a Creative Commons Attribution 4.0 International License, which permits use, sharing, adaptation, distribution and reproduction in any medium or format, as long as you give appropriate credit to the original author(s) and the source, provide a link to the Creative Commons licence, and indicate if changes were made. The images or other third party material in this article are included in the article's Creative Commons licence, unless indicated otherwise in a credit line to the material. If material is not included in the article's Creative Commons licence and your intended use is not permitted by statutory regulation or exceeds the permitted use, you will need to obtain permission directly from the copyright holder. To view a copy of this licence, visit <http://creativecommons.org/licenses/by/4.0/>.

## References

- Baldocchi D, Falge E, Gu L, Olson R, Hollinger D, Running S, Anthoni P, Bernhofer C, Davis K, Evans R, Fuentes J, Goldstein A, Katul G, Law B, Lee X, Malhi Y, Meyers T, Munger W, Oechel W, Paw KT, Pilegaard K, Schmid HP, Valentini R, Verma S, Vesala T, Wilson K, Wofsy S (2001) FLUXNET: a new tool to study the temporal and spatial variability of ecosystem-scale carbon dioxide, water vapor, and energy flux densities. *Bull Am Meteorol Soc* 82(11):2415–2434. [https://doi.org/10.1175/1520-0477\(2001\)082%3c2415:FANTTS%3e2.3.CO;2](https://doi.org/10.1175/1520-0477(2001)082%3c2415:FANTTS%3e2.3.CO;2)
- Basu S, Lacser A (2017) A cautionary note on the use of Monin-Obukhov similarity theory in very high-resolution large-eddy simulations. *Boundary-Layer Meteorol* 163(2):351–355. <https://doi.org/10.1007/s10546-016-0225-y>
- Bou-Zeid E, Meneveau C, Parlange M (2005) A scale-dependent Lagrangian dynamic model for large eddy simulation of complex turbulent flows. *J Fluid Mech* 17(2):25105. <https://doi.org/10.1063/1.1839152>
- Bou-Zeid E, Anderson W, Katul GG, Mahrt L (2020) The persistent challenge of surface heterogeneity in boundary-layer meteorology: a review. *Boundary-Layer Meteorol* 177(2–3):227–245. <https://doi.org/10.1007/s10546-020-00551-8>
- Butterworth BJ, Desai AR, Metzger S, Townsend PA, Schwartz MD, Petty GW, Mauder M, Vogelmann H, Andresen CG, Augustine TJ, Bertram TH, Brown WO, Buban M, Clearly P, Durden DJ, Florian CR, Iglinski TJ, Kruger EL, Lantz K, Lee TR, Meyers TP, Mineau JK, Olson ER, Oncley SP, Paleri S, Pertzborn RA,

- Petersen C, Plummer DM, Riihimaki L, Guzman ER, Sedlar J, Smith EN, Speidel J, Stoy PC, Sühling M, Thom JE, Turner DD, Vermeuel MP, Wagner TJ, Wang Z, Wanner L, White LD, Wilczak JM, Wright DB, Zheng T (2021) Connecting land-atmosphere interactions to surface heterogeneity in CHEESEHEAD19. *Bull Am Meteorol Soc* 102(2):E421–E445. <https://doi.org/10.1175/BAMS-D-19-0346.1>
- De Roo F, Zhang S, Huq S, Mauder M (2018) A semi-empirical model of the energy balance closure in the surface layer. *PLoS ONE* 13(12):e0209022. <https://doi.org/10.1371/journal.pone.0209022>
- Deardorff JW (1980) Stratocumulus-capped mixed layers derived from a three-dimensional model. *Boundary-Layer Meteorol* 18(4):495–527. <https://doi.org/10.1007/BF00119502>
- Eder F, Schmidt M, Damian T, Träumner K, Mauder M (2015a) Mesoscale eddies affect near-surface turbulent exchange: evidence from lidar and tower measurements. *J Appl Meteorol Climatol* 54(1):189–206. <https://doi.org/10.1175/JAMC-D-14-0140.1>
- Eder F, De Roo F, Rotenberg E, Yakir D, Schmid HP, Mauder M (2015b) Secondary circulations at a solitary forest surrounded by semi-arid shrubland and their impact on eddy-covariance measurements. *Agric for Meteorol* 211–212:115–127. <https://doi.org/10.1016/j.agrformet.2015.06.001>
- Finnigan JJ, Clement R, Malhi Y, Leuning R, Cleugh HA (2003) A re-evaluation of long-term flux measurement techniques part I: averaging and coordinate rotation. *Boundary-Layer Meteorol* 107(1):1–48. <https://doi.org/10.1023/A:1021554900225>
- Finnigan JJ, Shaw RH, Patton EG (2009) Turbulence structure above a vegetation canopy. *J Fluid Mech* 637:387–424. <https://doi.org/10.1017/S0022112009990589>
- Foken T, Göckede M, Mauder M, Mahrt L, Amiro B, Munger W (2004) Post-field data quality control. In: Lee X (ed) *Handbook of micrometeorology: a guide for surface flux measurement and analysis*. Kluwer Academic Publication, Dordrecht, pp 181–208
- Foken T, Wimmer F, Mauder M, Thomas C, Liebethal C (2006) Some aspects of the energy balance closure problem. *Atmos Chem Phys* 6(12):4395–4402. <https://doi.org/10.5194/acp-6-4395-2006>
- Foken T (2008) The energy balance closure problem: an overview. *Ecol Appl* 18(6):1351–1367. <https://doi.org/10.1890/06-0922.1>
- Foken T (2017) Basic equations of atmospheric turbulence. In: Foken T (ed) *Micrometeorology*. Springer, Berlin, pp 33–81
- Foken T, Mauder M, Liebethal C, Wimmer F, Beyrich F, Leps J-P, Raasch S, DeBruin HAR, Meijninger WML, Bange J (2010) Energy balance closure for the LITFASS-2003 experiment. *Theor Appl Climatol* 101(1–2):149–160. <https://doi.org/10.1007/s00704-009-0216-8>
- Frank JM, Massman WJ, Ewers BE (2013) Underestimates of sensible heat flux due to vertical velocity measurement errors in non-orthogonal sonic anemometers. *Agric for Meteorol* 171–172:72–81. <https://doi.org/10.1016/j.agrformet.2012.11.005>
- Gehrke KF, Sühling M, Maronga B (2020) Modeling of land-surface interactions in the PALM model system 6.0: Land surface model description, first evaluation, and sensitivity to model parameters. *Geosci Model Dev Discuss*. <https://doi.org/10.5194/gmd-2020-197> (in review)
- Goulden ML, Munger JW, Fan S-M, Daube BC, Wofsy SC (1996) Measurements of carbon sequestration by long-term eddy covariance: methods and a critical evaluation of accuracy. *Glob Change Biol* 2(3):169–182. <https://doi.org/10.1111/j.1365-2486.1996.tb00070.x>
- Hellsten A, Ketelsen K, Sühling M, Auvinen M, Maronga B, Knigge C, Barmpas F, Tsegas G, Mousiopoulos N, Raasch S (2021) A nested multi-scale system implemented in the large-eddy simulation model PALM model system 6.0. *Geosci Model Dev* 14:3185–3214. <https://doi.org/10.5194/gmd-14-3185-2021>
- Hendricks-Franssen HJ, Stöckli R, Lehner I, Rotenberg E, Seneviratne SI (2010) Energy balance closure of eddy-covariance data: a multisite analysis for European FLUXNET stations. *Agric Forest Meteorol* 150(12):1553–1567. <https://doi.org/10.1016/j.agrformet.2010.08.005>
- Huang J, Lee X, Patton EG (2008) A modelling study of flux imbalance and the influence of entrainment in the convective boundary layer. *Boundary-Layer Meteorol* 127(2):273–292. <https://doi.org/10.1007/s10546-007-9254-x>
- Inagaki A, Letzel MO, Raasch S, Kanda M (2006) Impact of surface heterogeneity on energy imbalance: a study using LES. *J Meteorol Soc Jpn* 84(1):187–198. <https://doi.org/10.2151/jmsj.84.187>
- Kanani F, Träumner K, Ruck B, Raasch S (2014) What determines the differences found in forest edge flow between physical models and atmospheric measurements?—An LES study. *Meteorol Z* 23(1):33–49. <https://doi.org/10.1127/0941-2948/2014/0542>
- Kanani-Sühling F, Raasch S (2017) Enhanced scalar concentrations and fluxes in the lee of forest patches: a large-eddy simulation study. *Boundary-Layer Meteorol* 164(1):1–17. <https://doi.org/10.1007/s10546-017-0239-0>

- Kanda M, Inagaki A, Letzel MO, Raasch S, Watanabe T (2004) LES study of the energy imbalance problem with eddy covariance fluxes. *Boundary-Layer Meteorol* 110(3):381–404. <https://doi.org/10.1023/B:BOUN.0000007225.45548.7a>
- Kenny WT, Bohrer G, Morin TH, Vogel CS, Matheny AM, Desai AR (2017) A numerical case study of the implications of secondary circulations to the interpretation of eddy-covariance measurements over small lakes. *Boundary-Layer Meteorol* 165(2):311–332. <https://doi.org/10.1007/s10546-017-0268-8>
- Kochendorfer J, Meyers TP, Frank J, Massman WJ, Heuer MW (2012) How well can we measure the vertical wind speed? Implications for fluxes of energy and mass. *Boundary-Layer Meteorol* 145(2):383–398. <https://doi.org/10.1007/s10546-012-9738-1>
- Kohsiek W, Liebethal C, Foken T, Vogt R, Oncley SP, Bernhofer C, Debruin HAR (2007) The Energy Balance Experiment EBEX-2000. Part III: behaviour and quality of the radiation measurements. *Boundary-Layer Meteorol* 123(1):55–75. <https://doi.org/10.1007/s10546-006-9135-8>
- Krč P, Resler J, Sühling M, Schubert S, Salim MH, Fuka V (2021) Radiative Transfer Model 3.0 integrated into the PALM model system 6.0. *Geosci Model Dev* 14:3095–3120. <https://doi.org/10.5194/gmd-14-3095-2021>
- Kröniger K, De Roo F, Brugger P, Huq S, Banerjee T, Zinsler J, Rotenberg E, Yakir D, Rohatyn S, Mauder M (2018) Effect of secondary circulations on the surface-atmosphere exchange of energy at an isolated semi-arid forest. *Boundary-Layer Meteorol* 169(2):209–232. <https://doi.org/10.1007/s10546-018-0370-6>
- Laubach J, Raschendorfer M, Kreilein H, Gravenhorst G (1994) Determination of heat and water vapour fluxes above a spruce forest by eddy correlation. *Agric for Meteorol* 71(3–4):373–401. [https://doi.org/10.1016/0168-1923\(94\)90021-3](https://doi.org/10.1016/0168-1923(94)90021-3)
- Leuning R, van Gorsel E, Massman WJ, Isaac PR (2012) Reflections on the surface energy imbalance problem. *Agric for Meteorol* 156:65–74. <https://doi.org/10.1016/j.agrformet.2011.12.002>
- Liebethal C, Huwe B, Foken T (2005) Sensitivity analysis for two ground heat flux calculation approaches. *Agric for Meteorol* 132(3–4):253–262. <https://doi.org/10.1016/j.agrformet.2005.08.001>
- Lindroth A, Mölder M, Lagergren F (2010) Heat storage in forest biomass improves energy balance closure. *Biogeosciences* 7(1):301–313. <https://doi.org/10.5194/bg-7-301-2010>
- Liu S, Shao Y (2013) Soil-layer configuration requirement for large-eddy atmosphere and land surface coupled modeling. *Atmos Sci Lett* 14(2):112–117. <https://doi.org/10.1002/asl2.426>
- Margairaz F, Pardyjak ER, Calaf M (2020) Surface thermal heterogeneities and the atmospheric boundary layer: the thermal heterogeneity parameter. *Boundary-Layer Meteorol* 177(1):49–68. <https://doi.org/10.1007/s10546-020-00544-7>
- Maronga B, Gryschka M, Heinze R, Hoffmann F, Kanani-Sühling F, Keck M, Ketelsen K, Letzel MO, Sühling M, Raasch S (2015) The Parallelized Large-Eddy Simulation Model (PALM) version 4.0 for atmospheric and oceanic flows: model formulation, recent developments, and future perspectives. *Geosci Model Dev* 8(8):2515–2551. <https://doi.org/10.5194/gmd-8-2515-2015>
- Maronga B, Banzhaf S, Burmeister C, Esch T, Forkel R, Fröhlich D, Fuka V, Gehrke KF, Geletič J, Giersch S, Gronemeier T, Groß G, Heldens W, Hellsten A, Hoffmann F, Inagaki A, Kadasch E, Kanani-Sühling F, Ketelsen K, Khan BA, Knigge C, Knoop H, Krč P, Kurppa M, Maamari H, Matzarakis A, Mauder M, Pallasch M, Pavlik D, Pfafferoth J, Resler J, Rissmann S, Russo E, Salim M, Schrempf M, Schwenkel J, Seckmeyer G, Schubert S, Sühling M, von Tils R, Vollmer L, Ward S, Witha B, Wurps H, Zeidler J, Raasch S (2020) Overview of the PALM model system 6.0. *Geosci Model Dev* 13(3):1335–1372. <https://doi.org/10.5194/gmd-13-1335-2020>
- Mauder M (2013) A comment on “How well can we measure the vertical wind speed? Implications for fluxes of energy and mass” by Kochendorfer et al. *Boundary-Layer Meteorol* 147(2):329–335. <https://doi.org/10.1007/s10546-012-9794-6>
- Mauder M, Liebethal C, Göckede M, Leps J-P, Beyrich F, Foken T (2006) Processing and quality control of flux data during LITFASS-2003. *Boundary-Layer Meteorol* 121(1):67–88. <https://doi.org/10.1007/s10546-006-9094-0>
- Mauder M, Foken T, Cuxart J (2020) Surface-energy-balance closure over land: a review. *Boundary-Layer Meteorol* 9(8):3587. <https://doi.org/10.1007/s10546-020-00529-6>
- Moeng C-H, Wyngaard JC (1988) Spectral analysis of large-eddy simulations of the convective boundary layer. *J Atmos Sci* 45(23):3573–3587. [https://doi.org/10.1175/1520-0469\(1988\)045%3c3573:SAOLES%3e2.0.CO;2](https://doi.org/10.1175/1520-0469(1988)045%3c3573:SAOLES%3e2.0.CO;2)
- Nakai T, Shimoyama K (2012) Ultrasonic anemometer angle of attack errors under turbulent conditions. *Agric for Meteorol* 162–163:14–26. <https://doi.org/10.1016/j.agrformet.2012.04.004>
- Novick KA, Biederman JA, Desai AR, Litvak ME, Moore D, Scott RL, Torn MS (2018) The AmeriFlux network: a coalition of the willing. *Agric for Meteorol* 249:444–456. <https://doi.org/10.1016/j.agrformet.2017.10.009>

- Oncley SP, Foken T, Vogt R, Kohsiek W, Debruin HAR, Bernhofer C, Christen A, van Gorsel E, Grantz D, Feigenwinter C, Lehner I, Liebenthal C, Liu H, Mauder M, Pitacco A, Ribeiro L, Weidinger T (2007) The Energy Balance Experiment EBEX-2000. Part I: overview and energy balance. *Boundary-Layer Meteorol* 123(1):1–28. <https://doi.org/10.1007/s10546-007-9161-1>
- Panofsky HA, Tennekes H, Lenschow DH, Wyngaard JC (1977) The characteristics of turbulent velocity components in the surface layer under convective conditions. *Boundary-Layer Meteorol* 11(3):355–361. <https://doi.org/10.1007/BF02186086>
- Panofsky HA, Dutton JA (1984) *Atmospheric turbulence: models and methods for engineering applications*. Wiley, New York
- Patton EG, Sullivan PP, Shaw RH, Finnigan JJ, Weil JC (2016) Atmospheric stability influences on coupled boundary layer and canopy turbulence. *J Atmos Sci* 73(4):1621–1647. <https://doi.org/10.1175/JAS-D-15-0068.1>
- Rannik Ü, Markkanen T, Raittila J, Hari P, Vesala T (2003) Turbulence statistics inside and over forest: influence on footprint prediction. *Boundary-Layer Meteorol* 109(2):163–189. <https://doi.org/10.1023/A:1025404923169>
- Reithmaier LM, Göckede M, Markkanen T, Knohl A, Churkina G, Rebmann C, Buchmann N, Foken T (2006) Use of remotely sensed land use classification for a better evaluation of micrometeorological flux measurement sites. *Theor Appl Climatol* 84(4):219–233. <https://doi.org/10.1007/s00704-005-0168-6>
- Saiki EM, Moeng C-H, Sullivan PP (2000) Large-eddy simulation of the stably stratified planetary boundary layer. *Boundary-Layer Meteorol* 95(1):1–30. <https://doi.org/10.1023/A:1002428223156>
- Schalkwijk J, Jonker HJJ, Siebesma AP (2016) An investigation of the eddy-covariance flux imbalance in a year-long large-eddy simulation of the weather at Cabauw. *Boundary-Layer Meteorol* 160(1):17–39. <https://doi.org/10.1007/s10546-016-0138-9>
- Shaw RH, Schumann U (1992) Large-eddy simulation of turbulent flow above and within a forest. *Boundary-Layer Meteorol* 61(1–2):47–64. <https://doi.org/10.1007/BF02033994>
- Soltani M, Mauder M, Laux P, Kunstmann H (2018) Turbulent flux variability and energy balance closure in the TERENO prealpine observatory: a hydrometeorological data analysis. *Theor Appl Climatol* 133(3–4):937–956. <https://doi.org/10.1007/s00704-017-2235-1>
- Steinfeld G, Letzel MO, Raasch S, Kanda M, Inagaki A (2007) Spatial representativeness of single tower measurements and the imbalance problem with eddy-covariance fluxes: results of a large-eddy simulation study. *Boundary-Layer Meteorol* 123(1):77–98. <https://doi.org/10.1007/s10546-006-9133-x>
- Stoy PC, Mauder M, Foken T, Marcolla B, Boegh E, Ibrom A, Arain MA, Arneth A, Aurela M, Bernhofer C, Cescatti A, Dellwik E, Duce P, Gianelle D, van Gorsel E, Kiely G, Knohl A, Margolis H, McCaughey H, Merbold L, Montagnani L, Papale D, Reichstein M, Saunders M, Serrano-Ortiz P, Sotocornola M, Spano D, Vaccari F, Varlagin A (2013) A data-driven analysis of energy balance closure across FLUXNET research sites: the role of landscape scale heterogeneity. *Agric for Meteorol* 171–172:137–152. <https://doi.org/10.1016/j.agrformet.2012.11.004>
- Sühring M, Metzger S, Xu K, Durden D, Desai A (2018) Trade-offs in flux disaggregation: a large-eddy simulation study. *Boundary-Layer Meteorol* 170(1):69–93. <https://doi.org/10.1007/s10546-018-0387-x>
- Swenson SC, Burns SP, Lawrence DM (2019) The impact of biomass heat storage on the canopy energy balance and atmospheric stability in the community land model. *J Adv Model Earth Syst* 11(1):83–98. <https://doi.org/10.1029/2018MS001476>
- Watanabe T (2004) Large-eddy simulation of coherent turbulence structures associated with scalar ramps over plant canopies. *Boundary-Layer Meteorol* 112(2):307–341. <https://doi.org/10.1023/B:BOUN.0000027912.84492.54>
- Wicker LJ, Skamarock WC (2002) Time-splitting methods for elastic models using forward time schemes. *Mon Weather Rev* 130(8):2088–2097. [https://doi.org/10.1175/1520-0493\(2002\)130%3c2088:TSM-FEM%3e2.0.CO;2](https://doi.org/10.1175/1520-0493(2002)130%3c2088:TSM-FEM%3e2.0.CO;2)
- Williamson J (1980) Low-storage Runge-Kutta schemes. *J Comput Phys* 35(1):48–56. [https://doi.org/10.1016/0021-9991\(80\)90033-9](https://doi.org/10.1016/0021-9991(80)90033-9)
- Xu K, Sühring M, Metzger S, Durden D, Desai AR (2020) Can data mining help eddy covariance see the landscape? A Large-Eddy simulation study. *Boundary-Layer Meteorol* 176(1):85–103. <https://doi.org/10.1007/s10546-020-00513-0>
- Zhou Y, Li D, Li X (2019) The effects of surface heterogeneity scale on the flux imbalance under free convection. *J Geophys Res Atmos*. <https://doi.org/10.1029/2018JD029550>

## Authors and Affiliations

Luise Wanner<sup>1</sup>  · Frederik De Roo<sup>2</sup> · Matthias Sühling<sup>3</sup> · Matthias Mauder<sup>1,4</sup>

<sup>1</sup> Institute of Meteorology and Climate Research – Atmospheric Environmental Research, Karlsruhe Institute of Technology, 82467 Garmisch-Partenkirchen, Germany

<sup>2</sup> Development Centre for Weather Forecasting, Norwegian Meteorological Institute, 0371 Oslo, Norway

<sup>3</sup> Institute of Meteorology and Climatology, Leibniz University Hannover, 30167 Hannover, Germany

<sup>4</sup> Institute of Geography and Geoecology, Karlsruhe Institute of Technology, 76131 Karlsruhe, Germany



## **C Incorporating the effect of heterogeneous surface heating into a semi-empirical model of the surface energy balance closure**

Wanner L, Calaf M, Mauder M (2022): Incorporating the effect of heterogeneous surface heating into a semi-empirical model of the surface energy balance closure, PLoS ONE, 17(6):e0268097, doi: 10.1371/journal.pone.0268097

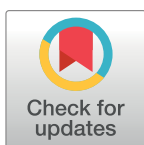


## RESEARCH ARTICLE

# Incorporating the effect of heterogeneous surface heating into a semi-empirical model of the surface energy balance closure

Luise Wanner<sup>1,2\*</sup>, Marc Calaf<sup>3</sup>, Matthias Mauder<sup>1,2,4</sup>

**1** Institute of Meteorology and Climate Research, Atmospheric Environmental Research, Karlsruhe Institute of Technology, Garmisch-Partenkirchen, Germany, **2** Institute of Hydrology and Meteorology, Technische Universität Dresden, Tharandt, Germany, **3** Department of Mechanical Engineering, University of Utah, Salt Lake City, UT, United States of America, **4** Institute of Geography and Geoecology, Karlsruhe Institute of Technology, Karlsruhe, Germany

\* [luise.wanner@kit.edu](mailto:luise.wanner@kit.edu)**OPEN ACCESS**

**Citation:** Wanner L, Calaf M, Mauder M (2022) Incorporating the effect of heterogeneous surface heating into a semi-empirical model of the surface energy balance closure. PLoS ONE 17(6): e0268097. <https://doi.org/10.1371/journal.pone.0268097>

**Editor:** Débora Regina Roberti, Universidade Federal de Santa Maria, BRAZIL

**Received:** November 11, 2021

**Accepted:** April 21, 2022

**Published:** June 1, 2022

**Copyright:** © 2022 Wanner et al. This is an open access article distributed under the terms of the [Creative Commons Attribution License](https://creativecommons.org/licenses/by/4.0/), which permits unrestricted use, distribution, and reproduction in any medium, provided the original author and source are credited.

**Data Availability Statement:** The LES dataset used in this study can be downloaded here: <https://doi.org/10.5281/zenodo.6342278>.

**Funding:** This study was financially supported by Deutsche Forschungsgemeinschaft (DFG) Award #406980118 and the MICMoR Research School of KIT. Marc Calaf thanks the support of the National Science Foundation Grants PDM-1649067, and PDM-1712538 as well as the support of the Alexander von Humboldt Stiftung/Foundation, Humboldt Research Fellowship for Experienced

## Abstract

It was discovered several decades ago that eddy covariance measurements systematically underestimate sensible and latent heat fluxes, creating an imbalance in the surface energy budget. Since then, many studies have addressed this problem and proposed a variety of solutions to the problem, including improvements to instruments and correction methods applied during data postprocessing. However, none of these measures have led to the complete closure of the energy balance gap. The leading hypothesis is that not only surface-attached turbulent eddies but also sub-mesoscale atmospheric circulations contribute to the transport of energy in the atmospheric boundary layer, and the contribution from organized motions has been grossly neglected. The problem arises because the transport of energy through these secondary circulations cannot be captured by the standard eddy covariance method given the relatively short averaging periods of time (~30 minutes) used to compute statistics. There are various approaches to adjust the measured heat fluxes by attributing the missing energy to the sensible and latent heat flux in different proportions. However, few correction methods are based on the processes causing the energy balance gap. Several studies have shown that the magnitude of the energy balance gap depends on the atmospheric stability and the heterogeneity scale of the landscape around the measurement site. Based on this, the energy balance gap within the surface layer has already been modelled as a function of a nonlocal atmospheric stability parameter by performing a large-eddy simulation study with idealized homogeneous surfaces. We have further developed this approach by including thermal surface heterogeneity in addition to atmospheric stability in the parameterization. Specifically, we incorporated a thermal heterogeneity parameter that was shown to relate to the magnitude of the energy balance gap. For this purpose, we use a Large-Eddy Simulation dataset of 28 simulations with seven different atmospheric conditions and three heterogeneous surfaces with different heterogeneity scales as well as one homogeneous surface. The newly developed model captures very well the variability in the magnitude of the energy balance gap under different conditions. The model covers a wide range of both atmospheric stabilities and landscape heterogeneity scales and is well suited

Researchers, during the sabbatical year at the Karlsruhe Institute of Technology Campus Alpin in Garmisch-Partenkirchen. The funders had no role in study design, data collection and analysis, decision to publish, or preparation of the manuscript.

**Competing interests:** The authors have declared that no competing interests exist.

for application to eddy covariance measurements since all necessary information can be modelled or obtained from a few additional measurements.

## Introduction

Understanding how energy in the form of sensible and latent heat is exchanged between the biosphere and the atmosphere is of great importance in different fields. For example, it is critical for weather forecasting and climate modelling [1–4], understanding of CO<sub>2</sub> sequestration by plants [5–9], and developing management recommendations for pastures, croplands, and forestry that enable efficient use of water resources [10–15].

Traditionally, the eddy covariance (EC) method is the approach used to measure the momentum, energy, and mass fluxes between the earth's surface and the atmosphere [16, 17]. This is the most direct and non-destructive method to quantify momentum, energy, and mass fluxes between a given ecosystem and the atmospheric boundary layer (ABL) [18]. Nonetheless, it has been repeatedly found that when experimentally measuring the surface energy balance (SEB, balance between the energy reaching/leaving the ground surface through net radiation and the corresponding ground and turbulent fluxes, storage, and metabolic terms) there is a 10–30% imbalance, resulting in an energy gap in the SEB [19–21].

Multiple possible causes for this gap have been investigated over the years. Some of them are instrument errors, including the systematic error of sonic anemometers or humidity measurements [22–27], systematic error in measurements of other SEB components like soil heat flux or radiation [28–30], footprint mismatch [31], and heat storage in tall vegetation canopies [32–35]. These error sources have been progressively addressed by improving the measurement techniques and the development of correction methods that can be applied during data post-processing [36–38]. Nonetheless, besides all these significant efforts there remains an important SEB gap [37, 39, 40].

The EC method relies on very high temporal resolution measurements of the three-dimensional wind speed and any other additional scalar of interest. For example, if one is interested in measuring the sensible heat flux, then the temperature would be the additional scalar of interest. The sensible heat flux is then calculated as the covariance of the vertical wind speed and the temperature around the average for a defined time period of typically 30 minutes [17, 41]. As a result, the EC method can only capture the turbulent contribution of the energy fluxes, where the turbulent fluctuations are defined around the adopted averaging period [42]. Initially, this was thought to be sufficient given that almost all atmospheric transport in the boundary layer is considered of turbulent nature [43, 44].

However, more recently, it was found that, under certain atmospheric conditions, a significant part of the energy is not transported by turbulent motions but rather large-scale persistent atmospheric circulations that contribute to the vertical mean wind and reach far into the atmospheric surface layer [45, 46]. This transport of sensible and latent heat by secondary circulations can significantly contribute to the SEB non-closure [30, 40]. However, because it is expressed through a mean advective transport in the differential equations, it can only be captured through a spatial array of sensors and not by single-tower EC measurements [47–49]. At present, it is possible to differentiate between two types of secondary circulations. The first type are the so-called thermally-induced mesoscale circulations (TMCs) which result from heterogeneous surface forcing and are therefore spatially bound [30, 40, 50, 51]. The second type are slow-moving turbulent organized structures (TOSs) that develop randomly even over homogeneous surfaces [52, 53] and can translate with time. Recent data analysis has shown that extending the averaging period to several days instead of 30 minutes could almost close

the energy balance gap for some sites [37, 54] but not for all [41]. This could be explained because the TMCs are bound to the surface and thus do not move over time [40, 53, 55]. Moreover, such long averaging periods typically violate the stationarity requirement that has to be fulfilled to calculate a covariance [37, 40].

Multiple approaches to correct for the SEB non-closure have been developed already, e.g. by extending the averaging period [37, 41, 54] applying the Bowen ratio of the measured turbulent fluxes to the missing dispersive fluxes [38], attributing the entire residual to the sensible [56] or latent [57] heat flux, or modelling the energy balance gap [58–60]. While some of these correction methods have proven to improve SEB closure [61–63], these models do not consider the factors and processes that cause the SEB gap. Some approaches consider the influence of atmospheric stability or heterogeneity in surface roughness [59, 60], but they do not take into account the influence of thermal surface heterogeneity.

We hypothesize that it is possible to overcome the SEB non-closure problem by considering both, the influence of thermal landscape heterogeneity, and the effect of atmospheric stability. Our study expands beyond the earlier LES works of De Roo et al. [58], and Margairaz et al. [64]. Specifically, we use the correction method developed by De Roo et al. [58] that models the SEB non-closure as a function of the atmospheric stability factor  $u^*/w^*$  (here  $w^*$  is the Deardorff velocity) and take it one step further by including the effect of landscape heterogeneity. For this second step, we use the thermal heterogeneity parameter defined in Margairaz et al. [64]. The use of the LES technology is ideally suited to investigate the influence of atmospheric stability and surface heterogeneity on the SEB gap because it allows the control of both, the atmospheric conditions, and the surface characteristics. This facilitates the development of idealized analysis that can later shed light on the datasets of more complex field experiments [53, 65, 66]. Furthermore, LESs provide information on the structure of the atmospheric flow as a function of time, and the contribution of turbulent and advective transport of latent and sensible heat fluxes at each point in space [53, 65].

This paper is organized as follows. In the next section, we provide a brief overview of former LES-based energy balance closure approaches, the two studies by De Roo et al. [58] and Margairaz et al. [64], and the theory underlying our new model. This is followed by a description of the dataset and study cases. Afterwards, we present the resulting reference models and our new model, which are then further discussed. The last section provides a short summary of our findings.

## Theory

Several field studies have investigated EC measurements at multiple sites to understand the systematic behavior of the SEB closure, and have found relations with surface inhomogeneity [60, 67–70], friction velocity  $u^*$  [19, 20, 71, 72], and atmospheric stability [19, 20, 72, 73]. Also, large-eddy simulation (LES) studies confirm the dependence of the SEB gap with surface heterogeneity [74],  $u^*$  [65] and atmospheric stability [59, 75]. The relation between the SEB gap and surface heterogeneity can be explained as follows: the patches in heterogeneous surfaces heat up differently, which favors the formation of TMCs in addition to TOSs, with the amplitude and size of the individual surfaces conditioning how strongly these TMCs will be [53, 66, 76, 77]. There is also a causal relation between the SEB gap and atmospheric stability: a large horizontal geostrophic wind speed, i.e., neutral to stable atmospheric stratification, results in enhanced horizontal mixing, which is why the influence of TOSs and TMCs on the measured flux is less pronounced than under free convective conditions [65, 78].

At present, there exists only a reduced set of approaches to model the SEB closure based on the underlying processes by considering the factors that determine the magnitude of the energy balance gap such as atmospheric stability or surface heterogeneity. One of them is the model of

Huang et al. [59] that depends on  $u^*$  and  $w^*$ , the measurement height  $z$ , and the atmospheric boundary layer height  $z_i$ . This model is applicable to 30-min flux measurements, but it was only developed for homogeneous surfaces, and only heights between 0.3 and 0.5  $z/z_i$  were considered, so it is not applicable to typical EC measurement heights within the surface layer [58].

Another model is the one of Panin and Bernhofer [60]. They developed a heterogeneity-dependent energy balance gap parametrization that depends on changes in surface roughness and a corresponding heterogeneity length scale. However, this model does not include the effect of thermal heterogeneity [45, 53]. Furthermore, it does not account for the effect of changing atmospheric conditions [30, 50] and only provides the average energy balance closure for a site. As a result, it is rarely applicable to 30-min flux measurements.

### The atmospheric stability dependent energy balance gap model of De Roo et al. [58]

De Roo et al. [58] developed a parametrization for the SEB gap within the surface layer that results from the energy transport by TOSs. They use the so-called imbalance ( $I$ ) as a suitable measure of the missing part of the energy fluxes, i.e., the advective and dispersive fluxes that do not contribute to the Reynolds flux [58, 59]. It is based on the flux balance ratio that is computed as the Reynolds sensible heat flux  $H$  divided by the total available sensible heat flux, which equals the surface flux  $H_s$  at the bottom of the domain, and defined as

$$I = 1 - \frac{H}{H_s}. \quad (1)$$

Following the findings of Huang et al. [59], De Roo et al. [58] assumed that the underestimation of the heat fluxes, i.e. the imbalance  $I$  can be described by a function of the non-dimensional scaling parameter  $u^*/w^*$ , as well as a function of the measurement height  $z$  relative to the boundary layer height  $z_i$ :

$$I = F_1\left(\frac{u^*}{w^*}\right)F_2\left(\frac{z}{z_i}\right). \quad (2)$$

To determine the shape of functions  $F_1$  and  $F_2$ , they developed a LES dataset of ABL flow over idealized homogeneous surfaces using PALM [79]. They considered nine combinations of atmospheric stability and Bowen ratios (Bo) with a vertical grid spacing of only 2 m to investigate the energy imbalance at a height of 0.04  $z_i$ , i.e. within the atmospheric surface layer where most EC stations around the world are employed [19, 80].

They found that combining two sets of scaling functions described well the imbalances in the sensible and latent heat fluxes. Specifically, they found that the sensible heat flux imbalance within the surface layer can be described with

$$F_{1,DR} = 0.197 \exp\left(-17.0 \frac{u^*}{w^*}\right) + 0.156 \quad (3)$$

and

$$F_{2,DR} = 10.69 \frac{z}{z_i} + 0.21. \quad (4)$$

### The thermal heterogeneity parameter of Margairaz et al. [64]

As part of the Idealized Planar Array study for Quantifying Spatial heterogeneity (IPAQS) [70], Margairaz et al. [81] developed a set of idealized LES of convective boundary layers over

homogeneously rough surfaces with embedded thermal heterogeneities of different scales. In their work, a wide range of mean geostrophic wind was implemented to vary the flow characteristics from inertia driven to buoyancy dominated. The goal of the study was to determine under what flow conditions TMCs are formed and to unravel the relation between the surface heterogeneity length scales and the dynamic length scales characterizing the TMCs. In their work, the authors show how TMCs express through mean advective transport of heat, which when unresolved either due to coarse numerical grid resolution or coarse experimental distribution of sensors can then be equivalently expressed through dispersive fluxes [81].

Furthermore, in their work, a scaling analysis between the vertical mean momentum equation and the continuity equation lead the authors to a non-dimensional parameter, referred to therein as heterogeneity parameter, that was shown to scale well with the contribution of dispersive fluxes when normalized by the turbulent fluxes [64].

The thermal heterogeneity parameter developed therein not only depends on the horizontal heterogeneity length scale  $L_h$  but also on the length scale characteristic of the TMCs,  $L_d$  which also depends on buoyancy and the mean horizontal wind speed. Specifically, the thermal heterogeneity parameter was defined as

$$\mathcal{H} = \frac{g L_h \Delta T}{U_g^2 \langle \overline{T_s} \rangle}, \quad (5)$$

where  $T_s$  is the surface temperature and  $\Delta T$  is the amplitude of the surface temperature heterogeneities, calculated from the absolute deviations (indicated by the vertical bars) of  $T_s$  from the averaged  $T_s$  following

$$\Delta T = \langle |\overline{T_s} - \langle \overline{T_s} \rangle| \rangle. \quad (6)$$

The angular brackets denote horizontal averaging over the entire domain and the overbars denote temporal averaging over 30 minutes. Interestingly, the heterogeneity parameter can also be interpreted as a modified Richardson number, representing a balance between the mean buoyancy forces developed by the thermal surface heterogeneities, and the inertia forces represented by the geostrophic wind that tend to blend the surface effects.

In this work, we will revisit the scaling relation from De Roo et al. [58] developed for homogeneous surfaces, and the one from Margairaz et al. [64] for heterogeneous surfaces, and we will illustrate how they complement each other and can be generalized to a single relation valid for both, TMCs and TOSs. Results from the work presented herein will therefore lead to a generalization of the correction scaling relation for the closure of the SEB presented initially in De Roo et al. [58].

### The combination of the atmospheric stability and thermal heterogeneity parameters into a new model

To our knowledge, no existing approach considers both the influence of atmospheric stability and thermal surface heterogeneity on the magnitude of the SEB gap. The SEB model based on the atmospheric stability of De Roo et al. [58] and the thermal heterogeneity parameter developed by Margairaz et al. [64] proved to capture the changes in the magnitude of the SEB very well. We hypothesize, that combining their findings in one model will lead to a very powerful tool to parameterize the SEB gap in EC measurements. This new model could then be applied to various combinations of atmospheric stability and surface heterogeneity found in numerous eddy covariance measurements worldwide.

In this work, the focus is placed on the atmospheric surface layer (ASL) because eddy-covariance measurements are typically carried out close to the ground, within the surface layer

[19, 80]. Correspondingly, the analysis is carried out at the height of  $z = 0.04 z_i$ , which corresponds to 52–59 m above the surface in our simulations. We calculate the imbalance ratio as defined in De Roo et al. [58] following Eq 1. Specifically, the turbulent flux,  $H$ , is calculated using the 30-min averaged values of vertical wind speed  $w$  and temperature  $\theta$ , as well as the 30-min averaged temporal covariance of  $w$  and  $\theta$  and the subgrid-scale contribution  $H_{sgs}$ ,

$$H = \langle \overline{w\theta} - \overline{w}\overline{\theta} + \overline{H_{sgs}} \rangle. \tag{7}$$

The overbars indicate temporal averaging and the angled brackets denote horizontal averaging over the entire extent of the domain. In contrast to De Roo et al. [58], we therefore use the horizontally averaged imbalance instead of the local one. The sensible surface heat flux at the ground  $H_s$  corresponds to  $H$  at the lowest grid point ( $dz/2$ ).

To parametrize the imbalance, we first produce a set of reference models by adapting the existing model of De Roo et al. [58] to each heterogeneity scale in our dataset as described in the following subsection. Then, we proceed with developing the new model by including another scaling function that accounts for the influence of heterogeneity.

**Parametrization of the imbalance with respect to atmospheric stability (reference models).** First, we adapt the existing model of De Roo et al. [58] to each of the datasets to obtain a benchmark for our new model. This results in four  $F_1$  scaling functions that are similar to the scaling function presented in De Roo et al. [58], but represent one heterogeneity case, respectively. Following De Roo et al. [58], we factorize the imbalance following Eq 1, assuming that the imbalance can be described by two scaling functions that are functions of the stability parameter  $u^*/w^*$  and the normalized measurement height  $z/z_i$ . Based on the findings by De Roo et al. [58], we first assume that  $F_1$  is an exponential function of the form  $F_1 = a \exp(b u^*/w^*) + c$ , and  $F_2$  is a linear function of the form  $F_2 = i z/z_i + j$ , where  $a, b, c, i, j$ , are fitting constants. Thus, we first fit  $F_1$  to each of the simulation sets, individually, and later, we fit all of them onto a single  $F_2$  function to observe their collapse on a unique curve.

For this analysis, we calculate the friction velocity  $u^*$  and the Deardorff velocity  $w^*$  directly using the 30-min averaged covariances as it would be done with experimental data obtained from EC systems. Thus, we calculate  $u^*$  following

$$u_* = \langle (\overline{u'w'^2} + \overline{v'w'^2})^{1/4} \rangle, \tag{8}$$

where  $u$  and  $v$  are the horizontal wind speeds in x- and y-direction, and  $w^*$  following

$$w_* = \langle \left( \frac{g}{\theta} z_i \overline{w'\theta'} \right)^{1/3} \rangle, \tag{9}$$

where  $g$  is the gravitational acceleration ( $9.81 \text{ m s}^{-2}$ ). Here,  $z_i$  is determined as the height at which the total sensible heat flux crosses the zero value prior to reaching the capping inversion. The resulting set of four  $F_1$  scaling functions for each of the datasets and one  $F_2$  scaling function for all of the datasets is then used as a benchmark for our new model and referred hereafter as reference models.

**Parametrization of the imbalance with respect to atmospheric stability and surface heterogeneity (new model).** To consider the effect of surface heterogeneity, we assume that instead of describing the imbalance with a different scaling function  $F_1$  for each set of simulations, it is possible to use the scaling function that describes the imbalance in the simulations with a homogeneous surface,  $F_{1,HM}$ , and add another scaling function,  $F_3$ , that accounts for the

heterogeneity:

$$I\left(z, \frac{u_*}{w_*}\right) = F_{1,HM}\left(\frac{u_*}{w_*}\right)F_2\left(\frac{z}{z_i}\right)F_3(\mathcal{H}), \quad (10)$$

where  $\mathcal{H}$  is the thermal heterogeneity parameter introduced in Margairaz et al. [64] (Eq 4).

After analyzing the relationship between  $I$  normalized with  $F_{1,HM}$ , we assume that the relationship between  $I/F_{1,HM}$  and  $\mathcal{H}$  is of linear nature and fit  $I/F_{1,HM}$  to  $F_3 = m\mathcal{H} + n$ . Once  $F_3$  is found, we proceed to identify the new  $F_2$  similarly to the previous section.

## Dataset and study cases

The data used in this study was originally developed in the computational work of Margairaz et al. [64, 81]. They used the pseudo-spectral LES approach that was first introduced by Moeng [82] and Albertson and Parlange [83] and further developed by Bou-Zeid et al. [84], Calaf et al. [85], and Margairaz et al. [86]. The data consists of a set of numerical simulations of a characteristic ABL developed over a homogeneously rough and flat surface. The simulations represent an idealized dry ABL, forced through a geostrophic wind at the top with Coriolis force, and an imposed surface temperature at the bottom of the domain.

Study cases include a set of simulations with homogenous surface temperature (referred hereafter as HM) and a second set with heterogeneous surface temperature distributions (referred hereafter as HT). In both sets, the geostrophic wind is varied between  $1 \text{ m s}^{-1}$  to  $15 \text{ m s}^{-1}$ . For the set of heterogeneous surface temperature conditions, the corresponding length scale of the characteristic surface heterogeneities is also varied, considering cases with 800 m, 400 m, and 200 m patches (referred hereafter as HT200, HT400, HT800, see Fig 1). In this case, the surface temperature variations are randomly distributed following a gaussian distribution with a standard deviation of  $\pm 5 \text{ K}$  and mean temperature equal to that of the homogenous cases, namely 290 K.

In all cases the surface temperature is initialized at a temperature of 5 K higher than the air temperature to promote the development of a convective boundary layer. All simulations have a domain size  $(l_x, l_y, l_z) = (2\pi, 2\pi, 2) \text{ km}$  with a horizontal grid-spacing of  $\Delta x = \Delta y = 24.5 \text{ m}$  and a vertical grid-spacing of  $\Delta z = 7.8 \text{ m}$ , resulting in  $(N_x, N_y, N_z) = (256, 256, 256)$  grid points. At the bottom boundary, the surface heat flux is computed from the imposed surface temperature  $\theta_s$  using Monin-Obukhov similarity theory.

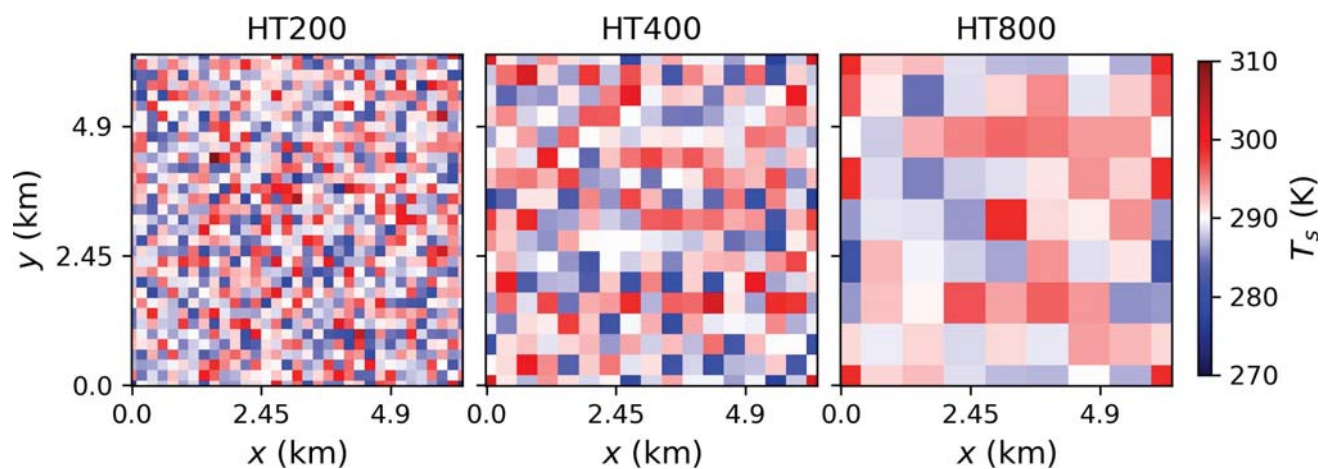


**Fig 1. Temperature distribution at the surface for the three sets of simulations with heterogeneous surfaces.**

<https://doi.org/10.1371/journal.pone.0268097.g001>

In all cases, the initial boundary layer height  $z_i$  was set to 1000 m by applying a capping inversion of  $0.012 \text{ K m}^{-1}$ . While  $\theta_s$  remains stable over the entire simulation time, the air temperature increases over time, leading to slightly less unstable atmospheric conditions over time. However, this effect was found to be negligible over the short duration of the simulation [64].

In total, 28 simulations were performed with different atmospheric conditions, controlled by seven different geostrophic wind speeds (i.e.  $U_g = 1, 2, 3, 4, 5, 6, 9, 15 \text{ m s}^{-1}$ ) for each set of homogeneous and heterogeneous surface conditions. In the simulations, the Coriolis parameter was set to  $10^{-4} \text{ Hz}$ , representative of a latitude of  $43.3^\circ \text{ N}$ . Also, the roughness length was set to 0.1 m for all simulations, and the used thermal roughness was set to  $1/10 z_0$  following [87]. More details on the numerical simulations can be found in the original work of Margairaz et al. [64].

For the analysis presented in this work, we use statistics over a 30-minute interval recorded after 4 hours of spin-up time.

## Results

### Reference models

As described previously, we first fitted the exponential function  $F_I$  to each one of the simulation cases resulting in four different sets of parameters, shown in Table 1 for the scaling function  $F_{I,h}$ :

$$F_{I,h} = a_h \exp\left(b_h \frac{u_*}{w_*}\right) + c_h. \quad (11)$$

Note that for each simulation case, there exist seven data points corresponding to the changes in geostrophic forcing and hence to different thermal stratification. These four different fits describe the imbalance ratio for each surface heterogeneity condition as a function of the non-dimensional term  $u_*/w_*$ .

The values calculated for  $u_*/w_*$  are shown in Table 2 where all relevant parameters characterizing the simulations are summarized. Fig 2A shows that these fitted functions for  $I$  collapse into the same value of roughly 6% of  $H_s$  under less unstable conditions ( $u_*/w_* > 0.4$ ). Only for HT800, the imbalance ( $I$ ) settles at around 8% of  $H_s$ , the total available flux for the weaker unstable conditions. Alternatively, the imbalance increases with increasing instability, with the weakest increase found in the homogeneous surface cases and stronger increases with heterogeneous surfaces. The increase also depends on the patch size, being strongest with the largest patch size.

We then normalized the imbalance ratios (i.e. Eq 1, also vertical axis in Fig 2A) with the four different scaling functions for the respective simulations (Eq 11, Table 1). Results are then represented in Fig 2B as a function of the second non-dimensional term identified in De Roo

**Table 1. Fitting parameters for all simulation cases with different surface characteristics.**

$h$	$a_h$	$b_h$	$c_h$
HM	0.133	-15.3	0.056
HT200	0.203	-12.6	0.058
HT400	0.289	-10.2	0.055
HT800	0.435	-14.3	0.073

<https://doi.org/10.1371/journal.pone.0268097.t001>

Table 2. Overview over characteristic variables that are relevant for this study, including geostrophic wind speed  $U_g$ , boundary layer height  $z_i$ , the friction velocity  $u_*$ , the Deardorff velocity  $w_*$ , the atmospheric stability parameters  $u_*/w_*$  and  $-z_i/L$ , the heterogeneity parameter  $H$ , and the energy imbalance  $I$  for each simulation.

Name	$U_g$ (m s <sup>-1</sup> )	$z_i$ (m)	$u_*$	$w_*$	$u_*/w_*$	$-z_i/L$	$H$	$I$ (%)	
HM-1		1	1328	0.15	1.59	0.09	493.65	0	8.79
HM-2		2	1318	0.22	1.57	0.14	156.17	0	7.28
HM-3		3	1306	0.27	1.56	0.17	75.30	0	6.40
HM-4		4	1293	0.33	1.54	0.21	42.30	0	6.02
HM-6		6	1295	0.43	1.55	0.28	18.58	0	6.08
HM-9		9	1307	0.57	1.59	0.36	8.63	0	5.60
HM-15		15	1340	0.81	1.64	0.49	3.33	0	5.46
HT200-1		1	1439	0.11	1.55	0.07	1230.97	27.09	14.38
HT200-2		2	1434	0.17	1.58	0.11	328.31	6.77	10.86
HT200-3		3	1430	0.24	1.63	0.15	128.00	3.01	9.22
HT200-4		4	1434	0.30	1.67	0.18	67.68	1.69	8.01
HT200-6		6	1402	0.41	1.72	0.24	28.75	0.75	6.49
HT200-9		9	1374	0.56	1.79	0.31	12.88	0.33	6.31
HT200-15		15	1383	0.81	1.96	0.41	5.60	0.12	5.92
HT400-1		1	1487	0.09	1.55	0.06	1951.94	52.14	21.14
HT400-2		2	1463	0.17	1.63	0.11	336.34	13.03	15.34
HT400-3		3	1452	0.24	1.65	0.14	135.45	5.79	13.28
HT400-4		4	1434	0.30	1.68	0.18	67.56	3.26	9.56
HT400-6		6	1406	0.41	1.72	0.24	29.07	1.45	7.09
HT400-9		9	1390	0.56	1.80	0.31	13.02	0.64	6.59
HT400-15		15	1404	0.81	1.95	0.42	5.59	0.23	6.52
HT800-1		1	1487	0.10	1.57	0.07	1428.40	79.16	25.07
HT800-2		2	1459	0.17	1.59	0.11	338.84	19.77	14.66
HT800-3		3	1448	0.24	1.62	0.15	117.37	8.8	12.59
HT800-4		4	1431	0.30	1.63	0.19	60.98	4.95	12.49
HT800-6		6	1397	0.41	1.65	0.25	26.56	2.2	8.21
HT800-9		9	1394	0.56	1.69	0.33	10.93	0.98	7.20
HT800-15		15	1407	0.81	1.79	0.46	4.22	0.35	6.83

<https://doi.org/10.1371/journal.pone.0268097.t002>

et al. [58], namely  $z/z_i$ . At this stage, the data presents a nice unique collapse for  $z/z_i < 0.07$ , representative of the surface layer region.

This unified scaling is well represented by function  $F_{2,R}$

$$F_{2,R} = i_R \frac{z}{z_i} + j_R, \quad (12)$$

where  $i_R$  is 20.05 and  $j_R$  is 0.157.

## New model

Fig 3 also shows the normalized imbalances, but in this case, the scaling function that was derived for the homogeneous simulations ( $F_{1,HM}$ , Eq 11, Table 2) was used for all simulations. Here, the profiles don't collapse into a single curve, but instead present a data spread, with the largest deviation found once again in the  $L_h = 800$  m configuration.

Next, we investigate whether these deviations can be reduced if the imbalance ( $I$ ) is normalized by  $F_{1,HM}$  and represented as a function of the thermal heterogeneity parameter ( $\mathcal{H}$ ). In this case, Fig 4 shows that two different linear relationships can be differentiated for those cases with weak geostrophic forcing ( $U_g = 1$  m s<sup>-1</sup>) and those with a more moderate or stronger

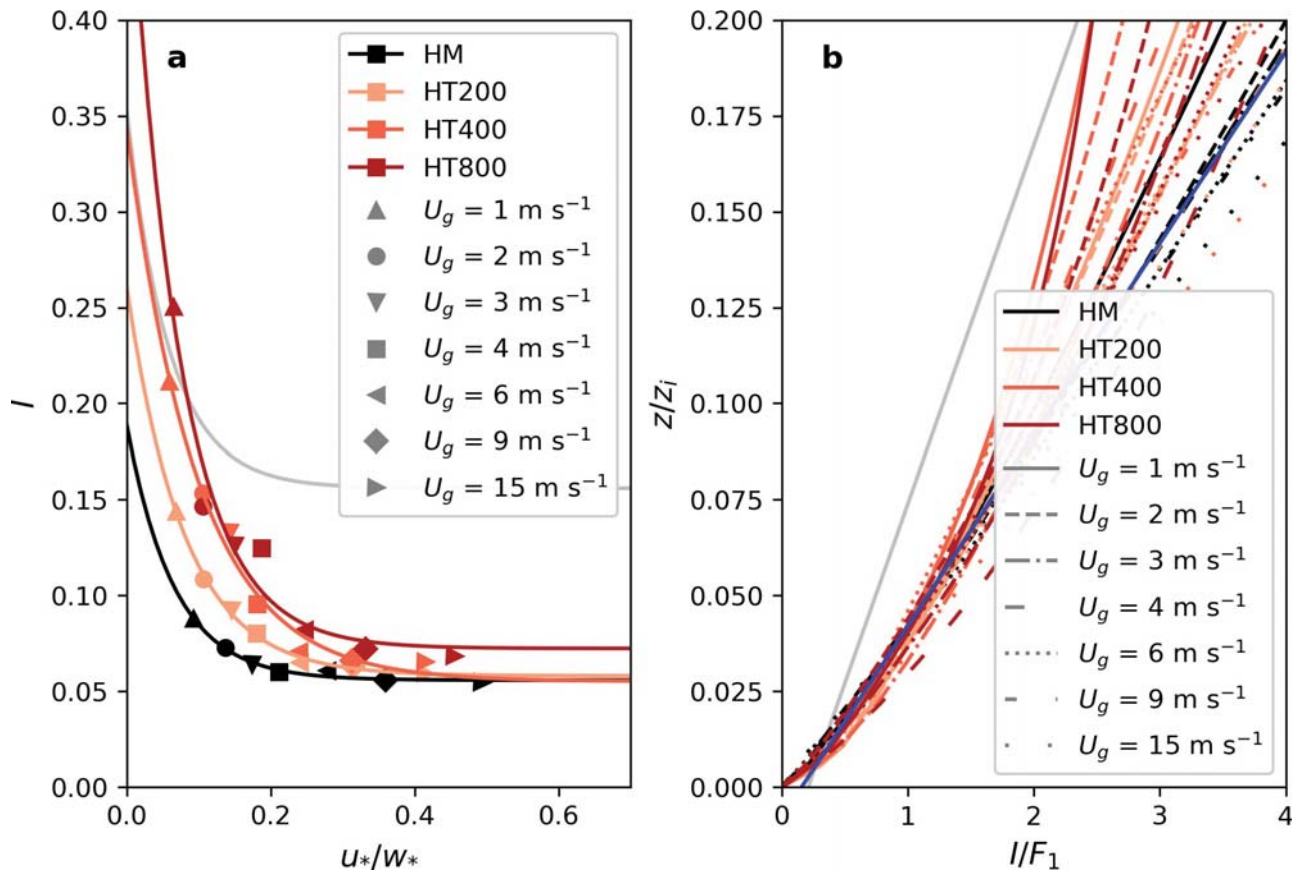


**Fig 2. Imbalance ratios as a function of the atmospheric stability.** Panel a shows the imbalance ratio  $I$  at  $0.04 z/z_i$  as a function of the stability parameter  $u^*/w^*$ . The four simulation sets are represented by different colors. For each simulation set, a separate fit of the scaling function  $F_1$  was performed, resulting in Eq 11 with different fitting parameters shown in Table 1. The atmospheric stability is steered by changes in  $U_g$ , shown by different marker shapes. The grey line shows the fit obtained by De Roo et al. [58] (Eq 3) for comparison. Panel b shows the vertical profiles of the imbalance normalized with the four fits of  $F_1$  (Eq 11), respectively. The blue line shows the fitted scaling function  $F_{2,R}$  (Eq 12). Again, the respective scaling function derived by De Roo et al. [58] (Eq 4) is shown in grey for comparison.

<https://doi.org/10.1371/journal.pone.0268097.g002>

wind ( $U_g \geq 3 \text{ m s}^{-1}$ ). We find those two groups to correspond to the formation of cellular and roll-like secondary circulations. This is shown in Fig 5 where xy-cross-sections of the 30-min averaged vertical wind speed  $w$  for combinations of  $U_g = 1, 2, 3, 4 \text{ m s}^{-1}$  and  $L_n = 200, 400 \text{ m}$  are displayed. While in the case of  $U_g = 1 \text{ m s}^{-1}$  (Fig 5A and 5E) there are large cellular circulations taking place, they disappear with increasing wind speed to give place to the formation of roll-type turbulent structures for  $U_g > 3 \text{ m s}^{-1}$  (Fig 5C, 5D, 5G and 5H). The structures resulting from  $U_g = 2 \text{ m s}^{-1}$  (Fig 5B and 5F) are neither cellular nor roll-like and are therefore excluded from the analysis.

Fitting  $F_3$  to the two datasets, we receive the following scaling functions:

$$F_{3,c} = m_c \mathcal{H} + n_c, \tag{13}$$

with  $m_c = 0.018$  and  $n_c = 0.973$  for  $u^*/w^* < 0.1$ , which is valid for all simulations where cellular structures develop ( $U_g = 1 \text{ m s}^{-1}$ ), and

$$F_{3,r} = m_r \mathcal{H} + n_r, \tag{14}$$

with  $m_r = 0.116$  and  $n_r = 1.07$  for  $u^*/w^* > 0.14$ , which is valid for all simulations where roll-like

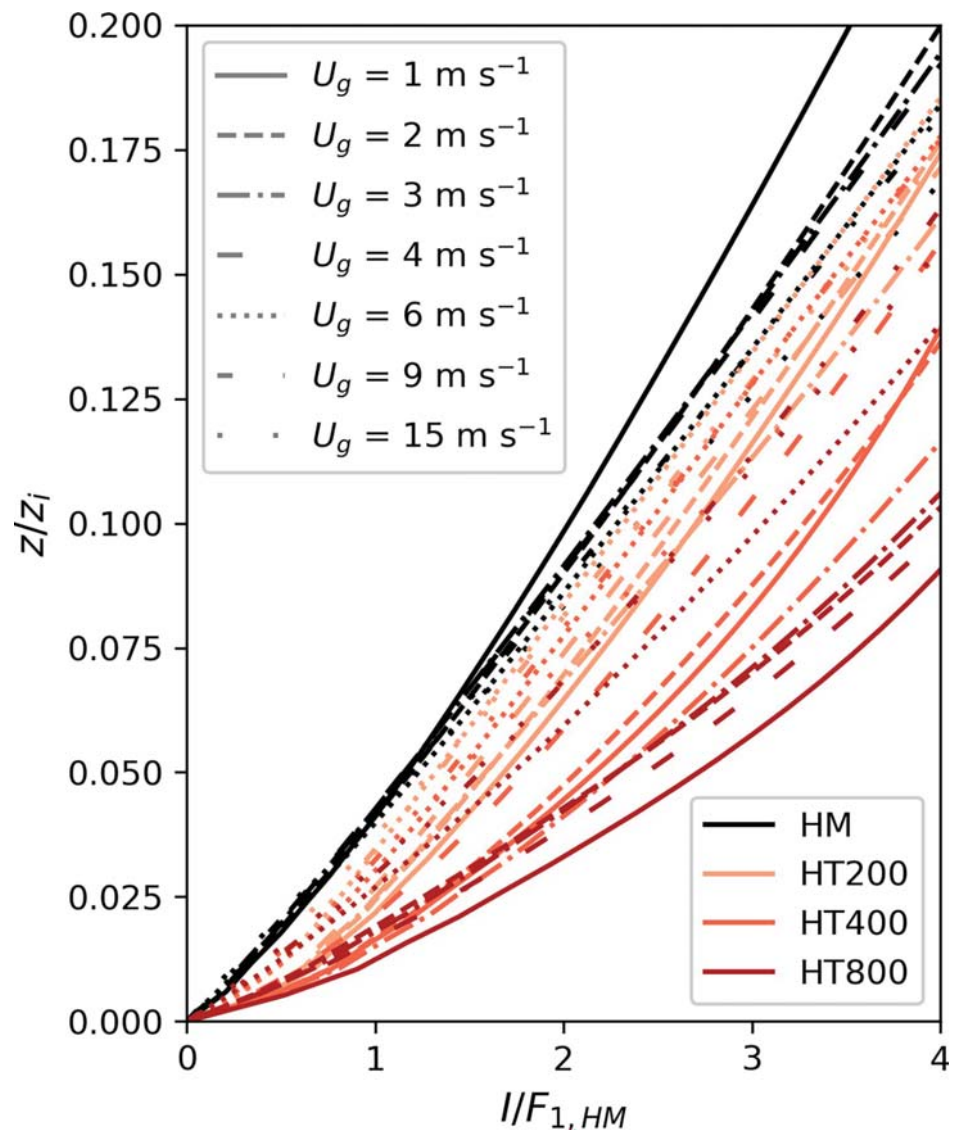


Fig 3. Vertical profiles of the imbalance all normalized with the same scaling function  $F_{1, HM}$  (Eq 11, Table 2).

<https://doi.org/10.1371/journal.pone.0268097.g003>

structures develop ( $U_g \geq 3 \text{ m s}^{-1}$ ). The fit for the very unstable simulations ( $u/w_* < 0.1$ ) describes the normalized imbalance with a very high  $R^2$  of 0.996. For the corresponding fit to the less unstable conditions ( $u/w_* > 0.14$ ), the  $R^2$  value is slightly lower with 0.841.

When normalizing the imbalance additionally with  $F_{3,c}$  or  $F_{3,r}$ , respectively, the vertical profiles of imbalance collapse similar to when they are normalized with different  $F_i$  scaling functions for each stability, as shown in Fig 6. In this case, the remaining imbalance can be described following Eq (15):

$$F_{2,N} = i_N \frac{z}{z_i} + j_N, \tag{15}$$

with  $i_N = 20.2$  and  $j_N = 0.153$ .

All characteristic variables that are relevant for our simulations are summarized in Table 2.

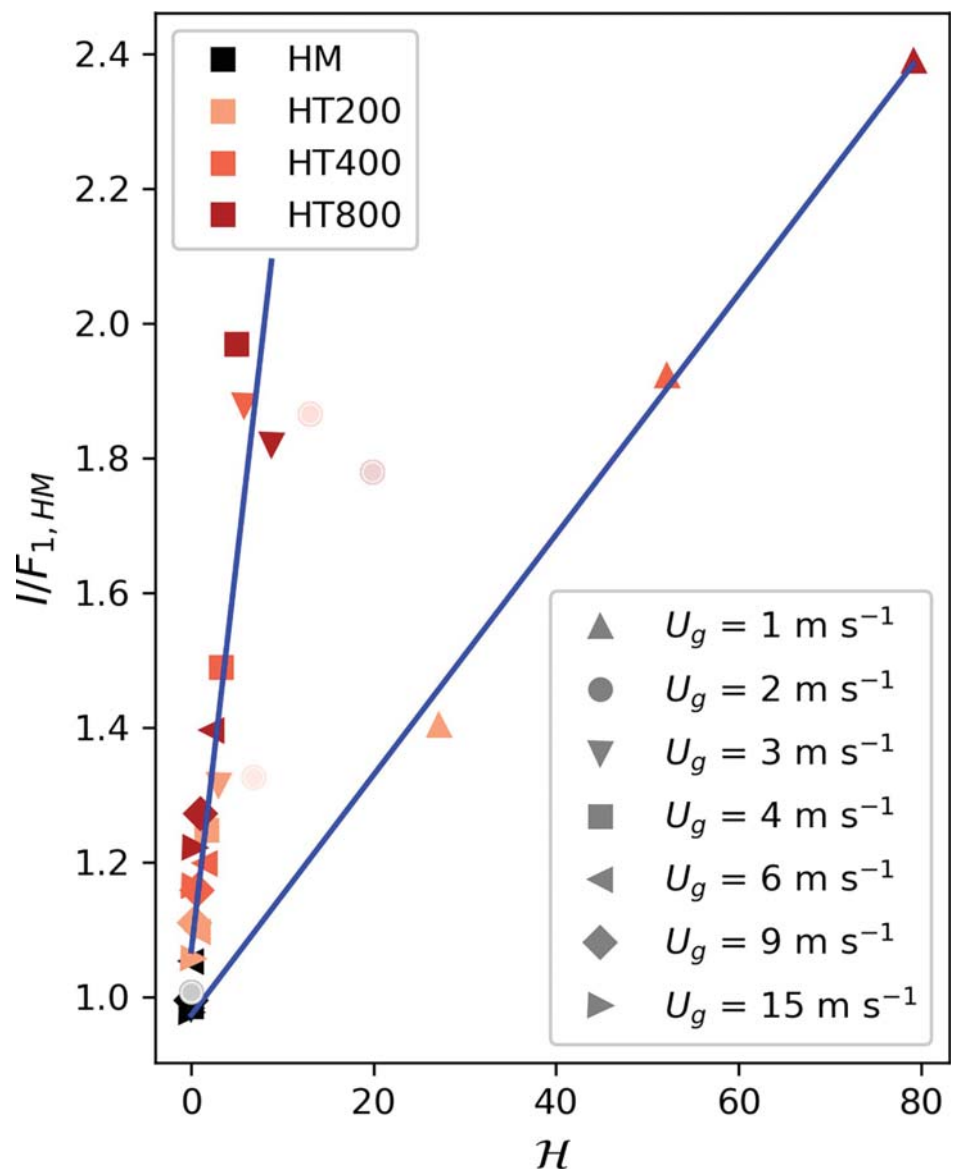


**Fig 4.** Dependence of the imbalances at  $0.04 z_i$  all normalized with the same scaling function  $F_{1, HM}$  (Eq 11, Table 1) on the heterogeneity parameter  $H$ . The data is separated into two groups: (1) simulations with  $U_g = 1 \text{ m s}^{-1}$  that show cellular shaped secondary circulations and (2) simulations with  $U_g \geq 3 \text{ m s}^{-1}$  simulation that show roll-shaped secondary circulations. Simulations with  $U_g = 2 \text{ m s}^{-1}$  are discarded because they show no clearly cellular nor roll-shaped structures. The two blue lines show the fits of the third scaling function to the two groups ( $F_{3,c}$  and  $F_{3,r}$ , Eqs 13–14).

<https://doi.org/10.1371/journal.pone.0268097.g004>

## Discussion

The reference models derived by fitting one curve for each heterogeneity scale are a more direct way to parametrize the energy imbalance than the new model, as they rely on fewer assumptions. Specifically, they are tailored to each heterogeneity scale and do not rely on the additional assumption that the magnitude of the SEB gap relates to the heterogeneity scale. However, it is not practical to use as a correction method to real measurements because it is only applicable to the discrete heterogeneity scales covered in this study. This means, that for each study case, there is a need to re-derive the corresponding scaling relation.

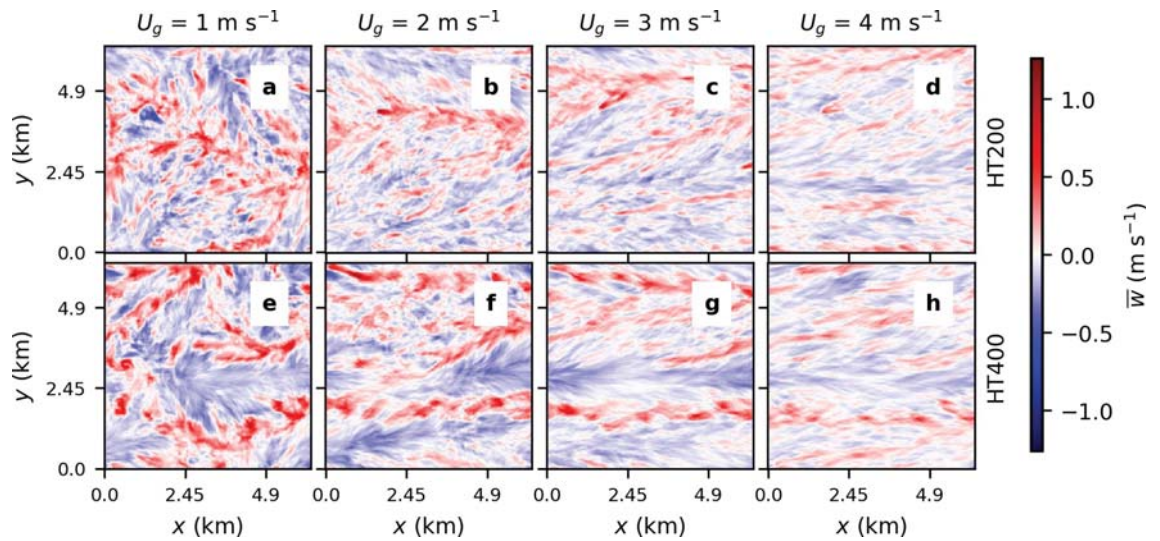


**Fig 5. Exemplary horizontal cross-sections of the half-hourly averaged vertical wind speed  $w$  at  $0.04 z_i$  for HT200 and HT400 simulations with  $U_g$  up to  $4 \text{ m s}^{-1}$ .**

<https://doi.org/10.1371/journal.pone.0268097.g005>

Alternatively, using the new method proposed in this work that adds a third scaling function to parametrize the imbalance as a function of the heterogeneity parameter to account for the surface characteristics which facilitates the generalization of the correction method to EC towers surrounded by landscapes featuring any characteristic heterogeneity scale. However, because our dataset only covered heterogeneity length scales up to  $L_h = 800 \text{ m}$ , which corresponds to  $0.57 z_i$  on average, it is questionable whether the resulting scaling function  $F_3$  would hold for larger heterogeneity length scales. Zhou et al. [76] investigated the relation between the scale of surface heterogeneity and the SEB gap and found that the SEB gap increases with heterogeneity length scale, reaching its maximum when the heterogeneity length scale is of the order of the boundary layer height, and decreases again, with even larger heterogeneity length scales. Our results confirm that the imbalance increases with the heterogeneity scale, especially under very unstable conditions (Fig 2A, Table 2), at least up to  $L_h = 0.57 z_i$  which is the heterogeneity scale our study is limited to.

While the new model is very flexible regarding the landscape heterogeneity scale, it is not applicable to all atmospheric conditions. This is because we were unable to define the scaling function  $F_3$  for the atmospheric conditions that cause sub-mesoscale circulations to form neither uniquely cellular nor roll-shaped. While Margairaz et al. [81] found that different geostrophic forcing leads to clearly cellular or roll-like structures using the roll factor defined by Salesky et al. [88], there is a transition zone in which the structures could not be clearly assigned to a cell or roll regime. In our analysis, we therefore excluded the simulations with  $U_g = 2 \text{ m s}^{-1}$ . Several studies found the transition from cellular to roll-like structures to be rather sharp, occurring somewhere between  $-z_i/L = 4.5$  and  $-z_i/L = 45$  [89] or  $-z_i/L = 8$  and  $-z_i/L = 65$  [90], or at around  $-z_i/L = 25$ . Other studies have found the transition to occur more gradually with transitional structures or co-existing rolls and cells for  $-z_i/L = 14.1$  [91], or for  $-z_i/L < 21$  [92]. For better comparison, we converted  $u_* / w_*$  to  $-z_i/L$  for our simulations using

$$-\frac{z_i}{L} = \kappa \left( \frac{u_*}{w_*} \right)^{-3}, \tag{16}$$

where  $\kappa$  is the von Kármán constant (0.4) [93]. The resulting  $-z_i/L$  values are shown in Table 2.

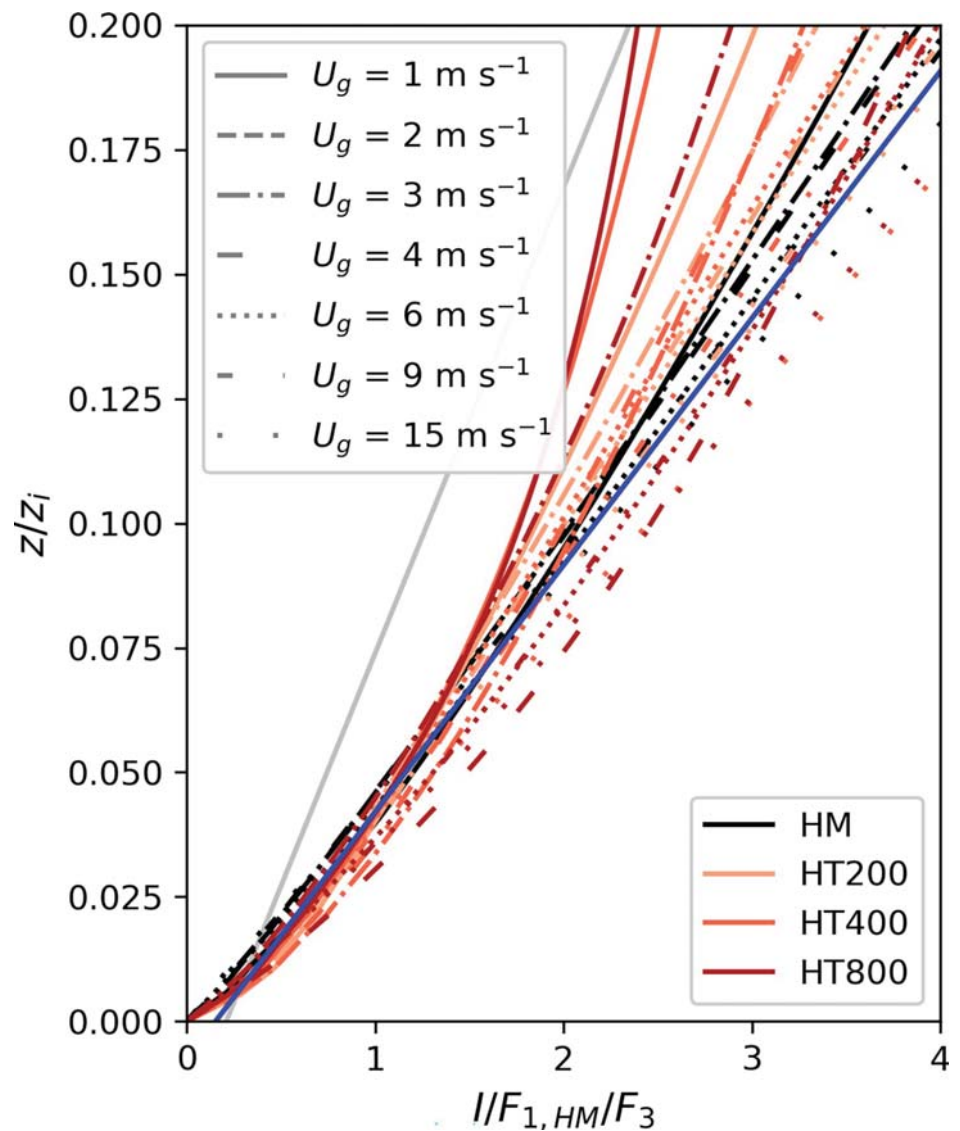


**Fig 6.** Vertical profiles of the imbalance all normalized with the same scaling function  $F_{1, HM}$  (Eq 11, Table 1) and the respective scaling functions  $F_{3, c}$  or  $F_{3, r}$  (Eqs 13–14). The blue line shows the fitted scaling function  $F_{2, N}$  (Eq 15). The scaling function derived by De Roo et al. [58] is shown in grey for comparison.

<https://doi.org/10.1371/journal.pone.0268097.g006>

For the simulations with  $U_g = 2 \text{ m s}^{-1}$ ,  $-z_i/L$  varies between 156.17 and 338.84, indicating that the transition to clearly roll-like structures occurs at larger  $-z_i/L$  values than reported by other studies. The model presented in this study can be applied to correct field measurements under unstable and free convective atmospheric conditions with  $u^*/w_* < 0.1$  (or  $-z_i/L > 400$ ) using  $F_{3, c}$  or  $u^*/w_* > 0.14$  (or  $-z_i/L < 145$ ) using  $F_{3, r}$ .

To apply the correction method, a certain amount of information on the atmospheric conditions and the surrounding landscape is required. The atmospheric conditions are considered in  $F_1$ , using  $u^*/w_*$  which can be calculated from the EC measurements similar to Eqs 8–9.  $F_2$  is a function of  $z/z_i$  which means that  $z_i$  needs to be known, which cannot be derived from EC measurements, only. Mauder et al. [61] already tested the correction method proposed by De Roo et al. [58] using ceilometer measurements of  $z_i$ . For one site where no ceilometer

measurements were available, they followed the method of Batchvarova and Gryning [94] to calculate  $z_i$  using radiosonde measurements of the morning temperature gradient. They found the correction method leading to a good energy balance closure, even though the radiosonde measurements were taken at a distance of 170 km. Finally, the characteristic heterogeneity parameter can be derived using remote sensing methods or already available land cover maps [60]. At permanent measurement sites with continuous flux measurements, the temperature amplitude can be derived by performing ground-based measurements of surface temperature over the different landcover types surrounding the tower. In extensive measurement campaigns, additional airborne measurements can provide information on the temperature amplitude [80]. If additional measurements are too costly, however, it is also possible to model the surface temperature using the radiation measurements and landcover characteristics [95–97]. What is clear from these results, is that for accurate SEB studies, the use of single point measurements is not sufficient, but obtaining spatial information of the surroundings as well as from the flow is proven to be critical. This is a strong motivation for a paradigm change in the standard single point EC measurement approaches.

To compare the performance of our newly developed model with the reference models and with the parametrization developed by De Roo et al. 2018, we computed the dispersive flux  $H_d$  using the scaling functions derived by the different approaches with

$$H_d = \frac{F_1 F_2 F_3}{1 - F_1 F_2 F_3} H. \quad (17)$$

The share of  $H$  and  $H_d$  in  $H_s$ , i.e. the total available heat flux, is shown in Fig 7. Without any correction,  $H$  is on average  $90.24 \pm 4.77\%$  of the total heat flux at  $0.04 z/z_i$ . With  $H_d$  calculated using the reference models based on De Roo et al. [58], we obtain  $H + H_{d,R} = 99.49 \pm 0.86\%$ . Reaching nearly 100% means that the energy balance gap is almost closed. At the same time, the standard deviation becomes significantly smaller, indicating that the method captured the deviations in the energy balance gap well. The use of our newly developed model for imbalance calculation gives similar results with  $H + H_{d,N} = 99.53 \pm 0.87\%$ . This shows that the newly developed model, which is much more flexible in its application to measurements, achieves just as good results as the reference models.

Using the scaling functions defined by De Roo et al. [58] (Eqs 3–4) results in  $H + H_{d,DR} = 101.28 \pm 4.2\%$ . This shows that the method of De Roo et al. [58] generally works well with our data set, but it slightly overestimates the energy balance gap on average. This correction method has already been tested on EC measurements by Mauder et al. [61] who also found the method to yield good results. Furthermore, it does not capture the deviation of the imbalance due to heterogeneity as shown in Fig 7, which is also reflected in the almost unchanged standard deviation. This is to be expected since this method was developed for homogeneous surfaces only. However, we do not recommend combining the scaling functions defined in De Roo et al. [58] and  $F_3$  derived in this study to address the effect of the heterogeneity as it leads to a clear overcorrection with  $H + H_{d,DR,N} = 106.34 \pm 2.41\%$ .

## Conclusion

We extended the energy balance gap correction method initially developed by De Roo et al. [58] taking into account the effects of spatial surface heterogeneity onto the atmospheric flow. We compared our new model to the reference models that are based on the already existing approach. The use of the reference models resulted in sets of two scaling functions for different heterogeneity scales, respectively. This approach is the more direct way to determine the imbalance and produces very good results. However, those sets of scaling functions are

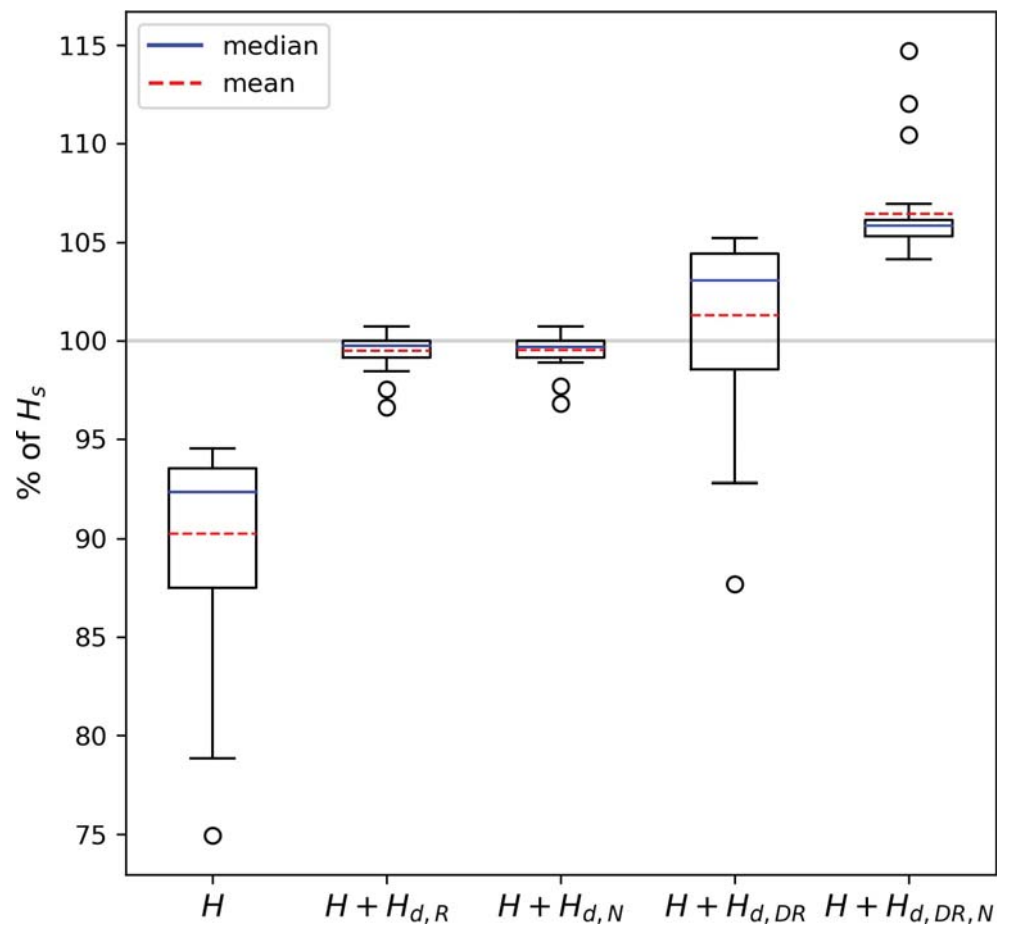


**Fig 7. Comparison of different correction methods.** The distribution of the heat flux  $H$  among all simulations is shown in box plots, where the blue line represents the median and the dashed red line represents the mean. At the very left, the distribution of the uncorrected  $H$  at  $0.04 z_i$  is shown. In second and third place, the  $H$  corrected with our approaches A and B are shown. In the fourth place,  $H$  corrected with the method by De Roo et al. [58] is shown. At the very right,  $H$  is corrected with a combination of  $F_1$  and  $F_2$  derived by De Roo et al. [58] and  $F_3$  derived in approach B in this study.

<https://doi.org/10.1371/journal.pone.0268097.g007>

restricted to the distinct heterogeneity scales used in this study, which is why this approach is not transferable to all characteristic continuously distributed heterogeneity scales of the landscape surrounding an EC system, i.e. an area of about  $20 \times 20$  km [20, 60]. Our new model proved to yield similar results and its application to real-world EC tower sites is very flexible, since a third scaling function characterizing the influence of heterogeneity was introduced. Therefore, this correction method can be used for a wide range of characteristic heterogeneity scales of a landscape surrounding an EC tower. To apply the correction method, the atmospheric stability parameter  $u^*/w^*$ , the boundary layer height  $z_i$ , the heterogeneity scale  $L_h$ , and the amplitude of the surface temperature  $\Delta T$  need to be known that can be either calculated from the EC measurements together with nearby operational radiosonde measurements or by using a ceilometer, and remotely-sensed land-surface-temperature data products.

## Author Contributions

**Conceptualization:** Luise Wanner, Matthias Mauder.

**Data curation:** Marc Calaf.

**Formal analysis:** Luise Wanner.

**Investigation:** Luise Wanner, Matthias Mauder.

**Methodology:** Luise Wanner, Matthias Mauder.

**Software:** Luise Wanner, Marc Calaf.

**Supervision:** Matthias Mauder.

**Writing – original draft:** Luise Wanner.

**Writing – review & editing:** Marc Calaf, Matthias Mauder.

## References

1. Arneeth A, Mercado L, Kattge J, Booth BBB. Future challenges of representing land-processes in studies on land-atmosphere interactions. *Biogeosciences*. 2012; 9:3587–99. <https://doi.org/10.5194/bg-9-3587-2012>
2. Cuxart J, Conangla L, Jiménez MA. Evaluation of the surface energy budget equation with experimental data and the ECMWF model in the Ebro Valley. *J Geophys Res Atmos*. 2015; 120(3):1008–22. <https://doi.org/10.1002/2014JD022296>
3. Green JK, Konings AG, Alemohammad SH, Berry J, Entekhabi D, Kolassa J, et al. Regionally strong feedbacks between the atmosphere and terrestrial biosphere. *Nat Geosci*. 2017; Volume 10:410–4. <https://doi.org/10.1038/ngeo2957> PMID: 31709007.
4. Sellers PJ, Mintz Y, Sud YC, Dalcher A. A Simple Biosphere Model (SIB) for Use within General Circulation Models. *J Atmos Sci*. 1986; 43:505–31. [https://doi.org/10.1175/1520-0469\(1986\)043<0505:ASBMFU>2.0.CO;2](https://doi.org/10.1175/1520-0469(1986)043<0505:ASBMFU>2.0.CO;2)
5. Cremonese E, Filippa G, Galvagno M, Siniscalco C, Oddi L, Di Morra Cella U, et al. Heat wave hinders green wave: The impact of climate extreme on the phenology of a mountain grassland. *Agricultural and Forest Meteorology*. 2017; 247:320–30. <https://doi.org/10.1016/j.agrformet.2017.08.016>
6. Reichstein M, Ciais P, Papale D, Valentini R, Running S, Viovy N, et al. Reduction of ecosystem productivity and respiration during the European summer 2003 climate anomaly: a joint flux tower, remote sensing and modelling analysis. *Global Change Biol*. 2007; 13:634–51. <https://doi.org/10.1111/j.1365-2486.2006.01224.x>
7. Qu L, Chen J, Dong G, Jiang S, Li L, Guo J, et al. Heat waves reduce ecosystem carbon sink strength in a Eurasian meadow steppe. *Environ Res*. 2016; 144:39–48. Epub 2015/09/29. <https://doi.org/10.1016/j.envres.2015.09.004> PMID: 26392406.
8. van Gorsel E, Wolf S, Cleverly J, Isaac P, Haverd V, Ewenz C, et al. Carbon uptake and water use in woodlands and forests in southern Australia during an extreme heat wave event in the “Angry Summer” of 2012/2013. *Biogeosciences*. 2016; 13:5947–64. <https://doi.org/10.5194/bg-13-5947-2016>
9. Fu Z, Ciais P, Bastos A, Stoy PC, Yang H, Green JK, et al. Sensitivity of gross primary productivity to climatic drivers during the summer drought of 2018 in Europe. *Philos Trans R Soc Lond B Biol Sci*. 2020; 375:20190747. Epub 2020/09/07. <https://doi.org/10.1098/rstb.2019.0747> PMID: 32892724.
10. Bernacchi CJ, Hollinger SE, Meyers T. The conversion of the corn/soybean ecosystem to no-till agriculture may result in a carbon sink. *Global Change Biol*. 2005; 0:051013014052001-??. <https://doi.org/10.1111/j.1365-2486.2005.01050.x>
11. Bernacchi CJ, Hollinger SE, Meyers TP. The conversion of the corn/soybean ecosystem to no-till agriculture may result in a carbon sink. *Global Change Biol*. 2006; 12:1585–6. <https://doi.org/10.1111/j.1365-2486.2006.01195.x>
12. Ceschia E, Béziat P, Dejoux JF, Aubinet M, Bernhofer C, Bodson B, et al. Management effects on net ecosystem carbon and GHG budgets at European crop sites. *Agriculture, Ecosystems & Environment*. 2010; 139:363–83. <https://doi.org/10.1016/j.agee.2010.09.020>
13. Graham SL, Kochendorfer J, McMillan AM, Duncan MJ, Srinivasan MS, Hertzog G. Effects of agricultural management on measurements, prediction, and partitioning of evapotranspiration in irrigated grasslands. *Agricultural Water Management*. 2016; 177:340–7. <https://doi.org/10.1016/j.agwat.2016.08.015>

14. O'Dell D, Eash NS, Hicks BB, Oetting JN, Sauer TJ, Lambert DM, et al. Conservation agriculture as a climate change mitigation strategy in Zimbabwe. *International Journal of Agricultural Sustainability*. 2020; 18:250–65. <https://doi.org/10.1080/14735903.2020.1750254>
15. Stork M, Menzel L. Analysis and simulation of the water and energy balance of intense agriculture in the Upper Rhine valley, south-west Germany. *Environ Earth Sci*. 2016; 75. <https://doi.org/10.1007/s12665-016-5980-z>
16. Baldocchi DD. Assessing the eddy covariance technique for evaluating carbon dioxide exchange rates of ecosystems: past, present and future. *Global Change Biol*. 2003; 9:479–92. <https://doi.org/10.1046/j.1365-2486.2003.00629.x>
17. Aubinet M, Vesala T, Papale D. *Eddy Covariance*. Dordrecht: Springer Netherlands; 2012.
18. Mauder M, Desjardins RL, MacPherson I. Scale analysis of airborne flux measurements over heterogeneous terrain in a boreal ecosystem. *J Geophys Res Atmos*. 2007; 112. <https://doi.org/10.1029/2006JD008133>
19. Hendricks-Franssen HJ, Stöckli R, Lehner I, Rotenberg E, Seneviratne SI. Energy balance closure of eddy-covariance data: A multisite analysis for European FLUXNET stations. *Agricultural and Forest Meteorology*. 2010; 150(12):1553–67. <https://doi.org/10.1016/j.agrformet.2010.08.005>
20. Stoy PC, Mauder M, Foken T, Marcolla B, Boegh E, Ibrom A, et al. A data-driven analysis of energy balance closure across FLUXNET research sites: The role of landscape scale heterogeneity. *Agricultural and Forest Meteorology*. 2013; 171–172:137–52. <https://doi.org/10.1016/j.agrformet.2012.11.004>
21. Soltani M, Mauder M, Laux P, Kunstmann H. Turbulent flux variability and energy balance closure in the TERENO prealpine observatory: a hydrometeorological data analysis. *Theor Appl Climatol*. 2018; 133(3–4):937–56. <https://doi.org/10.1007/s00704-017-2235-1>
22. Laubach J, Raschendorfer M, Kreilein H, Gravenhorst G. Determination of heat and water vapour fluxes above a spruce forest by eddy correlation. *Agricultural and Forest Meteorology*. 1994; 71(3–4):373–401. [https://doi.org/10.1016/0168-1923\(94\)90021-3](https://doi.org/10.1016/0168-1923(94)90021-3)
23. Goulden ML, Munger JW, Fan S-M, Daube BC, Wofsy SC. Measurements of carbon sequestration by long-term eddy covariance: methods and a critical evaluation of accuracy. *Global Change Biol*. 1996; 2(3):169–82. <https://doi.org/10.1111/j.1365-2486.1996.tb00070.x>
24. Kochendorfer J, Meyers TP, Frank J, Massman WJ, Heuer MW. How Well Can We Measure the Vertical Wind Speed? Implications for Fluxes of Energy and Mass. *Boundary-Layer Meteorol*. 2012; 145(2):383–98. <https://doi.org/10.1007/s10546-012-9738-1>
25. Nakai T, Shimoyama K. Ultrasonic anemometer angle of attack errors under turbulent conditions. *Agricultural and Forest Meteorology*. 2012; 162–163:14–26. <https://doi.org/10.1016/j.agrformet.2012.04.004>
26. Frank JM, Massman WJ, Ewers BE. Underestimates of sensible heat flux due to vertical velocity measurement errors in non-orthogonal sonic anemometers. *Agricultural and Forest Meteorology*. 2013; 171–172:72–81. <https://doi.org/10.1016/j.agrformet.2012.11.005>
27. Mauder M. A Comment on “How Well Can We Measure the Vertical Wind Speed? Implications for Fluxes of Energy and Mass” by Kochendorfer et al. *Boundary-Layer Meteorol*. 2013; 147(2):329–35. <https://doi.org/10.1007/s10546-012-9794-6>
28. Liebethal C, Huwe B, Foken T. Sensitivity analysis for two ground heat flux calculation approaches. *Agricultural and Forest Meteorology*. 2005; 132(3–4):253–62. <https://doi.org/10.1016/j.agrformet.2005.08.001>
29. Kohsiek W, Liebethal C, Foken T, Vogt R, Oncley SP, Bernhofer C, et al. The Energy Balance Experiment EBEX-2000. Part III: Behaviour and quality of the radiation measurements. *Boundary-Layer Meteorol*. 2007; 123(1):55–75. <https://doi.org/10.1007/s10546-006-9135-8>
30. Foken T. The Energy Balance Closure Problem: An Overview. *Ecological Applications*. 2008; 18(6):1351–67. <https://doi.org/10.1890/06-0922.1> PMID: 18767615
31. Schmid HP. Experimental design for flux measurements: matching scales of observations and fluxes. *Agricultural and Forest Meteorology*. 1997; 87:179–200. [https://doi.org/10.1016/S0168-1923\(97\)00011-7](https://doi.org/10.1016/S0168-1923(97)00011-7)
32. Lindroth A, Mölder M, Lagergren F. Heat storage in forest biomass improves energy balance closure. *Biogeosciences*. 2010; 7(1):301–13. <https://doi.org/10.5194/bg-7-301-2010>
33. Leuning R, van Gorsel E, Massman WJ, Isaac PR. Reflections on the surface energy imbalance problem. *Agricultural and Forest Meteorology*. 2012; 156:65–74. <https://doi.org/10.1016/j.agrformet.2011.12.002>
34. Moderow U, Aubinet M, Feigenwinter C, Kolle O, Lindroth A, Mölder M, et al. Available energy and energy balance closure at four coniferous forest sites across Europe. *Theor Appl Climatol*. 2009; 98:397–412. <https://doi.org/10.1007/s00704-009-0175-0>

35. Haverd V, Cuntz M, Leuning R, Keith H. Air and biomass heat storage fluxes in a forest canopy: Calculation within a soil vegetation atmosphere transfer model. *Agricultural and Forest Meteorology*. 2007; 147:125–39. <https://doi.org/10.1016/j.agrformet.2007.07.006>
36. Mauder M, Foken T. Impact of post-field data processing on eddy covariance flux estimates and energy balance closure. *metz*. 2006; 15(6):597–609. <https://doi.org/10.1127/0941-2948/2006/0167>
37. Mauder M, Liebethal C, Göckede M, Leps J-P, Beyrich F, Foken T. Processing and quality control of flux data during LITFASS-2003. *Boundary-Layer Meteorol*. 2006; 121(1):67–88. <https://doi.org/10.1007/s10546-006-9094-0>
38. Twine TE, Kustas WP, Norman JM, Cook DR, Houser PR, Meyers TP, et al. Correcting eddy-covariance flux underestimates over a grassland. *Agricultural and Forest Meteorology*. 2000; 103:279–300. [https://doi.org/10.1016/S0168-1923\(00\)00123-4](https://doi.org/10.1016/S0168-1923(00)00123-4)
39. Mauder M, Oncley SP, Vogt R, Weidinger T, Ribeiro L, Bernhofer C, et al. The energy balance experiment EBEX-2000. Part II: Intercomparison of eddy-covariance sensors and post-field data processing methods. *Boundary-Layer Meteorol*. 2007; 123:29–54. <https://doi.org/10.1007/s10546-006-9139-4>
40. Mauder M, Foken T, Cuxart J. Surface-Energy-Balance Closure over Land: A Review. *Boundary-Layer Meteorol*. 2020; 9(8):3587. <https://doi.org/10.1007/s10546-020-00529-6>
41. Charuchittipan D, Babel W, Mauder M, Leps J-P, Foken T. Extension of the Averaging Time in Eddy-Covariance Measurements and Its Effect on the Energy Balance Closure. *Boundary-Layer Meteorol*. 2014; 152(3):303–27. <https://doi.org/10.1007/s10546-014-9922-6>
42. Metzger M, Holmes H. Time Scales in the Unstable Atmospheric Surface Layer. *Boundary-Layer Meteorol*. 2007; 126:29–50. <https://doi.org/10.1007/s10546-007-9219-0>
43. Stull RB. *An Introduction to Boundary Layer Meteorology*. Dordrecht: Springer; 1988.
44. Kaimal JC, Finnigan JJ. *Atmospheric Boundary Layer Flows*. Oxford University Press; 1994.
45. Eder F, De Roo F, Rotenberg E, Yakir D, Schmid HP, Mauder M. Secondary circulations at a solitary forest surrounded by semi-arid shrubland and their impact on eddy-covariance measurements. *Agricultural and Forest Meteorology*. 2015; 211–212:115–27. <https://doi.org/10.1016/j.agrformet.2015.06.001>
46. Patton EG, Sullivan PP, Shaw RH, Finnigan JJ, Weil JC. Atmospheric Stability Influences on Coupled Boundary Layer and Canopy Turbulence. *J Atmos Sci*. 2016; 73(4):1621–47. <https://doi.org/10.1175/JAS-D-15-0068.1>
47. Mahrt L. Flux Sampling Errors for Aircraft and Towers. *J Atmos Oceanic Technol*. 1998; 15(2):416–29. [https://doi.org/10.1175/1520-0426\(1998\)015<0416:FSEFAA>2.0.CO;2](https://doi.org/10.1175/1520-0426(1998)015<0416:FSEFAA>2.0.CO;2)
48. Mauder M, Desjardins RL, Pattey E, Gao Z, van Haarlem R. Measurement of the Sensible Eddy Heat Flux Based on Spatial Averaging of Continuous Ground-Based Observations. *Boundary-Layer Meteorol*. 2008; 128(1):151–72. <https://doi.org/10.1007/s10546-008-9279-9>
49. Steinfeld G, Letzel MO, Raasch S, Kanda M, Inagaki A. Spatial representativeness of single tower measurements and the imbalance problem with eddy-covariance fluxes: results of a large-eddy simulation study. *Boundary-Layer Meteorol*. 2007; 123(1):77–98. <https://doi.org/10.1007/s10546-006-9133-x>
50. Kenny WT, Bohrer G, Morin TH, Vogel CS, Matheny AM, Desai AR. A Numerical Case Study of the Implications of Secondary Circulations to the Interpretation of Eddy-Covariance Measurements Over Small Lakes. *Boundary-Layer Meteorol*. 2017; 165(2):311–32. <https://doi.org/10.1007/s10546-017-0268-8>
51. Bou-Zeid E, Anderson W, Katul GG, Mahrt L. The Persistent Challenge of Surface Heterogeneity in *Boundary-Layer Meteorology: A Review*. *Boundary-Layer Meteorol*. 2020; 177(2–3):227–45. <https://doi.org/10.1007/s10546-020-00551-8>
52. Kanda M, Inagaki A, Letzel MO, Raasch S, Watanabe T. LES Study of the Energy Imbalance Problem with Eddy Covariance Fluxes. *Boundary-Layer Meteorol*. 2004; 110(3):381–404. <https://doi.org/10.1023/B:BOUN.0000007225.45548.7a>
53. Inagaki A, Letzel MO, Raasch S, Kanda M. Impact of Surface Heterogeneity on Energy Imbalance: A Study Using LES. *JMSJ*. 2006; 84(1):187–98. <https://doi.org/10.2151/jmsj.84.187>
54. Finnigan JJ, Clement R, Malhi Y, Leuning R, Cleugh HA. A Re-Evaluation of Long-Term Flux Measurement Techniques Part I: Averaging and Coordinate Rotation. *Boundary-Layer Meteorol*. 2003; 107(1):1–48. <https://doi.org/10.1023/A:1021554900225>
55. Mahrt L. Computing turbulent fluxes near the surface: Needed improvements. *Agricultural and Forest Meteorology*. 2010; 150:501–9. <https://doi.org/10.1016/j.agrformet.2010.01.015>
56. Ingwersen J, Steffens K, Högy P, Warrach-Sagi K, Zhunusbayeva D, Poltoradnev M, et al. Comparison of Noah simulations with eddy covariance and soil water measurements at a winter wheat stand. *Agricultural and Forest Meteorology*. 2011; 151:345–55. <https://doi.org/10.1016/j.agrformet.2010.11.010>

57. Wohlfahrt G, Irschick C, Thalinger B, Hörtnagl L, Obojes N, Hammerle A. Insights from Independent Evapotranspiration Estimates for Closing the Energy Balance: A Grassland Case Study. *Vadose Zone Journal*. 2010; 9:1025–33. <https://doi.org/10.2136/vzj2009.0158>
58. De Roo F, Zhang S, Huq S, Mauder M. A semi-empirical model of the energy balance closure in the surface layer. *PLoS ONE*. 2018; 13(12):e0209022. <https://doi.org/10.1371/journal.pone.0209022> PMID: 30540830.
59. Huang J, Lee X, Patton EG. A Modelling Study of Flux Imbalance and the Influence of Entrainment in the Convective Boundary Layer. *Boundary-Layer Meteorol*. 2008; 127(2):273–92. <https://doi.org/10.1007/s10546-007-9254-x>
60. Panin GN, Bernhofer C. Parametrization of turbulent fluxes over inhomogeneous landscapes. *Izv Atmos Ocean Phys*. 2008; 44(6):701–16. <https://doi.org/10.1134/S0001433808060030>
61. Mauder M, Ibrom A, Wanner L, Roo F de, Brügger P, Kiese R, et al. Options to correct local turbulent flux measurements for large-scale fluxes using a LES-based approach. *Geosci Model Dev Discuss* [preprint]. 2021. <https://doi.org/10.5194/amt-2021-126>
62. Eder F, Roo F de, Kohnert K, Desjardins RL, Schmid HP, Mauder M. Evaluation of Two Energy Balance Closure Parametrizations. *Boundary-Layer Meteorol*. 2014; 151:195–219. <https://doi.org/10.1007/s10546-013-9904-0>
63. Choi M, Kustas WP, Anderson MC, Allen RG, Li F, Kjaersgaard JH. An intercomparison of three remote sensing-based surface energy balance algorithms over a corn and soybean production region (Iowa, U. S.) during SMACEX. *Agricultural and Forest Meteorology*. 2009; 149:2082–97. <https://doi.org/10.1016/j.agrformet.2009.07.002>
64. Margairaz F, Pardyjak ER, Calaf M. Surface Thermal Heterogeneities and the Atmospheric Boundary Layer: The Thermal Heterogeneity Parameter. *Boundary-Layer Meteorol*. 2020; 177(1):49–68. <https://doi.org/10.1007/s10546-020-00544-7>
65. Schalkwijk J, Jonker HJJ, Siebesma AP. An Investigation of the Eddy-Covariance Flux Imbalance in a Year-Long Large-Eddy Simulation of the Weather at Cabauw. *Boundary-Layer Meteorol*. 2016; 160(1):17–39. <https://doi.org/10.1007/s10546-016-0138-9>
66. Sührling M, Metzger S, Xu K, Durden D, Desai A. Trade-Offs in Flux Disaggregation: A Large-Eddy Simulation Study. *Boundary-Layer Meteorol*. 2018; 170(1):69–93. <https://doi.org/10.1007/s10546-018-0387-x>
67. Mauder M, Jegede OO, Okogbue EC, Wimmer F, Foken T. Surface energy balance measurements at a tropical site in West Africa during the transition from dry to wet season. *Theor Appl Climatol*. 2007; 89(3–4):171–83. <https://doi.org/10.1007/s00704-006-0252-6>
68. Foken T, Mauder M, Liebethal C, Wimmer F, Beyrich F, Leps J-P, et al. Energy balance closure for the LITFASS-2003 experiment. *Theor Appl Climatol*. 2010; 101(1–2):149–60. <https://doi.org/10.1007/s00704-009-0216-8>
69. Panin GN, Tetzlaff G, Raabe A. Inhomogeneity of the Land Surface and Problems in the Parameterization of Surface Fluxes in Natural Conditions. *Theor Appl Climatol*. 1998; 60(1–4):163–78. <https://doi.org/10.1007/s007040050041>
70. Morrison T, Calaf M, Higgins CW, Drake SA, Perelet A, Pardyjak E. The Impact of Surface Temperature Heterogeneity on Near-Surface Heat Transport. *Boundary-Layer Meteorol*. 2021; 180:247–72. <https://doi.org/10.1007/s10546-021-00624-2>
71. Wilson K, Goldstein A, Falge E, Aubinet M, Baldocchi D, Berbigier P, et al. Energy balance closure at FLUXNET sites. *Agricultural and Forest Meteorology*. 2002; 113(1–4):223–43. [https://doi.org/10.1016/S0168-1923\(02\)00109-0](https://doi.org/10.1016/S0168-1923(02)00109-0)
72. Barr AG, Morgenstern K, Black TA, McCaughey JH, Nesic Z. Surface energy balance closure by the eddy-covariance method above three boreal forest stands and implications for the measurement of the CO<sub>2</sub> flux. *Agricultural and Forest Meteorology*. 2006; 140:322–37. <https://doi.org/10.1016/j.agrformet.2006.08.007>
73. Stoy PC, Katul GG, Siqueira MBS, Juang J-Y, Novick KA, McCarthy HR, et al. Separating the effects of climate and vegetation on evapotranspiration along a successional chronosequence in the southeastern US. *Global Change Biol*. 2006; 12:2115–35. <https://doi.org/10.1111/j.1365-2486.2006.01244.x>
74. De Roo F, Mauder M. The influence of idealized surface heterogeneity on virtual turbulent flux measurements. *Atmos Chem Phys*. 2018; 18(7):5059–74. <https://doi.org/10.5194/acp-18-5059-2018>
75. Zhou Y, Li D, Liu H, Li X. Diurnal Variations of the Flux Imbalance Over Homogeneous and Heterogeneous Landscapes. *Boundary-Layer Meteorol*. 2018; 168(3):417–42. <https://doi.org/10.1007/s10546-018-0358-2>
76. Zhou Y, Li D, Li X. The Effects of Surface Heterogeneity Scale on the Flux Imbalance under Free Convection. *J Geophys Res Atmos*. 2019. <https://doi.org/10.1029/2018JD029550>

77. Letzel MO, Raasch S. Large Eddy Simulation of Thermally Induced Oscillations in the Convective Boundary Layer. *J Atmos Sci*. 2003; 60(18):2328–41. [https://doi.org/10.1175/1520-0469\(2003\)060<2328:LESOTI>2.0.CO;2](https://doi.org/10.1175/1520-0469(2003)060<2328:LESOTI>2.0.CO;2)
78. Katul GG. The anatomy of large-scale motion in atmospheric boundary layers. *J Fluid Mech*. 2019; 858:1–4. <https://doi.org/10.1017/jfm.2018.731>
79. Maronga B, Gryscha M, Heinze R, Hoffmann F, Kanani-Sühring F, Keck M, et al. The Parallelized Large-Eddy Simulation Model (PALM) version 4.0 for atmospheric and oceanic flows: model formulation, recent developments, and future perspectives. *Geosci Model Dev*. 2015; 8(8):2515–51. <https://doi.org/10.5194/gmd-8-2515-2015>
80. Butterworth BJ, Desai AR, Metzger S, Townsend PA, Schwartz MD, Petty GW, et al. Connecting Land-Atmosphere Interactions to Surface Heterogeneity in CHEESEHEAD19. *Bull Amer Meteor Soc*. 2021; 102(2):E421–E445. <https://doi.org/10.1175/BAMS-D-19-0346.1>
81. Margairaz F, Pardyjak ER, Calaf M. Surface Thermal Heterogeneities and the Atmospheric Boundary Layer: The Relevance of Dispersive Fluxes. *Boundary-Layer Meteorol*. 2020; 175:369–95. <https://doi.org/10.1007/s10546-020-00509-w>
82. Moeng C-H. A Large-Eddy-Simulation Model for the Study of Planetary Boundary-Layer Turbulence. *J Atmos Sci*. 1984; 41:2052–62. [https://doi.org/10.1175/1520-0469\(1984\)041<2052:ALESMF>2.0.CO;2](https://doi.org/10.1175/1520-0469(1984)041<2052:ALESMF>2.0.CO;2)
83. Albertson JD, Parlange MB. Surface length scales and shear stress: Implications for land-atmosphere interaction over complex terrain. *Water Resour Res*. 1999; 35:2121–32. <https://doi.org/10.1029/1999WR900094>
84. Bou-Zeid E, Meneveau C, Parlange M. A scale-dependent Lagrangian dynamic model for large eddy simulation of complex turbulent flows. *J Fluid Mech*. 2005; 17(2):25105. <https://doi.org/10.1063/1.1839152>
85. Calaf M, Meneveau C, Parlange M. Large Eddy Simulation study of a fully developed thermal wind-turbine array boundary layer. In: Kuerten H, Geurts B, Armenio V, Fröhlich J, editors. *Direct and Large-Eddy Simulation VIII*. Dordrecht: Springer Netherlands; 2011. pp. 239–44.
86. Margairaz F, Giometto MG, Parlange MB, Calaf M. Comparison of dealiasing schemes in large-eddy simulation of neutrally stratified atmospheric flows. *Geosci Model Dev*. 2018; 11:4069–84. <https://doi.org/10.5194/gmd-11-4069-2018>
87. Brutsaert W. *Evaporation into the Atmosphere. Theory, History and Applications*. Dordrecht: Springer; 1982.
88. Salesky ST, Chamecki M, Bou-Zeid E. On the Nature of the Transition Between Roll and Cellular Organization in the Convective Boundary Layer. *Boundary-Layer Meteorol*. 2017; 163(1):41–68. <https://doi.org/10.1007/s10546-016-0220-3>
89. Deardorff JW. Numerical Investigation of Neutral and Unstable Planetary Boundary Layers. *J Atmos Sci*. 1972; 29:91–115. [https://doi.org/10.1175/1520-0469\(1972\)029<0091:NIONAU>2.0.CO;2](https://doi.org/10.1175/1520-0469(1972)029<0091:NIONAU>2.0.CO;2)
90. Khanna S, Brasseur JG. Three-Dimensional Buoyancy- and Shear-Induced Local Structure of the Atmospheric Boundary Layer. *J Atmos Sci*. 1998; 55:710–43. [https://doi.org/10.1175/1520-0469\(1998\)055<0710:TDBASI>2.0.CO;2](https://doi.org/10.1175/1520-0469(1998)055<0710:TDBASI>2.0.CO;2)
91. Park S-B, Baik J-J. Large-Eddy Simulations of Convective Boundary Layers over Flat and Urbanlike Surfaces. *J Atmos Sci*. 2014; 71:1880–92. <https://doi.org/10.1175/JAS-D-13-0191.1>
92. Grossman RL. An analysis of vertical velocity spectra obtained in the bomex fair-weather, trade-wind boundary layer. *Boundary-Layer Meteorol*. 1982; 23:323–57. <https://doi.org/10.1007/BF00121120>
93. Panofsky HA, Tennekes H, Lenschow DH, Wyngaard JC. The characteristics of turbulent velocity components in the surface layer under convective conditions. *Boundary-Layer Meteorol*. 1977; 11(3):355–61. <https://doi.org/10.1007/BF02186086>
94. Batchvarova E, Gryning S-E. Applied model for the growth of the daytime mixed layer. *Boundary-Layer Meteorol*. 1991; 56:261–74. <https://doi.org/10.1007/BF00120423>
95. Best MJ. A Model to Predict Surface Temperatures. *Boundary-Layer Meteorol*. 1998; 88:279–306. <https://doi.org/10.1023/A:1001151927113>
96. Herb WR, Janke B, Mohseni O, Stefan HG. Ground surface temperature simulation for different land covers. *Journal of Hydrology*. 2008; 356:327–43. <https://doi.org/10.1016/j.jhydrol.2008.04.020>
97. Leaf JS, Erell E. A model of the ground surface temperature for micrometeorological analysis. *Theor Appl Climatol*. 2018; 133:697–710. <https://doi.org/10.1007/s00704-017-2207-5>



## **D Towards energy-balance closure with a model of dispersive heat fluxes**

Wanner L, Jung M, Paleri S, Butterworth B, Desai A, Sühring M, Mauder M (2023): Towards Energy-Balance Closure with a Model of Dispersive Heat Fluxes, PREPRINT (Version 1) available at Research Square, doi: 10.21203/rs.3.rs-3449667/v1

This manuscript was published after the submission of this dissertation. The peer-reviewed article can be found here:

Wanner L, Jung M, Paleri S, Butterworth B, Desai A, Sühring M, Mauder M (2024): Towards Energy-Balance Closure with a Model of Dispersive Heat Fluxes, *Boundary-Layer Meteorology* 190, 25 (2024), doi: 10.1007/s10546-024-00868-8



# 1 Towards Energy-Balance Closure With a Model of Dispersive 2 Heat Fluxes

3 Luise Wanner<sup>1,2</sup> • Martin Jung<sup>3</sup> • Sreenath Paleri<sup>4,5,6</sup>, Brian J. Butterworth<sup>7</sup>, Ankur  
4 R. Desai<sup>4</sup>, Matthias Sühring<sup>8,9</sup>, Matthias Mauder<sup>1,2,10</sup>

5 Received: DD Month YEAR/ Accepted: DD Month YEAR/ Published online: DD Month YEAR  
6 © Springer Science + Business Media B. V.

## 7 Abstract

8 The energy-balance-closure problem in eddy-covariance measurements has been known  
9 for decades. It has been thoroughly investigated from different angles, resulting in  
10 approaches to reduce but not completely close the surface energy balance gap. Energy  
11 balance transport through secondary circulations has been identified as a major cause of  
12 the remaining energy imbalance, which is not captured by eddy covariance measurements  
13 and can only be measured additionally with great effort. Several models have already been  
14 developed to close the energy balance gap that account for factors affecting the magnitude

---

✉ Luise Wanner  
luise.wanner@tu-dresden.de

<sup>1</sup> Institute of Hydrology and Meteorology, TUD Dresden Technical University, SN, 01062, Germany

<sup>2</sup> Institute of Meteorology and Climate Research, Karlsruhe Institute of Technology, BY, 82467, Germany

<sup>3</sup> Department of Biogeochemical Integration, Max Planck Institute for Biogeochemistry, TH, 07745, Germany

<sup>4</sup> Department of Atmospheric and Oceanic Sciences, University of Wisconsin-Madison, WI, 53706, United States of America

<sup>5</sup> Cooperative Institute for Severe and High-Impact Weather Research and Operations, University of Oklahoma, OK, 73069, United States of America

<sup>6</sup> Atmospheric Turbulence and Diffusion Division, NOAA/Air Resources Laboratory, TN, 37830, United States of America

<sup>7</sup> Physical Sciences Laboratory, National Oceanic and Atmospheric Administration, CO, 80305, United States of America

<sup>8</sup> Institute of Meteorology and Climatology, Leibniz Universität Hannover, NI, 30167, Germany

<sup>9</sup> Pecanode GmbH, NI, 38640, Germany

<sup>10</sup> Institute of Geography and Geoecology, Karlsruhe Institute of Technology, BW, 76131, Germany

15 of the energy transport by secondary circulations. However, to our knowledge, there is  
16 currently no model that accounts thermal surface heterogeneity and that can predict the  
17 transport of both sensible and latent energy. Using a machine-learning approach, we  
18 developed a new model of energy transport by secondary circulations based on a large data  
19 set of idealized large-eddy simulations covering a wide range of unstable atmospheric  
20 conditions and surface-heterogeneity scales. In this paper, we present the development of  
21 the model and its promising test on more realistic large-eddy simulations and field  
22 measurements from the CHEESEHEAD19 project. We further show that it can be applied  
23 without additional measurements and, thus, can retrospectively be applied to other eddy  
24 covariance measurements to model energy transport through secondary circulations. Our  
25 work provides a promising mechanistic energy balance closure approach to 30-minute flux  
26 measurements.

27 **Keywords** Dispersive fluxes · Eddy Covariance · Large-eddy simulation · Machine  
28 learning · Secondary circulations

## 29 **1 Introduction**

30 The quantification of energy transport between ecosystems and the atmosphere provides  
31 an important basis for various areas of environmental science. Some examples are  
32 operational weather forecasting and climate modelling (e.g. Arneth et al. 2012; Cuxart et  
33 al. 2015; Green et al. 2017), or investigating the reaction of ecosystems to changing climate  
34 conditions (e.g. Cremonese et al. 2017; Fu et al. 2020; Qu et al. 2016; Reichstein et al.  
35 2007; van Gorsel et al. 2016) to come up with sustainable management strategies for  
36 ecosystems and adapt agriculture (e.g. Bernacchi et al. 2005; Bernacchi et al. 2006; Ceschia  
37 et al. 2010; Graham et al. 2016; O'Dell et al. 2020; Stork and Menzel 2016). For decades,  
38 the eddy covariance (EC) method has been used to quantify energy transport in the  
39 atmospheric boundary layer in terms of sensible and latent heat fluxes at the ecosystem  
40 scale as it facilitates the direct measurement of turbulent energy fluxes without disturbing  
41 the investigated ecosystem (Aubinet et al. 2012; Baldocchi 2003; Baldocchi 2014; Foken  
42 2017; Mauder et al. 2007b).

43 However, the systematic study of measurements at EC stations has shown that the  
44 surface-energy balance (SEB, balance between incoming and outgoing energy at the

45 surface in the form of radiation, heat fluxes and storage change) is usually not closed, but  
46 shows a gap of 10-30%, always in the same direction (Hendricks-Franssen et al. 2010;  
47 Soltani et al. 2018; Stoy et al. 2013). The SEB can therefore be expressed in simplified  
48 form as

$$R_{net} = H_t + \lambda E_t + G + I, \quad (1)$$

49 where  $R_{net}$  is the net radiation, which is defined to be positive during daytime,  $H_t$  and  $\lambda E_t$   
50 are the sensible and latent turbulent fluxes measured with the EC method,  $G$  is the ground  
51 heat flux and  $I$  is the remaining SEB gap (Mauder et al. 2020). The terms on the right-hand  
52 side of the equation are defined to be positive when they transport energy away from the  
53 surface.

54 The SEB gap has been the subject of research for a long time and many factors, such  
55 as systematic errors in the measurement of the vertical wind component and humidity  
56 (Frank et al. 2013; Goulden et al. 1996; Kochendorfer et al. 2012; Laubach et al. 1994;  
57 Mauder 2013; Nakai and Shimoyama 2012), which are used to calculate heat fluxes, and  
58 systematic errors in the measurement of other components of the SEB, such as radiation  
59 and ground heat flux (Foken 2008; Kohsiek et al. 2007; Liebethal et al. 2005), and the scale  
60 mismatch between the footprint of the EC measurement and the radiation measurement  
61 (Schmid 1997) have been studied. Especially for measurement towers above high  
62 vegetation, the energy storage in the air volume and biomass below the measurement  
63 instruments also plays a non-negligible role and should be captured by profile  
64 measurements of temperature and humidity (Leuning et al. 2012; Lindroth et al. 2010;  
65 Moderow et al. 2009; Xu et al. 2019). The influences of systematic measurement errors  
66 were minimized or can be accounted for by appropriate measures in the data processing  
67 (Mauder et al. 2006; Mauder and Foken 2006; Twine et al. 2000) but a significant gap in  
68 the SEB remains (Mauder et al. 2006; Mauder et al. 2007c; Mauder et al. 2020).

69 One reason for the remaining SEB gap could be the fact that the EC method, given  
70 typical approaches and measurement limitations, only captures turbulent transport: the flux  
71 is calculated as the covariance of the vertical wind speed and a scalar of interest (e.g.,  
72 temperature for the sensible heat flux  $H$  or humidity for the latent heat flux  $\lambda E$ ) from high-  
73 frequency time series. The covariance is based on the fluctuations around an average over  
74 a certain averaging period of typically 30 minutes (Aubinet et al. 1999; Mauder et al. 2020).

75 The averages of the wind speed and scalar of interest are not considered and any energy  
76 transport by structures that contribute to the mean vertical wind speed is neglected  
77 (Metzger and Holmes 2007). The temporal or spatial averaging period used to represent  
78 the Reynolds' average defines which atmospheric structures ultimately contribute to  
79 "turbulent" and which contribute to "non-turbulent" transport.

80 After assuming for a long time that energy transport in the atmospheric boundary layer  
81 (ABL) is exclusively turbulent in nature, i.e., that all relevant transport is captured by  
82 applying 30-minute averaging intervals, it has been found that large eddies, also known as  
83 secondary circulations (SCs) reach near the surface (Eder et al. 2015; Patton et al. 2016).  
84 SCs contribute to the mean wind speed at typical EC averaging periods which is why the  
85 energy transport by SCs is not considered in EC measurements and instead contributes to  
86 the SEB gap (Foken 2008; Mauder et al. 2020).

87 Two main types of SCs can be distinguished. The first type are randomly developing  
88 large eddies that are turbulent in nature but so large that they are not considered in the  
89 covariance over the averaging period and even form over homogeneous surfaces, so called  
90 turbulent organized structures (TOSs) (Inagaki et al. 2006; Kanda et al. 2004). The second  
91 type are systematically developing secondary circulations caused by differential heating  
92 from the earth surface and therefore bound in space, so called thermally-induced mesoscale  
93 circulations (TMCs) (Bou-Zeid et al. 2020; Foken 2008; Kenny et al. 2017; Mauder et al.  
94 2020). Increasing the averaging periods might sample more of the energy transported due  
95 to the randomly organized and quasi-stationary TOSs with longer time scales as they move  
96 slowly with the mean wind within the tower footprint. However, TMCs are spatially bound  
97 to surface characteristics which is why they still contribute to the mean wind even with  
98 long averaging periods as they might not be sampled by fixed-point EC tower  
99 measurements. This may explain why in some cases, increasing the averaging period had  
100 no effect on the SEB closure in some cases (Charuchittipan et al. 2014) but improved the  
101 SEB closure, though not entirely resolved it, in other cases (Finnigan et al. 2003; Mauder  
102 et al. 2006). Furthermore, increasing the averaging period in EC measurements beyond  
103 multiple hours will eventually violate the assumption of stationarity (Mauder et al. 2006;  
104 Mauder et al. 2020). Wavelet-based flux calculation approaches that incorporate longer

105 wavelength turbulent transport have been shown to improve the SEB gap, also implying a  
106 role for SCs in energy transport (Metzger et al. 2013; Xu et al. 2020).

107 The contribution of the transport by secondary circulations can be quantified by spatial  
108 measurements using an array of tower measurements or aircraft measurements  
109 (Feigenwinter et al. 2008; Mahrt 1998; Mauder et al. 2008; Paleri et al. 2022b; Steinfeld et  
110 al. 2007). However, those measurements are expensive and cannot be carried out at each  
111 EC station or over long periods. Another possibility is to model the energy transport by  
112 secondary circulations based on atmospheric and landscape parameters that can be gathered  
113 for single-tower EC measurements (e.g. Choi et al. 2009; De Roo et al. 2018; Eder et al.  
114 2014; Huang et al. 2008; Mauder et al. 2021; Panin and Bernhofer 2008).

115 Systematic studies at multiple EC sites were carried out that found surface  
116 heterogeneity (Foken et al. 2010; Mauder et al. 2007a; Morrison et al. 2021; Panin et al.  
117 1998; Panin and Bernhofer 2008), friction velocity  $u_*$  (Barr et al. 2006; Hendricks-  
118 Franssen et al. 2010; Stoy et al. 2013; Wilson et al. 2002), and atmospheric stability (Barr  
119 et al. 2006; Hendricks-Franssen et al. 2010; Stoy et al. 2006; Stoy et al. 2013) to be related  
120 to the SEB gap. The SEB gap was also studied with large-eddy simulations (LES), which  
121 also found surface heterogeneity (De Roo and Mauder 2018; Zhou et al. 2019),  $u_*$   
122 (Schalkwijk et al. 2016) and atmospheric stability (Huang et al. 2008; Zhou et al. 2018)  
123 were influencing the SEB gap.

124 That the SEB gap depends on atmospheric stability follows from the fact that  
125 convectively driven eddies predominate under unstable conditions. Their vertical extent  
126 can reach the ABL depth (Maronga and Raasch 2013; Sührling and Raasch 2013), and their  
127 horizontal extent can reach two to three times the boundary layer depth (Paleri et al. 2022a;  
128 Stull 1988). These large eddies are not captured in 30-minute EC measurements and  
129 therefore are considered TOSs. Furthermore, large horizontal wind speeds that are  
130 associated with neutral to stable atmospheric conditions increase the horizontal mixing  
131 (Katul 2019; Schalkwijk et al. 2016), and TOSs are carried along faster with the wind,  
132 increasing the likelihood of them being captured within a typical 30-min measurement  
133 period. The thermal surface heterogeneity affects the SEB gap through its influence on the  
134 formation of SCs: different surface properties of the individual patches cause the surfaces  
135 and also the air above them to heat up to different extents, resulting in the formation of

136 TMCs in addition to the TOSs that are already randomly formed. The magnitude of the  
137 TMCs depends on the prevalent size and temperature amplitude of the individual surface  
138 patches (Inagaki et al. 2006; Letzel and Raasch 2003; Sühling et al. 2018; Zhou et al. 2019).

139 Several studies proposed models of the SEB gap based on atmospheric stability and  
140 measurement height (e.g. De Roo et al. 2018; Huang et al. 2008). Recently, a model of the  
141 SEB gap including the effect of thermal surface heterogeneity was published (Wanner et  
142 al. 2022b), however, it was only developed to predict the imbalance in the sensible heat  
143 flux. These models all have in common that they model the entire SEB gap, i.e., the gap  
144 between the available energy at the surface and the measured turbulent heat fluxes.

145 However, the energy being stored in the air layer and biomass beneath the instruments  
146 were identified as another major contribution to the SEB gap in EC measurements over tall  
147 vegetation, as mentioned above. We hypothesize that the amount of energy supplied to this  
148 storage does not depend on the same factors as the magnitude of the energy transport by  
149 secondary circulations. It is possible to measure the energy storage change in the air by  
150 simply adding few sensors below the EC instrumentation (Lindroth et al. 2010; Moderow  
151 et al. 2009). This is already implemented by default in some large EC networks like ICOS  
152 (Heiskanen et al. 2022) and provides a more direct way of obtaining the storage change  
153 contribution to the SEB than predicting it by a model. Since storage change is being  
154 routinely measured at EC sites and its effect on the long-term mean SEB is negligible, we  
155 propose to measure the storage directly and model the energy transport by secondary  
156 circulations separately.

157 Considering the mentioned contributions to the SEB gap, we can rewrite Eq. 1 as

$$R_{net} = H_t + \lambda E_t + H_{nt} + \lambda E_{nt} + G + H_{\Delta St,a} + \lambda E_{\Delta St,a} + H_{\Delta St,b} + I, \quad (2)$$

158 where  $H_{nt}$  and  $\lambda E_{nt}$  are non-turbulent transport of sensible- and latent heat which is missed  
159 by EC measurement,  $H_{\Delta St,a}$  and  $\lambda E_{\Delta St,a}$  are storage changes of sensible heat in the air  
160 volume below the EC measurement, and  $H_{\Delta St,b}$  is the storage change of sensible heat in the  
161 biomass. By considering  $H_{nt}$ ,  $\lambda E_{nt}$ ,  $H_{\Delta St,a}$ ,  $\lambda E_{\Delta St,a}$ , and  $H_{\Delta St,b}$   $I$  becomes smaller.  
162 Therefore, to close the energy balance gap eventually, all known factors contributing to the  
163 energy balance must be quantified.

164 Since the long-term measurement of non-turbulent fluxes at all EC sites is not possible,  
165 the objectives of this study are (1) to develop a model that can predict the transport of

166 sensible and latent heat by SCs under unstable conditions at the site of an EC station based  
167 on as few additional measurements as possible, (2) to test how well the model predicts the  
168 partitioning into sensible and latent energy transport by secondary circulations in a more  
169 realistic LES, and (3) to show how the model can be applied to field measurements and  
170 test if considering the modelled dispersive fluxes results in an SEB closure in EC field  
171 measurements. The first objective is achieved by further developing an existing model  
172 (Wanner et al. 2022b). Following De Roo et al. (2018) it uses the atmospheric stability  
173 measure  $u_*/w_*$ , where  $w_*$  is the Deardorff velocity, and the measurement height  $z$   
174 normalized with the atmospheric boundary-layer height  $z_i$ , as well as a thermal surface  
175 heterogeneity parameter  $\mathcal{H}$  (Margairaz et al. 2020b) to predict the entire energy balance  
176 gap. The new model developed in this study additionally considers the gradients of  
177 potential temperature  $\theta$  to predict the non-turbulent transport of  $H$  and mixing ratio  $q$  to  
178 predict the non-turbulent transport of  $\lambda E$ . We hypothesize that the consideration of these  
179 gradients improves the prediction of energy transport by SCs since they define whether  
180 there is any energy to be transported by secondary circulations. The model is based on a  
181 large set of idealized large-eddy simulations introduced in section 2.1 and also contributes  
182 to a better understanding of the partitioning of the SEB gap into sensible and latent heat as  
183 well as non-turbulent fluxes and storage change, respectively.

184 The second objective is addressed by applying the model to more realistic LES (Section  
185 2.3, Paleri et al. (submitted)) and field measurements at EC stations (section 2.4) from the  
186 CHEESEHEAD19 campaign (Butterworth et al. 2021). The application to the more  
187 realistic LES allows a separate analysis of the surface balances of sensible and latent heat,  
188 which is not possible with field measurements, where only the total available energy can  
189 be used as a reference. The test using the field measurements is intended to show how  
190 practicable the model application is and how well the findings from the LES can be  
191 transferred to the real world.

192 The development and application of the model are described in section 2. The results  
193 are shown in section 3 and discussed in section 4.

## 194 2 Methods

### 195 2.1 Set-up of Idealized Large-Eddy Simulations

196 We used PALM V6, revision 4849 to run a set of idealized simulations. PALM is a  
197 parallelized large-eddy simulation model based on the non-hydrostatic incompressible  
198 Boussinesq equations (Maronga et al. 2020; Raasch and Schröter 2001). The sub-grid  
199 model is based on the kinetic energy scheme of Deardorff (1980) which was modified by  
200 Moeng and Wyngaard (1988) and Saiki et al. (2000). A fifth-order scheme (Wicker and  
201 Skamarock 2002) was used to discretize the advection terms, and for the time integration,  
202 a third-order Runge–Kutta scheme (Williamson 1980) was used.

203 In total, we ran 148 simulations with different combinations of geostrophic wind speeds  
204 ( $U_g$ , 0.5–9.0 m s<sup>-1</sup>), surface patch sizes of sensible ( $H_s$ ) and latent ( $\lambda E_s$ ) surface fluxes  
205 (homogeneous, 200 m, 400 m, 800 m), and Bowen ratios ( $\beta$ ) of surface fluxes (0.1–1.3),  
206 following the setup used in Margairaz et al. (2020a) and Wanner et al. (2022b). The  
207 randomly assigned surface fluxes follow a Gaussian normal distribution, where the  
208 standard deviation was also varied. Table 6 in Appendix 1 gives an overview over the  
209 individual simulations. The variation in  $U_g$ ,  $H_s$ , and  $\lambda E_s$  leads to differences in  
210 atmospheric stability and the variation in heterogeneity scales of surface fluxes causes the  
211 development different patterns of surface temperature ( $T_s$ ). Examples of the spatial  
212 distribution of surface fluxes and resulting surface temperatures can be found in Fig. 11  
213 (Appendix 1).

214 Following Margairaz et al. (2020a) and Wanner et al. (2022b), the horizontal grid  
215 spacing was 24.5 m and the vertical grid spacing was 7.8 m. With  $(x,y,z) = 256 \times 256 \times 256$   
216 grid points, this results in a horizontal domain extent of  $6272 \times 6272$  m<sup>2</sup> and a vertical  
217 domain extent of roughly 2000 m. All simulations were carried out with cyclic horizontal  
218 boundary conditions. At the lower boundary, Dirichlet conditions were used for the wind  
219 velocity components, while Monin-Obukhov similarity theory was used to determine the  
220 lower boundary condition for the momentum equations, and Neumann conditions were  
221 used for potential temperature, humidity, pressure and turbulent kinetic energy. The  
222 roughness length was set to 0.1 m, following Margairaz et al. (2020a) and Wanner et al.  
223 (2022b).

224 The initialization profiles were set up following De Roo et al. (2018). The same  
225 horizontally homogeneous initial vertical profiles of potential temperature  $\theta$  and mixing  
226 ratio  $q$  were used in all 148 simulations. The surface temperature was horizontally  
227 homogeneous and set to 285 K. A vertical gradient of  $3 \cdot 10^{-3} \text{ K m}^{-1}$  was applied between 40  
228 and 800 m and a vertical gradient of  $8 \cdot 10^{-3} \text{ K m}^{-1}$  was applied between 800 and 1000 m,  
229 ensuring that the top of the domain lies within an inversion layer and the atmospheric  
230 processes in the boundary layer are not affected by the upper border of the domain. The  
231 humidity is set to  $1 \cdot 10^{-3} \text{ kg kg}^{-1}$  at the surface and only between 1000 and 1100 m, a vertical  
232 gradient of  $-1 \cdot 10^{-5} \text{ kg kg}^{-1} \text{ m}^{-1}$  is applied.

233 The initial profile of horizontal wind speed was homogeneously and vertically constant.  
234 The wind speed varied among the simulations between  $0.5\text{--}9.0 \text{ m s}^{-1}$  (Table 6, Appendix  
235 1) and generated a horizontal pressure gradient in x-direction. A small vertical pressure  
236 gradient to counteract destabilizing was introduced by a vertical subsidence velocity  
237 gradient ( $-4 \cdot 10^{-5} \text{ s}^{-1}$  between 0 and 800 m and  $-2 \cdot 10^{-5} \text{ s}^{-1}$  between 8 and 1000 m).

238 After a 4-hour spin-up period, the output data was collected for a 30-min averaging  
239 period representing typical eddy-covariance averaging periods (Rebmann et al. 2012). The  
240 profiles of temperature, humidity, and horizontal wind speed during the data collection  
241 period is shown as an example for two simulations in Fig. 12, Appendix 1.

## 242 **2.2 Development of the Dispersive Flux Model**

### 243 *2.2.1 Data Processing*

244 Following the approach of former models, we developed a model using horizontally  
245 domain-averaged values from an idealized set of LESs. The energy transport by SCs can  
246 be divided in a horizontal component, i.e., advection, and a vertical component, i.e.,  
247 dispersive flux. In a horizontally endless observation area, the advection component  
248 becomes zero and all energy transport by secondary circulations is combined in the  
249 dispersive flux. Since the idealized LESs have cyclic horizontal boundary conditions,  
250 advection becomes zero on the ecosystem scale. Therefore, the horizontally averaged total  
251 available energy at the surface, i.e., the heat fluxes originating from the surface ( $\langle H_s \rangle$ ,  
252  $\langle \lambda E_s \rangle$ ), is divided into horizontally averaged non-organized randomly distributed turbulent  
253 fluxes ( $\langle H_t \rangle$ ,  $\langle \lambda E_t \rangle$ ), including the sub-grid-scale contributions ( $\langle H_{sgs} \rangle$ ,  $\langle \lambda E_{sgs} \rangle$ ), dispersive

254 fluxes ( $H_d$ ,  $\lambda E_d$ ), and horizontally averaged storage change of energy in the underlying air  
 255 mass ( $\langle H_{\Delta St} \rangle$ ,  $\langle \lambda E_{\Delta St} \rangle$ ) as follows:

$$\langle H_s \rangle + \langle \lambda E_s \rangle = \langle H_t \rangle + \langle \lambda E_t \rangle + H_d + \lambda E_d + \langle H_{\Delta St} \rangle + \langle \lambda E_{\Delta St} \rangle. \quad (3)$$

256 The 30-min horizontally averaged turbulent sensible heat flux  $\langle H_t \rangle$  was calculated for  
 257 each grid level up to  $z/z_i = 0.1$  using the 30-min averaged vertical wind speed  $w$  and  
 258 potential temperature  $\theta$ , the 30-min averaged temporal covariance of  $w$  and  $\theta$ , and the sub-  
 259 grid-scale contribution  $H_{sgs}$ , following

$$\langle H_t \rangle(z) = \langle \overline{w\theta}(z) - \bar{w}(z) \bar{\theta}(z) \rangle c_p \rho + \langle H_{sgs} \rangle, \quad (4)$$

260 where  $c_p$  is the specific heat capacity of air and  $\rho$  is the air density. The overbars indicate  
 261 temporal averaging and the angled brackets denote horizontal averaging over the entire  
 262 extent of the domain. The same procedure was used to calculate the horizontally averaged  
 263 30-min turbulent latent heat flux  $\langle \lambda E_t \rangle$ , however, instead of  $\theta$ , the mixing ratio  $q$  was used:

$$\langle \lambda E_t \rangle(z) = \langle \overline{wq}(z) - \bar{w}(z) \bar{q}(z) \rangle \lambda_v \rho + \langle \lambda E_{sgs} \rangle, \quad (5)$$

264 where  $\lambda_v$  is the latent heat of vaporization.

265 The dispersive sensible heat flux  $H_d$  is calculated as the spatial covariance of 30-min  
 266 averaged  $w$  and  $\theta$ , following

$$H_d(z) = \langle \bar{w}^* \bar{\theta}^* \rangle(z) c_p \rho, \quad (6)$$

267 with

$$\langle \bar{w}^* \bar{\theta}^* \rangle(z) = \frac{1}{nx \times ny} \sum_0^x \sum_0^y (\bar{w}(x, y, z) - \langle \bar{w} \rangle(z)) (\bar{\theta}(x, y, z) - \langle \bar{\theta} \rangle(z)). \quad (7)$$

268 Equation 6 shows that  $H_d$  is by definition already horizontally averaged. Again,  $\lambda E_d$  was  
 269 calculated similarly, following

$$\lambda E_d(z) = \langle \bar{w}^* \bar{q}^* \rangle(z) \lambda_v \rho, \quad (8)$$

270 with

$$\langle \bar{w}^* \bar{q}^* \rangle(z) = \frac{1}{nx \times ny} \sum_0^x \sum_0^y (\bar{w}(x, y, z) - \langle \bar{w} \rangle(z)) (\bar{q}(x, y, z) - \langle \bar{q} \rangle(z)). \quad (9)$$

271 Since the LESs had cyclic boundary conditions and any other flux contributions could  
 272 be ruled out, the change of energy stored in the underlying air mass ( $H_{\Delta St}$ ,  $\lambda E_{\Delta St}$ ) was  
 273 calculated as the residual of the other contributions to the total available surface flux:

$$\langle H_{\Delta St} \rangle = \langle H_s \rangle - \langle H_t \rangle - H_d \quad (10)$$

274 and

$$\langle \lambda E_{\Delta St} \rangle = \langle \lambda E_s \rangle - \langle \lambda E_t \rangle - \lambda E_d. \quad (11)$$

275 To model  $H_d$  and  $\lambda E_d$ , we propose variables of atmospheric stability  $\langle \overline{u_* / w_*} \rangle$ , the  
 276 thermal heterogeneity parameter  $\mathcal{H}$ , the measurement height  $z_m$  normalized with the  
 277 atmospheric boundary layer height  $\langle \overline{z_l} \rangle$ , and the vertical gradients of potential temperature  
 278 theta  $\langle \Delta \overline{\theta} \rangle$  (for  $H_d$ ) and mixing ratio  $\langle \Delta \overline{q} \rangle$  (for  $\lambda E_d$ ), respectively, as our driving factors.  
 279 We calculate  $\langle \overline{u_* / w_*} \rangle$ , for one grid level near the surface based on the 30-min averaged  
 280 covariances following

$$\overline{u_*} = \left( (\overline{u'w'_{res}} + \langle \overline{u'w'_{sgs}} \rangle)^2 + (\overline{v'w'_{res}} + \langle \overline{v'w'_{sgs}} \rangle)^2 \right)^{1/4}, \quad (12)$$

281 where  $u$  and  $v$  are the horizontal wind speeds in x- and y-direction, and the index *res*  
 282 indicates the covariance resolved by the grid, and

$$\overline{w_*} = \left( \frac{g}{\theta} \langle z_i \rangle (\overline{w'\theta'_{res}} + \langle \overline{w'\theta'_{sgs}} \rangle) \right)^{1/3}, \quad (13)$$

283 where  $g$  is the gravitational acceleration ( $9,81 \text{ m s}^{-2}$ ) and  $z_i$  is determined as the height at  
 284 which the total sensible heat flux crosses the zero value prior to reaching the capping  
 285 inversion.

286 The thermal heterogeneity parameter was introduced by Margairaz et al. (2020b) as

$$\mathcal{H} = \frac{g \overline{L_h} \Delta \overline{T}}{\langle \overline{U_g} \rangle^2 \langle \overline{T_s} \rangle}, \quad (14)$$

287 where  $\langle \overline{T_s} \rangle$  is the averaged surface temperature,  $\Delta \overline{T}$  is the amplitude of the surface  
 288 temperature heterogeneities, calculated following

$$\Delta \overline{T} = \langle |\overline{T_s} - \langle \overline{T_s} \rangle| \rangle, \quad (15)$$

289 and  $\langle \overline{U_g} \rangle$  is the geostrophic wind speed. The heterogeneity length scale  $\overline{L_h}$  was calculated  
 290 following an approach of Panin and Bernhofer (2008):

291 We calculated the spatial spectra of  $\overline{T_s}$  by performing a Fourier transformation along ten  
 292 transects in the x- and y-direction of the domain, respectively. Before performing the  
 293 Fourier transformation, a bell taper was applied to smooth the edges and thereby reduce  
 294 leakage (Stull 1988). The length scale that contributes the most to the variability in  $\overline{T_s}$  along  
 295 each transect was identified by the location of the maximum of the spectrum. By averaging

296 over the predominant length scales derived from each transect along both directions, we  
 297 derived the predominant length scale  $\overline{L_h}$  of the entire domain.  
 298 The boundary layer height is directly extracted from the LES output and is defined as the  
 299 height where  $\langle \overline{w'\theta'} \rangle$  becomes negative for the first time from surface.

300 The vertical gradients  $\langle \Delta \bar{\theta} \rangle$  and  $\langle \Delta \bar{q} \rangle$  were calculated following

$$\langle \Delta \bar{\theta} \rangle = \langle \bar{\theta} \rangle(0 \text{ m}) - \langle \bar{\theta} \rangle(0.5 z_i) \quad (16)$$

301 and

$$\langle \Delta \bar{q} \rangle = \langle \bar{q} \rangle(0 \text{ m}) - \langle \bar{q} \rangle(0.5 z_i). \quad (17)$$

### 302 2.2.2 Model fitting

303 We used the Random Forest machine-learning model (Breiman 2001) to predict  $H_d$  and  
 304  $\lambda E_d$  from 148 idealized LESs that were set up to represent a wide range of boundary  
 305 conditions with respect to thermal surface heterogeneity and atmospheric stability (Sect.  
 306 2.1). The models were trained separately for  $H_d$  and  $\lambda E_d$  using  $\langle \overline{u_* / w_*} \rangle$ ,  $z / \langle z_i \rangle$ ,  $\mathcal{H}$ , and  
 307  $\langle \Delta \bar{\theta} \rangle$  (only for  $H_d$ ) or  $\langle \Delta \bar{q} \rangle$  (only for  $\lambda E_d$ ) as predictor variables. The entire training data is  
 308 attached as a supplementary file. The modelling was performed in Python 3.7 using the  
 309 Random Forest implementation in scikit-learn (Pedregosa et al. 2012) with default settings  
 310 and 200 regression tree estimators.

311 To evaluate the approach, we use a leave-one simulation-out-cross-validation such that  
 312 predictors for  $H_d$  and  $\lambda E_d$  for each simulation have never seen the specific simulation  
 313 results during training. We calculate predictor importance based on so called SHapley  
 314 Additive exPlanations (SHAP) values (Lundberg et al. 2020; Lundberg and Lee 2017)  
 315 which estimate how much each predictor contributes to the variation of the predictions. We  
 316 use the mean absolute SHAP value for each predictor as a metric of variable importance.

### 317 2.3 Testing the Model on the More Realistic CHEESEHEAD19 LES

318 To test how well the model of sensible and latent dispersive heat fluxes works, we applied  
 319 from the model of dispersive heat fluxes to the realistic large eddy simulations of two days  
 320 in August (Aug 22-23 2019) of the CHEESEHEAD19 campaign ( Paleri et al. (submitted))  
 321 for which we performed eight ensemble simulations. These simulations were carried out  
 322 with PALM v6, revision 21.10-rc.2 and consist of one parent domain and two 3D child  
 323 domains, nested recursively within each other.

324 The extent and resolution of the domains is shown in Table 1. The parent domain has  
 325 a large extent to ensure that turbulence can properly develop and adapt to the surface  
 326 conditions. The first child domain (C1) covers the surroundings of the CHEESEHEAD19  
 327 area with a moderate resolution. The smallest child domain (C2) has a very high resolution  
 328 to enable the investigation at field-measurement heights and covers the locations of the EC  
 329 stations that were deployed during the CHEESEHEAD19 campaign. The child domains  
 330 are shown in Fig. 1.

331 The realistic simulations were carried out with lateral and top boundary conditions  
 332 informed by the National Centers for Environmental Prediction (NCEP) High Resolution  
 333 Rapid Refresh data assimilation product (Horel and Blaylock 2017) over the study domain  
 334 and coupled to a land-surface model (LSM) and plant-canopy model (PCM) informed by  
 335 field-campaign observations and the WISCLAND2 dataset (Wisconsin Department of  
 336 Natural Resources 2016). Paleri et al. (submitted) gives a detailed description of the model  
 337 setup and comparisons with field measurements.

338 Similar to the idealized simulation,  $\langle \bar{z}_i \rangle$  is directly extracted from the C2 LES output  
 339 and is defined as the height where  $\overline{w'\theta'}$  becomes negative for the first time.  $\langle \overline{U}_g \rangle$  was  
 340 extracted as the horizontal wind speed at  $1.1 \langle \bar{z}_i \rangle$  in the C2 domain. The predominant  
 341 landcover types in the C2 domain are forests, resulting in a domain-averaged canopy height  
 342 of  $\langle z_c \rangle = 22.08$  m and a displacement height of  $\langle z_d \rangle = 15.46$  m. We considered different  
 343 measurement heights  $z_m$  up to 60 m above  $z_c$  but periods for which  $z/\langle \bar{z}_i \rangle > 0.1$  where  
 344 discarded because the model was developed to predict dispersive fluxes in the inertial  
 345 surface layer, only. When calculating  $z/\langle \bar{z}_i \rangle$ , the displacement height  $\langle z_d \rangle$  was taken into  
 346 account, with  $z = z_m - \langle z_d \rangle$  and  $\langle \bar{z}_i \rangle = \langle \bar{z}_i \rangle_0 - \langle z_d \rangle$ , where  $\langle \bar{z}_i \rangle_0$  refers to the boundary-  
 347 layer height relative to the bottom of the domain.

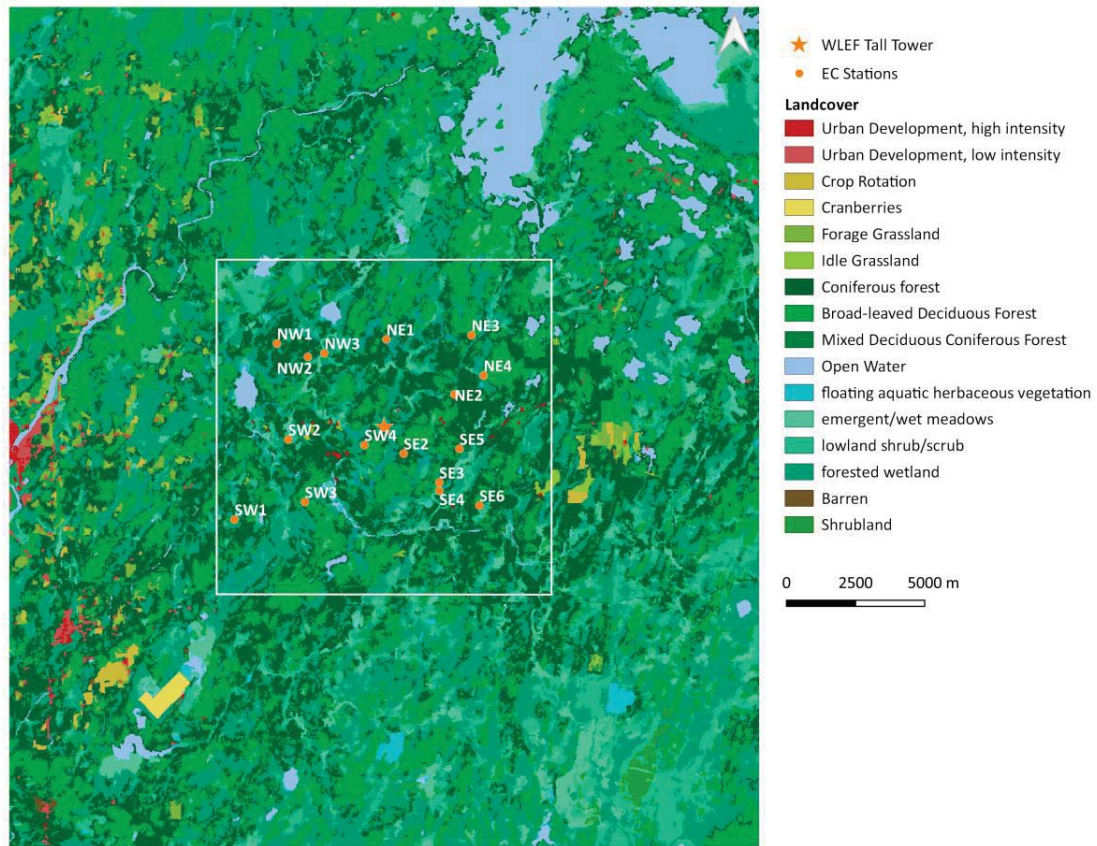
348 Since the active surface is not located at the lower boundary of the domain in areas with  
 349 high vegetation, we defined the surface in the realistic simulations to be located at the  
 350 canopy top level in all areas where the PCM was used, and at the lower boundary of the  
 351 domain in all areas where no PCM was used. This definition of surface is used for  $\langle \overline{u_*}/w_* \rangle$   
 352 and  $\overline{T}_s$ , and the surface fluxes.

353 Again,  $\langle \overline{u_*}/w_* \rangle$  were calculated following Eq. 12-13 and averaged over the entire  
 354 horizontal extent of the C2 domain. The surface temperature was extracted from the true

355 surface temperature output in all non-forested areas where only the LSM but not the PCM  
356 was deployed. In the forested areas,  $\bar{T}_s$  was extracted from the tree-dimensional output of  
357 potential air temperature at the top of the canopy, assuming that the leaf surface  
358 temperature equals the air temperature. Based on this combined surface temperature map,  
359  $\Delta\bar{T}$ ,  $\langle\bar{T}_s\rangle$  and  $\bar{L}_h$  were calculated over a  $12.5\times 12.5\text{ m}^2$  model extent. The latter was  
360 calculated using the same approach as for determining  $\bar{L}_h$  in the idealized simulations used  
361 to develop the models which is described in section 3.2.  $\mathcal{H}$  was then calculated for the  
362 entire horizontal extent of the C2 domain similar to the calculation of dispersive fluxes in  
363 the idealized LES following Eq. 14.

364 To calculate the vertical gradients  $\langle\Delta\bar{\theta}\rangle$  and  $\langle\Delta\bar{q}\rangle$ ,  $\langle\bar{\theta}\rangle$  and  $\langle\bar{q}\rangle$  were extracted from the  
365 C1 output at  $0.5\langle\bar{z}_i\rangle$  and at the second grid layer. The C1 domain was used to calculate the  
366 vertical gradients because the vertical extent of the C2 domain is too small to include  
367  $0.5\langle\bar{z}_i\rangle$  under strongly unstable conditions.  $\langle\Delta\bar{\theta}\rangle$  and  $\langle\Delta\bar{q}\rangle$  were then calculated following  
368 Eq.16-17.

369 To compare the true dispersive heat fluxes to the predicted dispersive heat fluxes, we  
370 estimated the true dispersive heat fluxes by calculating  $H_{d,LES}$  and  $\lambda E_{d,LES}$  as spatial  
371 covariances of  $\bar{w}$ ,  $\bar{\theta}$ , and  $\bar{q}$  over the entire horizontal extent of the C2 domain for each  
372 measurement level following Eq. 6-9.



373  
 374 **Fig. 1** The map shows landcover types extracted from the WISCLAND 2.0 dataset (Wisconsin Department  
 375 of Natural Resources 2016) that was used to inform the CHEESEHEAD LES (Sect. 2.3). The extent of the  
 376 map corresponds to the C1 domain and the white square shows the border of the C2 domain in the  
 377 CHEESEHEAD LES. The domains are centred around the WLEF Tall Tower (45.9459, -90.2723). The  
 378 orange points represent the EC stations in the field (Sect. 2.4).

379 **Table 1** Grid resolution and domain extents for the realistic CHEESEHEAD LES.

	Domain extent (km)			Grid spacing (m)		
	lx	ly	lz	dx	dy	dz
parent	48.60	51.84	5.00	90.0	90.0	12.0
C1	27.00	30.24	2.49	30.0	30.0	12.0
C2	12.00	12.00	0.24	6.0	6.0	4.0

380

## 381 2.4 Testing the Model on CHEESEHEAD19 Field Measurements

382 To test the model on real field measurements, the model was furthermore applied to the  
 383 eddy-covariance measurements at 16 of the 17 stations from the CHEESEHEAD19

384 campaign. An overview of the stations is given in table 2. Station NW4 was excluded from  
385 the analysis because it is expected to be strongly influenced by topography due to its  
386 location on a steep lake shore, rendering it unsuitable for this analysis as topography effects  
387 are not considered in the model of dispersive fluxes. The campaign took place from late  
388 June until early October 2019 on a  $10 \times 10 \text{ km}^2$  area surrounding the nearly 400 m tall  
389 AmeriFlux tower US-PFa located in northern Wisconsin, USA (45.9459, -90.2723) (Desai  
390 et al. 2022). The tower is surrounded by a nearly flat landscape that is mainly covered by  
391 a mix of deciduous and coniferous forests, swamplands, and waterbodies. The locations of  
392 the 16 eddy-covariance stations are shown in Fig. 1 and the respective measurement heights  
393 and landcover characteristics are shown in Table 2. A detailed description of the  
394 measurement campaign, including additional measurements can be found in (Butterworth  
395 et al. 2021).

396 Fluxes of sensible ( $H_t$ ) and latent heat ( $\lambda E_t$ ) were calculated for 30-minute intervals  
397 using detrended 20 Hz measurements of temperature, water vapor, and vertical wind speed.  
398 For the  $H_t$  calculation, the dry air temperature was calculated from the sonic temperature  
399 after correction for the effect of water vapor on the speed of sound (Schotanus et al. 1983).  
400 For the  $\lambda E_t$  calculation, the water vapor measurements were corrected for density effects  
401 (Webb et al. 1980). Vertical wind speed was extracted from the raw 3-dimensional wind  
402 vector after a double rotation coordinate rotation.

403 To apply the model to field measurements, additional information is needed, as single-  
404 tower measurements do not provide information on boundary-layer height, geostrophic  
405 wind speed, thermal surface heterogeneity or vertical gradients of potential temperature  
406 and mixing ratio. The CHEESEHEAD19 dataset provides a unique opportunity to test this  
407 model, because it provides a lot of the needed additional information. However, to show  
408 that the application to other eddy-covariance measurements is possible, as well, we used  
409 no additional information acquired during the CHEESEHEAD19 campaign and only  
410 utilized the dense tower network as a test bed for the dispersive flux model in field settings.  
411 Instead, ERA5 reanalysis data and satellite-based land-surface temperature maps were used  
412 to inform the dispersive flux model.

413 The boundary layer height, the gradients of  $\bar{\theta}$  and  $\bar{q}$ , and  $\overline{U_g}$  used to calculate the  
414 thermal heterogeneity parameter were extracted from the hourly ERA5 reanalysis data

415 (Hersbach et al. 2023a, 2023b). The boundary layer height can be directly extracted from  
 416 the single-level reanalysis data (Hersbach et al. 2023b). To derive  $\overline{U}_g$ , the horizontal wind  
 417 speed at pressure levels (Hersbach et al. 2023a) was calculated from the  $\bar{u}$ - and  $\bar{v}$ -  
 418 component of the wind vector at each pressure level. The height above ground of each  
 419 pressure level was derived using the barometric formula. Finally,  $\overline{U}_g$  was derived as the  
 420 wind speed at 1.1 times the boundary layer top by linearly interpolating between the  
 421 adjacent model output levels. To calculate the gradients of  $\bar{\theta}$  and  $\bar{q}$ , the potential  
 422 temperature and the mixing ratio were derived from the pressure level output and the single  
 423 level output. At  $0.5 z_i$ ,  $\bar{\theta}$  was calculated from the absolute air temperature and the pressure  
 424 and  $\bar{q}$  was calculated from the specific humidity provided by the pressure level output.  
 425 Again, the height above the ground of each pressure level was calculated using the  
 426 barometric formula and linear interpolation was applied to derive theta and q at  $0.5 \bar{z}_i$ . For  
 427 the near-surface value, we used the 2 m dewpoint temperature and absolute air  
 428 temperature, as well as the surface pressure provided by the single-layer ERA5  
 429 output to calculate  $\bar{\theta}$  and  $\bar{q}$ . The vertical gradients were then calculated as  $\Delta\bar{\theta} =$   
 430  $\bar{\theta}(2m) - \bar{\theta}(0.5\bar{z}_i)$  and  $\Delta\bar{q} = \bar{q}(2m) - \bar{q}(0.5\bar{z}_i)$ , respectively.

431 Even though  $\langle \overline{u_* / w_*} \rangle$  can be calculated from the high-frequency data provided by  
 432 eddy-covariance measurements, it is not necessarily representative of a larger area  
 433 surrounding the measurement. Furthermore,  $\langle \overline{u_* / w_*} \rangle$  are defined as near-surface values  
 434 making the calculation of  $\langle \overline{u_* / w_*} \rangle$  from measurements at roughly 30 m above the ground  
 435 not ideal. Therefore,  $\langle \overline{u_* / w_*} \rangle$  was also extracted from the ERA5 reanalysis data. While  $\bar{u}_*$   
 436 could be directly extracted from the ERA5 reanalysis data,  $\bar{w}_*$  was calculated from the  
 437 sensible surface-heat flux, boundary-layer height, 2 m air temperature and surface pressure  
 438 provided in the ERA5 single-level output following Eq.13.

439 To calculate the thermal heterogeneity parameter, the predominant length scale of  
 440 thermal surface heterogeneities as well as the amplitude of the surface temperature need to  
 441 be known which are not available from the ERA5 reanalysis data. Surface temperature  
 442 maps with a 50 m spatial resolution and 1 hr temporal resolution generated from satellite  
 443 data (Desai et al. 2021) were used to calculate the same. For each EC station, we selected  
 444 a  $10 \times 10 \text{ km}^2$  area surrounding the tower location and then followed the approach of Panin

445 and Bernhofer (2008) described in section 3.2 to derive  $\overline{L_h}$ .  $\Delta\overline{T}$  and  $\langle\overline{T_s}\rangle$  were also  
 446 calculated from the same maps. Since the land-surface temperature maps had a temporal  
 447 resolution of 60 minutes, the resulting  $\overline{L_h}$ ,  $\langle\overline{T_s}\rangle$ , and  $\Delta\overline{T}$  were linearly interpolated to 30-  
 448 min values.

449 **Table 2** Overview of the 16 CHEESEHEAD19 EC stations used for testing the application of the model on  
 450 field measurements, including canopy heights ( $z_{c,field}$ ), measurement heights ( $z_{m,field}$ ), and displacement  
 451 heights ( $z_{d,field}$ ), and vegetation types. The last two columns show number of 30-minute measurement  
 452 periods for which all necessary data is available and  $H_t \geq 10 \text{ W m}^{-2}$  ( $n_{meas}$ ) and the percentage of 30-minute  
 453 measurement periods for which all predictor variables lie within the model limits ( $n_{meas,ML}$ ).

tower ID	$z_{c,field}$ (m)	$z_{m,field}$ (m)	$z_{d,field}$ (m)	vegetation type	$n_{meas}$	$n_{meas,ML}$ (%)
NW1	25.0	32.0	17.5	pine	827	1.09
NW2	3.0	12.0	2.1	aspen	543	0.00
NW3	0.3	3.0	0.2	tussock	1319	0.00
NE1	33.2	32.0	23.2	pine	991	0.91
NE2	19.2	32.0	13.4	pine	1113	1.17
NE3	18.3	32.0	12.8	hardwood	668	1.65
NE4	18.3	32.0	12.8	maple	1110	0.99
SW1	24.4	32.0	17.1	aspen	838	1.07
SW2	19.2	25.0	13.4	aspen	765	1.31
SW3	15.0	32.0	10.5	hardwood	467	0.43
SW4	25.9	32.0	18.1	hardwood	713	0.42
SE2	24.4	32.0	17.1	hardwood	433	0.69
SE3	14.3	32.0	10.0	Aspen	582	2.23
SE4	0.3	3.0	0.2	tussock	1455	0.00
SE5	3.1	12.0	2.2	aspen	439	0.00
SE6	21.6	32.0	15.1	pine	1001	1.50

454

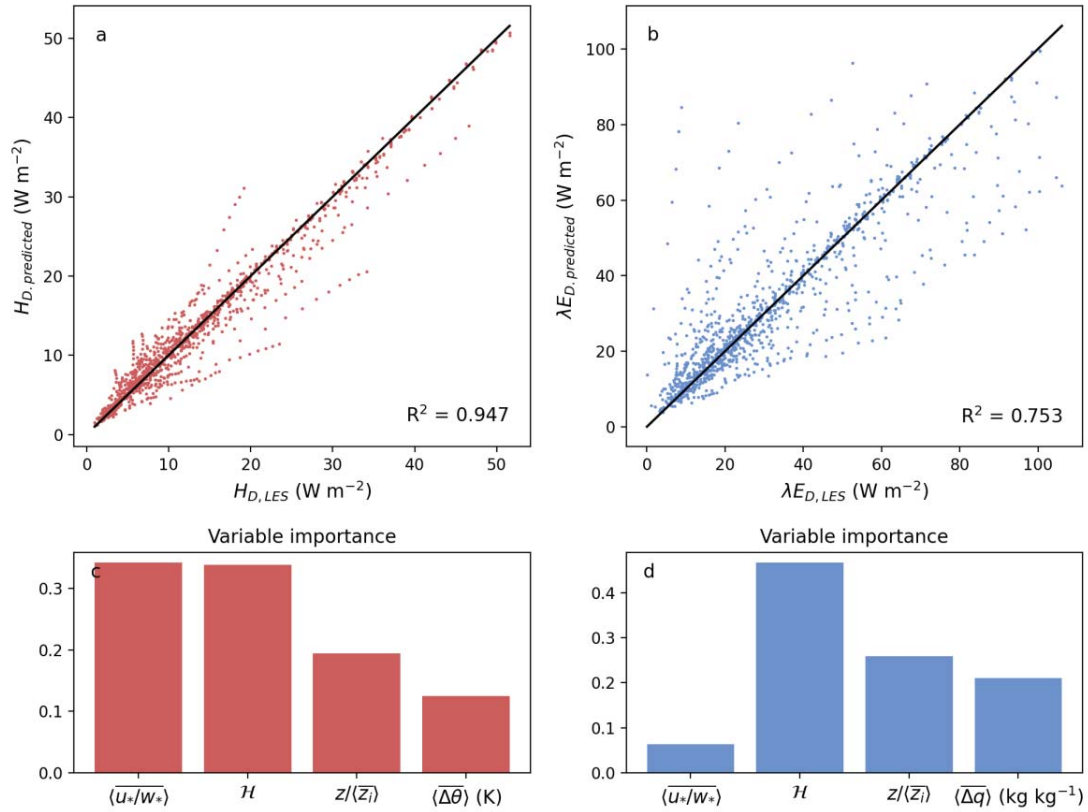
## 455 **3 Results**

### 456 **3.1 Model Based on Domain-Averaged Values**

457 Figure 2a-b shows the results of the cross-validation of the models for sensible (Fig. 2a)  
458 and latent (Fig. 2b) dispersive heat fluxes based on domain-averaged values. The training  
459 and test data were shuffled in such a way that  $H_d$  and  $\lambda E_d$  for each simulation were  
460 predicted by the model trained by the output of all other simulations. The predicted  
461 dispersive heat fluxes are compared to the true dispersive heat fluxes computed from the  
462 LES output following Eq. 6-9. There is a strong correlation between the modelled sensible  
463 dispersive heat flux  $H_{d,predicted}$  and the true dispersive sensible heat flux  $H_{d,LES}$ , with  
464  $R^2 = 0.947$ , which is shown in Fig. 2a. For the latent heat flux, the agreement between  
465 modelled ( $\lambda E_{d,predicted}$ ) and true ( $\lambda E_{d,LES}$ ) dispersive fluxes is weaker, with  $R^2 = 0.753$ .

466 Figure 2c-d shows the relative importance of predicting variables in the models of  
467 dispersive heat fluxes. The most important predicting variables for  $H_{d,predicted}$  (Fig. 2c)  
468 are the heterogeneity parameter  $\mathcal{H}$  and the atmospheric stability parameter  $\langle \overline{u_* / w_*} \rangle$ . The  
469 normalized measurement height  $z / \langle \overline{z_l} \rangle$  and the vertical gradient of potential temperature  
470  $\langle \overline{\Delta \theta} \rangle$  are less important but not negligible.

471 For  $\lambda E_{d,predicted}$ , the most important predicting variable is, again, the heterogeneity  
472 parameter  $\mathcal{H}$ . However, the importance of the atmospheric stability parameter  $\langle \overline{u_* / w_*} \rangle$  is  
473 much lower. The importance of the normalized measurement height  $z / \langle \overline{z_l} \rangle$  and the vertical  
474 gradient of mixing ratio  $\langle \overline{\Delta q} \rangle$  in predicting  $\lambda E_{d,predicted}$  compared to  $\mathcal{H}$  is, again, lower  
475 but not negligible.



476

477

478

479

480

481

482

483

484

485

486

487

488

489

490

491

492

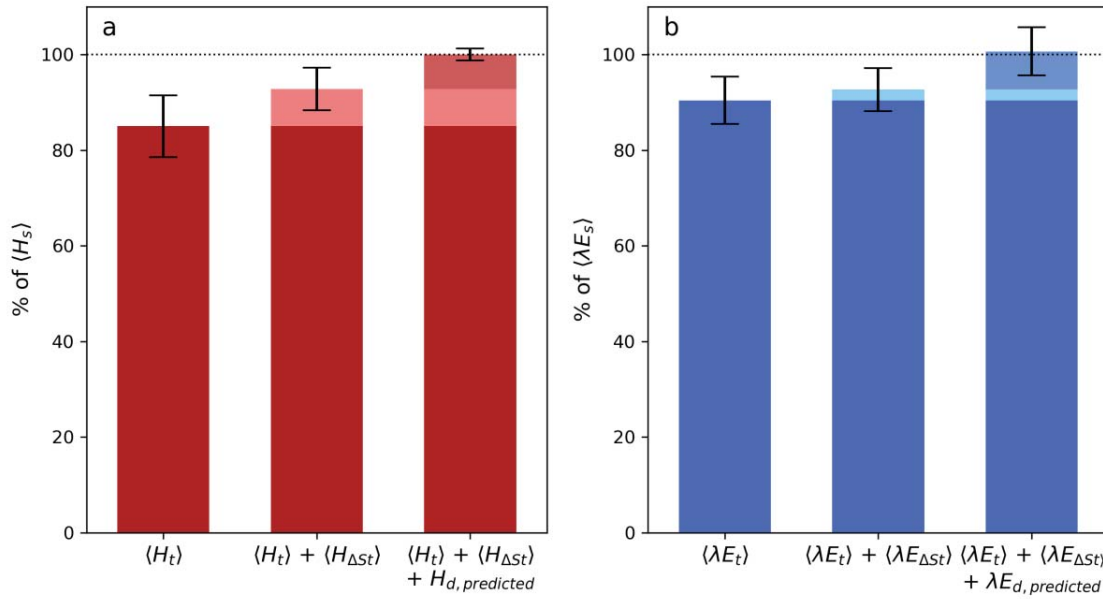
**Fig. 2** Performance of the model based on domain-averaged values. Panels a-b show comparisons of modelled dispersive heat fluxes (y-axis) versus true dispersive heat fluxes calculated directly from the LES output (x-axis) for sensible (panel a) and latent (panel b) dispersive heat fluxes. Panels c-d show the relative importance of predicting variables in the models of sensible dispersive heat flux (panel c) and latent dispersive heat flux (panel d).

Figure 3 shows the relative contribution of the domain-averaged storage and the dispersive fluxes predicted by the model based on domain-averaged values to the SEB gap. The gap between the surface fluxes, i.e., the total available energy, and the turbulent fluxes is on average  $15.0 \pm 6.4\%$  for the sensible heat and  $9.6 \pm 4.9\%$  for the latent heat.

With  $7.7 \pm 3.3\%$  of  $\langle H_s \rangle$ ,  $\langle H_{\Delta St} \rangle$  contributes to more than 50% to the gap in the sensible heat fluxes. The contribution of  $H_{d,predicted}$  is slightly smaller with  $7.2 \pm 4.4\%$  of  $\langle H_s \rangle$ .  $\langle H_t \rangle$ ,  $\langle H_{\Delta St} \rangle$  and  $H_{d,predicted}$  sum up to  $100.0 \pm 1.3\%$  of  $\langle H_s \rangle$ , indicating that the application of the model leads to a good closure of the gap in the sensible heat flux and the inclusion of the predicted dispersive heat flux leads to a significant reduction of the scatter.

In the latent heat flux, the partitioning between  $\langle \lambda E_{\Delta St} \rangle$  and  $\lambda E_{d,predicted}$  is different.  $\langle \lambda E_{\Delta St} \rangle$  has a smaller share in the flux gap ( $2.3 \pm 1.2\%$  of  $\langle \lambda E_s \rangle$ ) than the predicted

493 dispersive flux ( $8.0 \pm 6.4\%$  of  $\langle \lambda E_s \rangle$ ). Thus, the dispersive flux share of the surface flux is  
 494 larger in the latent heat flux than in the sensible heat flux, although the total gap is smaller  
 495 in the latent heat flux compared to the sensible heat flux. In sum,  $\langle \lambda E_t \rangle$ ,  $\langle \lambda E_{\Delta St} \rangle$  and  
 496  $\lambda E_{d,predicted}$  equal  $100.7 \pm 5.0\%$  of  $\langle \lambda E_{\Delta St} \rangle$ , resulting in a good closure of the gap in the  
 497 latent heat fluxes on average. However, the addition of  $\lambda E_{d,predicted}$  does not cause a  
 498 reduction of the scatter.



499  
 500 **Fig. 3** Relative contributions of the domain-averaged storage and dispersive fluxes predicted by the model  
 501 based on domain-averaged values to the gaps in sensible and latent heat fluxes. The error bars show the  
 502 standard deviation of the sums shown in each bar.

503 Table 3 shows that the Bowen ratio ( $\beta$ ), i.e., the partitioning between sensible and latent  
 504 heat, is smaller in the turbulent flux compared to the surface flux. The Bowen ratio of the  
 505 true dispersive flux  $\beta(F_{d,LES})$  calculated directly from the LES output is larger than the  
 506 Bowen ratio of turbulent heat fluxes  $\beta(\langle F_t \rangle)$ . The Bowen ratio of the storage change  
 507  $\beta(\langle F_{\Delta St} \rangle)$  is much larger than the Bowen ratio of the other fluxes.

508 **Table 3** Absolute values of the flux contributions and Bowen ratios ( $\beta$ ) show the different partitioning into  
 509 sensible and latent heat in the surface fluxes ( $\langle F_s \rangle$ ), turbulent fluxes ( $\langle F_t \rangle$ ), change in energy storage ( $\langle F_{\Delta St} \rangle$ ),  
 510 as well as true ( $F_d$ ) and predicted ( $F_{d,predicted}$ ) dispersive heat fluxes.

	$\langle F_s \rangle$	$\langle F_t \rangle$	$\langle F_{\Delta St} \rangle$	$F_{d,LES}$	$F_{d,predicted}$
$H$ ( $\text{W m}^{-2}$ )	$198.6 \pm 83.7$	$169.6 \pm 74.1$	$15.1 \pm 9.2$	$13.9 \pm 10.2$	$13.9 \pm 10.2$

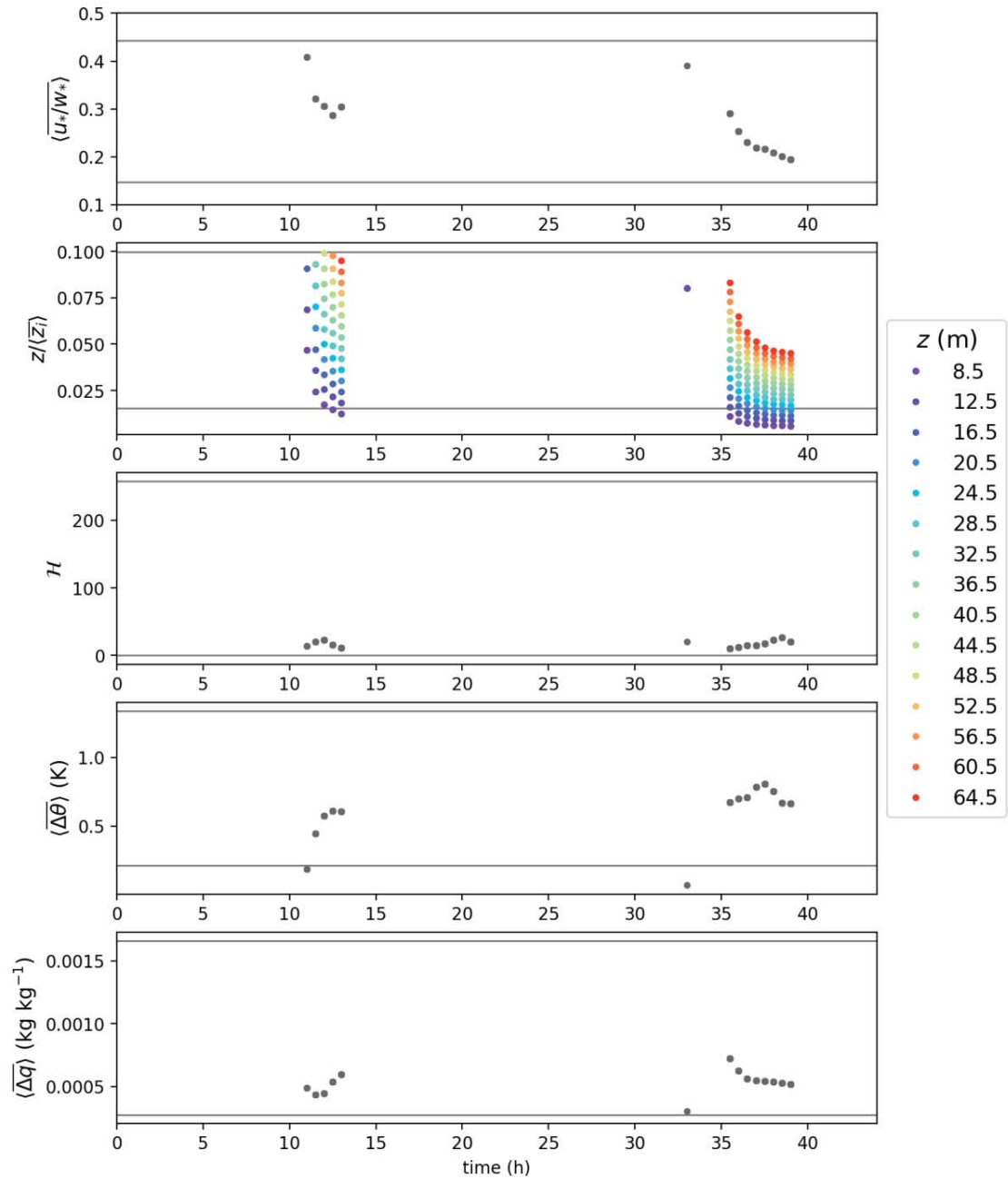
$\lambda E$ (W m <sup>-2</sup> )	450.0±144.3	407.6±134.4	10.5±6.9	31.9±21.7	31.9±21.7
$\beta$ (%)	0.441±0.0	0.416±0.228	1.441±1.294	0.435±0.436	0.427±0.402

### 511 3.3 Model Application to More Realistic CHEESEHEAD19 LES

512 To test the performance of the model based on domain-averaged values on more realistic  
513 scenarios, it was applied to the simulations of two days of the CHEESEHEAD19 campaign.  
514 The final model uses the output of all 148 idealized LESs as training data, which is attached  
515 as a supplementary file, together with an example dataset and a python code to apply the  
516 model. For this analysis, only 30-minute observations where  $\langle H_s \rangle \geq 10 \text{ W m}^{-2}$  were  
517 considered to ensure the model was only applied to unstable conditions. Due to issues with  
518 the data output, five 30-minute intervals had to be discarded, additionally.

519 Figure 4 shows the behaviour of predictor variables over the remaining 30-min  
520 intervals of the two days simulation time. The majority of predictor variables encountered  
521 in the CHEESEHEAD19 LES lies within the range of predictor variables from the idealized  
522 LES that were used to train the model. However, since the models of sensible and latent  
523 dispersive heat fluxes cannot be extrapolated, they provide unreliable values for  
524 measurements for which the predictors lie outside the range of training data. Therefore, all  
525 30-minute intervals where one of the predictors lies outside the range of model training  
526 data were discarded. This affected 18% of the available data, mostly due to small  $z/\langle \bar{z}_l \rangle$   
527 as shown in Fig. 4.

528

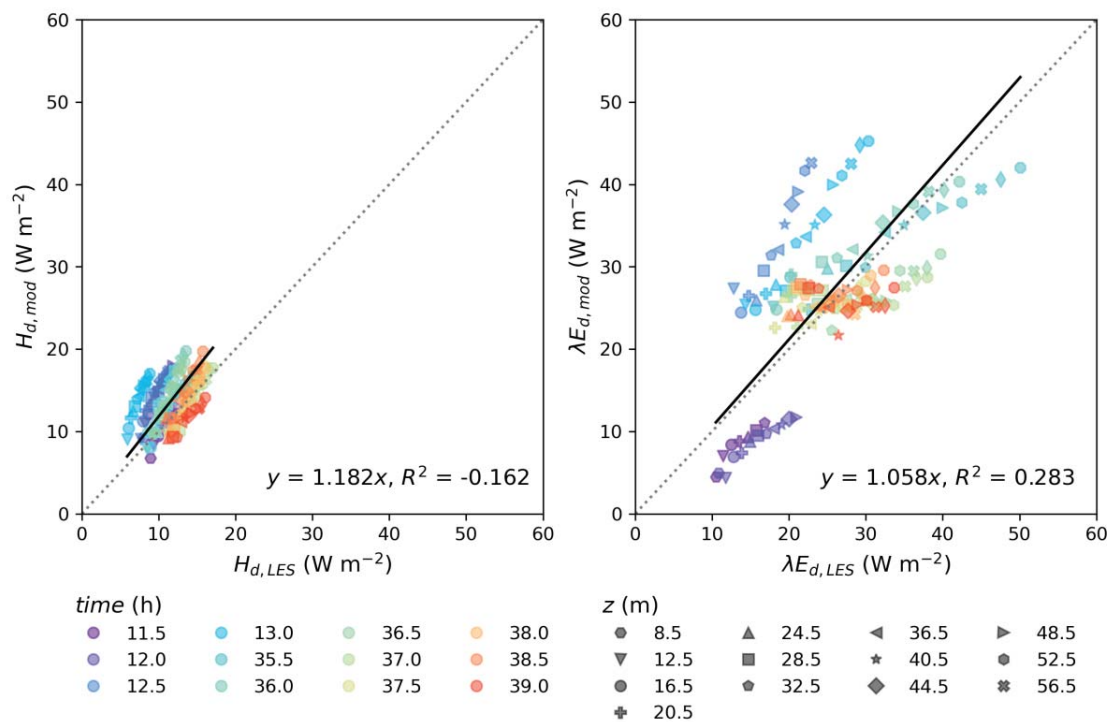


529

530 **Fig. 4** Time series of the predicting variables  $(\langle \overline{u_* / w_*} \rangle, \mathcal{H}, z / \langle \bar{z}_i \rangle, \langle \overline{\Delta \theta} \rangle, \langle \overline{\Delta q} \rangle)$  that were encountered in the  
 531 CHEESEHEAD simulations. The limits of the predictor variables used for training the model are shown by the grey horizontal lines. Since most predictor variables refer to a specific level, they are the same for any  
 532 height considered and therefore shown in grey. Only  $z / \langle \bar{z}_i \rangle$  varies with height. In  $z$  and in  $z_i$ , the  
 533 displacement height (15.47 m) is considered.  
 534

535 Figure 5 shows the comparison of the modelled dispersive heat fluxes ( $H_{d,mod}$  and  
 536  $\lambda E_{d,mod}$ ) with the dispersive heat fluxes directly calculated from the LES output as the

537 spatial covariance ( $H_{d,LES}$  and  $\lambda E_{d,LES}$ ). The model clearly overestimates  $H_{d,LES}$  by 18.2%  
 538 on average and slightly overestimates  $\lambda E_{d,LES}$  by 5.8%. Table 4 shows that in the  
 539 CHEESEHEAD19 LES, the Bowen ratios of the surface  $\beta(\langle F_s \rangle)$  and turbulent  $\beta(\langle F_t \rangle)$   
 540 heat fluxes are nearly similar whereas the Bowen ratio in the dispersive heat fluxes  
 541  $\beta(\langle F_{d,LES} \rangle)$  is considerably lower. The stronger overestimation of  $H_d$  leads to a higher  
 542 Bowen ratio in the modelled dispersive heat fluxes  $\beta(\langle F_{d,mod} \rangle)$  compared to  $\beta(\langle F_{d,LES} \rangle)$ ,  
 543 which is closer to  $\beta(\langle F_s \rangle)$  and  $\langle F_t \rangle$ . The sum of the modelled sensible and latent  
 544 dispersive heat fluxes overestimates the sum of sensible and latent heat fluxes directly  
 545 calculated from the LES output by 9.4% which is shown in Fig. 6.



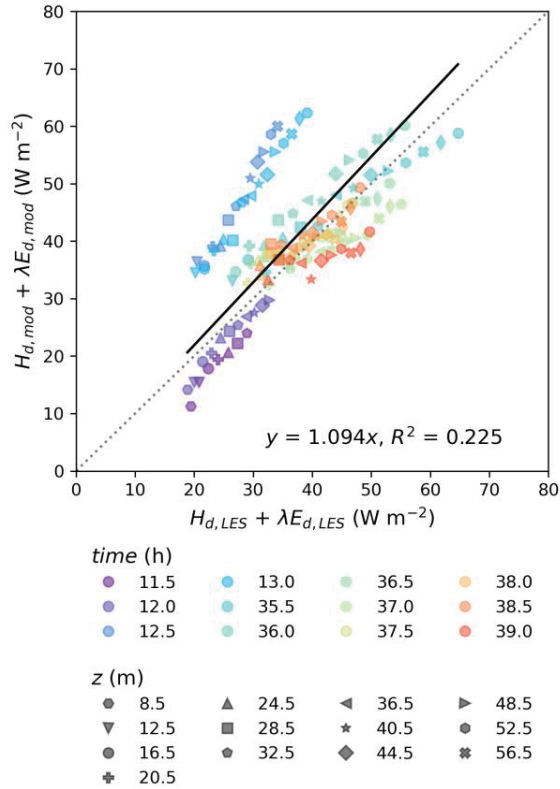
546  
 547 **Fig. 5** Comparison of modelled sensible (panel a) and latent (panel b) dispersive heat fluxes with the sensible  
 548 and latent dispersive heat fluxes calculated as spatial covariances from the output of the more realistic  
 549 CHEESEHEAD LES. The different colours represent 30-minute observation periods used for this analysis  
 550 and the different symbols represent the height above the displacement height.

551 **Table 4** Bowen ratios ( $\beta$ ) show the different partitioning into sensible and latent heat in the domain-averaged  
 552 surface fluxes ( $\langle F_s \rangle$ ), turbulent fluxes ( $\langle F_t \rangle$ ), and true ( $F_{d,LES}$ ) dispersive heat fluxes directly calculated from  
 553 the LES output, as well as modelled ( $F_{d,mod}$ ) dispersive heat fluxes.

	$\langle F_s \rangle$	$\langle F_t \rangle$	$F_{d,LES}$	$F_{d,mod}$
--	-----------------------	-----------------------	-------------	-------------

$\beta$	$0.669 \pm 0.129$	$0.647 \pm 0.115$	$0.461 \pm 0.176$	$0.541 \pm 0.221$
---------	-------------------	-------------------	-------------------	-------------------

554



555

556

557

558

559

Fig. 6 Comparison of modelled total dispersive heat fluxes with total dispersive fluxes calculated as spatial covariances from the output of the more realistic CHEESEHEAD LES. The different colours represent 30-minute observation periods used for this analysis and the different symbols represent the height above the displacement height.

560

### 3.4 Model Application to CHEESEHEAD Field Measurements

561

562

563

564

565

566

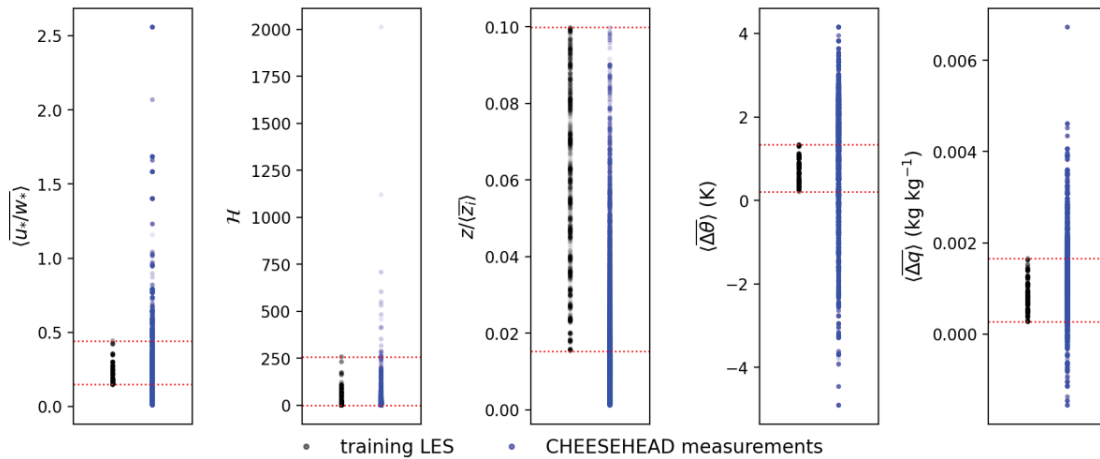
567

568

569

The model was also tested on the CHEESEHEAD19 field measurements carried out at 16 eddy-covariance stations over a period of roughly three months. For this analysis, only 30-minute observations where  $H_t \geq 10 W m^{-2}$  and  $R_{net} > 0 W m^{-2}$  were considered to ensure the model was only applied to unstable conditions. For quality assurance, observations with unrealistically high turbulent heat fluxes of  $(H_t + \lambda E_t) > 1.5 R_{net}$  and observations with  $(H_t + \lambda E_t + H_{\Delta St} + \lambda E_{\Delta St}) < 0.5 (R_{net} - G)$  were discarded. While the latter case would be physically possible, it would result in the SEB gap being larger than the sum of the measured atmospheric heat fluxes and storage changes. In this case, the uncertainty is so high that the data should be rejected rather than corrected.

570 Figure 7 shows that not all conditions encountered in the field measurements were  
571 represented in the training dataset from the idealized LES. While  $\mathcal{H}$  values observed in the  
572 CHEESEHEAD19 surface temperature maps are covered quite well by the training data,  
573 the range of  $\langle \overline{u_* / w_*} \rangle$  and also  $\langle \overline{\Delta q} \rangle$  is wider in the field measurements compared to the  
574 idealized LES. Again, smaller  $z / \langle \overline{z_i} \rangle$  values occur in the field data due to larger  $\langle \overline{z_i} \rangle$  values  
575 in the ERA5 reanalysis data and lower measurement heights in the field. The vertical  
576 gradients of  $\langle \overline{\theta} \rangle$  observed in the ERA5 reanalysis data were typically much larger than the  
577 values used to train the model. The percentage of CHEESEHEAD19 predictor variables  
578 that fall into the limits of the training data for each predictor variable is shown in table 5.  
579 After considering all predictor variables, almost 95% of the CHEESEHEAD19  
580 measurements were discarded before applying the model to the measurements.



581

582 **Fig. 7** Distribution of the predicting variables ( $\langle \overline{u_* / w_*} \rangle$ ,  $\mathcal{H}$ ,  $z / z_i$ ,  $\langle \overline{\Delta \theta} \rangle$ ,  $\langle \overline{\Delta q} \rangle$ ) used for the model training  
583 (gray) and of the predicting variables that occur in the CHEESEHEAD19 field measurements (blue). The  
584 limits of the predictor variables used for training the model are shown by the red dotted lines.

585

586 **Table 5** Percentage of CHEESEHEAD19 field measurements that fall into the range of the predictor variables  
587 used to train the model.

	$\langle \overline{u_* / w_*} \rangle$	$\mathcal{H}$	$z / z_i$	$\langle \overline{\Delta \theta} \rangle$	$\langle \overline{\Delta q} \rangle$	total
%	45.27	99.62	37.60	27.60	67.20	5.08

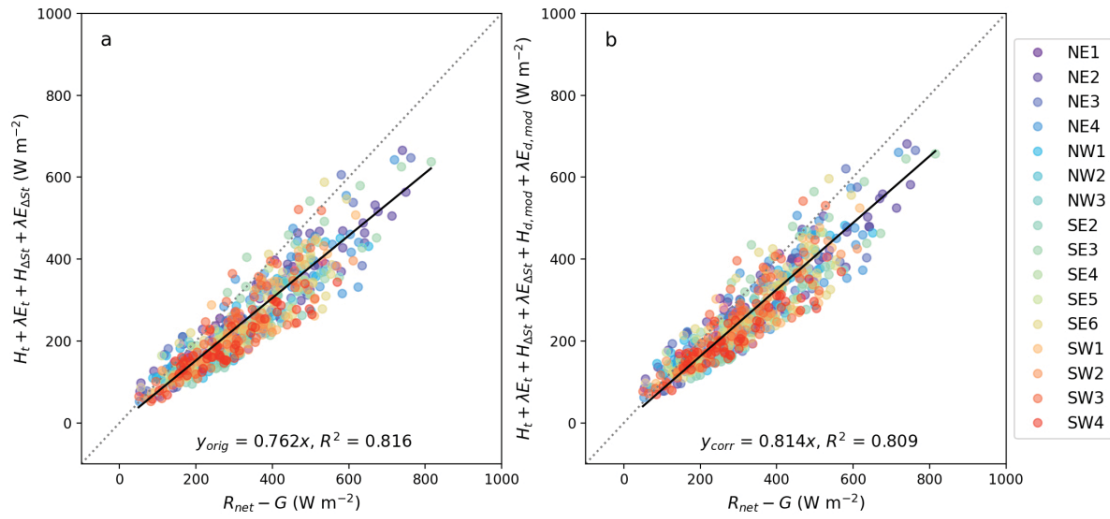
588

589

590

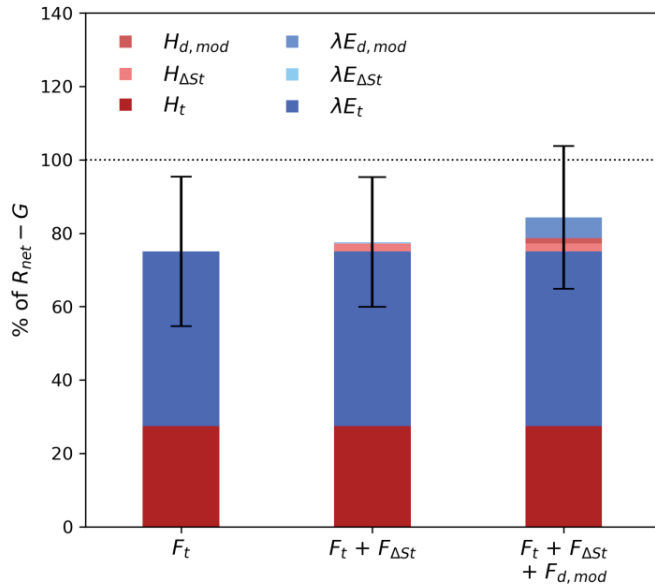
In the field measurements, the total sensible and latent heat fluxes at the surface are not known. Therefore, it is only possible to compare the sum of measured and latent heat fluxes to the available energy at the surface ( $R_{net} - G$ ). In Fig. 8, the storage change of sensible

591 and latent heat in the air between the surface and the instruments ( $H_{\Delta St} + \lambda E_{\Delta St}$ ) is  
 592 subtracted from the available energy at the surface. The remaining energy is transported to  
 593 the atmosphere and should therefore equal the sum of turbulent and dispersive fluxes.  
 594 Figure 8a compares the measured turbulent fluxes against this remaining energy and shows  
 595 a large gap of 23.8% in the energy flux towards the atmosphere. In Fig. 8b, the modelled  
 596 dispersive fluxes are added to the measured turbulent fluxes, reducing the SEB gap to  
 597 18.6 %.



598  
 599 **Fig. 8** Comparison of measured turbulent heat fluxes (panel a) and measured turbulent and modelled  
 600 dispersive heat fluxes (panel b) to the total energy flux to the atmosphere. The total energy flux to the  
 601 atmosphere is calculated as the available energy at the surface ( $R_{net} - G$ ) minus the storage change in form  
 602 of sensible and latent heat ( $H_{\Delta St} + \lambda E_{\Delta St}$ ). The different colours represent the 16 individual eddy-covariance  
 603 stations that were used for this analysis.

604 Even though we do not know the actual breakdown of total available energy ( $R_{net} -$   
 605  $G$ ) into sensible and latent heat, we can consider the contributions of each energy balance  
 606 component shown in Fig. 9. The turbulent fluxes measured at the EC stations make up  
 607  $27.48 \pm 11.38\%$  ( $H_t$ ) and  $47.54 \pm 18.33\%$  ( $\lambda E_t$ ) of the total available energy at the surface,  
 608 resulting in a Bowen ratio of  $0.602 \pm 0.458$ . The storage change accounts for  $2.58 \pm 3.85\%$   
 609 ( $H_{\Delta St}$ ) and nearly 0% ( $\lambda E_{\Delta St}$ ). The modelled dispersive fluxes account for  $1.55 \pm 1.10\%$   
 610 ( $H_{d,mod}$ ) and  $5.62 \pm 4.76\%$  ( $\lambda E_{d,mod}$ ) of the total available energy. The Bowen ratio of the  
 611 dispersive fluxes is  $0.283 \pm 0.245$ , which is considerably lower than the Bowen ratio  
 612 observed in the turbulent flux measurements.



613

614

615

616

Fig. 9 Share of turbulent heat fluxes ( $H_t$ ,  $\lambda E_t$ ), air storage change ( $H_{\Delta St}$ ,  $\lambda E_{\Delta St}$ ) and modelled dispersive heat fluxes ( $H_{d,mod}$ ,  $\lambda E_{d,mod}$ ) of the total available energy ( $R_{net} - G$ ). The error bars represent the standard deviation of the sums shown in each bar.

617

## 4 Discussion

618

### 4.1 The Model of Energy Transport by Secondary Circulations

619

620

621

622

623

624

625

626

627

628

629

630

631

Instead of modelling the entire energy imbalance as it was proposed by former models to close the energy balance gap (De Roo et al. 2018; Huang et al. 2008; Wanner et al. 2022b) we decided to predict only the contribution of energy transport by SCs. The storage change in the air layer below the measurement altitude is possible to measure through vertical profiles of  $\theta$  and  $q$ , which is a more direct way to quantify it than modelling it. The storage change in the biomass is more difficult to determine by measurements. If the storage change cannot be measured or older measurements are to be corrected for which no storage change measurements are available, it must still be modelled to to achieve SEB closure on a 30-min measurement basis. However, it is unlikely that the storage change depends on the same parameters as the energy transport through SCs, so these two aspects should be considered separately. Furthermore, even for observation periods longer than one day, the contribution of the storage change to the SEB gap becomes very small and can therefore be neglected if SEB closure is to be achieved only for longer time scales.

632 The cross-validation of the model for  $H_d$  (Fig 2a) and  $\lambda E_d$  (Fig 2b) show that the  
633 correlation between predicted dispersive fluxes and true dispersive fluxes in the LES is  
634 very high for  $H$  but considerably lower for  $\lambda E$ . We investigated whether the particularly  
635 large underestimates and overestimates of  $\lambda E_d$  are linked to particularly high or low values  
636 of individual input variables. However, the values were always in the range of the input  
637 variables that achieved a suitable prediction of  $\lambda E_{d,true}$ . The large deviations are probably  
638 the result of a factor influencing  $\lambda E_d$  that is not considered by the model.

639 One possible reason why  $H_d$  prediction performs better than  $\lambda E_d$  prediction is that the  
640 atmospheric stability, represented by  $\langle \overline{u_* / w_*} \rangle$ , is directly linked to the magnitude of SCs  
641 and the magnitude of the sensible heat flux. A negative vertical gradient of  $\theta$  leads to  
642 convective conditions under which the development of secondary circulations is favoured  
643 (De Roo et al. 2018; Huang et al. 2008; Wanner et al. 2022b) and also means that warmer  
644 air is available near the surface and can be transported upwards by those SCs.

645 The vertical moisture gradient, on the other hand, is not directly related to atmospheric  
646 stability but rather to the ratio between latent surface heat flux and dry air entrainment. For  
647 example, over vegetated, non-water-limited surfaces, the surface is typically a source of  
648 moisture, but this might be counterbalanced by dry air entrainment at the boundary-layer  
649 top, resulting in different  $\langle \overline{\Delta q} \rangle$ . If lapse-rate stratification causes the formation of SCs but  
650  $\langle \overline{\Delta q} \rangle = 0$ , the movement of air masses will not contribute to the transport of moisture.  
651 Including entrainment as a predictor variable could therefore potentially improve the model,  
652 especially for  $\lambda E_d$ .

653 This phenomenon is illustrated by the importance of input variables for predicting  $H_d$   
654 and  $\lambda E_d$  shown in Fig. 2c-d, where  $\langle \overline{u_* / w_*} \rangle$  and  $\mathcal{H}$  have the strongest predictive power for  
655  $H_d$ , but in comparison, the predictive power of  $\langle \overline{u_* / w_*} \rangle$  for  $\lambda E_d$  is much lower.  $\mathcal{H}$  is also  
656 the most important predictive variable for  $\lambda E_d$ . The normalized measurement height  $z / \langle \overline{z_l} \rangle$   
657 has an intermediate predictive power in both cases, which is due to increasing fraction of  
658 energy transport by SCs within the surface layers with increasing height.

659 The rather high scatter in the correlation of  $\lambda E_{d,predicted}$  and  $\lambda E_{d,true}$  does not have a  
660 negative effect if the total fluxes are considered (Fig 2b). The standard deviation of the  
661 corrected fluxes ( $\lambda E_t + \lambda E_{\Delta st} + \lambda E_{d,predicted}$ ) remains almost unchanged compared to the

662 standard deviation of the uncorrected turbulent fluxes. For the sensible heat flux (Fig 2a),  
663 the correction even provides a significant improvement, as the standard deviation of the  
664 corrected fluxes ( $H_t + H_{\Delta St} + H_{d,predicted}$ ) is significantly smaller than for the turbulent  
665 fluxes alone.

666 In Fig. 3 and Table 3, another interesting aspect can be observed: when considering  
667 domain-averaged values, the Bowen ratio of turbulent and dispersive fluxes are the same,  
668 although the gap between surface fluxes and turbulent fluxes is different for  $H_d$  and  $\lambda E_d$ .  
669 This difference is compensated by the storage change alone. Thus, one could conclude that  
670 to close the SEB gap, it may be sufficient in many cases to measure  $H_{\Delta St}$  and  $\lambda E_{\Delta St}$  and fill  
671 the remaining gap according to the Bowen ratio of the measured turbulent heat fluxes. This  
672 approach has been discussed several times (Gebler et al. 2015; Hirschi et al. 2017; Mauder  
673 et al. 2007b; Mauder et al. 2013; Mauder et al. 2020; Twine et al. 2000). However, the  
674 relation between Bowen ratios of storage change and surface, turbulent, and dispersive heat  
675 fluxes is different in the more realistic CHEESEHEAD19 LES which is discussed in the  
676 next section. It furthermore remains questionable whether this assumption still holds if  
677 locally measured heat fluxes differ considerably from the average heat fluxes of the  
678 surroundings, which is typically the case in heterogeneous areas.

679 Due to the rather coarse resolution in the idealized LESs that were used to train the  
680 model, one has to assume that the strength of the SCs is underestimated, especially near  
681 the lower boundary of the domain. It is therefore likely that the model underestimates the  
682 transport of energy by SCs. The magnitude of this systematic error, however, is not known  
683 and requires further investigation in follow-up studies.

#### 684 **4.2 Application to the More Realistic CHEESEHEAD19 LES**

685 Figure 4 shows that the model could be applied to almost all 30-minute intervals with  
686 unstable conditions and for a wide range of measurement heights. A few observations near  
687 the canopy top had to be discarded because of the low values of  $z/\langle\bar{z}_t\rangle$ . However, this  
688 affected mostly measurement heights of less than 16.5 m, which corresponds to  
689 approximately 10 m above the canopy top. To avoid individual roughness elements  
690 affecting the measured turbulent fluxes, EC measurements should not be carried out within

691 the roughness sublayer (Katul et al. 1999) and are often located more than 10 m above the  
692 canopy top at forest locations.

693 In comparison with the dispersive fluxes calculated from the CHEESEHEAD19 LES  
694 output, the model slightly overestimates  $\lambda E_d$  and clearly overestimates  $H_d$  (Fig. 5),  
695 resulting in a general overestimation of dispersive fluxes (Fig. 6) and a slightly higher  
696 Bowen ratio (Table 4). The fact that  $H_{d,mod}$  and  $\lambda E_{d,mod}$  are slightly larger than the actual  
697 fluxes could be due to non-cyclic boundary conditions in the CHEESEHEAD19 LES. This  
698 arrangement raises the possibility that some of the energy transport is not captured in the  
699 dispersive fluxes. Another reason could be the different setup of the simulations. In the  
700 idealized simulations, the fluxes were specified at the surface, whereas in the realistic  
701 simulations, an LSM was used in combination with PCM. Wanner et al. (2022a) showed  
702 that the use of LSM and PCM increases the dispersive heat fluxes directly above the canopy  
703 but decreases the dispersive fluxes further up, compared to dispersive fluxes in simulations  
704 with prescribed surface fluxes, owing to feedbacks between atmosphere and surface.

705 In contrast to the results from the idealized LESs,  $\beta(\langle F_{d,LES} \rangle)$  does not equal  $\beta(\langle F_t \rangle)$   
706 in the CHEESEHEAD19 LES but is considerably lower, indicating that SCs have a larger  
707 relative share in the transport of latent heat than in the transport of sensible heat. It follows  
708 that the Bowen ratio approach to fill the SEB gap is not so well suited under more realistic  
709 conditions. Our dispersive flux model is capable of partially capturing the difference  
710 between  $\beta(\langle F_{d,LES} \rangle)$  and  $\beta(\langle F_t \rangle)$ , but due to the strong overestimation of the sensible  
711 dispersive heat flux by roughly 18%, the partitioning of dispersive fluxes in the realistic  
712 LES is not ideally captured by the model.

713 Another factor that could alter the partitioning is the influence of entrainment on the  
714 transport of energy by secondary circulations (Gao et al. 2017; Huang et al. 2008; Mauder  
715 et al. 2020) which is not considered in our model. A temperature or humidity gradient in  
716 the boundary layer is the basic prerequisite for any transport of sensible or latent energy  
717 through SC which is why we included  $\langle \overline{\Delta\theta} \rangle$  and  $\langle \overline{\Delta q} \rangle$  as predictors in our model. The  
718 properties of the air mixed into the boundary layer at the upper boundary should also affect  
719 the transport of heat or water vapor. Since  $\langle \overline{\Delta\theta} \rangle$  and  $\langle \overline{\Delta q} \rangle$  only represent the lower half of  
720 the atmospheric boundary layer (see Eq. 16-17), this influence is only partially considered  
721 in the model and could also contribute to the underestimation of the dispersive fluxes. Since

722 the ABL is confined by an inversion at the top, the influence of entrainment on the  $H_d$  may  
723 be quite small. However, the humidity above the boundary layer is highly variable, so the  
724 effect of entrainment could also be a reason for the high uncertainty in the prediction of  
725  $\lambda E_d$ . The heat flux profiles (not shown) confirm that the flux regime in the  
726 CHEESEHEAD19 LES was driven rather by dry air entrainment at the ABL top than by  
727 the surface fluxes at some times. As already discussed in the previous section, including  
728 entrainment as a predictor variable might therefore improve the model performance.

729 Furthermore, with non-cyclic boundary conditions it is possible that weather fronts pass  
730 through the domain which can carry warmer/cooler or moister/dryer air into the domain,  
731 affecting  $\bar{w}$ ,  $\bar{\theta}$ , and  $\bar{q}$  used to calculate the dispersive fluxes. In the CHEESEHEAD19 LES,  
732 a front passed through the domain in the afternoon on the first day, causing the boundary  
733 layer to collapse at 2:30 p.m. which is shown by the increase of  $z/\langle\bar{z}_l\rangle$  (Fig. 4). Figure 13  
734 (Appendix 2) shows that the surface fluxes started decreasing at 1:00 p.m., indicating that  
735 advection may already have played a minor role, affecting  $H_{d,LES}$  and  $\lambda E_{d,LES}$ . The effect  
736 of weather fronts passing by is generally less relevant for EC measurements, as they would  
737 typically be discarded in the affected periods, due to the violation of the stationarity  
738 requirement (Mauder et al. 2006).

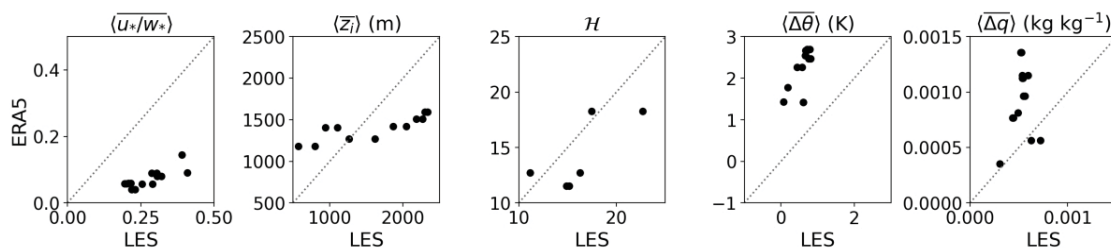
### 739 **4.3 Application to the CHEESEHEAD19 Field Measurements**

740 The application of the model to field measurements was very limited because the ranges of  
741 the predictor variables in the field measurements were significantly larger than covered by  
742 the idealized LESs used to train the model (Fig. 7). The ranges of  $\langle\overline{u_*}/w_*\rangle$ ,  $\mathcal{H}$  and  $\langle\overline{\Delta q}\rangle$   
743 encountered in the ERA5 reanalysis data is much larger than in the idealized LES. However,  
744 this seems to be caused by extreme cases and outliers since a considerable number of  
745 observations (45.27%, 99.62%, and 67.20%, respectively) were covered by the training  
746 data (Table 5). The range of  $z/\langle\bar{z}_l\rangle$  encountered in the field is only slightly larger than in  
747 the idealized LES. Nevertheless, only 37.60% were covered by the training data (Table 5).  
748 This is due to the low measurement heights in some of the field stations (12 m at NW2 and  
749 SE5 and 3 m at NW3 and SE5) whose data were entirely discarded. Such low measurement  
750 heights could not be covered by the idealized LES due to the coarse grid resolution. Most

751 measurements had to be discarded due to insufficient coverage of  $\langle \overline{\Delta\theta} \rangle$ , as only 27.60% of  
 752 the observed values were covered by the idealized LES (Table 5).

753 To investigate whether the large ranges in predictor variables are realistic, we compared  
 754 the predictor variables derived from the ERA5 reanalysis data to the predictor variables  
 755 derived from the CHEESEHEAD19 LES for 22-23 August 2019 (Fig. 10). They show a  
 756 good agreement in  $\mathcal{H}$  and  $\langle \bar{z}_t \rangle$ , although ERA5 does not capture the variability in  $\langle \bar{z}_t \rangle$   
 757 as well as the CHEESEHEAD19 LES. Compared to the CHEESEHEAD19 LES, ERA5  
 758 underestimates  $\langle \overline{u_*}/w_* \rangle$  and overestimates  $\langle \overline{\Delta\theta} \rangle$  and  $\langle \overline{\Delta q} \rangle$ . The comparison of hourly  
 759 vertical profiles (Fig. 14, Appendix 3) shows that the overestimation of  $\langle \overline{\Delta\theta} \rangle$  results mainly  
 760 from a stronger increase in theta near the surface, whereas the profiles agree very well  
 761 within the mixed layer.

762 The CHEESEHEAD19 LES was validated against field measurements and the domain-  
 763 averaged vertical profiles showed good agreement with radiosonde measurements (Paleri  
 764 et al. (submitted)). Nevertheless, it must be noted, that the domain was mostly forested  
 765 with an average canopy height of 22.08 m. The active surface is therefore not clearly  
 766 defined and the lowest grid points receive less radiation.  $\langle \bar{\theta} \rangle$  may therefore be slightly  
 767 underestimated near the surface.



768  
 769 **Fig. 10** Comparison of predictor variables for the dispersive flux model from the CHEESEHEAD19 LES (x-  
 770 axis) and ERA5 reanalysis data (y-axis) for all 30-min intervals on 22-23 August used for the analysis. Note  
 771 that the second panel shows  $\langle \bar{z}_t \rangle$  instead of  $z/\langle \bar{z}_t \rangle$  for better comparability.

772 Figure 8 shows that adding the modelled energy transport by secondary circulations  
 773 considerably decreases the SEB gap from 23.8% on average to 18.6% on average but the  
 774 SEB is still not closed. As mentioned in Section 4.1, one reason for the remaining gap is  
 775 that the model might underestimate the transport by SCs due to the coarse grid spacing.  
 776 However, there are more reasons why considering the energy transport by SCs alone does  
 777 not result in SEB closure.

778 Because the model predicts only the dispersive heat fluxes and not the entire SEB gap,  
779 the storage of energy in the underlying air volume and canopy must be measured at tall EC  
780 stations since it also contributes significantly to the SEB gap. The measurement of the  
781 energy storage in the air volume beneath an EC station can be realized by simple profile  
782 measurements of temperature and humidity. This is already standard in some EC stations  
783 (Heiskanen et al. 2022) and was also included in the CHEESEHEAD19 measurements.  
784 However, the biomass storage change is typically not measured at EC stations and adds  
785 uncertainty to the energy storage quantification. It was not included in the energy storage  
786 measurements at the CHEESEHEAD19 sites, though tree biomass heat storage was  
787 measured at several sites subsequent to the campaign, where it averaged 6.5% of the energy  
788 balance gap (Butterworth et al. submitted). This agrees with other studies which have found  
789 the biomass storage change to be of the same magnitude as the storage change in the air  
790 (Lindroth et al. 2010) or even twice as high (Haverd et al. 2007) at forest locations. Figure  
791 9 shows that the addition of modelled dispersive heat fluxes to measured heat fluxes and  
792 air storage change decreases the SEB gap from  $22.82 \pm 17.67\%$  to  $15.66 \pm 19.44\%$ . Including  
793 the biomass storage change would further decrease the SEB gap to roughly 9 % on average.

794 As discussed in section 4.1, a slight underestimation of the dispersive fluxes by the  
795 model is expected due to the coarse grid spacing in the idealized LESs providing the  
796 training data. However, there are some more minor factors that contribute to the SEB gap  
797 that were not considered in this analysis.

798 First, the model only considers the effect of atmospheric stability and thermal surface  
799 heterogeneity on the energy transport by secondary circulations, which were identified as  
800 the major factors. However, topography effects can also enhance the energy transport of  
801 energy by SCs (Finnigan et al. 2003) but are not included in the model. Even though the  
802 measurement area was chosen in part because of its weak topography, the area in which  
803 the CHEESEHEAD19 campaign took place is not entirely flat. This may have strengthened  
804 the SCs, especially near the numerous water bodies in the domain which would also explain  
805 why the dispersive fluxes in the field measurements are larger than in both the idealized  
806 and CHEESEHEAD19 LESs.

807 Finally, the turbulent heat fluxes might be underestimated as CSAT3AW (Campbell  
808 Scientific) sonic anemometers were used. For this type of sonic anemometer, a correction

809 to account for transducer shadowing was developed that increases the fluxes by up to 5%  
810 (Horst et al. 2015) which was not applied to the CHEESEHEAD19 field measurements.  
811 Also, minor contributions to the SEB gap are not considered, like energy consumption by  
812 photosynthesis, which is estimated to account for roughly 1% of  $R_{net}$  (Finnigan 2008).  
813 Taking these factors into account, the remaining SEB gap would be only about 3%, which  
814 suggests that the underestimation of energy transport by SCs by our model is quite small.

#### 815 **4.4 Different Data Availability in Idealized LES, More Realistic LES, and Field** 816 **Measurements**

817 Fundamental differences in data availability in the idealized and more realistic LES and  
818 field measurements complicate the accurate application of the model. This includes the  
819 determination of  $\mathcal{H}$ , the true dispersive fluxes and the vertical gradients  $\langle \overline{\Delta\theta} \rangle$  and  $\langle \overline{\Delta q} \rangle$ .

820 The calculation of  $\mathcal{H}$  involves  $\Delta\bar{T}$ ,  $\langle \bar{T}_s \rangle$ , and  $L_h$ . All three parameters are calculated  
821 based on the two-dimensional surface temperature. In the idealized LES, the surface  
822 temperature is clearly defined as the temperature at the lower boundary of the domain. In  
823 the CHEESEHEAD19 simulations, where a plant canopy model has been used in the  
824 forested areas, the surface is not so clearly defined. The temperature at the lower boundary  
825 of the domain is not very meaningful because it is mostly shaded and the majority of  
826 radiative transfer happens at the canopy level. We therefore used the air temperature at the  
827 top of the vegetation instead of the actual surface temperature as  $T_s$ , but this is based on  
828 the assumption that the vegetation has the same temperature as the air and introduces  
829 additional uncertainty. In field measurements,  $T_s$  is difficult to determine at sufficiently  
830 high spatial and especially temporal resolution. Therefore, we used the surface-temperature  
831 maps from Desai et al. (2021), which are a fusion data product using land-surface models,  
832 satellite and hyperspectral imagery to apply the model to the CHEESEHEAD19 field  
833 measurements.

834 The dispersive fluxes can be computed directly as the spatial covariance of  $w$  and  $\theta$  or  
835  $w$  and  $q$  in the idealized LESs with cyclic boundary conditions and thus quasi-infinite  
836 horizontal extent. In the realistic LES, the dispersive fluxes can also be computed as spatial  
837 covariance in a defined area. This area must be sufficiently large to fully cover the  
838 horizontal extent of the secondary circulations, similarly to how the averaging period in

839 classical EC measurements must theoretically be sufficiently long to cover all relevant time  
840 scales. Since the horizontal extent of secondary circulations can reach about  $2-3 z_i$  (Paleri  
841 et al. 2022a; Stull 1988), we recommend using an area with an edge length of at least  $4 z_i$   
842 to calculate the dispersive fluxes. If the area is too small, SCs partially contribute to  
843 horizontal transport, i.e., advection, that is not captured by the spatial covariance of  $w$  and  
844  $\theta$  or  $q$ . If the area is very large or includes an area where land cover or topography changes  
845 significantly the resulting dispersive flux is not representative of the area in which the EC  
846 measurement takes place. For typical single-tower field measurements, the dispersive flux  
847 cannot be calculated directly, as the calculation of covariances would require high-  
848 resolution spatial measurements of  $w$ ,  $q$  and  $\theta$ . Instead, the amount of energy transported  
849 by the SCs must be calculated indirectly as a residual from the available energy at the  
850 surface ( $R_{net} - G$ ) minus the energy stored in the air volume between the surface and the  
851 measurement height ( $H_{\Delta St} + \lambda E_{\Delta St}$ ) and the turbulent transport of energy ( $H_t + \lambda E_t$ ). A  
852 drawback of this approach is the scale mismatch between the measurement of  $R_{net}$  and  $G$ ,  
853 which is only representative for the location of the EC station, and  $H$  and  $\lambda E$ , which reflect  
854 the energy flux of the entire footprint, which covers a much larger area depending on the  
855 measurement height and atmospheric stability (Kljun et al. 2015).

856 For the model training, the output from the idealized LESs was used where the vertical  
857 gradients  $\langle \overline{\Delta \theta} \rangle$  and  $\langle \overline{\Delta q} \rangle$  were calculated as the difference between surface values and the  
858  $0.5 \langle \bar{z}_i \rangle$ . Since surface values are not available in the ERA5 reanalysis data, we used the  
859 2 m temperature and humidity measurements instead to predict the dispersive fluxes in the  
860 CHEESEHEAD19 measurements. Under unstable conditions, the temperature gradient  
861 near the surface is very steep. Thus, the 2 m temperature is expected to be lower than the  
862 air temperature directly above the surface, resulting in an underestimation of the vertical  
863 temperature gradient between the surface and the middle of the boundary layer. Over  
864 vegetated surfaces, which typically serve as a source of moisture unless they experience  
865 water stress, using the 2 m humidity instead of a near-ground measurement also results in  
866 an underestimation of the vertical gradient. However, as shown in Fig. 10,  $\langle \overline{\Delta \theta} \rangle$  derived  
867 from ERA5 reanalysis data is not underestimated but overestimated compared to the  
868 CHEESEHEAD19 LES.

869 In the more realistic CHEESEHEAD19 LES, a PCM is used in forested areas, which is  
870 why the active surface is not as clearly defined as in the idealized LES. This increases the  
871 uncertainty in the calculation of  $T_s$ ,  $\langle \Delta\bar{\theta} \rangle$  and  $\langle \Delta\bar{q} \rangle$  and  $\langle \overline{u_* / w_*} \rangle$ , as well as the surface  
872 fluxes.

#### 873 **4.5 Feasibility of the Model Application to Eddy-Covariance Stations**

874 Single point EC field measurements typically only represent a limited area, referred to as  
875 footprint. The size of this area depends on various factors such as measurement height,  
876 atmospheric stability, and horizontal wind speed (Kljun et al. 2015), but it is always only  
877 a subset of the area that influences the development of SCs. Since the horizontal extent of  
878 SCs can reach 2-3 times the boundary layer height  $z_i$ , they can span multiple kilometres  
879 and the area that has an effect on their development is correspondingly large. Therefore,  
880 EC measurements are likely to differ from the average values representing the entire area  
881 and are not suited as predicting variables for a model based on domain-averaged values.

882 This is why we used the ERA5 reanalysis data to provide the majority of the predictor  
883 variables for the application of the model to the CHEESEHEAD19 EC measurements. One  
884 advantage of the ERA5 reanalysis data is that it is available in all locations where EC  
885 measurements are carried out and thus can be used to predict dispersive fluxes at any tower  
886 without installing additional measurement instruments. This also facilitates the prediction  
887 of dispersive fluxes for EC measurements carried out in the past for which no field  
888 measurements of predictor variables are available. Since the ERA5 reanalysis data is  
889 available for the past 80 decades it can be used to consistently improve the energy-balance  
890 closure in long existing time series. However, with a spatial resolution of  $0.25^\circ$ , one grid  
891 cell in the ERA5 data is representative of up to  $28 \times 28 \text{ km}^2$ , which might include landscapes  
892 that are not representative of the surroundings of an EC tower.

893 The only parameters not derived from the ERA5 reanalysis data were  $\Delta\bar{T}$ ,  $\langle \bar{T}_s \rangle$ , and  $L_h$   
894 used to calculate the thermal heterogeneity parameter as their calculation requires spatially  
895 highly resolved surface-temperature maps. We used the land-surface temperature fusion  
896 maps provided by Desai et al. (2021) which are derived by combining the information  
897 gathered from different satellite observations with high temporal resolution (NLDAS-2  
898 (Xia et al. 2012), GOES-R (Yu et al. 2009)) and high spatial resolution (ECOSTRESS

899 (Hulley et al. 2022)). Desai et al. (2021) showed that these maps represent the spatial and  
900 temporal variation in surface temperature in the CHEESEHEAD19 domain. Their  
901 approach can be used to generate land-surface temperature fusion maps with a spatial  
902 resolution of 50 m and a temporal resolution of 1 h for any location where temporally  
903 frequent geostationary (such as GOES) and high-spatial resolution less frequent land  
904 surface-temperature data (such as ECOSTRESS) are available and therefore can as well be  
905 derived for many EC stations without additionally carrying out measurements.

## 906 **5 Conclusion**

907 We have developed a model to predict 30-min dispersive heat fluxes, i.e., the energy  
908 transport by SCs. A python script to apply the model, including the training dataset, is  
909 included in the supplements.

910 By applying it to the CHEESEHEAD19 LES, we have shown that it reproduces the  
911 partitioning into sensible and latent heat quite well. The application to CHEESEHEAD19  
912 field measurements showed that the model currently covers only a limited range of  
913 atmospheric conditions and is only applicable to measurement heights where  
914  $z_m - z_d > 10$  m. Therefore, to predict dispersive fluxes under all typical conditions at eddy  
915 covariance stations, the training data set must be extended to cover a wider range of  $\langle \overline{\Delta\theta} \rangle$ ,  
916  $\langle \overline{\Delta q} \rangle$ ,  $\mathcal{H}$ , and  $z / \langle z_i \rangle$ .

917 However, application to the measurements that were within the model limits showed  
918 that the modelled dispersive fluxes resulted in a significant reduction in the SEB gap,  
919 although it did not close it completely. A variety of possible reasons were discussed,  
920 including the low resolution of the LESs the training data was extracted from, the different  
921 availability of information on vertical gradients of  $\langle \bar{\theta} \rangle$  and  $\langle \bar{q} \rangle$  in the LES and the ERA5  
922 reanalysis data, and uncertainties associated with the use of modelled surface temperature  
923 and atmospheric variables as predictor variables. These issues can partially be further  
924 improved by increasing the resolution of the LESs that provide the training data, which  
925 will allow for an enhanced representation of SCs near the surface and the gradients of  
926  $\langle \bar{\theta} \rangle$  and  $\langle \bar{q} \rangle$  can be defined in accordance to data availability in field measurements.

927 We conclude that these factors likely cause a slight underestimation of the dispersive  
928 fluxes by the model. However, a large portion of the remaining gap could be filled by

929 adding the ignored biomass storage change, which is estimated to account for 6.5% of the  
 930 total available energy at 30-minute intervals.

931 We have also shown that it is possible to apply this model of dispersive heat fluxes to  
 932 field measurements without performing any additional field measurements. The  
 933 application of the model is based on ERA5 reanalysis data and remote sensing products  
 934 that are available for most EC stations around the world and can also be used to model the  
 935 dispersive fluxes retrospectively.

936 **Acknowledgements** This project was financially supported by Deutsche Forschungsgemeinschaft (DFG)  
 937 Award #406980118, National Science Foundation (NSF) Grant AGS-1822420 and the MICMoR Research  
 938 School of the Karlsruhe Institute of Technology.

## 939 **Appendix 1: The Idealized Large-Eddy Simulations**

940 **Table 6** Characteristic values of each of the 148 idealized simulations

sim ID	$U_g$	$\beta$	$\langle H_S \rangle$	$\langle \lambda E_S \rangle$	$\langle u_* / w_* \rangle$	$z_i$	$\langle \bar{T}_S \rangle$	$\Delta \bar{T}$	$\langle \bar{Q}_S \rangle$	$\mathcal{H}$
1	0.5	0.185	115.7	616.5	0.188	671.2	289.4	0.136	0.0113	16.028
2	1.0	0.184	115.7	616.5	0.190	675.5	289.4	0.119	0.0113	3.464
3	2.0	0.184	115.7	616.5	0.182	673.6	289.4	0.100	0.0114	0.776
4	4.0	0.183	115.7	616.5	0.216	667.6	289.4	0.084	0.0115	0.179
5	9.0	0.184	115.7	616.5	0.347	672.6	289.5	0.081	0.0117	0.028
6	0.5	0.177	114.0	618.6	0.185	678.1	289.3	0.517	0.0114	47.100
7	1.0	0.179	114.0	618.6	0.188	670.9	289.3	0.486	0.0114	10.131
8	2.0	0.179	114.0	618.6	0.180	670.9	289.3	0.458	0.0114	2.230
9	4.0	0.180	114.0	618.6	0.217	657.8	289.4	0.425	0.0116	0.564
10	9.0	0.180	114.0	618.6	0.354	660.6	289.5	0.336	0.0117	0.088
11	0.5	0.187	119.9	611.3	0.184	661.3	289.4	0.613	0.0113	90.096
12	0.5	0.187	119.9	611.3	0.184	661.3	289.4	0.613	0.0113	90.096
13	1.0	0.191	119.9	611.3	0.181	686.9	289.4	0.544	0.0113	14.999
14	1.0	0.191	119.9	611.3	0.181	686.9	289.4	0.544	0.0113	14.999
15	2.0	0.191	119.9	611.3	0.180	680.6	289.4	0.507	0.0113	3.499
16	2.0	0.191	119.9	611.3	0.180	680.6	289.4	0.507	0.0113	3.499
17	4.0	0.192	119.9	611.3	0.211	671.6	289.5	0.492	0.0115	0.946
18	9.0	0.191	119.9	611.3	0.346	673.3	289.6	0.428	0.0116	0.155
19	0.5	0.177	113.2	619.6	0.183	647.1	289.3	0.556	0.0114	91.261
20	0.5	0.177	113.2	619.6	0.183	647.1	289.3	0.556	0.0114	91.261
21	1.0	0.175	113.2	619.6	0.185	651.8	289.3	0.547	0.0115	22.314
22	1.0	0.175	113.2	619.6	0.185	651.8	289.3	0.547	0.0115	22.314
23	2.0	0.178	113.2	619.6	0.181	661.9	289.3	0.497	0.0115	4.464
24	2.0	0.178	113.2	619.6	0.181	661.9	289.3	0.497	0.0115	4.464

25	4.0	0.179	113.2	619.6	0.220	653.6	289.3	0.493	0.0117	1.216
26	9.0	0.178	113.2	619.6	0.355	649.2	289.4	0.459	0.0118	0.221
27	0.5	0.487	232.6	473.4	0.163	870.8	291.5	0.215	0.0095	28.519
28	1.0	0.485	232.6	473.4	0.163	868.9	291.5	0.198	0.0095	5.867
29	2.0	0.484	232.6	473.4	0.162	868.2	291.6	0.163	0.0095	0.949
30	4.0	0.484	232.6	473.4	0.172	864.6	291.6	0.141	0.0096	0.237
31	9.0	0.482	232.6	473.4	0.272	866.8	291.8	0.132	0.0097	0.052
32	0.5	0.479	231.8	474.4	0.161	873.0	291.5	0.437	0.0095	45.086
33	1.0	0.480	231.8	474.4	0.164	862.2	291.5	0.398	0.0095	9.300
34	2.0	0.480	231.8	474.4	0.162	867.7	291.5	0.389	0.0095	2.262
35	4.0	0.480	231.8	474.4	0.173	863.2	291.6	0.367	0.0096	0.600
36	9.0	0.480	231.8	474.4	0.271	865.5	291.8	0.304	0.0097	0.092
37	0.5	0.471	229.6	477.1	0.159	867.8	291.5	0.499	0.0095	68.753
38	0.5	0.471	229.6	477.1	0.159	867.8	291.5	0.499	0.0095	68.753
39	1.0	0.473	229.6	477.1	0.162	869.5	291.5	0.467	0.0095	13.356
40	1.0	0.473	229.6	477.1	0.162	869.5	291.5	0.467	0.0095	13.356
41	2.0	0.473	229.6	477.1	0.158	862.7	291.5	0.451	0.0095	3.817
42	2.0	0.473	229.6	477.1	0.158	862.7	291.5	0.451	0.0095	3.817
43	4.0	0.473	229.6	477.1	0.173	853.9	291.6	0.444	0.0096	0.881
44	9.0	0.472	229.6	477.1	0.277	854.6	291.7	0.395	0.0098	0.155
45	0.5	0.489	236.5	468.7	0.154	888.4	291.6	0.559	0.0094	106.074
46	0.5	0.489	236.5	468.7	0.154	888.4	291.6	0.559	0.0094	106.074
47	1.0	0.495	236.5	468.7	0.158	887.1	291.6	0.521	0.0094	24.269
48	1.0	0.495	236.5	468.7	0.158	887.1	291.6	0.521	0.0094	24.269
49	2.0	0.495	236.5	468.7	0.158	875.3	291.6	0.468	0.0095	4.959
50	2.0	0.495	236.5	468.7	0.158	875.3	291.6	0.468	0.0095	4.959
51	4.0	0.496	236.5	468.7	0.173	865.2	291.7	0.480	0.0096	1.336
52	9.0	0.496	236.5	468.7	0.268	868.3	291.8	0.509	0.0097	0.289
53	0.5	0.116	79.3	661.1	0.231	443.4	288.5	0.112	0.0121	15.021
54	1.0	0.117	79.3	661.1	0.225	446.9	288.5	0.095	0.0122	2.706
55	2.0	0.117	79.3	661.1	0.212	464.0	288.5	0.077	0.0122	0.660
56	4.0	0.117	79.3	661.1	0.258	499.5	288.6	0.070	0.0124	0.163
57	9.0	0.117	79.3	661.1	0.426	498.5	288.6	0.064	0.0126	0.023
58	0.5	0.115	79.8	660.4	0.228	444.2	288.5	0.598	0.0122	72.087
59	1.0	0.116	79.8	660.4	0.224	454.9	288.5	0.551	0.0122	15.560
60	2.0	0.116	79.8	660.4	0.215	483.6	288.5	0.508	0.0123	3.899
61	4.0	0.117	79.8	660.4	0.254	524.2	288.6	0.452	0.0125	0.760
62	9.0	0.118	79.8	660.4	0.423	502.8	288.7	0.342	0.0125	0.111
63	0.5	0.101	73.1	668.7	0.226	403.8	288.3	0.864	0.0126	122.025
64	1.0	0.105	73.1	668.7	0.229	416.4	288.3	0.741	0.0125	22.001
65	2.0	0.105	73.1	668.7	0.223	450.7	288.3	0.602	0.0125	4.434
66	4.0	0.106	73.1	668.7	0.276	458.1	288.4	0.540	0.0127	0.942
67	9.0	0.106	73.1	668.7	0.443	467.1	288.5	0.425	0.0128	0.171

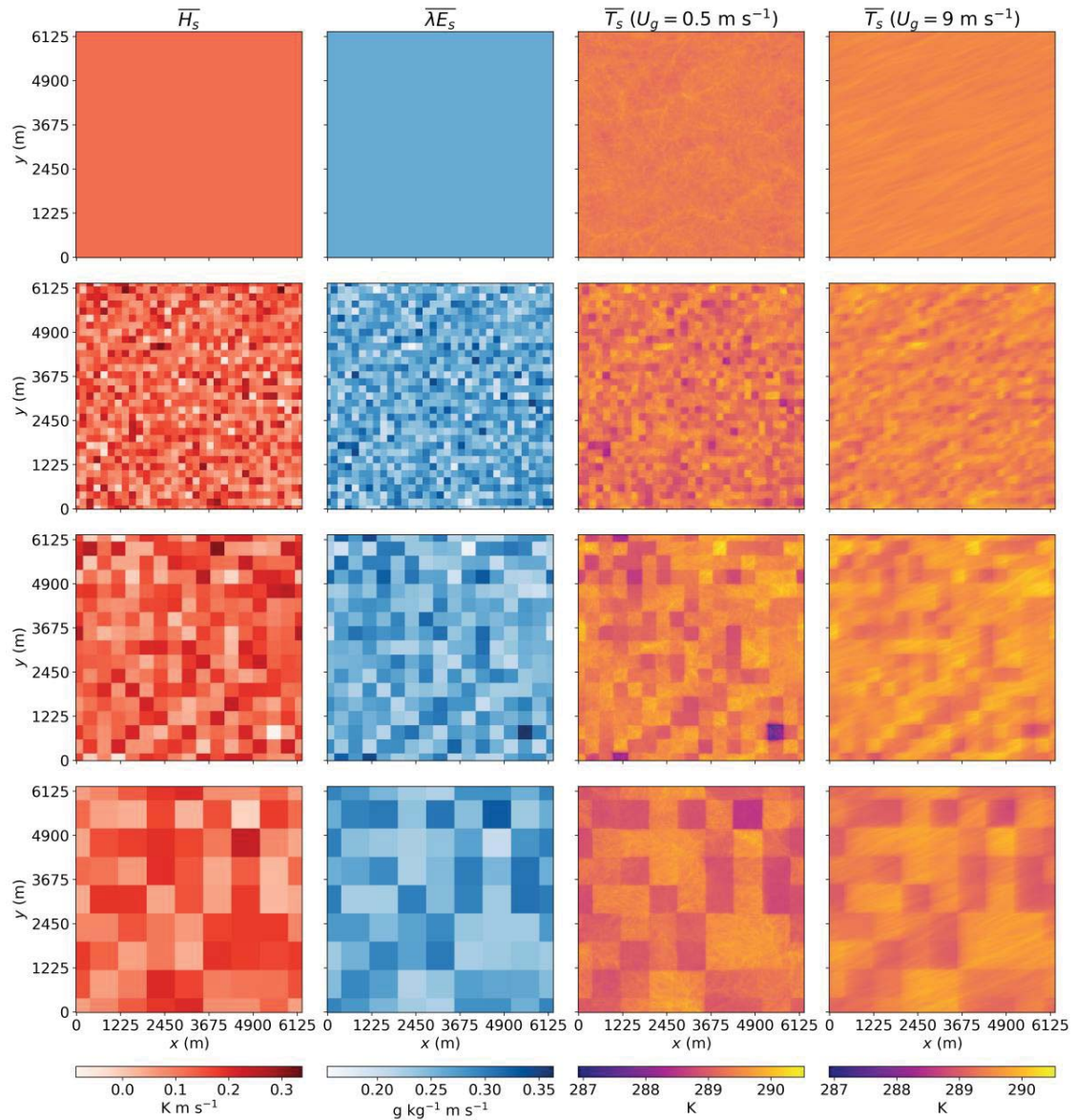
68	0.5	0.123	84.9	654.2	0.212	457.9	288.6	0.534	0.0121	100.453
69	1.0	0.124	84.9	654.2	0.205	511.7	288.6	0.543	0.0122	25.607
70	2.0	0.125	84.9	654.2	0.200	564.1	288.6	0.543	0.0122	6.572
71	4.0	0.126	84.9	654.2	0.249	542.4	288.7	0.506	0.0124	1.377
72	9.0	0.126	84.9	654.2	0.418	502.3	288.8	0.469	0.0124	0.276
73	0.5	0.329	179.2	538.7	0.169	784.9	290.6	0.181	0.0102	17.725
74	1.0	0.328	179.2	538.7	0.174	784.9	290.6	0.160	0.0102	3.707
75	2.0	0.327	179.2	538.7	0.169	776.7	290.6	0.133	0.0102	0.849
76	4.0	0.326	179.2	538.7	0.184	780.6	290.7	0.116	0.0103	0.183
77	9.0	0.326	179.2	538.7	0.298	778.1	290.8	0.109	0.0105	0.040
78	0.5	0.323	179.0	539.1	0.171	788.7	290.6	0.480	0.0102	53.100
79	1.0	0.325	179.0	539.1	0.174	782.5	290.6	0.439	0.0102	10.971
80	2.0	0.324	179.0	539.1	0.168	778.9	290.6	0.420	0.0102	2.251
81	4.0	0.325	179.0	539.1	0.185	776.8	290.7	0.392	0.0104	0.575
82	9.0	0.326	179.0	539.1	0.298	783.1	290.8	0.320	0.0105	0.138
83	0.5	0.323	179.4	538.5	0.166	789.1	290.6	0.495	0.0102	64.815
84	1.0	0.327	179.4	538.5	0.172	789.3	290.6	0.454	0.0102	13.765
85	2.0	0.326	179.4	538.5	0.169	781.0	290.6	0.443	0.0102	3.640
86	4.0	0.326	179.4	538.5	0.186	775.8	290.7	0.436	0.0104	0.781
87	9.0	0.325	179.4	538.5	0.300	779.9	290.8	0.397	0.0105	0.151
88	0.5	0.323	179.4	538.6	0.165	789.3	290.6	0.521	0.0102	84.199
89	1.0	0.327	179.4	538.6	0.168	787.1	290.6	0.475	0.0102	22.673
90	2.0	0.328	179.4	538.6	0.168	778.5	290.6	0.468	0.0103	5.139
91	4.0	0.327	179.4	538.6	0.185	771.9	290.7	0.472	0.0104	1.309
92	9.0	0.327	179.4	538.6	0.299	782.7	290.8	0.435	0.0105	0.228
93	0.5	0.833	314.6	373.0	0.148	1005.4	292.8	0.262	0.0086	27.786
94	1.0	0.834	314.6	373.0	0.155	999.4	292.8	0.236	0.0086	6.943
95	2.0	0.832	314.6	373.0	0.151	995.4	292.8	0.203	0.0086	1.499
96	4.0	0.832	314.6	373.0	0.159	988.1	292.9	0.182	0.0086	0.435
97	9.0	0.830	314.6	373.0	0.242	994.4	293.1	0.154	0.0087	0.066
98	0.5	0.820	312.4	375.7	0.151	993.2	292.8	0.443	0.0086	46.124
99	1.0	0.823	312.4	375.7	0.153	997.2	292.8	0.412	0.0086	9.446
100	2.0	0.818	312.4	375.7	0.152	991.9	292.8	0.389	0.0086	2.445
101	4.0	0.816	312.4	375.7	0.157	982.6	292.9	0.370	0.0087	0.728
102	9.0	0.818	312.4	375.7	0.245	992.2	293.1	0.315	0.0088	0.106
103	0.5	0.807	310.0	378.6	0.149	996.5	292.7	0.461	0.0086	68.539
104	0.5	0.807	310.0	378.6	0.149	996.5	292.7	0.461	0.0086	68.539
105	1.0	0.808	310.0	378.6	0.153	995.8	292.7	0.425	0.0086	12.896
106	1.0	0.808	310.0	378.6	0.153	995.8	292.7	0.425	0.0086	12.896
107	2.0	0.804	310.0	378.6	0.155	988.3	292.7	0.415	0.0086	2.919
108	2.0	0.804	310.0	378.6	0.155	988.3	292.7	0.415	0.0086	2.919
109	4.0	0.807	310.0	378.6	0.160	978.5	292.8	0.388	0.0087	0.672
110	9.0	0.807	310.0	378.6	0.246	977.8	293.0	0.378	0.0088	0.153

111	0.5	0.870	321.3	364.8	0.148	1018.7	292.9	0.443	0.0085	68.882
112	0.5	0.870	321.3	364.8	0.148	1018.7	292.9	0.443	0.0085	68.882
113	1.0	0.867	321.3	364.8	0.152	1009.3	292.9	0.435	0.0085	16.297
114	1.0	0.867	321.3	364.8	0.152	1009.3	292.9	0.435	0.0085	16.297
115	2.0	0.870	321.3	364.8	0.153	995.9	292.9	0.393	0.0085	4.114
116	2.0	0.870	321.3	364.8	0.153	995.9	292.9	0.393	0.0085	4.114
117	4.0	0.865	321.3	364.8	0.157	1006.9	293.0	0.395	0.0086	0.946
118	9.0	0.867	321.3	364.8	0.242	1000.0	293.2	0.397	0.0087	0.176
119	0.5	0.301	118.7	375.9	0.174	672.0	289.3	0.627	0.0098	96.847
120	1.0	0.307	118.7	375.9	0.177	661.3	289.3	0.566	0.0098	17.707
121	2.0	0.306	118.7	375.9	0.175	654.2	289.3	0.545	0.0098	3.693
122	0.5	0.236	101.4	397.1	0.173	632.9	288.9	0.665	0.0102	111.370
123	1.0	0.245	101.4	397.1	0.179	627.8	288.9	0.582	0.0101	25.164
124	2.0	0.246	101.4	397.1	0.182	621.6	288.9	0.538	0.0102	5.395
125	0.5	0.578	115.3	190.5	0.168	643.8	289.2	0.533	0.0084	69.781
126	1.0	0.576	115.3	190.5	0.170	634.8	289.2	0.510	0.0084	15.802
127	2.0	0.580	115.3	190.5	0.170	631.6	289.2	0.495	0.0085	3.626
128	0.5	0.618	121.7	182.7	0.160	656.9	289.3	0.898	0.0085	168.688
129	1.0	0.630	121.7	182.7	0.162	655.0	289.3	0.842	0.0085	42.160
130	2.0	0.638	121.7	182.7	0.167	644.8	289.3	0.669	0.0084	7.558
131	0.5	0.573	78.8	121.5	0.160	571.6	288.3	0.937	0.0083	162.036
132	1.0	0.606	78.8	121.5	0.171	561.4	288.3	0.799	0.0082	33.584
133	2.0	0.616	78.8	121.5	0.177	550.6	288.3	0.671	0.0082	6.379
134	0.5	0.742	90.3	107.5	0.160	591.0	288.4	1.446	0.0083	257.571
135	1.0	0.776	90.3	107.5	0.163	586.3	288.5	1.261	0.0082	54.134
136	2.0	0.790	90.3	107.5	0.171	578.8	288.6	0.957	0.0081	9.803
137	0.5	0.303	78.1	236.1	0.171	574.8	288.2	1.233	0.0094	174.427
138	1.0	0.311	78.1	236.1	0.179	568.5	288.2	1.045	0.0093	38.336
139	2.0	0.312	78.1	236.1	0.182	562.6	288.3	0.841	0.0093	7.335
140	0.5	0.347	86.6	225.7	0.165	598.3	288.4	1.323	0.0093	230.985
141	1.0	0.364	86.6	225.7	0.172	584.5	288.4	1.209	0.0093	52.784
142	2.0	0.366	86.6	225.7	0.178	582.0	288.5	0.833	0.0091	8.293
143	0.5	1.255	237.8	182.7	0.154	860.4	291.6	0.488	0.0078	59.748
144	1.0	1.276	237.8	182.7	0.157	850.9	291.6	0.441	0.0078	13.092
145	2.0	1.278	237.8	182.7	0.157	847.1	291.6	0.420	0.0078	3.059
146	0.5	1.210	233.3	188.2	0.155	852.9	291.5	0.483	0.0079	82.348
147	1.0	1.214	233.3	188.2	0.158	847.7	291.5	0.433	0.0079	18.663
148	2.0	1.214	233.3	188.2	0.155	839.9	291.5	0.397	0.0079	4.192

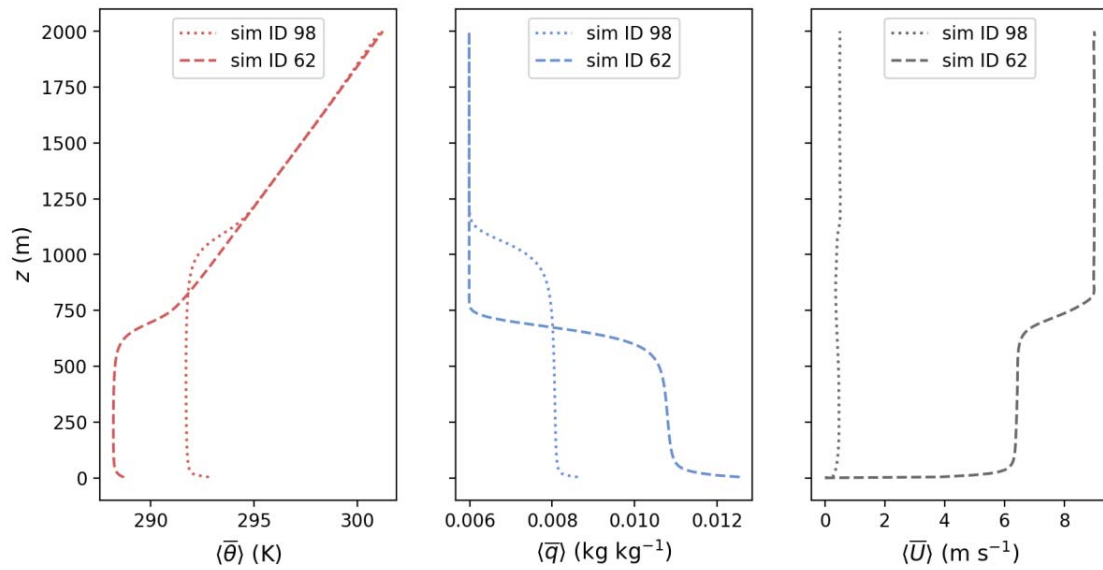
941

942 Figure 11 shows that even with horizontally homogeneous surface fluxes, a weak pattern  
943 of cells (low  $U_g$ ) or stripes (high  $U_g$ ) develops. This pattern is superimposed over the  
944 much stronger pattern resulting from the heterogeneous surface fluxes. However, the

945 surface temperature still exhibits a pattern of accurate squares with a low  $U_g$ , whereas the  
 946 surface temperature pattern becomes more blurred when  $U_g$  is high.



947  
 948 **Fig. 11** The left two columns show prescribed surface fluxes ( $\overline{H_s}$ ,  $\overline{\lambda E_s}$ ) from exemplary simulations with the  
 949 same Bowen ratio ( $\beta$ ). The right two columns show the resulting surface temperatures ( $\overline{T_s}$ ) for simulations  
 950 with the lowest ( $U_g = 0.5 \text{ m s}^{-1}$ ) and highest ( $U_g = 9 \text{ m s}^{-1}$ ) geostrophic wind speed. The top row shows  
 951 simulations with homogeneous surface fluxes. The rows below show simulations with heterogeneous surface  
 952 fluxes with increasing patch size (200 m, 400 m, 800 m).



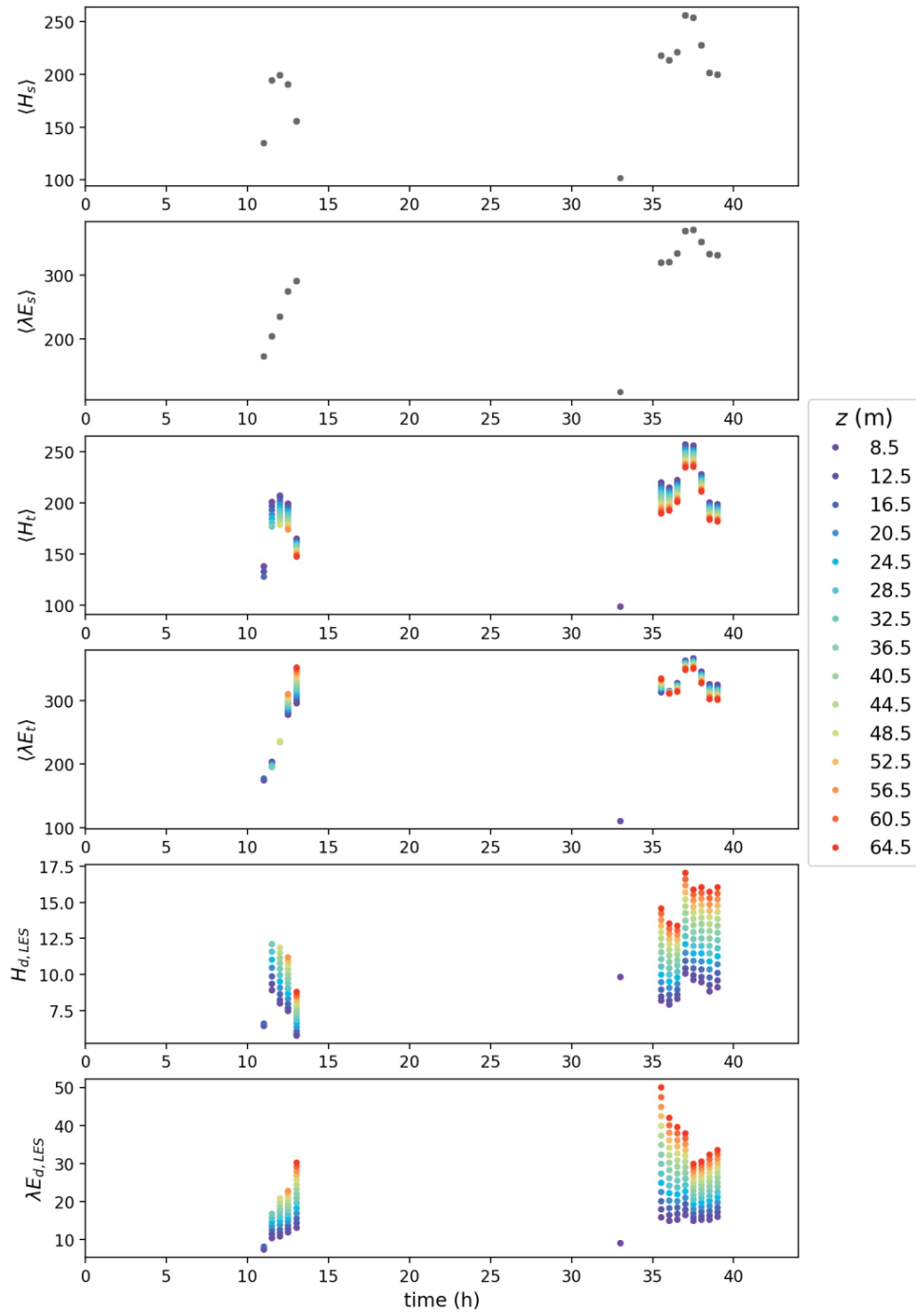
953

954 **Fig. 12** Profiles of 30-min and domain-averaged potential temperature ( $\theta$ ), mixing ratio ( $q$ ), and horizontal  
 955 wind speed ( $U$ ) for two example simulations. The simulation with ID 98 has very low horizontal wind speed  
 956 and high sensible surface heat flux, and the simulation with ID 62 has very high horizontal wind speed and  
 957 low sensible surface heat flux.

958

## 959 **Appendix 2: The More Realistic CHEESEHEAD LES**

960 Fig. 13 shows the time series of horizontally domain-averaged surface, turbulent and  
 961 dispersive heat fluxes with  $\langle H_s \rangle > \text{W m}^{-2}$ . Only grid levels above the average canopy  
 962 height  $z_c$  are considered.



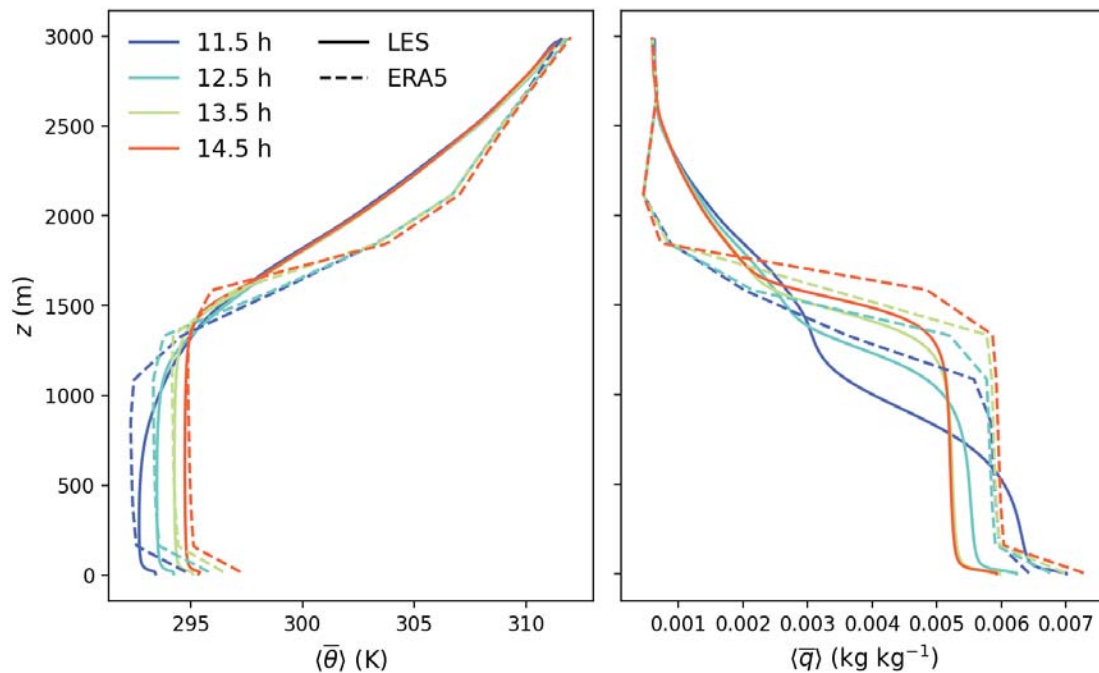
963

964

965

**Fig. 13** Time series of the surface fluxes ( $\langle H_s \rangle$  and  $\langle \lambda E_s \rangle$ ), turbulent flux contributions ( $\langle H_t \rangle$  and  $\langle \lambda E_t \rangle$ ) and dispersive flux contributions ( $H_{d,LES}$  and  $\lambda E_{d,LES}$ ) that were encountered in the CHEESEHEAD simulations.

966 **Appendix 3: The ERA5 Reanalysis Data**



967  
 968 **Fig. 14** Comparison of hourly averaged vertical profiles of potential temperature ( $\langle\bar{\theta}\rangle$ ) and mixing ratio ( $\langle\bar{q}\rangle$ )  
 969 between the CHEESEHEAD LES and ERA5 reanalysis data for August 23, 2019.

970 **References**

- 971 Arneth A, Mercado L, Kattge J, Booth BBB (2012) Future challenges of representing land-processes in  
 972 studies on land-atmosphere interactions. *Biogeosciences* 9:3587–3599. [https://doi.org/10.5194/bg-9-](https://doi.org/10.5194/bg-9-3587-2012)  
 973 3587-2012
- 974 Aubinet M, Grelle A, Ibrom A, Rannik Ü, Moncrieff J, Foken T, Kowalski AS, Martin PH, Berbigier P,  
 975 Bernhofer C, Clement R, Elbers J, Granier A, Grünwald T, Morgenstern K, Pilegaard K, Rebmann C,  
 976 Snijders W, Valentini R, Vesala T (1999) Estimates of the Annual Net Carbon and Water Exchange of  
 977 Forests: The EUROFLUX Methodology. In: *Advances in Ecological Research* Volume 30, vol 30.  
 978 Elsevier, pp 113–175
- 979 Aubinet M, Vesala T, Papale D (eds) (2012) *Eddy covariance: A practical guide to measurement and data*  
 980 *analysis*. Springer, New York
- 981 Baldocchi D (2014) Measuring fluxes of trace gases and energy between ecosystems and the atmosphere -  
 982 the state and future of the eddy covariance method. *Global Change Biol* 20:3600–3609.  
 983 <https://doi.org/10.1111/gcb.12649>
- 984 Baldocchi DD (2003) Assessing the eddy covariance technique for evaluating carbon dioxide exchange  
 985 rates of ecosystems: past, present and future. *Global Change Biol* 9:479–492.  
 986 <https://doi.org/10.1046/j.1365-2486.2003.00629.x>
- 987 Barr AG, Morgenstern K, Black TA, McCaughey JH, Nescic Z (2006) Surface energy balance closure by  
 988 the eddy-covariance method above three boreal forest stands and implications for the measurement of  
 989 the CO<sub>2</sub> flux. *Agricultural and Forest Meteorology* 140:322–337.  
 990 <https://doi.org/10.1016/j.agrformet.2006.08.007>
- 991 Bernacchi CJ, Hollinger SE, Meyers T (2005) The conversion of the corn/soybean ecosystem to no-till  
 992 agriculture may result in a carbon sink. *Global Change Biol* 0:051013014052001-???
- 993 <https://doi.org/10.1111/j.1365-2486.2005.01050.x>

- 994 Bernacchi CJ, Hollinger SE, Meyers TP (2006) The conversion of the corn/soybean ecosystem to no-till  
 995 agriculture may result in a carbon sink. *Global Change Biol* 12:1585–1586.  
 996 <https://doi.org/10.1111/j.1365-2486.2006.01195.x>
- 997 Bou-Zeid E, Anderson W, Katul GG, Mahrt L (2020) The Persistent Challenge of Surface Heterogeneity in  
 998 Boundary-Layer Meteorology: A Review. *Boundary-Layer Meteorol* 177(2-3):227–245.  
 999 <https://doi.org/10.1007/s10546-020-00551-8>
- 1000 Breiman L (2001) Random Forests. *Machine Learning* 45:5–32. <https://doi.org/10.1023/A:1010933404324>
- 1001 Butterworth BJ, Desai AR, Durden D, Kadum H, LaLuzerne D, Mauder M, Metzger S, Paleri S, Wanner L  
 1002 (submitted) Characterizing Energy Balance Closure over a Heterogeneous Ecosystem Using Multi-  
 1003 Tower Eddy Covariance. Submitted to *Frontiers in Earth Science*, section Atmospheric Science
- 1004 Butterworth BJ, Desai AR, Metzger S, Townsend PA, Schwartz MD, Petty GW, Mauder M, Vogelmann H,  
 1005 Andresen CG, Augustine TJ, Bertram TH, Brown WO, Buban M, Clearly P, Durden DJ, Florian CR,  
 1006 Iglinski TJ, Kruger EL, Lantz K, Lee TR, Meyers TP, Mineau JK, Olson ER, Oncley SP, Paleri S,  
 1007 Pertzborn RA, Pettersen C, Plummer DM, Riihimaki L, Guzman ER, Sedlar J, Smith EN, Speidel J,  
 1008 Stoy PC, Sührling M, Thom JE, Turner DD, Vermeuel MP, Wagner TJ, Wang Z, Wanner L, White  
 1009 LD, Wilczak JM, Wright DB, Zheng T (2021) Connecting Land-Atmosphere Interactions to Surface  
 1010 Heterogeneity in CHEESEHEAD19. *Bull. Amer. Meteor. Soc.* 102(2):E421-E445.  
 1011 <https://doi.org/10.1175/BAMS-D-19-0346.1>
- 1012 Ceschia E, Béziat P, Dejoux JF, Aubinet M, Bernhofer C, Bodson B, Buchmann N, CARRARA A, Cellier  
 1013 P, Di Tommasi P, Elbers JA, Eugster W, Grünwald T, Jacobs C, Jans W, Jones M, Kutsch W, Lanigan  
 1014 G, Magliulo E, Marloie O, Moors EJ, Moureaux C, Olioso A, Osborne B, Sanz MJ, Saunders M,  
 1015 Smith P, Soegaard H, Wattenbach M (2010) Management effects on net ecosystem carbon and GHG  
 1016 budgets at European crop sites. *Agriculture, Ecosystems & Environment* 139:363–383.  
 1017 <https://doi.org/10.1016/j.agee.2010.09.020>
- 1018 Charuchittipan D, Babel W, Mauder M, Leps J-P, Foken T (2014) Extension of the Averaging Time in  
 1019 Eddy-Covariance Measurements and Its Effect on the Energy Balance Closure. *Boundary-Layer  
 1020 Meteorol* 152(3):303–327. <https://doi.org/10.1007/s10546-014-9922-6>
- 1021 Choi M, Kustas WP, Anderson MC, Allen RG, Li F, Kjaersgaard JH (2009) An intercomparison of three  
 1022 remote sensing-based surface energy balance algorithms over a corn and soybean production region  
 1023 (Iowa, U.S.) during SMACEX. *Agricultural and Forest Meteorology* 149:2082–2097.  
 1024 <https://doi.org/10.1016/j.agrformet.2009.07.002>
- 1025 Cremonese E, Filippa G, Galvagno M, Siniscalco C, Oddi L, Di Morra Cella U, Migliavacca M (2017)  
 1026 Heat wave hinders green wave: The impact of climate extreme on the phenology of a mountain  
 1027 grassland. *Agricultural and Forest Meteorology* 247:320–330.  
 1028 <https://doi.org/10.1016/j.agrformet.2017.08.016>
- 1029 Cuxart J, Conangla L, Jiménez MA (2015) Evaluation of the surface energy budget equation with  
 1030 experimental data and the ECMWF model in the Ebro Valley. *J. Geophys. Res. Atmos.* 120(3):1008–  
 1031 1022. <https://doi.org/10.1002/2014JD022296>
- 1032 De Roo F, Mauder M (2018) The influence of idealized surface heterogeneity on virtual turbulent flux  
 1033 measurements. *Atmos. Chem. Phys.* 18(7):5059–5074. <https://doi.org/10.5194/acp-18-5059-2018>
- 1034 De Roo F, Zhang S, Huq S, Mauder M (2018) A semi-empirical model of the energy balance closure in the  
 1035 surface layer. *PLoS ONE* 13(12):e0209022. <https://doi.org/10.1371/journal.pone.0209022>
- 1036 Deardorff JW (1980) Stratocumulus-capped mixed layers derived from a three-dimensional model.  
 1037 *Boundary-Layer Meteorol* 18(4):495–527. <https://doi.org/10.1007/BF00119502>
- 1038 Desai AR, Khan AM, Zheng T, Paleri S, Butterworth B, Lee TR, Fisher JB, Hulley G, Kleynhans T,  
 1039 Gerace A, Townsend PA, Stoy P, Metzger S (2021) Multi-Sensor Approach for High Space and Time  
 1040 Resolution Land Surface Temperature. *Earth and Space Science* 8.  
 1041 <https://doi.org/10.1029/2021EA001842>
- 1042 Desai AR, Murphy BA, Wiesner S, Thom J, Butterworth BJ, Koupaei-Abyazani N, Muttaqin A, Paleri S,  
 1043 Talib A, Turner J, Mineau J, Merrelli A, Stoy P, Davis K (2022) Drivers of Decadal Carbon Fluxes  
 1044 Across Temperate Ecosystems. *JGR Biogeosciences* 127:e2022JG007014.  
 1045 <https://doi.org/10.1029/2022JG007014>
- 1046 Eder F, De Roo F, Kohnert K, Desjardins RL, Schmid HP, Mauder M (2014) Evaluation of Two Energy  
 1047 Balance Closure Parametrizations. *Boundary-Layer Meteorol* 151(2):195–219.  
 1048 <https://doi.org/10.1007/s10546-013-9904-0>

- 1049 Eder F, De Roo F, Rotenberg E, Yakir D, Schmid HP, Mauder M (2015) Secondary circulations at a  
1050 solitary forest surrounded by semi-arid shrubland and their impact on eddy-covariance measurements.  
1051 *Agricultural and Forest Meteorology* 211-212:115–127.  
1052 <https://doi.org/10.1016/j.agrformet.2015.06.001>
- 1053 Feigenwinter C, Bernhofer C, Eichelmann U, Heinesch B, Hertel M, Janous D, Kolle O, Lagergren F,  
1054 Lindroth A, Minerbi S, Moderow U, Mölder M, Montagnani L, Queck R, Rebmann C, Vestin P,  
1055 Yernaux M, Zeri M, Ziegler W, Aubinet M (2008) Comparison of horizontal and vertical advective  
1056 CO<sub>2</sub> fluxes at three forest sites. *Agricultural and Forest Meteorology* 148:12–24.  
1057 <https://doi.org/10.1016/j.agrformet.2007.08.013>
- 1058 Finnigan J (2008) An introduction to flux measurements in difficult conditions. *Ecological Applications*  
1059 18:1340–1350. <https://doi.org/10.1890/07-2105.1>
- 1060 Finnigan JJ, Clement R, Malhi Y, Leuning R, Cleugh HA (2003) A Re-Evaluation of Long-Term Flux  
1061 Measurement Techniques Part I: Averaging and Coordinate Rotation. *Boundary-Layer Meteorol*  
1062 107(1):1–48. <https://doi.org/10.1023/A:1021554900225>
- 1063 Foken T (2008) The Energy Balance Closure Problem: An Overview. *Ecological Applications* 18(6):1351–  
1064 1367. <https://doi.org/10.1890/06-0922.1>
- 1065 Foken T (2017) *Micrometeorology*. Springer Berlin Heidelberg, Berlin, Heidelberg
- 1066 Foken T, Mauder M, Liebenthal C, Wimmer F, Beyrich F, Leps J-P, Raasch S, DeBruin HAR, Meijninger  
1067 WML, Bange J (2010) Energy balance closure for the LITFASS-2003 experiment. *Theor Appl*  
1068 *Climatol* 101(1-2):149–160. <https://doi.org/10.1007/s00704-009-0216-8>
- 1069 Frank JM, Massman WJ, Ewers BE (2013) Underestimates of sensible heat flux due to vertical velocity  
1070 measurement errors in non-orthogonal sonic anemometers. *Agricultural and Forest Meteorology* 171-  
1071 172:72–81. <https://doi.org/10.1016/j.agrformet.2012.11.005>
- 1072 Fu Z, Ciais P, Bastos A, Stoy PC, Yang H, Green JK, Wang B, Yu K, Huang Y, Knohl A, Šigut L, Gharun  
1073 M, Cuntz M, Arriga N, Roland M, Peichl M, Migliavacca M, Cremonese E, Varlagin A, Brümmer C,  
1074 La Gourlez de Motte L, Fares S, Buchmann N, El-Madany TS, Pitacco A, Vendrame N, Li Z, Vincke  
1075 C, Magliulo E, Koebsch F (2020) Sensitivity of gross primary productivity to climatic drivers during  
1076 the summer drought of 2018 in Europe. *Philos Trans R Soc Lond B Biol Sci* 375:20190747.  
1077 <https://doi.org/10.1098/rstb.2019.0747>
- 1078 Gao Z, Liu H, Katul GG, Foken T (2017) Non-closure of the surface energy balance explained by phase  
1079 difference between vertical velocity and scalars of large atmospheric eddies. *Environ. Res. Lett.*  
1080 12(3):34025. <https://doi.org/10.1088/1748-9326/aa625b>
- 1081 Gebler S, Hendricks Franssen H-J, Pütz T, Post H, Schmidt M, Vereecken H (2015) Actual  
1082 evapotranspiration and precipitation measured by lysimeters: a comparison with eddy covariance and  
1083 tipping bucket. *Hydrol. Earth Syst. Sci.* 19:2145–2161. <https://doi.org/10.5194/hess-19-2145-2015>
- 1084 Goulden ML, Munger JW, Fan S-M, Daube BC, Wofsy SC (1996) Measurements of carbon sequestration  
1085 by long-term eddy covariance: methods and a critical evaluation of accuracy. *Global Change Biol*  
1086 2(3):169–182. <https://doi.org/10.1111/j.1365-2486.1996.tb00070.x>
- 1087 Graham SL, Kochendorfer J, McMillan AM, Duncan MJ, Srinivasan MS, Hertzog G (2016) Effects of  
1088 agricultural management on measurements, prediction, and partitioning of evapotranspiration in  
1089 irrigated grasslands. *Agricultural Water Management* 177:340–347.  
1090 <https://doi.org/10.1016/j.agwat.2016.08.015>
- 1091 Green JK, Konings AG, Alemohammad SH, Berry J, Entekhabi D, Kolassa J, Lee J-E, Gentine P (2017)  
1092 Regionally strong feedbacks between the atmosphere and terrestrial biosphere. *Nat Geosci* Volume  
1093 10:410–414. <https://doi.org/10.1038/ngeo2957>
- 1094 Haverd V, Cuntz M, Leuning R, Keith H (2007) Air and biomass heat storage fluxes in a forest canopy:  
1095 Calculation within a soil vegetation atmosphere transfer model. *Agricultural and Forest Meteorology*  
1096 147:125–139. <https://doi.org/10.1016/j.agrformet.2007.07.006>
- 1097 Heiskanen J, Brümmer C, Buchmann N, Calfapietra C, Chen H, Gielen B, Gkritzalis T, Hammer S,  
1098 Hartman S, Herbst M, Janssens IA, Jordan A, Juurola E, Karstens U, Kasurinen V, Kruijt B,  
1099 Lankreijer H, Levin I, Linderson M-L, Loustau D, Merbold L, Myhre CL, Papale D, Pavelka M,  
1100 Pilegaard K, Ramonet M, Rebmann C, Rinne J, Rivier L, Saltikoff E, Sanders R, Steinbacher M,  
1101 Steinhoff T, Watson A, Vermeulen AT, Vesala T, Vítková G, Kutsch W (2022) The Integrated Carbon  
1102 Observation System in Europe. *Bull. Amer. Meteor. Soc.* 103:E855-E872.  
1103 <https://doi.org/10.1175/BAMS-D-19-0364.1>

1104 Hendricks-Franssen HJ, Stöckli R, Lehner I, Rotenberg E, Seneviratne SI (2010) Energy balance closure of  
1105 eddy-covariance data: A multisite analysis for European FLUXNET stations. *Agricultural and Forest*  
1106 *Meteorology* 150(12):1553–1567. <https://doi.org/10.1016/j.agrformet.2010.08.005>  
1107 Hersbach H, Bell B, Berrisford P, Biavati G, Horányi A, Muñoz Sabater J, Nicolas J, Peubey C, Radu R,  
1108 Rozum I, Schepers D, Simmons A, Soci C, Dee D, Thépaut J-N (2023a) ERA5 hourly data on  
1109 pressure levels from 1940 to present. Accessed 13 July 2023  
1110 Hersbach H, Bell B, Berrisford P, Biavati G, Horányi A, Muñoz Sabater J, Nicolas J, Peubey C, Radu R,  
1111 Rozum I, Schepers D, Simmons A, Soci C, Dee D, Thépaut J-N (2023b) ERA5 hourly data on single  
1112 levels from 1940 to present. Accessed 14 July 2023  
1113 Hirschi M, Michel D, Lehner I, Seneviratne SI (2017) A site-level comparison of lysimeter and eddy  
1114 covariance flux measurements of evapotranspiration. *Hydrol. Earth Syst. Sci.* 21:1809–1825.  
1115 <https://doi.org/10.5194/hess-21-1809-2017>  
1116 Horst TW, Semmer SR, Maclean G (2015) Correction of a Non-orthogonal, Three-Component Sonic  
1117 Anemometer for Flow Distortion by Transducer Shadowing. *Boundary-Layer Meteorol* 155:371–395.  
1118 <https://doi.org/10.1007/s10546-015-0010-3>  
1119 Huang J, Lee X, Patton EG (2008) A Modelling Study of Flux Imbalance and the Influence of Entrainment  
1120 in the Convective Boundary Layer. *Boundary-Layer Meteorol* 127(2):273–292.  
1121 <https://doi.org/10.1007/s10546-007-9254-x>  
1122 Hulley GC, Gottsche FM, Rivera G, Hook SJ, Freepartner RJ, Martin MA, Cawse-Nicholson K, Johnson  
1123 WR (2022) Validation and Quality Assessment of the ECOSTRESS Level-2 Land Surface  
1124 Temperature and Emissivity Product. *IEEE Trans. Geosci. Remote Sensing* 60:1–23.  
1125 <https://doi.org/10.1109/TGRS.2021.3079879>  
1126 Inagaki A, Letzel MO, Raasch S, Kanda M (2006) Impact of Surface Heterogeneity on Energy Imbalance:  
1127 A Study Using LES. *JMSJ* 84(1):187–198. <https://doi.org/10.2151/jmsj.84.187>  
1128 Kanda M, Inagaki A, Letzel MO, Raasch S, Watanabe T (2004) LES Study of the Energy Imbalance  
1129 Problem with Eddy Covariance Fluxes. *Boundary-Layer Meteorol* 110(3):381–404.  
1130 <https://doi.org/10.1023/B:BOUN.0000007225.45548.7a>  
1131 Katul G, Hsieh C-I, Bowling D, Clark K, Shurpali N, Turnipseed A, Albertson J, Tu K, Hollinger D, Evans  
1132 B, Offerle B, Anderson D, Ellsworth D, Vogel C, Oren R (1999) Spatial Variability of Turbulent  
1133 Fluxes in the Roughness Sublayer of an Even-Aged Pine Forest. *Boundary-Layer Meteorol* 93:1–28.  
1134 <https://doi.org/10.1023/A:1002079602069>  
1135 Katul GG (2019) The anatomy of large-scale motion in atmospheric boundary layers. *J. Fluid Mech.*  
1136 858:1–4. <https://doi.org/10.1017/jfm.2018.731>  
1137 Kenny WT, Bohrer G, Morin TH, Vogel CS, Matheny AM, Desai AR (2017) A Numerical Case Study of  
1138 the Implications of Secondary Circulations to the Interpretation of Eddy-Covariance Measurements  
1139 Over Small Lakes. *Boundary-Layer Meteorol* 165(2):311–332. <https://doi.org/10.1007/s10546-017-0268-8>  
1140 Kljun N, Calanca P, Rotach MW, Schmid HP (2015) A simple two-dimensional parameterisation for Flux  
1141 Footprint Prediction (FFP). *Geosci. Model Dev.* 8:3695–3713. <https://doi.org/10.5194/gmd-8-3695-2015>  
1142 Kochendorfer J, Meyers TP, Frank J, Massman WJ, Heuer MW (2012) How Well Can We Measure the  
1143 Vertical Wind Speed? Implications for Fluxes of Energy and Mass. *Boundary-Layer Meteorol*  
1144 145(2):383–398. <https://doi.org/10.1007/s10546-012-9738-1>  
1145 Kohsiek W, Liebenthal C, Foken T, Vogt R, Oncley SP, Bernhofer C, Debruin HAR (2007) The Energy  
1146 Balance Experiment EBEX-2000. Part III: Behaviour and quality of the radiation measurements.  
1147 *Boundary-Layer Meteorol* 123(1):55–75. <https://doi.org/10.1007/s10546-006-9135-8>  
1148 Laubach J, Raschendorfer M, Kreilein H, Gravenhorst G (1994) Determination of heat and water vapour  
1149 fluxes above a spruce forest by eddy correlation. *Agricultural and Forest Meteorology* 71(3-4):373–  
1150 401. [https://doi.org/10.1016/0168-1923\(94\)90021-3](https://doi.org/10.1016/0168-1923(94)90021-3)  
1151 Letzel MO, Raasch S (2003) Large Eddy Simulation of Thermally Induced Oscillations in the Convective  
1152 Boundary Layer. *J. Atmos. Sci.* 60(18):2328–2341. [https://doi.org/10.1175/1520-0469\(2003\)060<2328:LESOTI>2.0.CO;2](https://doi.org/10.1175/1520-0469(2003)060<2328:LESOTI>2.0.CO;2)  
1153 Leuning R, van Gorsel E, Massman WJ, Isaac PR (2012) Reflections on the surface energy imbalance  
1154 problem. *Agricultural and Forest Meteorology* 156:65–74.  
1155 <https://doi.org/10.1016/j.agrformet.2011.12.002>  
1156  
1157  
1158

1159 Liebenthal C, Huwe B, Foken T (2005) Sensitivity analysis for two ground heat flux calculation approaches.  
1160 Agricultural and Forest Meteorology 132(3-4):253–262.  
1161 <https://doi.org/10.1016/j.agrformet.2005.08.001>

1162 Lindroth A, Mölder M, Lagergren F (2010) Heat storage in forest biomass improves energy balance  
1163 closure. Biogeosciences 7(1):301–313. <https://doi.org/10.5194/bg-7-301-2010>

1164 Lundberg SM, Erion G, Chen H, DeGrave A, Prutkin JM, Nair B, Katz R, Himmelfarb J, Bansal N, Lee S-I  
1165 (2020) From Local Explanations to Global Understanding with Explainable AI for Trees. Nat Mach  
1166 Intell 2:56–67. <https://doi.org/10.1038/s42256-019-0138-9>

1167 Mahrt L (1998) Flux Sampling Errors for Aircraft and Towers. J. Atmos. Oceanic Technol. 15(2):416–429.  
1168 [https://doi.org/10.1175/1520-0426\(1998\)015<0416:FSEFAA>2.0.CO;2](https://doi.org/10.1175/1520-0426(1998)015<0416:FSEFAA>2.0.CO;2)

1169 Margairaz F, Pardyjak ER, Calaf M (2020a) Surface Thermal Heterogeneities and the Atmospheric  
1170 Boundary Layer: The Relevance of Dispersive Fluxes. Boundary-Layer Meteorol 175:369–395.  
1171 <https://doi.org/10.1007/s10546-020-00509-w>

1172 Margairaz F, Pardyjak ER, Calaf M (2020b) Surface Thermal Heterogeneities and the Atmospheric  
1173 Boundary Layer: The Thermal Heterogeneity Parameter. Boundary-Layer Meteorol 177:49–68.  
1174 <https://doi.org/10.1007/s10546-020-00544-7>

1175 Maronga B, Raasch S (2013) Large-Eddy Simulations of Surface Heterogeneity Effects on the Convective  
1176 Boundary Layer During the LITFASS-2003 Experiment. Boundary-Layer Meteorol 146(1):17–44.  
1177 <https://doi.org/10.1007/s10546-012-9748-z>

1178 Maronga B, Banzhaf S, Burmeister C, Esch T, Forkel R, Fröhlich D, Fuka V, Gehrke KF, Geletić J,  
1179 Giersch S, Gronemeier T, Groß G, Heldens W, Hellsten A, Hoffmann F, Inagaki A, Kadasch E,  
1180 Kanani-Sühring F, Ketelsen K, Khan BA, Knigge C, Knoop H, Krč P, Kurppa M, Maamari H,  
1181 Matzarakis A, Mauder M, Pallasch M, Pavlik D, Pfafferoth J, Resler J, Rissmann S, Russo E, Salim M,  
1182 Schrempf M, Schwenkel J, Seckmeyer G, Schubert S, Sühring M, Tils R von, Vollmer L, Ward S,  
1183 Witha B, Wurps H, Zeidler J, Raasch S (2020) Overview of the PALM model system 6.0. Geosci.  
1184 Model Dev. 13(3):1335–1372. <https://doi.org/10.5194/gmd-13-1335-2020>

1185 Mauder M, Jegede OO, Okogbue EC, Wimmer F, Foken T (2007a) Surface energy balance measurements  
1186 at a tropical site in West Africa during the transition from dry to wet season. Theor Appl Climatol  
1187 89(3-4):171–183. <https://doi.org/10.1007/s00704-006-0252-6>

1188 Mauder M, Desjardins RL, Pattey E, Gao Z, van Haarlem R (2008) Measurement of the Sensible Eddy  
1189 Heat Flux Based on Spatial Averaging of Continuous Ground-Based Observations. Boundary-Layer  
1190 Meteorol 128(1):151–172. <https://doi.org/10.1007/s10546-008-9279-9>

1191 Mauder M (2013) A Comment on “How Well Can We Measure the Vertical Wind Speed? Implications for  
1192 Fluxes of Energy and Mass” by Kochendorfer et al. Boundary-Layer Meteorol 147(2):329–335.  
1193 <https://doi.org/10.1007/s10546-012-9794-6>

1194 Mauder M, Foken T (2006) Impact of post-field data processing on eddy covariance flux estimates and  
1195 energy balance closure. metz 15(6):597–609. <https://doi.org/10.1127/0941-2948/2006/0167>

1196 Mauder M, Liebenthal C, Göckede M, Leps J-P, Beyrich F, Foken T (2006) Processing and quality control  
1197 of flux data during LITFASS-2003. Boundary-Layer Meteorol 121(1):67–88.  
1198 <https://doi.org/10.1007/s10546-006-9094-0>

1199 Mauder M, Desjardins RL, MacPherson I (2007b) Scale analysis of airborne flux measurements over  
1200 heterogeneous terrain in a boreal ecosystem. J. Geophys. Res. Atmos. 112(D13):n/a-n/a.  
1201 <https://doi.org/10.1029/2006JD008133>

1202 Mauder M, Oncley SP, Vogt R, Weidinger T, Ribeiro L, Bernhofer C, Foken T, Kohsiek W, Bruin HAR  
1203 de, Liu H (2007c) The energy balance experiment EBEX-2000. Part II: Intercomparison of eddy-  
1204 covariance sensors and post-field data processing methods. Boundary-Layer Meteorol 123:29–54.  
1205 <https://doi.org/10.1007/s10546-006-9139-4>

1206 Mauder M, Cuntz M, Drüe C, Graf A, Rebmann C, Schmid HP, Schmidt M, Steinbrecher R (2013) A  
1207 strategy for quality and uncertainty assessment of long-term eddy-covariance measurements.  
1208 Agricultural and Forest Meteorology 169:122–135. <https://doi.org/10.1016/j.agrformet.2012.09.006>

1209 Mauder M, Foken T, Cuxart J (2020) Surface-Energy-Balance Closure over Land: A Review. Boundary-  
1210 Layer Meteorol 9(8):3587. <https://doi.org/10.1007/s10546-020-00529-6>

1211 Mauder M, Ibrom A, Wanner L, Roo F de, Brugger P, Kiese R, Pilegaard K (2021) Options to correct local  
1212 turbulent flux measurements for large-scale fluxes using an approach based on large-eddy simulation.  
1213 Atmos. Meas. Tech. 14:7835–7850. <https://doi.org/10.5194/amt-14-7835-2021>

- 1214 Metzger M, Holmes H (2007) Time Scales in the Unstable Atmospheric Surface Layer. *Boundary-Layer*  
1215 *Meteorol* 126:29–50. <https://doi.org/10.1007/s10546-007-9219-0>
- 1216 Metzger S, Junkermann W, Mauder M, Butterbach-Bahl K, Trancón y Widemann B, Neidl F, Schäfer K,  
1217 Wieneke S, Zheng XH, Schmid HP, Foken T (2013) Spatially explicit regionalization of airborne flux  
1218 measurements using environmental response functions. *Biogeosciences* 10(4):2193–2217.  
1219 <https://doi.org/10.5194/bg-10-2193-2013>
- 1220 Moderow U, Aubinet M, Feigenwinter C, Kolle O, Lindroth A, Mölder M, Montagnani L, Rebmann C,  
1221 Bernhofer C (2009) Available energy and energy balance closure at four coniferous forest sites across  
1222 Europe. *Theor Appl Climatol* 98:397–412. <https://doi.org/10.1007/s00704-009-0175-0>
- 1223 Moeng C-H, Wyngaard JC (1988) Spectral Analysis of Large-Eddy Simulations of the Convective  
1224 Boundary Layer. *J. Atmos. Sci.* 45(23):3573–3587. [https://doi.org/10.1175/1520-0469\(1988\)045<3573:SAOLES>2.0.CO;2](https://doi.org/10.1175/1520-0469(1988)045<3573:SAOLES>2.0.CO;2)
- 1226 Morrison T, Calaf M, Higgins CW, Drake SA, Perelet A, Pardyjak E (2021) The Impact of Surface  
1227 Temperature Heterogeneity on Near-Surface Heat Transport. *Boundary-Layer Meteorol* 180:247–272.  
1228 <https://doi.org/10.1007/s10546-021-00624-2>
- 1229 Nakai T, Shimoyama K (2012) Ultrasonic anemometer angle of attack errors under turbulent conditions.  
1230 *Agricultural and Forest Meteorology* 162-163:14–26. <https://doi.org/10.1016/j.agrformet.2012.04.004>
- 1231 O'Dell D, Eash NS, Hicks BB, Oetting JN, Sauer TJ, Lambert DM, Thierfelder C, Muoni T, Logan J, Zahn  
1232 JA, Goddard JJ (2020) Conservation agriculture as a climate change mitigation strategy in Zimbabwe.  
1233 *International Journal of Agricultural Sustainability* 18:250–265.  
1234 <https://doi.org/10.1080/14735903.2020.1750254>
- 1235 Paleri S, Wanner L, Sühling M, Desai AR, Mauder M (submitted) Coupled large eddy simulations of land  
1236 surface heterogeneity effects and diurnal evolution of late summer and early autumn atmospheric  
1237 boundary layers during the CHEESEHEAD19 field campaign. Submitted to *Geoscientific Model*  
1238 *Development*
- 1239 Paleri S, Butterworth B, Desai AR (2022a) Here, There and Everywhere: Spatial Patterns and Scales. In:  
1240 Hiscox AL (ed) *Conceptual boundary layer meteorology: The air near here*. Academic Press,  
1241 Cambridge, MA USA
- 1242 Paleri S, Desai AR, Metzger S, Durden D, Butterworth BJ, Mauder M, Kohnert K, Serafimovich A (2022b)  
1243 Space-Scale Resolved Surface Fluxes Across a Heterogeneous, Mid-Latitude Forested Landscape. *J.*  
1244 *Geophys. Res. Atmos.* 127. <https://doi.org/10.1029/2022JD037138>
- 1245 Panin GN, Bernhofer C (2008) Parametrization of turbulent fluxes over inhomogeneous landscapes. *Izv.*  
1246 *Atmos. Ocean. Phys.* 44(6):701–716. <https://doi.org/10.1134/S0001433808060030>
- 1247 Panin GN, Tetzlaff G, Raabe A (1998) Inhomogeneity of the Land Surface and Problems in  
1248 the Parameterization of Surface Fluxes in Natural Conditions. *Theor Appl Climatol* 60(1-4):163–178.  
1249 <https://doi.org/10.1007/s007040050041>
- 1250 Patton EG, Sullivan PP, Shaw RH, Finnigan JJ, Weil JC (2016) Atmospheric Stability Influences on  
1251 Coupled Boundary Layer and Canopy Turbulence. *J. Atmos. Sci.* 73(4):1621–1647.  
1252 <https://doi.org/10.1175/JAS-D-15-0068.1>
- 1253 Pedregosa F, Varoquaux G, Gramfort A, Michel V, Thirion B, Grisel O, Blondel M, Müller A, Nothman J,  
1254 Louppe G, Prettenhofer P, Weiss R, Dubourg V, Vanderplas J, Passos A, Cournapeau D, Brucher M,  
1255 Perrot M, Duchesnay É (2012) Scikit-learn: Machine Learning in Python.  
1256 <https://doi.org/10.48550/arXiv.1201.0490>
- 1257 Qu L, Chen J, Dong G, Jiang S, Li L, Guo J, Shao C (2016) Heat waves reduce ecosystem carbon sink  
1258 strength in a Eurasian meadow steppe. *Environ Res* 144:39–48.  
1259 <https://doi.org/10.1016/j.envres.2015.09.004>
- 1260 Raasch S, Schröter M (2001) PALM - A large-eddy simulation model performing on massively parallel  
1261 computers. *metz* 10:363–372. <https://doi.org/10.1127/0941-2948/2001/0010-0363>
- 1262 Rebmann C, Kolle O, Heinesch B, Queck R, Ibrom A, Aubinet M (2012) Data Acquisition and Flux  
1263 Calculations. In: Aubinet M, Vesala T, Papale D (eds) *Eddy covariance: A practical guide to*  
1264 *measurement and data analysis*. Springer, New York, pp 59–83
- 1265 Reichstein M, Ciais P, PAPALE D, Valentini R, Running S, Viovy N, Cramer W, Granier A, Ogée J,  
1266 Allard V, Aubinet M, BERNHOFER C, Buchmann N, CARRARA A, Grünwald T, Heimann M,  
1267 Heinesch B, Knohl A, Kutsch W, Loustau D, MANCA G, Matteucci G, Miglietta F, Ourcival JM,  
1268 Pilegaard K, Pumpanen J, Rambal S, Schaphoff S, Seufert G, Soussana J-F, Sanz M-J, Vesala T, Zhao  
1269 M (2007) Reduction of ecosystem productivity and respiration during the European summer 2003

1270 climate anomaly: a joint flux tower, remote sensing and modelling analysis. *Global Change Biol*  
1271 13:634–651. <https://doi.org/10.1111/j.1365-2486.2006.01224.x>

1272 Saiki EM, Moeng C-H, Sullivan PP (2000) Large-Eddy Simulation Of The Stably Stratified Planetary  
1273 Boundary Layer. *Boundary-Layer Meteorol* 95(1):1–30. <https://doi.org/10.1023/A:1002428223156>

1274 Schalkwijk J, Jonker HJJ, Siebesma AP (2016) An Investigation of the Eddy-Covariance Flux Imbalance in  
1275 a Year-Long Large-Eddy Simulation of the Weather at Cabauw. *Boundary-Layer Meteorol* 160(1):17–  
1276 39. <https://doi.org/10.1007/s10546-016-0138-9>

1277 Schmid HP (1997) Experimental design for flux measurements: matching scales of observations and fluxes.  
1278 *Agricultural and Forest Meteorology* 87:179–200. [https://doi.org/10.1016/S0168-1923\(97\)00011-7](https://doi.org/10.1016/S0168-1923(97)00011-7)

1279 Schotanus P, Nieuwstadt F, Bruin H de (1983) Temperature measurement with a sonic anemometer and its  
1280 application to heat and moisture fluxes. *Boundary-Layer Meteorol* 26:81–93.  
1281 <https://doi.org/10.1007/BF00164332>

1282 Soltani M, Mauder M, Laux P, Kunstmann H (2018) Turbulent flux variability and energy balance closure  
1283 in the TERENO prealpine observatory: a hydrometeorological data analysis. *Theor Appl Climatol*  
1284 133(3-4):937–956. <https://doi.org/10.1007/s00704-017-2235-1>

1285 Steinfeld G, Letzel MO, Raasch S, Kanda M, Inagaki A (2007) Spatial representativeness of single tower  
1286 measurements and the imbalance problem with eddy-covariance fluxes: results of a large-eddy  
1287 simulation study. *Boundary-Layer Meteorol* 123(1):77–98. <https://doi.org/10.1007/s10546-006-9133-x>

1288 Stork M, Menzel L (2016) Analysis and simulation of the water and energy balance of intense agriculture  
1289 in the Upper Rhine valley, south-west Germany. *Environ Earth Sci* 75.  
1290 <https://doi.org/10.1007/s12665-016-5980-z>

1291 Stoy PC, Katul GG, Siqueira MBS, Juang J-Y, Novick KA, McCarthy HR, Christopher Oishi A, Uebelherr  
1292 JM, Kim H-S, Oren RA (2006) Separating the effects of climate and vegetation on evapotranspiration  
1293 along a successional chronosequence in the southeastern US. *Global Change Biol* 12:2115–2135.  
1294 <https://doi.org/10.1111/j.1365-2486.2006.01244.x>

1295 Stoy PC, Mauder M, Foken T, Marcolla B, Boegh E, Ibrom A, Arain MA, Arneth A, Aurela M, Bernhofer  
1296 C, Cescatti A, Dellwik E, Duce P, Gianelle D, van Gorsel E, Kiely G, Knohl A, Margolis H,  
1297 McCaughey H, Merbold L, Montagnani L, Papale D, Reichstein M, Saunders M, Serrano-Ortiz P,  
1298 Sottocornola M, Spano D, Vaccari F, Varlagin A (2013) A data-driven analysis of energy balance  
1299 closure across FLUXNET research sites: The role of landscape scale heterogeneity. *Agricultural and*  
1300 *Forest Meteorology* 171-172:137–152. <https://doi.org/10.1016/j.agrformet.2012.11.004>

1301 Stull RB (1988) *An Introduction to Boundary Layer Meteorology*. Atmospheric Sciences Library, vol 13.  
1302 Springer, Dordrecht

1303 Sühling M, Raasch S (2013) Heterogeneity-Induced Heat-Flux Patterns in the Convective Boundary Layer:  
1304 Can they be Detected from Observations and is There a Blending Height?—A Large-Eddy Simulation  
1305 Study for the LITFASS-2003 Experiment. *Boundary-Layer Meteorol* 148(2):309–331.  
1306 <https://doi.org/10.1007/s10546-013-9822-1>

1307 Sühling M, Metzger S, Xu K, Durden D, Desai A (2018) Trade-Offs in Flux Disaggregation: A Large-  
1308 Eddy Simulation Study. *Boundary-Layer Meteorol* 170(1):69–93. <https://doi.org/10.1007/s10546-018-0387-x>

1309

1310 Twine TE, Kustas WP, Norman JM, Cook DR, Houser PR, Meyers TP, Prueger JH, Starks PJ, Wesely ML  
1311 (2000) Correcting eddy-covariance flux underestimates over a grassland. *Agricultural and Forest*  
1312 *Meteorology* 103:279–300. [https://doi.org/10.1016/S0168-1923\(00\)00123-4](https://doi.org/10.1016/S0168-1923(00)00123-4)

1313 van Gorsel E, Wolf S, Cleverly J, Isaac P, Haverd V, Ewenz C, Arndt S, Beringer J, Resco de Dios V,  
1314 Evans BJ, Griebel A, Hutley LB, Keenan T, Kljun N, Macfarlane C, Meyer WS, McHugh I, Pendall E,  
1315 Prober SM, Silberstein R (2016) Carbon uptake and water use in woodlands and forests in southern  
1316 Australia during an extreme heat wave event in the “Angry Summer” of 2012/2013. *Biogeosciences*  
1317 13:5947–5964. <https://doi.org/10.5194/bg-13-5947-2016>

1318 Wanner L, De Roo F, Sühling M, Mauder M (2022a) How Does the Choice of the Lower Boundary  
1319 Conditions in Large-Eddy Simulations Affect the Development of Dispersive Fluxes Near the  
1320 Surface? *Boundary-Layer Meteorol* 182:1–27. <https://doi.org/10.1007/s10546-021-00649-7>

1321 Wanner L, Calaf M, Mauder M (2022b) Incorporating the effect of heterogeneous surface heating into a  
1322 semi-empirical model of the surface energy balance closure. *PLoS ONE* 17:e0268097.  
1323 <https://doi.org/10.1371/journal.pone.0268097>

1324 Webb EK, Pearman GI, Leuning R (1980) Correction of flux measurements for density effects due to heat  
1325 and water vapour transfer. *Q.J.R. Meteorol. Soc* 106:85–100. <https://doi.org/10.1002/qj.49710644707>

1326 Wicker LJ, Skamarock WC (2002) Time-Splitting Methods for Elastic Models Using Forward Time  
 1327 Schemes. *Mon. Wea. Rev.* 130(8):2088–2097. <https://doi.org/10.1175/1520->  
 1328 0493(2002)130<2088:TSMFEM>2.0.CO;2  
 1329 Williamson J (1980) Low-storage Runge-Kutta schemes. *Journal of Computational Physics* 35(1):48–56.  
 1330 [https://doi.org/10.1016/0021-9991\(80\)90033-9](https://doi.org/10.1016/0021-9991(80)90033-9)  
 1331 Wilson K, Goldstein A, Falge E, Aubinet M, Baldocchi D, Berbigier P, Bernhofer C, Ceulemans R,  
 1332 Dolman H, Field C, Grelle A, Ibrom A, Law B, Kowalski A, Meyers T, Moncrieff J, Monson R,  
 1333 Oechel W, Tenhunen J, Valentini R, Verma S (2002) Energy balance closure at FLUXNET sites.  
 1334 *Agricultural and Forest Meteorology* 113(1-4):223–243. <https://doi.org/10.1016/S0168->  
 1335 1923(02)00109-0  
 1336 Wisconsin Department of Natural Resources (2016) Land Cover Data Wiscland 2.0.  
 1337 <https://dnr.wisconsin.gov/maps/WISCLAND>  
 1338 Xia Y, Mitchell K, Ek M, Sheffield J, Cosgrove B, Wood E, Luo L, Alonge C, Wei H, Meng J, Livneh B,  
 1339 Lettenmaier D, Koren V, Duan Q, Mo K, Fan Y, Mocko D (2012) Continental-scale water and energy  
 1340 flux analysis and validation for the North American Land Data Assimilation System project phase 2  
 1341 (NLDAS-2): 1. Intercomparison and application of model products. *J. Geophys. Res. Atmos.* 117:n/a-  
 1342 n/a. <https://doi.org/10.1029/2011JD016048>  
 1343 Xu K, Pingingtha-Durden N, Luo H, Durden D, Sturtevant C, Desai AR, Florian C, Metzger S (2019) The  
 1344 eddy-covariance storage term in air: Consistent community resources improve flux measurement  
 1345 reliability. *Agricultural and Forest Meteorology* 279:107734.  
 1346 <https://doi.org/10.1016/j.agrformet.2019.107734>  
 1347 Xu K, Sühling M, Metzger S, Durden D, Desai AR (2020) Can Data Mining Help Eddy Covariance See the  
 1348 Landscape? A Large-Eddy Simulation Study. *Boundary-Layer Meteorol* 176(1):85–103.  
 1349 <https://doi.org/10.1007/s10546-020-00513-0>  
 1350 Yu Y, Tarpley D, Privette JL, Goldberg MD, Rama Varma Raja MK, Vinnikov KY, Xu H (2009)  
 1351 Developing Algorithm for Operational GOES-R Land Surface Temperature Product. *IEEE Trans.*  
 1352 *Geosci. Remote Sensing* 47:936–951. <https://doi.org/10.1109/TGRS.2008.2006180>  
 1353 Zhou Y, Li D, Liu H, Li X (2018) Diurnal Variations of the Flux Imbalance Over Homogeneous and  
 1354 Heterogeneous Landscapes. *Boundary-Layer Meteorol* 168(3):417–442.  
 1355 <https://doi.org/10.1007/s10546-018-0358-2>  
 1356 Zhou Y, Li D, Li X (2019) The Effects of Surface Heterogeneity Scale on the Flux Imbalance under Free  
 1357 Convection. *J. Geophys. Res. Atmos.* <https://doi.org/10.1029/2018JD029550>  
 1358



## ACKNOWLEDGEMENTS

I would like to take this chance to thank all those who have made my work presented in this thesis possible, who have worked with me, supported, and accompanied me.

First, I would like to thank Matthias Mauder for giving me the opportunity to pursue my PhD within the TABLE group at IMK-IFU (KIT) and later at the Chair of Meteorology (TU Dresden). Thank you for the excellent supervision, the many inspiring discussions and answers to my questions. Thank you also for the many opportunities you gave me to present my work at international conferences and to make contacts in the scientific community.

I would also like to thank Ankur Desai for realizing the CHEESEHEAD19 project, without which this work would not have been possible. Thank you for welcoming me into your Ecometeorology Lab as a visiting scientist.

Many thanks to Sreenath Paleri for the great collaboration across an ocean. I am happy that we have grown to be good friends over the last few years.

Thanks to the CHEESEHEAD core team, Ankur Desai, Matthias Mauder, Stefan Metzger, Sreenath Paleri, Brian Butterworth, and David Durden and for the lively exchange of ideas every two weeks. Thanks to Johannes Speidel, Hannes Vogelmann and Matthias Perfahl for the good time in the crazy hunting cabin in the middle of nowhere during the field campaign. Thanks to everyone involved in the CHEESEHEAD project for the collaboration and for providing a treasure trove of data.

Great thanks to Matthias Sühling, Frederik De Roo and Basit Khan for explaining the PALM world to me.

Thanks to all my colleagues. First of all, to the ones at IMK-IFU, many of whom have become friends, for creating an inspiring work environment, especially the members of the TABLE working group, Jamie, Kevin, Ingo, Basit and Matthias. Thanks to Kevin for being the best office mate, and to Karina, Stephanie, Anne and Julius for sharing delicious lunch. Thanks to Christopher, you were a great Python and bouldering teacher.

Thanks to Sreenath, Bailey, Susi and Juliet for giving me a great time during my research stay in Madison.

Thanks to my new colleagues at the Chair of Meteorology at TUD for making me feel so welcome.

Special thanks as well to my co-authors, Matthias Sühling, Sreenath Paleri, Frederik De Roo, Marc Calaf, Martin Jung, Brian Butterworth, Ankur Desai and Matthias Mauder for the great collaborations and your contributions to the publication of the results that are presented in this thesis.

Also, thanks to Hanno, Klara and Sreenath for proofreading this thesis.

My work wouldn't have been possible without funding; therefore, I want to thank the National Science Foundation for funding the CHEESEHEAD19 project (Grant AGS-

1822420) and the Deutsche Forschungsgemeinschaft for funding the German contribution (Award #406980118). Thanks to the MICMoR Research School for providing funding for many of my visits at conferences and my research stay at the University of Wisconsin-Madison.

Finally, I would like to thank my family and friends for supporting me throughout the past few years. Special thanks to my husband Hanno, my sister Klara and my parents Hannelore and Alexander. You were always there to cheer me on and celebrate the small successes along the way.